Molecular machines and devices

Edited by Jan M. van Ruitenbeek

Imprint

Molecular machines and devices

Jan van Ruitenbeek

Editorial

Address:
Huygens-Kamerlingh Onnes Laboratory, Leiden Institute of Physics,
Leiden University, P.O. Box 9504, 2300 RA Leiden, The Netherlands

Email:
Jan van Ruitenbeek - ruitenbeek@physics.leidenuniv.nl

The suggestion to start this Thematic Series was first made at the symposium held on September 16–18, 2014 in Potsdam, Germany, under the same title, "Molecular Machines and Devices." The format of this Beilstein Nanotechnology Symposium is intended to bring a relatively small group of specialists together for a few days to discuss progress and open challenges. The range of topics is chosen such that it is not too wide in order to have enough concrete overlap of interests and backgrounds, but at the same time, wide enough to bring researchers together from fields that are somewhat disjoint. The three main topics in the 2014 Potsdam symposium were: molecular electronics, one-dimensional conductors, and synthetic molecular machines.

Molecular electronics is currently being developed mostly at the interface between organic chemistry and nanophysics, leaning strongly towards the fundamental understanding of electron transport at the smallest scale and applications in nanoelectronics. The second topic, one-dimensional conductors, has been studied both theoretically and experimentally in the field of mesoscopic physics. More recently, truly one-dimensional wires, which are assembled from molecular building blocks into conductive oligomeric chains, have started to be investigated.

This development provides a natural overlap between these two subfields of research. The third topic, synthetic molecular motors, has seen spectacular development in recent years, mostly in the research field of organic chemistry. In parallel, new theoretical ideas have been put forward by Tchavdar Todorov, Daniel Dundas, Mads Brandbyge, Per Hedegård, and others, which open the way for driving nanoscale motion by a dc current. The Potsdam meeting provided one of the first opportunities for researchers in each of these exciting but somewhat disconnected fields to interact and share ideas.

The format worked out beautifully. The number of participants, the setting at the shore of the beautiful Griebnitzsee, the diversity of research themes, the combination of theory and experiment, physics and chemistry, and the quality of the oral contributions all contributed to an atmosphere of enthusiasm and creativity. This can be judged from the fact that discussions continued over lunch and dinner and until late evening between participants with widely different backgrounds. One of the intriguing problems discussed included magnetic effects such as the giant, low field magnetoresistance observed at room temperature in organic nanowires presented by Wilfred van der Wiel [1]. The spin selectivity of transport through a helical organic

wire presented by Ron Naaman [2] provided ample food for debate and led to new ideas for experiments and theoretical interpretation. There is also an interesting link between the theme of the symposium to recent observations in biology. Spiros Skourtis introduced the audience to the remarkable discovery of electron transport along micrometer long biomolecular wires, so-called pilli, growing as extracellular appendages from the surface of certain bacteria. The present understanding of the electron-conduction mechanism is described in terms of a hopping mechanism having remarkable properties [3]. These and many more topics are represented by the contributions to this Thematic Series.

This series presents the current research developments for many of these scientific problems and challenges. The works illustrate the interesting combination of theoretical questions, dedicated instrumentation development, synthetic chemistry, and experimental observations. Concepts for electrically actuated, molecular scale motion are discussed in many of the contributions, where switches, pumps, or motors are considered, and first experimental evidence is presented. The progress in theory and experiment on single-molecule electron transport can be judged from many contributions in this volume. On the other hand, some subjects are not as well-covered, including electron transport in biomolecules and one-dimensional conductors. This is merely the result of fortuitous fluctuations in having the proper material timely available for this volume, rather than a bias of interest.

Indeed, important developments can be anticipated at the interface with biomolecular sciences. In parallel, the first applications of molecular electronics are appearing on the market in the form of molecular layers. The top-contact problem, which has hindered applications for a long time, is now at least partially resolved, so that we may anticipate more applications to follow. These will initially be in the form of layers of single molecules. The path to single-molecule devices is still long, but there is a lot of interesting material to be discovered on the way.

Jan van Ruitenbeek

Leiden, February 2016

References

1. Mahato, R. N.; Lülf, H.; Siekman, M. H.; Kersten, S. P.; Bobbert, P. A.; de Jong, M. P.; De Cola, L.; van der Wiel, W. G. *Science* **2013,** *341,* 257–260. doi:10.1126/science.1237242
2. Mathew, S. P.; Mondal, P. C.; Moshe, H.; Mastai, Y.; Naaman, R. *Appl. Phys. Lett.* **2014,** *105,* 242408. doi:10.1063/1.4904941
3. Polizzi, N. F.; Skourtis, S. S.; Beratan, D. N. *Faraday Discuss.* **2012,** *155,* 43–61. doi:10.1039/C1FD00098E

Charge carrier mobility and electronic properties of Al(Op)₃: impact of excimer formation

Andrea Magri[*1], Pascal Friederich[1], Bernhard Schäfer[1], Valeria Fattori[2], Xiangnan Sun[3], Timo Strunk[4], Velimir Meded[1], Luis E. Hueso[3], Wolfgang Wenzel[1] and Mario Ruben[1]

Abstract

We have studied the electronic properties and the charge carrier mobility of the organic semiconductor tris(1-oxo-1H-phenalen-9-olate)aluminium(III) (Al(Op)₃) both experimentally and theoretically. We experimentally estimated the HOMO and LUMO energy levels to be −5.93 and −3.26 eV, respectively, which were close to the corresponding calculated values. Al(Op)₃ was successfully evaporated onto quartz substrates and was clearly identified in the absorption spectra of both the solution and the thin film. A structured steady state fluorescence emission was detected in solution, whereas a broad, red-shifted emission was observed in the thin film. This indicates the formation of excimers in the solid state, which is crucial for the transport properties. The incorporation of Al(Op)₃ into organic thin film transistors (TFTs) was performed in order to measure the charge carrier mobility. The experimental setup detected no electron mobility, while a hole mobility between 0.6×10^{-6} and 2.1×10^{-6} cm²·V⁻¹·s⁻¹ was measured. Theoretical simulations, on the other hand, predicted an electron mobility of 9.5×10^{-6} cm²·V⁻¹·s⁻¹ and a hole mobility of 1.4×10^{-4} cm²·V⁻¹·s⁻¹. The theoretical simulation for the hole mobility predicted an approximately one order of magnitude higher hole mobility than was observed in the experiment, which is considered to be in good agreement. The result for the electron mobility was, on the other hand, unexpected, as both the calculated electron mobility and chemical common sense (based on the capability of extended aromatic structures to efficiently accept and delocalize additional electrons) suggest more robust electron charge transport properties. This discrepancy is explained by the excimer formation, whose inclusion in the multiscale simulation workflow is expected to bring the theoretical simulation and experiment into agreement.

Introduction

Since the field of organic electronics has emerged, interest in organic semiconductors (OSCs) has substantially increased [1]. The efficiency with which electron and/or holes move within the organic layer is crucial to device performance [2]. Since its first implementation in OLEDs devices [3], the small p-conjugated tris(8-hydroxyquinolinolate)aluminum(III) (Alq$_3$) is still the most commonly used and studied electron transport material among the small-molecule-based OSCs [4]. It is mostly chosen because of its integration properties, namely, it can be easily deposited as a thin film and included into devices with a variety of metallic electrodes. In addition, the electron mobility of Alq$_3$, which ranges between 10^{-5}–10^{-6} cm$^2\cdot$V$^{-1}\cdot$s^{-1}, is considerably higher than the corresponding hole mobility, measured between 10^{-8}–10^{-9} cm$^2\cdot$V$^{-1}\cdot$s^{-1} [5-12]. This is a principally important property that makes Alq$_3$ a fairly good electron transporting material and, in addition, an intrinsic hole blocking material, which is essential for charge recombination confinement and thereby increasing the efficiency of organic LED devices. As a result of the electron-deficient quinoline ligand, Alq$_3$ is characterized by HOMO and LUMO energy levels of $\approx$−5.95 and $\approx$−3.0 eV, respectively [13,14]. The LUMO and HOMO energy levels are fundamental parameters for charge transporting materials [15]. In particular, lower LUMO and HOMO energies enable easier reduction of the metal chelate, leading to enhanced electron injection and transport properties, and an increased resistance to oxidization, resulting in an improved hole blocking character. For this very reason we have synthesized and studied the phenalenyl-based alternative, OSC tris(1-oxo-1*H*-phenalen-9-olate)aluminum-(III) (Al(Op)$_3$) (see Figure 1), which is formed by ligands with an extended aromatic system. The expected result is an increased capability to accept and efficiently delocalize additional electrons, and thus, Al(Op)$_3$, should be characterized by both lower HOMO and LUMO energy levels as compared to Alq$_3$.
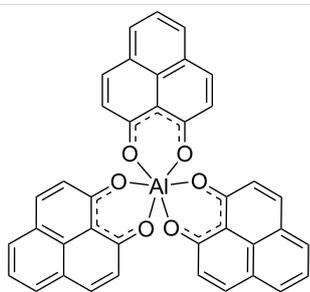
Figure 1: Tris(1-oxo-1*H*-phenalen-9-olate)aluminum(III) (Al(Op)$_3$) structure. H atoms are omitted for clarity.

In a recent work, Al(Op)$_3$ deposited on a magnetic cobalt substrate was investigated by means of ultraviolet photoemission spectroscopy (UPS) and near-threshold photoemission spectroscopy (NT-PS) [16]. The purpose was to study the spin-dependent properties of the Co/Al(Op)$_3$ hybrid interface in comparison with the Co/Alq$_3$ hybrid interface [17]. Due to the difference in the aromatic structures of Al(Op)$_3$ and Alq$_3$, which influences the chemisorption onto the cobalt substrate, it was demonstrated that the Co/Al(Op)$_3$ and the Co/Alq$_3$ interfaces have different electronic properties. In more detail, two hybrid interface states, which have energies (E−E_F) of −0.9 and −1.6 eV were detected in the Co/Al(Op)$_3$ interface, whereas in the Co/Alq$_3$, a single hybrid interface state at −0.8 was measured. In this work, the potential of the chemical tailoring of the aluminum complexes' ligands was successfully demonstrated along with the resulting effects on the electronic properties of the hybrid interfaces.

To our knowledge, this is surprisingly the first time that the electronic properties of Al(Op)$_3$ are reported. Phenalenyl-based complexes (more specifically lanthanoid phenalenyls) have been previously studied for their peculiar photoluminescence in the gas phase [18,19]. Greisch et al. observed that the alkali metal cationization of Eu(Op)$_3$ increases the capability of the ligand 1-oxo-1*H*-phenalen-9-olate to sensitize the europium ion. Furthermore, for lithium and sodium, the enhancement was found to be the most efficient. In these works, 9-hydroxy-phenalen-1-one was carefully chosen for its photophysical properties, namely, its high absorption cross section in the condensed phase between near-UV and 475 nm [20] and its phosphorescence at 17,350 cm^{-1}, which is characterized by a lifetime of about 25 ms [21]. Furthermore, Van Deun et al. demonstrated that 9-hydroxyphenalen-1-one can form stable complexes with lanthanides and transfer energy to europium in coordination complexes [22].

Many of the aforementioned properties stem either completely or mostly from the chosen ligand's chemical structure, specifically: the symmetrical geometry, the two oxygen atoms as chelating atoms, and the extended aromatic system. Considering this, we were interested in the possible impact of the given ligand on potential OSC opto-electronic performance.

Intrigued by establishing a direct relation between the chemical structure and the electronic properties of OSCs, we have fully characterized Al(Op)$_3$ by means of electrochemical and photophysical techniques in solution to estimate the HOMO/LUMO values as well as in thin films to investigate the solid state properties. Moreover, the aluminum complex has been implemented in organic thin film transistors devices (TFTs) to measure the charge carrier mobility. Finally, an extensive theoretical investigation has been carried out for comparison with the experimental data.

Results

Al(Op)$_3$ was synthesized as previously described [23]. To confirm the purity of the complex, proton and carbon nuclear magnetic resonance (NMR) spectroscopy and mass spectrometry (MS) were carried out and compared with the data reported in previous work [16].

Initially, in order to evaluate the potential incorporation of Al(Op)$_3$ in organic-based devices, we have estimated its HOMO/LUMO energies by electrochemical and photophysical methods in solution. The electron affinity (EA) was measured by means of cyclic voltammetry and the ionization potential (IP) was determined by the absorption spectrum. In experiment, the IP and the EA are referred to as the HOMO and LUMO energy levels of the molecule, respectively [15,24]. The cathodic cyclic voltammetry of Al(Op)$_3$, shown in Figure 2, is characterized by three, quasi-reversible, single-electron transfer processes at −1.63, −1.84 and −2.07 V. The subsequent formation of the mono-, di-, and tri-anion is assumed to occur due to the systematic reduction of each phenalenyl moiety [25]. Since electron transport can be represented as a series of consecutive redox processes, the reversible electrochemical reduction with an adequately high reduction potential is expected to promote the transport of electrons within the organic film [24]. From the onset of the first reduction wave, we have estimated a LUMO energy of Al(Op)$_3$ of −3.26 eV [26,27]. Implementing the same procedure, the LUMO energy of Alq$_3$ is −3.01 eV. As expected, the extended aromatic system of Al(Op)$_3$, which can more efficiently delocalize an additional electron, leads to a lower LUMO energy.

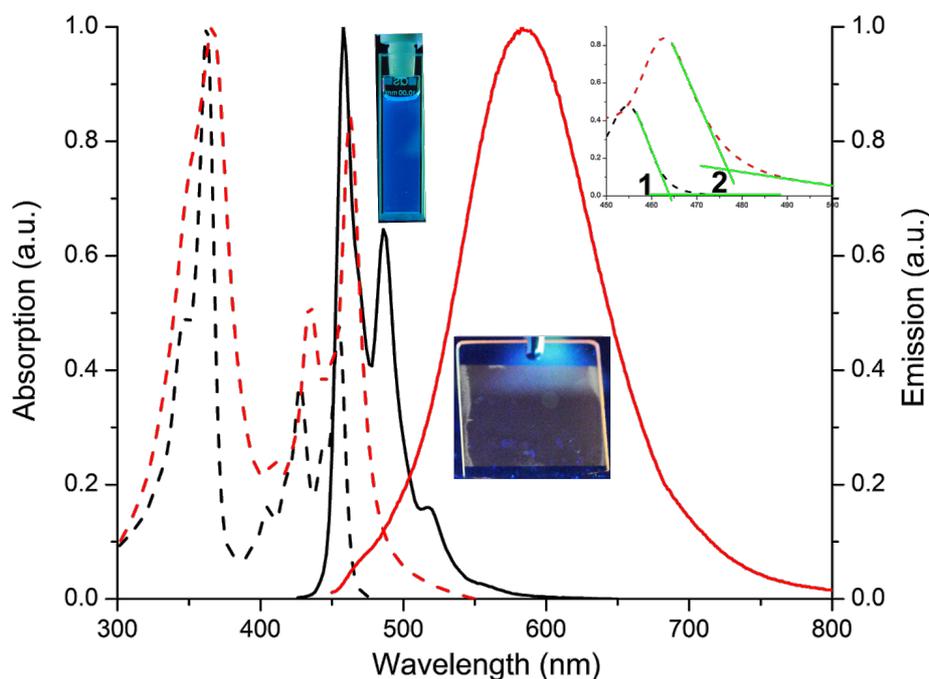Using the onset of the first band in the absorption spectrum in solution, as shown in Figure 3, an optical HOMO–LUMO gap of 2.67 eV was determined. Thus, the HOMO energy of Al(Op)$_3$ was calculated to be −5.93 eV, in fairly good agreement with the HOMO energy previously estimated by UPS on 1.5 and 5 nm films of Al(Op)$_3$ deposited on cobalt which are −6.5 and −6.9 eV, respectively [16]. According to the same procedure, the HOMO–LUMO gap and the HOMO energy of Alq$_3$ were estimated to be 2.82 and −5.83 eV, respectively. As a result of the lower LUMO energy of Al(Op)$_3$ compared to Alq$_3$, the injection of electrons should be not only possible, but enhanced, as a consequence of the reduced mismatch with a cathode such as aluminum with a work function of $\Phi \approx 4.3$ eV. In addition, considering the similar trend in the HOMO energies of Al(Op)$_3$ and Alq$_3$, we could, based on this single molecule energy analogy, assume that Al(Op)$_3$, when implemented in a device, would prevent hole diffusion in the same manner as Alq$_3$.

In order to confirm the thermal stability of Al(Op)$_3$, the complex was deposited by thermal evaporation onto a quartz substrate forming an 80 nm thin film and the photophysical properties were measured. The almost identical profiles of the absorption spectra in CH$_2$Cl$_2$ solution and in the thin film (see Figure 3) confirm that the complex was successfully grown onto the quartz substrate. Due to the solvatochromic effect, the absorption bands have different relative intensities and result in a slight shift [28,29]. Consequently, the HOMO–LUMO gap in the thin film is 2.60 eV, which is slightly narrower than in solution.

We have further investigated Al(Op)$_3$ by measuring the steady state emission spectra in solution and as a thin film at room temperature (see Figure 3). The emission in a CH$_2$Cl$_2$ diluted solution is characterized by a structured band with a maximum at 458 nm. Conversely, the emission in the thin film is dominated by a broad band peaked at 583 nm. To explain this, we have presumed excimer formation within the thin film. Normally, an excimer is caused by a charge-transfer interaction between an electronically excited species and a ground state molecule [30,31]. Often, the excimer possesses observable properties quite distinct from those of the single molecule [30,31]. The photophysical properties in solution and in thin film are summarized in Table 1 and are consistent with excimer formation. In more detail, Al(Op)$_3$ in solution is characterized by a photoluminescence quantum yield (Φ) of 0.027 and a lifetime (τ) of 0.7 ns. In the form of a thin film, the quantum yield (Φ) is considerably lower, 0.014, and the lifetime (τ) is an order of magnitude longer, 7.1 ns. The lifetimes were calculated by the luminescence decays, in solution and in the thin film, as shown in Figure 4.

Figure 2: Cyclic voltammogram for Al(Op)$_3$ recorded at room temperature in CH$_2$Cl$_2$ solution using TBAPF$_6$ as the electrolyte and ferrocene as an internal standard. Scan rate: 0.1 Vs^{-1}. The graphical estimation of the first reduction wave onset is highlighted in green. The LUMO energy level, −3.26 eV, was computed by using the onset of the first reduction wave at −1.54 V [24,25].

Figure 3: Absorption (dotted line) and emission spectra (solid line) of Al(Op)$_3$ in CH$_2$Cl$_2$ solution (black) and as a thin film on quartz (red). In the absorption spectra, the first band, between 325 and 375 nm (ε_{362} = 90.7 × 10^3 M^{-1}cm^{-1}), is associated with π→π* transitions. The second structured band, between 400 and 475 nm (ε_{454} = 43.6 × 10^3 M^{-1}cm^{-1}), is attributed to n→π* transitions. In the inset the region of the first absorption band and the graphical estimation of the onset of the bands are illustrated. The onset of Al(Op)$_3$ in solution is 464 nm (1) and in the thin film is 476 nm (2). The respective optical HOMO–LUMO band gaps converted to eV are 2.67 eV and 2.60 eV. The emission spectra were recorded with an excitation wavelength of 350 nm. The excimer formation is clearly noticeable from the difference in the emission peaks in solution and in the thin film. Photographs of the samples under UV irradiation are included to show the visible color change.

Table 1: Photophysical properties of Al(Op)$_3$ in CH$_2$Cl$_2$ solution and in the thin film at room temperature.

Al(Op)$_3$	$\lambda_{abs,max}$ [nm]	$\lambda_{emi,max}$ [nm]	Φ	τ [ns]
Solution	362	458	0.027	0.7
Thin film	366	583	0.014	7.1

Field effect mobility in TFT devices

From the electrical characteristics measured in a field-effect transistor (FET) configuration, it is possible to obtain the charge carrier mobility of electrons and holes [32]. Therefore, in order to measure the field-effect mobility of Al(Op)$_3$, thin film transistors (TFTs) based on Al(Op)$_3$ were fabricated. A series of Al(Op)$_3$-based TFTs were built with channel lengths ranging from 10 to 100 μm and with channel width/length (W/L) ratios of 20000/10, 20000/20, 10000/50, and 5000/100. From the electrical characterization of the TFT devices, the transfer curves, which yield the charge carrier mobility, were determined. As an example, in Figure 5, the transfer curve relative to the TFT device with a channel length of 100 μm is shown. The curve clearly outlines a p-type transistor behavior of the device [33-35], and the on/off current ratio calculated from this curve is
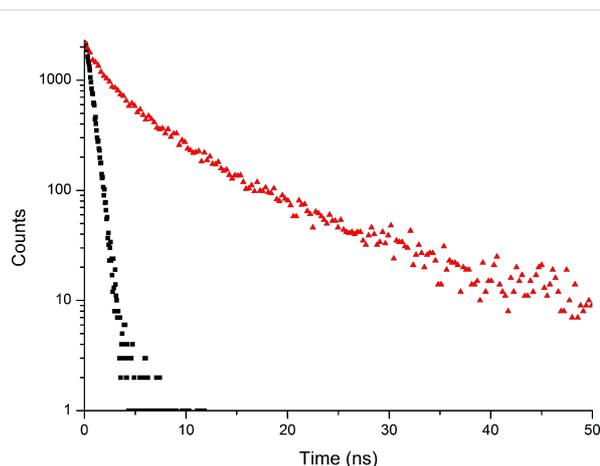
Figure 4: Luminescence decay in CH$_2$Cl$_2$ solution (black) and as a thin film on quartz (red). In solution, a mono-exponential decay is observed with a lifetime τ ≈ 0.7 ns, while in the thin film, a multi-exponential decay is observed with an average lifetime τ ≈ 7.1 ns.

greater than 10^4. As a result of the electrical characterization of four Al(Op)$_3$-based TFT devices, we have estimated the field effect mobility from the slope of the high-voltage section of the transfer curve by the equation for the saturation regime [34,35].

The hole mobility was found to range between 0.6×10^{-6} and 2.1×10^{-6} cm$^2 \cdot$V$^{-1} \cdot$s^{-1}, and the threshold voltage between -35 and -45 V.
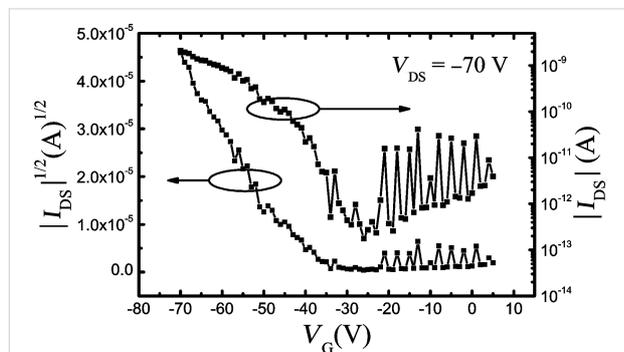
Figure 5: Transfer curve of the Al(Op)$_3$-based TFT with a channel length of 100 µm. In this figure, I_{DS} and V_{DS} are the source–drain current and voltage and V_G refers to the gate voltage. The hole mobility, extrapolated by the transfer characteristics, ranges between 0.6×10^{-6} and 2.1×10^{-6} cm$^2 \cdot$V$^{-1} \cdot$s^{-1}.

In the transfer characteristics (see Figure 6), the source–drain currents (I_{SD}) are far higher than the leakage current (gate current, I_G) in the high voltage regime in which the mobility has been calculated [34,35]. Therefore, we can conclude that the measured hole mobility from the transfer curves is reliable and not substantially impacted by the leakage current [34,35].
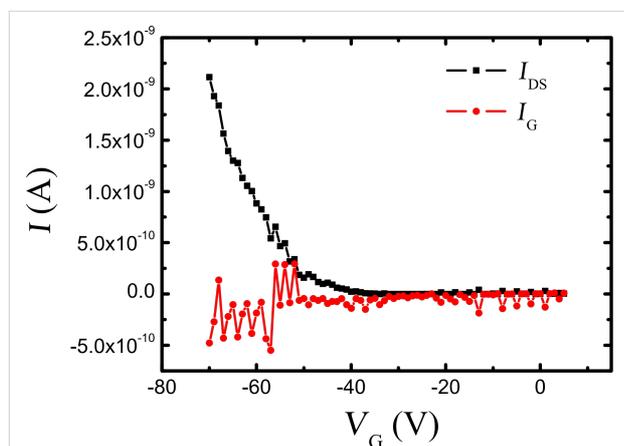
Figure 6: Comparison of the source–drain current (I_{DS}) and the leakage gate current (I_G) from the transfer characterization of the Al(Op)$_3$-based TFT with a channel length of 100 µm. The source–drain bias, V_{DS}, for this measurement is -70 V. I_{SD} currents are far higher than I_G in the high voltage regime, indicating that the mobility calculated from the transfer curves is reliable and not impacted by the leakage current.

In all the measurements performed on the Al(Op)$_3$-based TFTs no obvious electron mobility was detected. This was indeed expected, due to the excimer formation observed in the solid state photo-physical characterization. Excimers in the organic

thin film or at the organic/organic interface (exciplexes) act as electron traps, and as a result, the electron mobility can be lowered until the point of suppression (i.e., below the sensitivity of the instrumentation).

Theory of HOMO–LUMO level charge mobility

In order to shed more light on the problem at hand, we performed density functional-based [36-38] calculations for both a single molecule in vacuum and molecules embedded in an explicit matrix [39] and compared them to a de facto standard in the field, namely, Alq$_3$.

Structurally, Al(Op)$_3$ is formed by symmetric ligands that bind to the Al^{3+} ion via oxygen donor atoms only. As a consequence, the electron density of the HOMO/LUMO levels (shown in Figure 7a) is equally distributed over the three chelating moieties. In contrast, in Alq$_3$ oxygen and nitrogen atoms connect to the metal ion in symmetrically non-equivalent positions. Hence, the HOMO/LUMO energies of Alq**$_3$** are localized mainly on one ligand [40]. The results for HOMO/LUMO levels of Al(Op)$_3$ calculated with DFT (but on different level of theory) are shown in Figure 8. We calculated the ionic and electronic ground state of the molecule in vacuum and extracted the HOMO and the LUMO energies of -5.71 eV and -2.41 eV with a gap of 3.3 eV (376 nm). Compared to that, the HOMO and
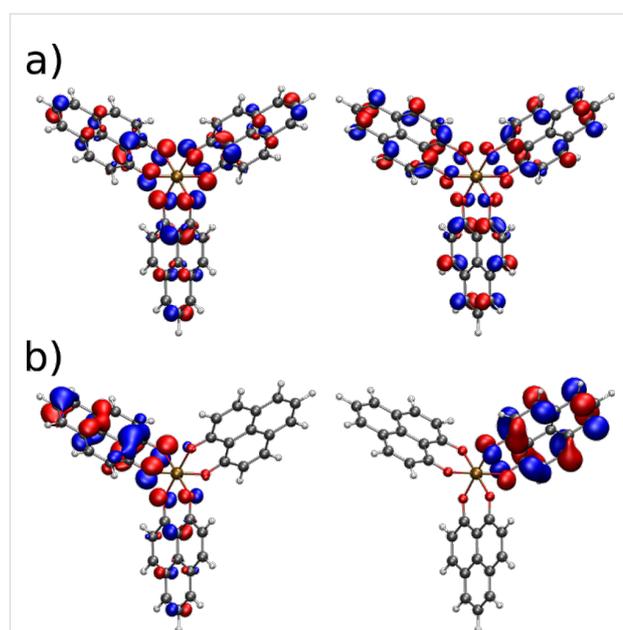
Figure 7: a) HOMO (left) and LUMO (right) orbitals of Al(Op)$_3$ calculated with TURBOMOLE [36] on a B3-LYP [37]/SV(P) [38] level of theory in vacuum. b) The same orbitals calculated in the explicit matrix, represented by a self-consistently evaluated cloud of point charges. The electrostatic interaction with the environment leads to the localization of the frontier orbitals.

LUMO energies of the widely studied Alq$_3$ molecule are −5.14 eV and −1.91 eV with a gap of 3.22 eV (385 nm).
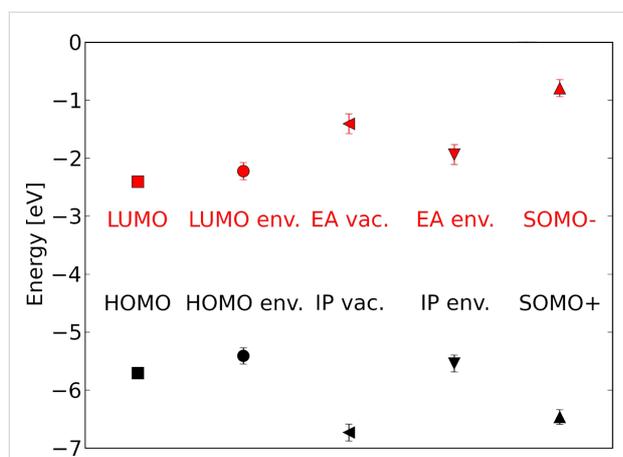
Figure 8: Energy levels of Al(Op)$_3$ calculated with different conditions, namely, HOMO and LUMO in vacuum (vac.) and in a self-consistent electrostatic environment (env.), with electron affinity (EA) and ionization potential (IP) in vacuum and environment and SOMO + and − orbitals in vacuum.

After performing the single molecule vacuum calculations, we set up calculations for molecules in a matrix, which gives the molecular properties in terms of distributions, with both center and width, rather than unique numbers. The calculation of HOMO and LUMO levels in the condensed phase from an atomistic morphology using the quantum patch method without additional charges [39] leads to −5.41 eV for the HOMO energy and −2.22 eV for the LUMO energy. The calculation of the ionization potential and the electron affinity by the self-consistent evaluation of the total energies of charged and uncharged molecules in the condensed phase leads to IP = 6.73 eV and EA = 1.41 eV in vacuum and IP = 5.54 eV and EA = 1.94 eV in environment. Additional charges in the system, which can be considered as SOMO+ and SOMO− orbital energies, lead to values of −6.47 eV for the oxidized state (hole) and −0.79 eV for the reduced state (electron). The self-consistently evaluated HOMO and LUMO levels in an Alq$_3$ matrix are −5.07 eV and −1.80 eV, respectively. The vacuum IP is 6.54 eV and the vacuum EA is 0.64 eV. In the matrix, the IP is 5.34 eV and the EA is 1.5 eV. The SOMO+ and SOMO− orbitals are at

−6.47 eV and 0.19 eV, respectively. All calculations were performed with the B3LYP [37] exchange correlation functional and an SV(P) [38] basis set.

The comparison between the calculated dipole moments of Al(Op)$_3$ and Alq$_3$ show a much weaker dipole moment of 0.10 D for Al(Op)$_3$ as compared to the vacuum dipole moment of 4.46 D for Alq$_3$. On the other hand, in the matrix, the dipole moment for Al(Op)$_3$ is 1.51 ± 0.60 D and 5.55 ± 0.91 D for Alq$_3$. The increase of the dipole moment of Al(Op)$_3$ is much more dramatic, indicating a break in the intrinsic, vacuum symmetry, which is reflected in the orbital localization and is clearly observable in Figure 7b. As we treated the molecules in the matrix to be rigid, the deviations between the vacuum and matrix dipole moments arise from induction and polarization effects present only in the matrix, which influence the energy disorder.

Furthermore, we calculated the width of the local density of states for additional charges (if a Gaussian shape is assumed, this is referred to as energy disorder, σ), the mean electronic coupling between molecules, $<J^2r^2>$, the mean number of neighbors, M, and the reorganization energy, $λ$. These results are shown in Table 2. These microscopic parameters can be used to calculate the charge carrier mobility [41]:

$$\mu = \frac{e\beta M \left\langle J^2 r^2 \right\rangle}{n\hbar\sqrt{\lambda}} \sqrt{\frac{\pi\beta}{1+\dfrac{\beta\sigma^2}{\lambda}}} \exp\left[-\frac{1}{4}\left((\beta\sigma)^2 - \beta\lambda\right)\right] \quad (1)$$

where e is the electric charge and $\hbar$ is the Plank constant. The reciprocal temperature, $β$, is defined as $β = 1/k_BT$, where k_B is the Boltzmann constant and T is the temperature, held constant at 290 K for these calculations. This analytic expression yields a zero-field charge carrier mobility of $1.4 × 10^{-4}$ cm^2·V^{-1}·s^{-1} for holes and $9.5 × 10^{-6}$ cm^2·V^{-1}·s^{-1} for electrons, which can be compared to Alq$_3$ having a hole mobility of $3.3 × 10^{-8}$ cm^2·V^{-1}·s^{-1} and an electron mobility of $9.2 × 10^{-8}$ cm^2·V^{-1}·s^{-1}. The differences between AlOp$_3$ and Alq$_3$ mainly arise from different dipole moments, which lead to

Table 2: Microscopic parameters and charge carrier mobility for Al(Op)$_3$ and Alq$_3$ used as input in Equation 1.

	σ [eV]	$<J^2r^2>$ [eV^{2}Å^2]	M	$λ$ [eV]	$μ$ [cm^2·V^{-1}·s^{-1}]
Al(Op)$_3$ hole transport	0.142	$4.42 × 10^{-3}$	7.9	0.055	$1.4 × 10^{-4}$
Al(Op)$_3$ electron transport	0.167	$7.04 × 10^{-3}$	7.9	0.060	$9.5 × 10^{-6}$
Alq$_3$ hole transport	0.187	$1.10 × 10^{-2}$	5.6	0.336	$3.3 × 10^{-8}$
Alq$_3$ electron transport	0.184	$1.34 × 10^{-2}$	5.6	0.285	$9.2 × 10^{-8}$

a higher energy disorder, σ, for Alq$_3$. Al(Op)$_3$ reacts less strongly on charging, leading to a smaller reorganization energy, λ, than for Alq$_3$. The slightly higher electronic coupling, $<J^2r^2>$, of Alq$_3$ is compensated by a smaller number of neighbors, *M*. The calculated HOMO and especially LUMO levels are comparable to those of Alq$_3$ (−5.14 and −1.91 eV without environment), making electron injection in general plausible. The simulated hole mobility is about one order of magnitude higher than the mobility of 9.5×10^{-6} cm^2·V^{-1}·s^{-1} measured in experiment. This overestimation is considered reasonable as our morphologies consist of rigid Al(Op)$_3$ molecules, which leads to a slight underestimation of the energy disorder, and therefore, a calculated mobility that is too high. Further, it is known from previous studies [39] that the experimental results for charge mobility can vary by up to two orders of magnitude, depending on the details of the experimental setup.

Nonetheless, the lack of electron mobility in the experiment can be explained by the observation of excimer formation in Al(Op)$_3$, as explained above. Accounting for the excimer formation in the charge mobility workflow is expected to considerably improve the agreement between theory and experiment.

Discussion

The initial estimate, which due to the extended aromatic system of the ligand Al(Op)$_3$ should be characterized by lower HOMO/LUMO energy levels as compared to Alq$_3$, has been proven by experimental and theoretical methods. The HOMO/LUMO energy levels of Al(Op)$_3$ are: −5.93 and −3.26 eV experimental, −5.71 and −2.42 eV theoretical in vacuum and −5.41 and −2.22 eV theoretical in the assumed amorphous film. The HOMO/LUMO energy levels of Alq$_3$ are: −5.83 and −3.01 eV experimental, −5.14 and −1.91 eV theoretical in vacuum and −5.07 and −1.80 eV theoretical in the assumed amorphous film. As a consequence, the electron injection from a cathode should be more efficient in Al(Op)$_3$ layers compared to Alq$_3$. Nonetheless, the Al(Op)$_3$ HOMO energy is high enough to prevent hole diffusion. The major drawback of the extended and flat aromatic system, which can accept and efficiently delocalize up to three electrons at relatively low reduction potentials (as shown by the cyclic voltammetry experiment in Figure 2), is the formation of excimers in the solid state (see Figure 3). Excimers or exciplexes are known to prevent electron diffusion, acting as traps in the organic layer. This is confirmed by the charge carrier mobility measured in TFT devices where a hole mobility between 0.6×10^{-6} and 2.1×10^{-6} cm^2·V^{-1}·s^{-1} was measured. However, no electron mobility was detected. Nevertheless, the experimentally measured Al(Op)$_3$ hole mobility is two orders of magnitude higher than the reported hole mobility of Alq$_3$, which ranges between 10^{-8} and 10^{-9} cm^2·V^{-1}·s^{-1}. This trend is

confirmed by simulations produced by the newly developed, multiscale, charge mobility workflow. Here, the calculated hole mobility for Al(Op)$_3$ and Alq$_3$ is 9.5×10^{-6} and 9.2×10^{-8} cm^2·V^{-1}·s^{-1}, respectively. The initial assumption of the easier delocalization and transport of electrons (sustained by the extended aromatic system of the ligand forming the coordination complex Al(Op)$_3$) is confirmed by the electron mobility calculation. The predicted electron mobility for Al(Op)$_3$ and Alq$_3$ is 1.4×10^{-4} and 3.3×10^{-8} cm^2·V^{-1}·s^{-1}, respectively. While the calculations exclude increased thin film disorder as a contributing factor to the experimentally observed low electron mobility, in order to obtain accurate and realistic predictions on the charge mobility, taking the formation of excimers in the thin film into account is of a primary importance.

Conclusion

We have synthesized and characterized a novel, Al-based, metallo-organic molecule as an alternative to the de facto, industry standard, electron transporting material, Alq$_3$. The initial assumptions based on the extended aromatic structure of Al(Op)$_3$ and confirmed by the theoretical DFT-based simulations (1.4×10^{-4} cm^2·V^{-1}·s^{-1} electron mobility and 9.5×10^{-6} cm^2·V^{-1}·s^{-1} hole mobility) indicated that the material would be a good Alq$_3$ alternative. However, excimer formation, as observed in the photoluminescence experiments in the solid state, may play the most decisive role in disrupting the electron flow through the deposited thin films. Indeed, this is confirmed by Al(Op)$_3$-based TFTs devices, in which a hole mobility between 0.6×10^{-6} and 2.1×10^{-6} cm^2·V^{-1}·s^{-1} was measured, whereas the electron mobility could not be determined. As such, including the excimeric effect into future multiscale simulations seems to be of great importance. The fact that the hole mobility in both theory and experiment as compared to Alq$_3$ is considerably higher by two to four orders of magnitude implies that this material cannot be considered as a good hole blocking layer material. As such, it could be used in organic electronic devices only together with an additional explicit hole blocking material layer.

Experimental

Al(Op)$_3$ was synthesized according to the procedure reported in [16]. The analytical characterization data of Al(Op)$_3$ can also be found in [16].

Characterization in solution

Cyclic voltammetry was performed using an Autolab PGSTAT10 potentiostat in a three-electrode single-compartment cell with a glassy carbon working electrode, an Ag/AgCl pseudo-reference electrode and a platinum wire as an auxiliary electrode, in an inert argon atmosphere. Tetrabutylammonium hexafluorophosphate (TBAPF$_6$) was used as a supporting elec-

trolyte (0.1 M) and CH_2Cl_2 was used as the solvent. The concentration of the samples was 1.0×10^{-4} M, and the solutions were degassed with argon prior to the measurements. A scan rate of 100 mV·s^{-1} was employed. Ferrocene was used as an internal standard to calculate the corrected redox potential. Absorption and emission spectra were acquired at room temperature for diluted CH_2Cl_2 solutions (8.0×10^{-6} M) on a Cary 500 Scan UV–vis–NIR spectrophotometer and a Cary Eclipse fluorescence spectrophotometer using a 1 cm quartz cell. The photoluminescence quantum yield was computed using rhodamine 6G as reference [42,43].

Characterization in thin film

The evaporation of the samples on quartz substrates was carried out using an Edwards Auto 306 evaporator equipped with a high vacuum chamber (10^{-6} mbar) and a frequency thickness monitor (FTM) to check the evaporation rate. The deposition rate was 0.5 nm·s^{-1} with a final thickness of 80 nm. The solid state absorption spectra were recorded on a Perkin-Elmer Lamba 900 UV–vis–NIR spectrophotometer, the photoluminescence spectra of Alq$_3$ and Al(Op)$_3$ were acquired on a Spex Fluorolog 2. The photoluminescence quantum yield in solid state was estimated by the absolute method using an integrating sphere [44]. The lifetimes were obtained on a time-correlated single photon counter (TCSPC) equipped with a NanoLED source and a Horiba Jobin-Yvon Fluorohub for the data elaboration.

TFT fabrication and characterization

The Al(Op)$_3$-based TFTs were fabricated with a bottom-gated bottom contact geometry. In these devices, highly doped p-type Si, which has a 150 nm thermally grown SiO$_2$ layer on the top, was employed as the substrate and as the bottom gate electrode. The source and drain electrodes were patterned on the Si–SiO$_2$ substrates by electron beam lithography (Raith 150). These electrodes were deposited under high vacuum (Oerlikon evaporator) with an architecture composed of a 1.2 nm Ti bottom part and a 42 nm Au top part. Before depositing the organic layer, the substrate was cleaned by oxygen plasma for 5 min and modified with trichloro(octadecyl)silane (OTS, ≥90%, Aldrich) by the vapor-phase modification method. This process was carried out in a vacuum oven placed inside a glove box with an inert N$_2$ atmosphere (H$_2$O and O$_2$ concentration <0.1 ppm). Finally, a 40 nm Al(Op)$_3$ layer was deposited on the OTS-modified substrate in a ultra-high vacuum evaporator (a dual chamber, Theva system). The Al(Op)$_3$-based TFTs were characterized in a Lake Shore probe station with a Keithley 4200 semiconductor characterization system. All the TFT electrical measurements were carried out under vacuum at room temperature and in the dark to avoid decomposition of the organic material.

Theoretical Method

The charge carrier mobility was calculated by means of the newly developed, multiscale, charge mobility workflow [39,41,45] for both Al(Op)$_3$ and Alq$_3$ in order to gain a detailed understanding of the differences in the electronic structure and microscopic properties between these two materials.

The simulation of the charge mobility requires coupling of macroscopic system properties, such as the intrinsic bulk mobility, temperature, applied bias voltage, etc., with the microscopic (often local) properties, such as energy disorder, intermolecular electronic coupling, reorganization energy, etc. Thus, this work thereby constitutes one of the quintessential multiscale problems. These properties by themselves require corresponding, often sophisticated and mutually very different, description formalisms. This is indicated by the term "multiscale" itself, as this formalism describes phenomena existing on vastly different time and length scales.

Atomistic morphologies were generated with a Monte Carlo-based, simulated annealing method [46]. The microscopic properties, such as energetic disorder and electronic coupling between the molecules and reorganization energies, were calculated with the quantum patch method as described in [39]. These microscopic parameters were used in an analytic, Marcus-rate-based [45], effective medium approach [38], in order to estimate the charge carrier mobility for electrons and holes in these materials for zero-field and low-carrier concentrations. All quantum chemical calculations were adapted directly into the multiscale workflow, as well as any additional quantum chemical characterization were performed with TURBOMOLE [36] on a B3-LYP [37]/SV(P) [38] level of theory. For the calculation of reorganization energy, a def2-TZVP [47] basis set was used.

References

1. Forrest, S.; Burrows, P.; Thompson, M. *IEEE Spectrum* **2000,** *37,* 29–34. doi:10.1109/6.861775
2. Coropceanu, V.; Cornil, J.; da Silva Filho, D. A.; Olivier, Y.; Silbey, R.; Brédas, J.-L. *Chem. Rev.* **2007,** *107,* 926–952. doi:10.1021/cr050140x
3. Tang, C. W.; VanSlyke, S. A. *Appl. Phys. Lett.* **1987,** *51,* 913–915. doi:10.1063/1.98799
4. Hung, L. S.; Chen, C. H. *Mater. Sci. Eng., R* **2002,** *39,* 143–222. doi:10.1016/S0927-796X(02)00093-1
5. Kepler, R. G.; Beeson, P. M.; Jacobs, S. J.; Anderson, R. A.; Sinclair, M. B.; Valencia, V. S.; Cahill, P. A. *Appl. Phys. Lett.* **1995,** *66,* 3618–3620. doi:10.1063/1.113806
6. Kalinowski, J.; Camaioni, N.; Di Marco, P.; Fattori, V.; Martelli, A. *Appl. Phys. Lett.* **1998,** *72,* 513–515. doi:10.1063/1.120805
7. Chen, B. J.; Lai, W. Y.; Gao, Z. Q.; Lee, C. S.; Lee, S. T.; Gambling, W. A. *Appl. Phys. Lett.* **1999,** *75,* 4010. doi:10.1063/1.125521

8. Mückl, A. G.; Berleb, S.; Brütting, W.; Schwoerer, M. *Synth. Met.* **2000,** *111,* 91–94. doi:10.1016/S0379-6779(99)00367-7
9. Naka, S.; Okada, H.; Onnagawa, H.; Yamaguchi, Y.; Tsutsui, T. *Synth. Met.* **2000,** *111,* 331–333. doi:10.1016/S0379-6779(99)00358-6
10. Barth, S.; Müller, P.; Riel, H.; Seidler, P. F.; Rieß, W.; Vestweber, H.; Bässler, H. *J. Appl. Phys.* **2001,** *89,* 3711–3719. doi:10.1063/1.1330766
11. Malliaras, G. G.; Shen, Y.; Dunlap, D. H.; Murata, H.; Kafafi, Z. H. *Appl. Phys. Lett.* **2001,** *79,* 2582. doi:10.1063/1.1410343
12. Fong, H. H.; So, S. K. *J. Appl. Phys.* **2006,** *100,* 094502. doi:10.1063/1.2372388
13. Anderson, J. D.; McDonald, E. M.; Lee, P. A.; Anderson, M. L.; Ritchie, E. L.; Hall, H. K.; Hopkins, T.; Mash, E. A.; Wang, J.; Padias, A.; Thayumanavan, S.; Barlow, S.; Marder, S. R.; Jabbour, G. E.; Shaheen, S.; Kippelen, B.; Peyghambarian, N.; Wightman, R. M.; Armstrong, N. R. *J. Am. Chem. Soc.* **1998,** *120,* 9646–9655. doi:10.1021/ja980707+
14. Montes, V. A.; Pohl, R.; Shinar, J.; Anzenbacher, P., Jr. *Chem. – Eur. J.* **2006,** *12,* 4523–4535. doi:10.1002/chem.200501403
15. Shirota, Y.; Kageyama, H. *Chem. Rev.* **2007,** *107,* 953–1010. doi:10.1021/cr050143+
16. Müller, S.; Steil, S.; Droghetti, A.; Großmann, N.; Sanvito, S.; Meded, V.; Magri, A.; Schäfer, B.; Fuhr, O.; Ruben, M.; Cinchetti, M.; Aeschlimann, M. *New J. Phys.* **2013,** *15,* 113054. doi:10.1088/1367-2630/15/11/113054
17. Steil, S.; Großmann, N.; Laux, M.; Ruffing, A.; Steil, D.; Wiesenmayer, M.; Mathias, S.; Monti, O. L. A.; Cinchetti, M.; Aeschlimann, M. *Nat. Phys.* **2013,** *9,* 242–247. doi:10.1038/nphys2548
18. Greisch, J.-F.; Harding, M. E.; Schäfer, B.; Rotter, M.; Ruben, M.; Klopper, W.; Kappes, M. M.; Schooss, D. *J. Phys. Chem. A* **2014,** *118,* 94–102. doi:10.1021/jp4086624
19. Greisch, J.-F.; Harding, M. E.; Schäfer, B.; Ruben, M.; Klopper, W.; Kappes, M. M.; Schooss, D. *J. Phys. Chem. Lett.* **2014,** *5,* 1727–1731. doi:10.1021/jz500614x
20. Haddon, R. C.; Rayford, R.; Hirani, A. M. *J. Org. Chem.* **1981,** *46,* 4587–4588. doi:10.1021/jo00335a060
21. Bondybey, V. E.; Haddon, R. C.; English, J. H. *J. Chem. Phys.* **1984,** *80,* 5432. doi:10.1063/1.446650
22. Van Deun, R.; Nockemann, P.; Fias, P.; Van Hecke, K.; Van Meervelt, L.; Binnemans, K. *J. Chem. Commun.* **2005,** 590–592. doi:10.1039/b414703k
23. Haddon, R. C. Electron transport material and light emitting diode that contains the electron transport material. U. S. Patent 6428912, Aug 6, 2002.
24. Kulkarni, A. P.; Tonzola, C. J.; Babel, A.; Jenekhe, S. A. *Chem. Mater.* **2004,** *16,* 4556–4573. doi:10.1021/cm049473l
25. Monzon, L. M. A.; Burke, F.; Coey, J. M. D. *J. Phys. Chem. C* **2011,** *115,* 9182–9192. doi:10.1021/jp201019c
26. Bard, A.; Faulkner, R. *Electrochemical Methods–Fundamentals and Applications,* 2nd ed.; Wiley-VCH: New York, NY, USA, 2001.
27. Pommerehne, J.; Vestweber, H.; Guss, W.; Mahrt, R.; Bässler, H.; Porsch, M.; Daub, J. *Adv. Mater.* **1995,** *7,* 551–554. doi:10.1002/adma.19950070608
28. Bykowski, D.; McDonald, R.; Hinkle, R. J.; Tykwinski, R. R. *J. Org. Chem.* **2002,** *67,* 2798–2804. doi:10.1021/jo015910t
29. Renger, T.; Grundkötter, B.; Madjet, M. E.-A.; Müh, F. F. *Proc. Natl. Acad. Sci. U. S. A.* **2008,** *105,* 13235–13240. doi:10.1073/pnas.0801025105
30. Birks, J. B. *Photophysics of Aromatic Molecules;* Wiley-Interscience: London, United Kingdom, 1970.
31. Turro, N. J. *Modern Molecular Photochemistry;* University Science Book: California, USA, 1991.
32. Horowitz, G. *Adv. Mater.* **1998,** *10,* 365–377. doi:10.1002/(SICI)1521-4095(199803)10:5<365::AID-ADMA365>3.0.CO;2-U
33. Reese, C.; Roberts, M.; Ling, M.-m.; Bao, Z. *Mater. Today* **2004,** *7,* 20–27. doi:10.1016/S1369-7021(04)00398-0
34. Klauk, H. *Chem. Soc. Rev.* **2010,** *39,* 2643–2666. doi:10.1039/b909902f
35. Bao, Z.; Locklin, J., Eds. *Organic Field-Effect Transistors;* CRC Press: Boca Raton, FL, USA, 2007. doi:10.1201/9781420008012
36. Ahlrichs, R.; Bär, M.; Häser, M.; Horn, H.; Kölmel, C. *Chem. Phys. Lett.* **1989,** *162,* 165–169. doi:10.1016/0009-2614(89)85118-8
37. Becke, A. D. *J. Chem. Phys.* **1993,** *98,* 1372–1377. doi:10.1063/1.464304
38. Schäfer, A.; Horn, H.; Ahlrichs, R. *J. Chem. Phys.* **1992,** *97,* 2571–2577. doi:10.1063/1.463096
39. Friederich, P.; Symalla, F.; Meded, V.; Neumann, T.; Wolfgang, W. *J. Chem. Theory Comput.* **2014,** *10,* 3720–3725. doi:10.1021/ct500418f
40. Curioni, A.; Boero, M.; Andreoni, W. *Chem. Phys. Lett.* **1998,** *294,* 263–271. doi:10.1016/S0009-2614(98)00829-X
41. Rodin, V.; Nelles, G.; von Wrochem, F.; Meded, V.; Danilov, D.; Poschlad, A.; Wenzel, W. *Phys. Rev. B* **2015,** in press.
42. Bindhu, C. V.; Harilal, S. S.; Nampoori, V. P. N.; Vallabhan, C. P. G. *Mod. Phys. Lett. B* **1999,** *13,* 563–576. doi:10.1142/S0217984999000725
43. Stürzl, N.; Lebedkin, S.; Kappes, M. M. *J. Phys. Chem. A* **2009,** *113,* 10238–10240. doi:10.1021/jp905166s
44. de Mello, J. C.; Wittmann, H. F.; Friend, R. H. *Adv. Mater.* **1997,** *9,* 230–232. doi:10.1002/adma.19970090308
45. Marcus, R. A. *Annu. Rev. Phys. Chem.* **1964,** *15,* 155–196. doi:10.1146/annurev.pc.15.100164.001103
46. Neumann, T.; Danilov, D.; Lennartz, C.; Wenzel, W. *J. Comput. Chem.* **2013,** *34,* 2716–2725. doi:10.1002/jcc.23445
47. Schäfer, A.; Huber, C.; Ahlrichs, R. *J. Chem. Phys.* **1994,** *100,* 5829–5835. doi:10.1063/1.467146

License and Terms

Closed-loop conductance scanning tunneling spectroscopy: demonstrating the equivalence to the open-loop alternative

Chris Hellenthal, Kai Sotthewes, Martin H. Siekman, E. Stefan Kooij[*]
and Harold J. W. Zandvliet

Abstract

We demonstrate the validity of using closed-loop $z(V)$ conductance scanning tunneling spectroscopy (STS) measurements for the determination of the effective tunneling barrier by comparing them to more conventional open-loop $I(z)$ measurements. Through the development of a numerical model, the individual contributions to the effective tunneling barrier present in these experiments, such as the work function and the presence of an image charge, are determined quantitatively. This opens up the possibility of determining tunneling barriers of both vacuum and molecular systems in an alternative and more detailed manner.

Introduction

Although the scanning tunneling microscope (STM) has been used for the topographical imaging of conductive samples since the early 1980s [1], recent times have seen an increasing interest in the possibilities of (semi-)quantitative analysis offered by scanning tunneling spectroscopy (STS). STS measurements are typically performed in a $X(Y)$ format, where variable Y is actively driven and the response of variable X is measured, with all other system variables being kept constant. Numerous types of STS techniques can be and have been performed on a wide variety of samples, with each different type of measurement yielding information on distinct properties of the probed sample [2].

The local density of states of a sample (LDOS) provides insight into the electronic and chemical properties of a sample. By making a spatial map of the LDOS, standing wave patterns and local electron distributions can be visualized, enabling further understanding of the exact local quantum behavior of features on the surface [3,4]. LDOS information is typically extracted through open-loop $I(V)$ measurements, although recent studies have reported on the possibility of obtaining LDOS information by using closed-loop $z(V)$ measurements [5-8].

Another field of interest is the determination of the work function of materials, through the use of either STS or mechanical

break junction (MBJ) measurements. In the case of STS measurements, perhaps the most simple method of determining the work function is performing $I(z)$ spectroscopy and plotting the natural logarithm of the measured tunneling conductance G as function of the tip–sample distance. The slope of the obtained line is equal to the inverse decay length κ which, for low bias voltages, is proportional to the square root of the work function. Several papers have also been written on the validity of applying this same method to $z(V)$ spectroscopy measurements [9-11], although no direct comparison between $z(V)$ and $I(z)$ measurements was performed. Another method relies on the observation of so-called Gundlach oscillations [12-14]. These oscillations can be observed in $I(V)$ and $z(V)$ measurements, but require the use of bias voltages that exceed the work function of the probed sample, often necessitating bias voltages in excess of 4 V. In order to get around this restriction, recent studies have focussed on the application of transition voltage spectroscopy (TVS) [15-17]. By determining the bias voltage at which tradiitional tunneling is replaced by Fowler–Nordheim transport as a function of the tip–sample distance, the work function can be determined at relatively low bias voltages of about 2 V.

A potential source of error when determining the work function in a vacuum system is the presence of image charges [18,19]. These image charges are induced by tunneling electrons and have an attractive interaction with them, lowering the measured effective barrier height. If one simply assumes that the effective barrier height is equal to the work function, the presence of image charges will lead to values for ϕ_0 that are significantly lower than one would expect.

Determining the tunnel behavior in molecular junctions can give an indication of the properties of the molecule under consideration, and extensive research has been performed on numerous different systems [20-24]. In 2004, Engelkes et al. determined the resistance of a molecular junction as a function of the length of the used molecule [25]. Additionally, the effective mass of electrons has also been determined through the use of tunneling measurements [26]. Another active area of research deals with the interfaces between the molecule and the metal contacts making up the junction [27].

In this article, the effective tunneling barrier height is determined through the use of conductance measurements performed in $I(z)$ and $z(V)$ spectroscopy mode. The equivalence of both methods is demonstrated by comparing the obtained results and plotting them in a single graph. Additionally, an alternative numerical method of determining the work function of a sample through $I(z)$ and $z(V)$ spectroscopy is presented. Using the proposed method enables one to decouple the contributions of the work function ϕ_0 and the image charge to the effective

potential barrier ϕ. Furthermore, there is no need for the elevated bias voltages associated with Gundlach oscillations and TVS measurements. Finally, the fact that the method can be applied by using $z(V)$ spectroscopy means that it can also be used with STM devices that can only measure in closed-loop mode.

Model

An often used expression for the tunneling current was introduced by Simmons in 1963 [18] and is given as

$$I = \frac{\rho V \sqrt{\phi}}{z} e^{-\alpha\sqrt{\phi}z} . \tag{1}$$

Here I is the tunneling current, $\rho = \rho(V)$ is the energy-dependent combined density of states of the tip and the sample, V is the applied tip–sample bias voltage, z is the tip–sample distance, ϕ is the tunneling barrier and $\alpha = 2\left(\sqrt{2m}\,/\,\hbar\right)$, with m the rest mass of the electron. The product $\alpha\sqrt{\phi}$ is sometimes referred to as the inverse decay length

$$\kappa = \alpha\sqrt{\phi} , \tag{2}$$

and provides a measure of the change in tunneling current for a given decrease or increase of the tip–sample separation.

Assuming a symmetrical, rectangular barrier, the term $\sqrt{\phi}$ is simply equal to the square root of the combined vacuum work function of the tip–sample system, i.e.,

$$\phi = \phi_0 \approx \frac{\phi_{\text{tip}} + \phi_{\text{sample}}}{2} . \tag{3}$$

However, applying a bias voltage between the tip and sample causes the barrier to lower in an asymmetrical fashion:

$$\phi(V) = \phi_0 - \frac{eV}{2} . \tag{4}$$

Any charge travelling between the tip and the sample will induce an image charge of equal magnitude but opposite polarity. In addition to lowering the barrier, the presence of an image charge effect will also narrow it. This effect can be included in the Simmons model by replacing the tip–sample separation z with the effective barrier width s:

$$I = \frac{\rho V \sqrt{\phi}}{s} e^{-\alpha\sqrt{\phi}s} , \tag{5}$$

where the effective barrier width s is given by [18,28]:

$$s = z\sqrt{1 - \frac{4a}{z}} \, . \qquad (6)$$

Here, a is given by

$$a = \zeta \frac{1.15e^2 \ln(2)}{16\pi\varepsilon_0\phi_0} \, , \qquad (7)$$

with ε_0 the electric permittivity of the vacuum and ζ a constant between 0 (two point charges) or 1 (two infinite parallel plates) determining the strength of the image charge effect.

The lowering effect of the image charge can be included in the effective barrier expression as follows [18]:

$$\phi(V,z) = \phi_0 - \frac{eV}{2} - \frac{2a\phi_0}{s}\ln\left[\frac{z+s}{z-s}\right] . \qquad (8)$$

Note that for small values of V and $\zeta = 0$, Equation 8 reduces to Equation 3 and Equation 5 reduces to Equation 1.

Current–distance spectroscopy

An often used and reasonably accurate way of determining ϕ from $I(z)$ measurements consists of plotting the natural logarithm of the conductance G of the tunneling barrier as a function of z. The conductance is equal to the measured tunneling current divided by the tip–sample bias, i.e., $G = (I/V)$. The linear slope of the obtained line is then approximately equal to κ, as can be deduced from Equation 1 and Equation 2. In the absence of image charge effects, the work function ϕ_0 can then be obtained through Equation 4.

The same method can be used when including the effect of image charges, although the inverse decay length will take a slightly different form:

$$\kappa^* = \alpha\sqrt{\phi - \frac{4a\phi}{z}} \, . \qquad (9)$$

It is directly apparent that a significant image charge effect will have a bending effect on the $\ln(G)$-vs-z curve. However, a quantitative analysis is made difficult by the non-straightforward dependence of κ^* on ζ.

In order to make a quantitative analysis possible, a numerical method will have to be developed. As a starting point, Equation 5 will have to be rewritten to eliminate as many unknown parameters as possible. By taking the the derivative dI/dz, the density of states ρ can be eliminated from the equation as follows:

$$\frac{dI}{dz} = -\frac{\rho V}{s^2}\frac{ds}{dz}\sqrt{\phi}e^{-\alpha s\sqrt{\phi}} + \frac{\rho V}{s}\frac{1}{2\sqrt{\phi}}\frac{d\phi}{dz}e^{-\alpha s\sqrt{\phi}}$$
$$- \frac{\rho V}{s}\sqrt{\phi}e^{-\alpha s\sqrt{\phi}}\left[\alpha\sqrt{\phi}\frac{ds}{dz} + \frac{\alpha s}{2\sqrt{\phi}}\frac{d\phi}{dz}\right] . \qquad (10)$$

Substituting Equation 5 then gives

$$\frac{dI}{dz} = -\frac{I}{s}\frac{ds}{dz} + \frac{I}{2\phi}\frac{d\phi}{dz} - I\left[\alpha\sqrt{\phi}\frac{ds}{dz} + \frac{\alpha s}{2\sqrt{\phi}}\frac{d\phi}{dz}\right] . \qquad (11)$$

Working through all the partial derivatives (see Supporting Information File 1 for a full derivation) eventually yields

$$\frac{dI}{dz}\Big/I = -\frac{1}{s}\frac{ds}{dz} - \alpha\sqrt{\phi}\frac{ds}{dz}$$
$$- \left[\frac{1}{2\phi} - \frac{\alpha s}{2\sqrt{\phi}}\right]\left[\frac{4a\phi_0}{s}\left[\frac{z\dfrac{ds}{dz} - s}{z^2 - s^2}\right] - \frac{M}{s}\frac{ds}{dz}\right] , \qquad (12)$$

with

$$M(z) = \frac{2a\phi_0}{s}\ln\left[\frac{z+s}{z-s}\right] . \qquad (13)$$

This resulting equation can be used to determine the work function ϕ_0 and image charge constant ζ from a standard, open-loop $I(z)$ measurement, as they are the only unknown variables remaining. These two unknowns can be extracted from measured data by fitting Equation 12 to the measured $I(z)$ data in a least-squares fashion.

Constant-current spectroscopy

When it is not possible, or not desirable, to perform experiments in open-loop mode, the effective barrier can also be determined from closed-loop $z(V)$ experiments. As is the case for $I(z)$ measurements, plotting the natural logarithm of the conductance as a function of tip–sample separation yields a good first approximation of the inverse decay length [10,11]. However, quantitatively decoupling the contributions of ϕ_0 and

ζ once again requires the use of a derivative numerical method. Taking into account that I does not vary as a function of V during closed-loop experiments, Equation 5 can be rewritten as:

$$I\frac{ds}{dV} = \left(\frac{d\rho}{dV}V\sqrt{\phi} + \rho\sqrt{\phi} + \frac{\rho V}{2\sqrt{\phi}}\frac{d\phi}{dV}\right)e^{-\alpha s\sqrt{\phi}}$$
$$+ \rho V\sqrt{\phi}e^{-\alpha s\sqrt{\phi}}\left(-\alpha\sqrt{\phi}\frac{ds}{dV} - \frac{\alpha s}{2\sqrt{\phi}}\frac{d\phi}{dV}\right). \tag{14}$$

Substituting Equation 5 into this expression and dividing by I gives:

$$\frac{ds}{dV} = \frac{d\rho}{dV}\frac{s}{\rho} + \frac{s}{V} + \frac{s}{2\phi}\frac{d\phi}{dV} - s\alpha\sqrt{\phi}\frac{ds}{dV} - \frac{s^2\alpha}{2\sqrt{\phi}}\frac{d\phi}{dV}. \tag{15}$$

Following the derivation given in Supporting Information File 1, this leads to the full expression

$$\frac{dz}{dV} = \frac{\dfrac{d\rho}{dV}\dfrac{s}{\rho} + \dfrac{s}{V} - \dfrac{se}{4\phi} + \dfrac{s^2\alpha e}{4\sqrt{\phi}}}{\dfrac{ds}{dz} + s\alpha\sqrt{\phi}\dfrac{ds}{dz} - \left[\dfrac{s^2\alpha}{2\sqrt{\phi}} - \dfrac{s}{2\phi}\right]\dfrac{dM}{dz}}, \tag{16}$$

with M given by Equation 13.

By using a least-squares fitting routine with parameters ϕ_0 and ζ, one can fit Equation 16 to the dz/dV data obtained from the experiment and, as such, determine the work function and image charge constant of the system.

An important limitation to the use of $z(V)$ measurements for the determination of the effective barrier height arises due to the density of states (DOS) of the studied sample. For samples with a featureless or weakly varying DOS, measured at limited bias voltages, the $(d\rho/dV)(s/\rho)$ term in Equation 16 can be neglected. However, for non-featureless densities of states, the LDOS of the tip and sample will have to be known in order to fully evaluate Equation 16. This necessitates additional or consecutive measurements in order to obtain the system LDOS [5-8,29].

Results and Discussion

To determine the effect of ζ on ϕ_0, three different sets of fit parameters were used: no image charge ($\zeta = 0$), maximum image charge ($\zeta = 1$) and variable image charge. The dI/dz signal determined from the measurement and the traces that were reconstructed from the fitted parameters can be seen in Figure 1.
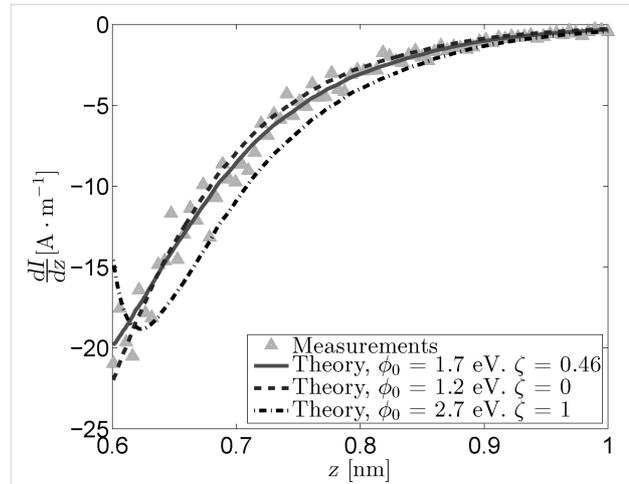
Figure 1: Measured and reconstructed *dI/dz* data obtained from *I*(*z*) measurements using three sets of fit parameters. The results for the "free" fit and the fit in absence of an image charge strongly resemble one another, indicating a masking interaction between ϕ_0 and ζ.

The most obvious conclusion that can be drawn from the obtained values of ϕ_0 and ζ is that the two are coupled, with an increase in one leading to an increase in the other. While there is a difference of 0.5 eV between ϕ_0 for the optimal fit and ϕ_0 in absence of an image charge, this seems to have little to no effect on the reconstructed signal. This shows that it is quite difficult to discriminate between the contributions of the effective work function and the image charge, as a change in one variable can be readily masked by a change in the other. The reconstructed trace for $\zeta = 1$, however, shows that there is a limit to this masking effect. For higher values of ζ, ϕ becomes more strongly dependent on z, which manifests itself in a change in curvature for the dI/dz signal.

Figure 2 shows the current signals reconstructed from the fit parameters shown in Figure 1 alongside the measured *I*(*z*) curve. All curves have been normalized to have the same starting point of roughly 2.2 nA at $z_0 = 0.6$ nm. This value for z_0 was estimated based on previous STM measurements [17] and will be used for all following analysis. While there is always a certain margin of error in estimating z_0, changing this value by a few angstroms does not significantly impact the results of the analysis, as can be seen in Supporting Information File 1. Figure 2 further emphasizes the difficulty in discriminating between the measured signal, the optimal fit reconstruction, and the reconstruction that does not incorporate image charge effects. The image also shows the decrease in curvature for the $\zeta = 1$ trace, although the difference between this trace and the measured signal is still rather small.

In order to further elucidate the effect of the image charge on the tunneling current, the logarithm of the measured conduc-
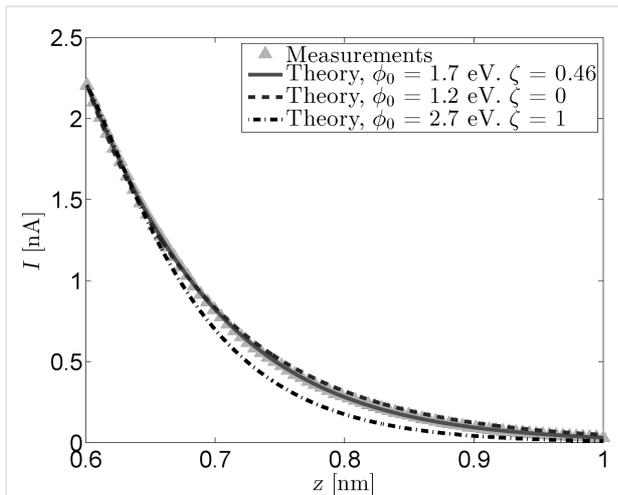
Figure 2: Measured and reconstructed *I*(*z*) data. The reconstructed traces were based on the fit parameters from Figure 1. All curves have been normalized to have a starting point of 2.2 nA at z_0 = 0.6 nm.

tance and the conductance reconstructed from the fitted parameters has been plotted in Figure 3 as a function of *z*. As mentioned in the Model section, the slope of these traces is equal to the inverse decay length κ^*. Figure 3 clearly shows the effect of including the image charge when reconstructing the tunneling current. While the effect is negligible for small tip–sample separations, the inclusion of an image charge term introduces a clear deviation from the linear trend observed for the reconstructed non-image charge current at larger separations. This same non-linearity is observed in the logarithm of the measured conductance, proving the need for the inclusion of a *z* dependent term in ϕ.
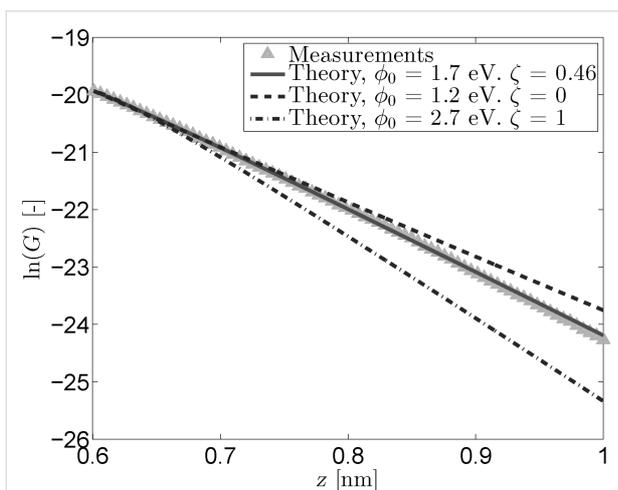
Figure 3: Logarithmic conductance versus tip-sample distance for measured and reconstructed *I*(*z*) data. The reconstructed traces were based on the fit parameters from Figure 1. The inclusion of an image charge term gives the reconstructed trace the curvature needed to follow the measured data.

Figure 4 shows the measured and reconstructed *dz*/*dV* traces. The reconstructed traces were based on Equation 16 under the assumption that the LDOS is slowly varying within the probed bias range. The difference between the optimal fit parameters and those obtained through the fit excluding image charge effects is very similar to that observed for the *I*(*z*) measurements. In addition, the difference between the reconstructed traces is practically invisible due to the masking effect of ϕ_0 on lower values of ζ. Forcing a maximum image charge contribution leads to an increase of 1.6 eV in ϕ_0, but also decreases the quality of the fit.
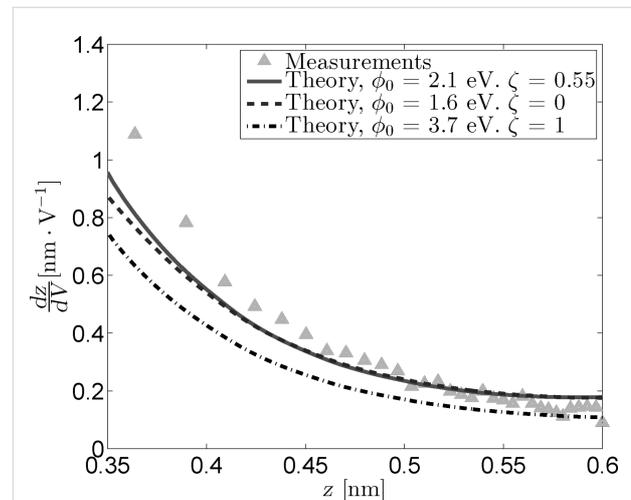
Figure 4: Measured and reconstructed *dz*/*dV* traces obtained from *z*(*V*) measurements by using three sets of fit parameters. As is the case for the *I*(*z*) data, the "free" fit and the fit in absence of an image charge overlap nearly completely.

The conductance plots shown in Figure 5 were obtained in the same manner as the *I*(*z*) conductance plots with the important difference that the offsets were subtracted to ensure that all curves start at z_0 = 0.6 nm. While the reconstructed *I*(*z*) curves can be scaled to have the same setpoint current, this same method can not be applied to the *z*(*V*) data. Instead, Equation 5 is used to reconstruct the (constant) current by using ρ = 1. This does not influence the slope of the obtained conductance curves, but it will introduce different offsets for each curve, which is why it is necessary to zero them on a common point. The conductance plot obtained in this manner (Figure 5) reveals a prominent curvature around *z* = 0.55 nm for the fitted parameters that is not present in the measurements. Additionally, the optimal fit and the fit excluding image charges perfectly overlap, further demonstrating the masking effect of ϕ_0 and ζ. The overall quality of the fitted traces is lower than that of the fitted *I*(*z*) traces. This could indicate an additional or stronger dependence of the tunneling current on the applied bias voltage or tip–sample separation than is present in the used model.
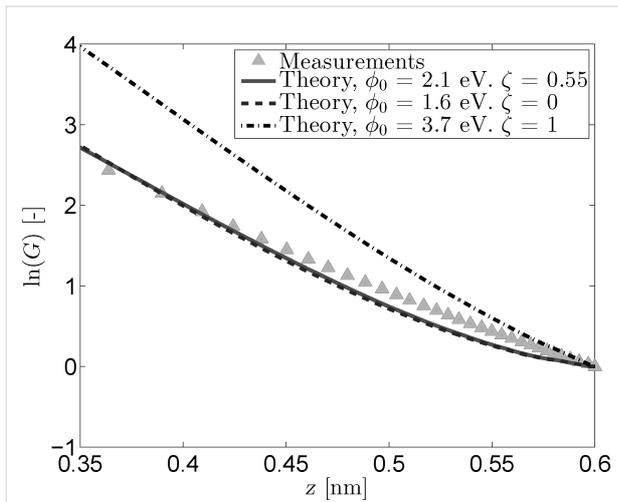
Figure 5: Logarithmic conductance versus tip-sample distance for measured and reconstructed $z(V)$ data. The reconstructed traces were based on the fit parameters from Figure 4. The logarithmic offsets have been subtracted so that $\ln(G) = 0$ at $z_0 = 0.6$ nm.

Figure 6: Combined logarithmic conductance versus tip–sample distance for $z(V)$ and $I(z)$ measurements. Logarithmic offsets for both types of measurements were zeroed at $z_0 = 0.6$ nm. The linear fit has a slope of -10.4 nm^{-1}.

By plotting the results of both $I(z)$ and $z(V)$ measurements in one figure, the equivalence of both methods can be demonstrated. Figure 6 shows the conductance data obtained from the $I(z)$ and $z(V)$ measurements, alongside a linear fit. The offsets of both data sets have been removed to ensure their intersection at $z = 0.6$ nm. From this figure, it is clear that the different types of measurements blend together practically seamlessly and that their slopes match closely. The fitted slope is equal to -10.4 nm^{-1}; approximately twice as small as the theoretical value. This leads to an effective barrier of 1 eV; approximately four to five times as small as the theoretical value [30,31]. Measurements performed with different W tips and/or different Au(111) samples yielded similar barrier heights.

Despite the fact that the conductance plots of the $I(z)$ and $z(V)$ measurements demonstrate that both methods are equally viable for the determination of the effective tunneling barrier, the obtained values for ϕ and ϕ_0 are lower than they should be according to theory. Additionally, the fitted parameters for the $z(V)$ and $I(z)$ measurements are not fully consistent and the fits themselves are not as accurate as one would hope. Abnormally low barriers obtained through STS studies have been reported in the past, with a variety of possible reasons being suggested [26,32-37].

As early as 1982, Binnig et al. reported work functions below 1 eV for a tungsten–platinum system, which they ascribed to poor vacuum conditions and contamination [32]. Similarly, the presence of water layers in the tunneling junction can also lead to lower apparent barrier heights [35,38]. However, the measurements presented in this article have been performed under UHV conditions, making it unlikely that (water) contamination is the cause of the low apparent barrier heights extracted from them.

Erroneous barrier heights can also be caused by misinterpretation of the tip–sample separation due to relaxation effects [36,39,40]. According to experimental results and theoretical calculations, these effects only take place at tip–sample separations below 500 pm, i.e., in the $z(V)$ regime of Figure 6. As such, any relaxation effects will be negated by the active feedback loop during $z(V)$ measurements. If this were not the case, the onset of relaxation effects below 500 pm should lead to a change in the slope of the measurements presented in Figure 6. Following the same line of reasoning, it is implausible that short-range electrostatic and exchange-interactions as suggested by Lang [34] are responsible for the low extracted barrier values.

In order to analyze direct tunneling experiments on large-area molecular junctions, Akkerman et al. included an additional exponential scaling factor in the Simmons model, which they later ascribed to the effective mass of the electrons tunneling through the molecules [26]. A similar effective mass correction has also been applied to tunneling junctions consisting of a single molecule attached to both the STM tip and the sample and to tip-molecule-vacuum-sample junctions [27,41,42]. While a non-unity effective mass does indeed lead to lower apparent barrier heights, the tip–vacuum–sample system described in this article should not contain any elements that could lead to the emergence of such an effective mass.

By introducing an additional scaling factor γ in the Simmons model, analogous to Akkerman et al. [26], the performance of the fitting model can be assessed for data values that result in a barrier height that is closer to theoretical values. Equation 5 is rewritten in the following form:

$$I = \frac{\rho V \sqrt{\phi}}{s} e^{-\alpha \gamma \sqrt{\phi} s} . \qquad (17)$$

Based on the linear slope extracted from Figure 6, γ was chosen to be equal to 0.5. As can be seen in Figure 7 and Figure 8, the introduction of γ has three major consequences. Firstly, the quality of both fits increases dramatically, especially for the $z(V)$ data. Secondly, the obtained values for ϕ_0 and ζ are now consistent between measurements, with only a 0.3 eV difference in ϕ_0 between the $I(z)$ and $z(V)$ measurements. Finally, the influence of the different fitted parameters on the shape of the reconstructed curves has diminished sharply, with all three curves overlapping for both types of measurements. In other words, while the mutual masking effect between ϕ_0 and ζ remains, the effective barrier ϕ is largely unaffected by changes in these parameters. This is consistent with a theoretical analysis performed by Coombs et al. [28], which showed that the effect of an image charge on the apparent tunneling barrier height is not readily extracted from $I(z)$ data. While the exact origin of γ is unclear, it is undeniable that its inclusion increases both the quality of the fits and the accuracy of the obtained values.

Conclusion

The conductances obtained from $I(z)$ and $z(V)$ spectroscopy can both be used to get a good indication of the effective tunneling barrier height ϕ_0 when plotted logarithmically as a function of the tip–sample separation. This means that the determination of the (local) work function of a material can be performed purely in the closed-loop operation mode present in all STM systems. Numerical analysis reveals a strong masking interaction between ϕ_0 and ζ, showing that neglecting the presence of an image charge can lead to one underestimating the value of ϕ_0.

The inclusion of an additional scaling factor γ has a positive impact on both the quality of the numerical fits as well as the values obtained from them. The exact physical origin of this term is, as of yet, unknown.

Experimental

Experiments were performed on an RHK ultra-high vacuum system at room temperature and a base pressure of 10^{-10} mbar. Measurement data was collected on a hydrogen flame-annealed Au(111) sample by using an electrochemically etched W tip.
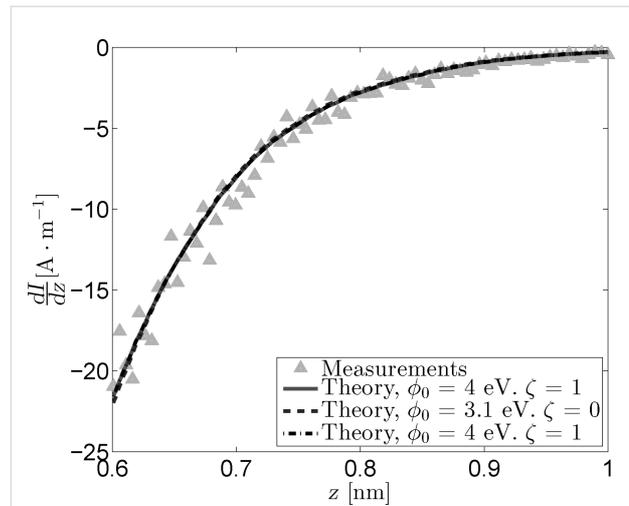
Figure 7: Measured and reconstructed *dI/dz* data obtained from *I(z)* measurements for γ = 0.5. The masking effect between ϕ_0 and ζ remains, but changes in these parameters do not significantly impact the effective barrier, leading to all reconstructed traces overlapping. The free parameter fit (solid line) leads to the maximum value for ξ (i.e., ξ = 1), causing the fitted parameters to be identical to those obtained from the fit with ξ fixed at its maximum value (dashdotted line).
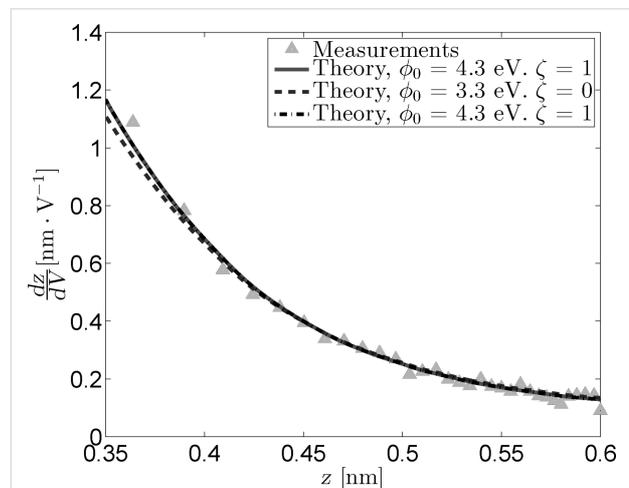
Figure 8: Measured and reconstructed *dz/dV* traces obtained from *z(V)* measurements for *γ=0.5*. The masking effect between ϕ_0 and ζ remains, but changes in these parameters do not significantly impact the effective barrier, leading to all reconstructed traces overlapping. The free parameter fit (solid line) leads to the maximum value for ξ (i.e., ξ = 1), causing the fitted parameters to be identical to those obtained from the fit with ξ fixed at its maximum value (dashdotted line).

The sample and tip had both been exposed to ultra-high vacuum conditions for several weeks prior to measuring. Spectroscopy traces were acquired by using an RHK IVP-200 preamplifier at a fixed gain of 10^8 V·A^{-1} and were performed within a short timeframe to minimize the effects of drift and possible changes to the tip or sample.

Experimental parameters were chosen to prevent changes in tip–sample distance between experiments. As such, $z(V)$ measurements were performed at a setpoint current of 2 nA over a range of 1 to 0.05 V. Subsequently, $I(z)$ measurements were performed at a current setpoint of 2 nA and a bias setpoint of 1 V. The $I(z)$ and $z(V)$ measurements presented in this article are based on an average of 200 traces per measurement. A topography image of the sample can be found in Supporting Information File 1.

Supporting Information

Supporting Information File 1
Additional experimental data.
[http://www.beilstein-journals.org/bjnano/content/supplementary/2190-4286-6-113-S1.pdf]

Acknowledgements

References

1. Binnig, G.; Rohrer, H.; Gerber, C.; Weibel, E. *Phys. Rev. Lett.* **1982,** *49,* 57–61. doi:10.1103/PhysRevLett.49.57
2. Feenstra, R. M. *Surf. Sci.* **1994,** *299–300,* 965–979. doi:10.1016/0039-6028(94)90710-2
3. Crommie, M. F.; Lutz, C. P.; Eigler, D. M. *Nature* **1993,** *363,* 524–527. doi:10.1038/363524a0
4. Heimbuch, R.; Kuzmin, M.; Zandvliet, H. J. W. *Nat. Phys.* **2012,** *8,* 697–698. doi:10.1038/nphys2414
5. Ziegler, M.; Néel, N.; Sperl, A.; Kröger, J.; Berndt, R. *Phys. Rev. B* **2009,** *80,* 125402. doi:10.1103/PhysRevB.80.125402
6. Pronschinske, A.; Mardit, D. J.; Dougherty, D. B. *Phys. Rev. B* **2011,** *84,* 205427. doi:10.1103/PhysRevB.84.205427
7. Hellenthal, C.; Heimbuch, R.; Sotthewes, K.; Kooij, E. S.; Zandvliet, H. J. W. *Phys. Rev. B* **2013,** *88,* 035425. doi:10.1103/PhysRevB.88.035425
8. Martins, B. V. C.; Smeu, M.; Livadaru, L.; Guo, H.; Wolkow, R. A. *Phys. Rev. Lett.* **2014,** *112,* 246802. doi:10.1103/PhysRevLett.112.246802
9. Binnig, G.; Garcia, N.; Rohrer, H.; Soler, J. M.; Flores, F. *Phys. Rev. B* **1984,** *30,* 4816–4818. doi:10.1103/PhysRevB.30.4816
10. Payne, M. C.; Inkson, J. C. *Surf. Sci.* **1985,** *159,* 485. doi:10.1016/0039-6028(85)90442-X
11. Pitarke, J. M.; Echenique, P. M.; Flores, F. *Surf. Sci.* **1989,** *217,* 267. doi:10.1016/0039-6028(89)90548-7
12. Gundlach, K. H. *Solid-State Electron.* **1966,** *9,* 949. doi:10.1016/0038-1101(66)90071-2
13. Lin, C. L.; Lu, S. M.; Su, W. B.; Shih, H. T.; Wu, B. F.; Yao, Y. D.; Chang, C. S.; Tsong, T. T. *Phys. Rev. Lett.* **2007,** *99,* 216103. doi:10.1103/PhysRevLett.99.216103
14. Garcia, R.; Saenz, J. J.; Soler, J. M.; Garcia, N. *J. Phys. C: Solid State Phys.* **1986,** *19,* L131. doi:10.1088/0022-3719/19/6/004
15. Beebe, J. M.; Kim, B.; Gadzuk, J. W.; Frisbie, C. D.; Kushmerick, J. G. *Phys. Rev. Lett.* **2006,** *97,* 026801. doi:10.1103/PhysRevLett.97.026801
16. Trouwborst, M. L.; Martin, C. A.; Smit, R. H. M.; Guédon, C. M.; Baart, T. A.; van der Molen, S. J.; van Ruitenbeek, J. M. *Nano Lett.* **2011,** *11,* 614–617. doi:10.1021/nl103699t
17. Sotthewes, K.; Hellenthal, C.; Kumar, A.; Zandvliet, H. J. W. *RSC Adv.* **2014,** *4,* 32438–32442. doi:10.1039/C4RA04651J
18. Simmons, J. G. *J. Appl. Phys.* **1963,** *34,* 1793–1803. doi:10.1063/1.1702682
19. Huisman, E. H.; Guédon, C. M.; van Wees, B. J.; van der Molen, S. J. *Nano Lett.* **2009,** *9,* 3909–3913. doi:10.1021/nl9021094
20. Akkerman, H. B.; de Boer, B. *J. Phys.: Condens. Matter* **2008,** *20,* 013001. doi:10.1088/0953-8984/20/01/013001
21. Néel, N.; Kröger, J.; Limot, L.; Frederiksen, T.; Brandbyge, M.; Berndt, R. *Phys. Rev. Lett.* **2007,** *98,* 065502. doi:10.1103/PhysRevLett.98.065502
22. Koslowski, B.; Tschetschetkin, A.; Maurer, N.; Ziemann, P. *Phys. Chem. Chem. Phys.* **2011,** *13,* 4045–4050. doi:10.1039/C0CP02162H
23. Feng, M.; Zhao, J.; Petek, H. *Science* **2008,** *320,* 359–362. doi:10.1126/science.1155866
24. Dougherty, D. B.; Maksymovych, P.; Lee, J.; Yates, J. T., Jr. *Phys. Rev. Lett.* **2006,** *97,* 236806. doi:10.1103/PhysRevLett.97.236806
25. Engelkes, V. B.; Beebe, J. M.; Frisbie, C. D. *J. Am. Chem. Soc.* **2004,** *126,* 14287–14296. doi:10.1021/ja046274u
26. Akkerman, H. B.; Naber, R. C. G.; Jongbloed, B.; van Hal, P. A.; Blom, P. W. M.; de Leeuw, D. M.; de Boer, B. *Proc. Natl. Acad. Sci. U. S. A.* **2007,** *104,* 11161–11166. doi:10.1073/pnas.0701472104
27. Zhou, J.; Guo, C.; Xu, B. *J. Phys.: Condens. Matter* **2012,** *24,* 164209. doi:10.1088/0953-8984/24/16/164209
28. Coombs, J. H.; Welland, M. E.; Pethica, J. B. *Surf. Sci.* **1988,** *198,* L353–L358. doi:10.1016/0039-6028(88)90365-2
29. Pfeifer, H.; Koslowski, B.; Ziemann, P. *Beilstein J. Nanotechnol.* **2011,** *2,* 607–617. doi:10.3762/bjnano.2.64
30. Anderson, P. A. *Phys. Rev.* **1959,** *115,* 553–554. doi:10.1103/PhysRev.115.553
31. Sachtler, W. M. H.; Dorgelo, G. J. H.; Holscher, A. A. *Surf. Sci.* **1966,** *5,* 221. doi:10.1016/0039-6028(66)90083-5
32. Binnig, G.; Rohrer, H.; Gerber, C.; Weibel, E. *Appl. Phys. Lett.* **1982,** *40,* 178–180. doi:10.1063/1.92999
33. Gimzewski, J. K.; Möller, R. *Phys. Rev. B* **1987,** *36,* 1284–1287. doi:10.1103/PhysRevB.36.1284
34. Lang, N. D. *Phys. Rev. B* **1988,** *37,* 10395–10398. doi:10.1103/PhysRevB.37.10395
35. Ahn, J.; Pyo, M. *Bull. Korean Chem. Soc.* **2000,** *21,* 644–646.
36. Lazo, C.; Néel, N.; Kröger, J.; Berndt, R.; Heinze, S. *Phys. Rev. B* **2012,** *86,* 180406. doi:10.1103/PhysRevB.86.180406
37. Seine, G.; Coratger, R.; Carladous, A.; Ajustron, F.; Pechou, R.; Beauvillain, J. *Phys. Rev. B* **1999,** *60,* 11045–11050. doi:10.1103/PhysRevB.60.11045
38. Halbritter, J.; Repphun, G.; Vinzelberg, S.; Staikov, G.; Lorenz, W. J. *Electrochim. Acta* **1995,** *40,* 1385. doi:10.1016/0013-4686(95)00038-G
39. Hofer, W. A.; Fisher, A. J.; Wolkow, R. A.; Grütter, P. *Phys. Rev. Lett.* **2001,** *87,* 236104. doi:10.1103/PhysRevLett.87.236104

40. Blanco, J. M.; González, C.; Jelínek, P.; Ortega, J.; Flores, F.; Pérez, R. *Phys. Rev. B* **2004,** *70,* 085405. doi:10.1103/PhysRevB.70.085405

41. Sotthewes, K.; Heimbuch, R.; Zandvliet, H. J. W. *J. Chem. Phys.* **2013,** *139,* 214709. doi:10.1063/1.4835675

42. Wang, K.; Zhou, J.; Hamill, J. M.; Xu, B. *J. Chem. Phys.* **2014,** *141,* 054712. doi:10.1063/1.4891862

Controlled switching of single-molecule junctions by mechanical motion of a phenyl ring

Yuya Kitaguchi[1], Satoru Habuka[1], Hiroshi Okuyama[*1], Shinichiro Hatta[1], Tetsuya Aruga[1], Thomas Frederiksen[*2,3], Magnus Paulsson[4] and Hiromu Ueba[5]

Full Research Paper

Address:
[1]Department of Chemistry, Graduate School of Science, Kyoto University, 606-8502 Kyoto, Japan, [2]Donostia International Physics Center (DIPC), 20018 San Sebastián, Spain, [3]IKERBASQUE, Basque Foundation for Science, 48013 Bilbao, Spain, [4]School of Computer Science, Physics and Mathematics, Linnaeus University, 391 82 Kalmar, Sweden and [5]Division of Nano and New Functional Materials Science, Graduate School of Science and Engineering, University of Toyama, 930-8555 Toyama, Japan

Email:
Hiroshi Okuyama[*] - hokuyama@kuchem.kyoto-u.ac.jp;
Thomas Frederiksen[*] - thomas_frederiksen@ehu.eus

* Corresponding author

Abstract

Mechanical methods for single-molecule control have potential for wide application in nanodevices and machines. Here we demonstrate the operation of a single-molecule switch made functional by the motion of a phenyl ring, analogous to the lever in a conventional toggle switch. The switch can be actuated by dual triggers, either by a voltage pulse or by displacement of the electrode, and electronic manipulation of the ring by chemical substitution enables rational control of the on-state conductance. Owing to its simple mechanics, structural robustness, and chemical accessibility, we propose that phenyl rings are promising components in mechanical molecular devices.

Introduction

Atomic-scale switches are key device components in future electronics for logic gates and memory elements operating in the limit of electronics miniaturization [1-5]. The mechanical control of single atoms has been employed to demonstrate the ultimate limit of electrical switches [6-8], but the use of single molecules as active units would be particularly appealing if device properties (such as switching power, speed, and stability) could be engineered and controlled by chemical design. By optimizing the on-state conductance, a large on/off ratio can be achieved, which is essential for the reliable operation of a molecular switch. In this context, π-conjugated species are promising because π orbitals can be manipulated by introducing functional groups, which illustrates a way to control the junction conductance [9] (e.g., via quantum interference effects [10,11]).

In a previous study [12], using a scanning tunneling microscope (STM), we demonstrated a molecular switch made functional by the mechanical motion of a phenyl ring, which is the atomic-scale analogue of the conventional toggle switch. A phenoxy (C_6H_5O, PhO) molecule bonded to the Cu(110) surface was reversibly lifted (released) to (from) the STM tip while being anchored to the surface via an oxygen atom. The reversible switching of the junction allowed us to explore the effect of molecular interaction on the molecular conductance. Here we extend this study and show that switching can be controlled by voltage pulses as well as by mechanical manipulation of the tip. Furthermore, the electronic levels are tunable through chemical manipulation of the phenyl ring, which in turn allows us to tailor the on-state conductance.

Methods

As described in the previous study [12], the experiments were carried out in an ultrahigh vacuum chamber equipped with an STM operating at 4.5 K. The Cu(110) surface was cleaned by repeated cycles of argon ion sputtering and annealing. PhO and thiophenoxy (C_6H_5S, PhS) were prepared on Cu(110) as reported previously [13]. Methyl-substituted phenol compounds (*meta*-cresol and 3,5-xylenol) were exposed to the surface at 300 K, which caused partial dehydrogenation as in the case of phenol. An electrochemically etched tungsten tip was used as an STM probe. The tips were repeatedly and gently touched to the Cu surface to coat them with copper, resulting in Cu-terminated tips for reliable switching [14]. We observed that sharp tips give high-contrast images and can successfully lift up the molecules.

The computational approach was detailed in [12]. Briefly, we used Kohn–Sham density functional theory (DFT) implemented in VASP [15,16] to obtain the atomic structure and total energy using the optPBE-vdW [17] exchange-correlation functional. Electron transport was computed with the DFT-based codes TranSIESTA [18,19] and Inelastica [20] using GGA-PBE [21] for the junctions connected to semi-infinite electrodes. The voltage-induced atomic forces were computed as the difference in the Hellman–Feynman force on each atom between the finite sample voltage, $V_S = \pm 0.5$ V, and zero voltage [19,22]. We define the lateral position of the tip, x, as the nominal distance (i.e., before relaxations) along [001] between the Cu tip apex atom and the Cu bridge site containing the chalcogen bond. Also, we define the tip height, h, as the distance between the planes containing the third Cu layers of the surface and of the tip pyramid.

Results and Discussion

Figure 1a shows the STM images of two PhO molecules on Cu(110) [13]. The images show a depression, which is ascribed

to the oxygen atom. The molecules are nearly flat lying and oriented along the [001] direction, as depicted by the illustration. As reported in the previous study [12], the molecule can be lifted up to the tip and reversibly released by controlling the tip–surface distance. The tip was first precisely positioned over the protrusion of the top molecule in Figure 1a at the set point corresponding to $I = 1$ nA at $V_S = 50$ mV. After the feedback was turned off, the tip was laterally displaced along the [001] direction by 2 Å (cross over the molecule) and then moved toward the molecule. Figure 1b shows a typical tunnel current recorded during the approach (black) and subsequent retraction (red), where remarkable hysteresis appears when the molecule is successfully lifted and released. Note that Δz is defined as the distance toward the molecule with respect to the initial set point, as depicted in the inset. The current during the approach shows a jump at $\Delta z = 2.6$ Å to the high-current state, which returns to the original state at $\Delta z = 1.0$ Å during the retraction. The high-current state is ascribed to the lift-up of PhO and the contact formation between tip and molecule [23-27]. After the
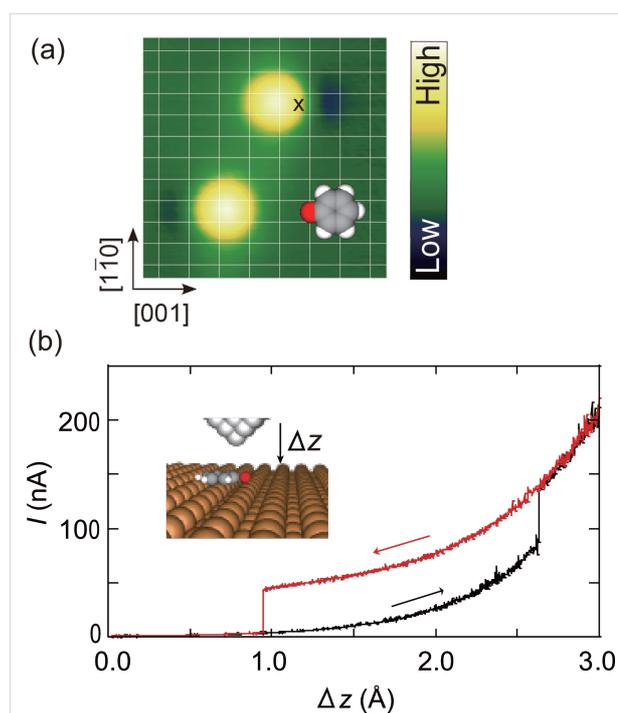
Figure 1: (a) An STM image of PhO molecules on Cu(110) with a schematic illustration superimposed. A protrusion and depression pair associated with the phenyl ring and oxygen atom, respectively. The white grid lines indicate the lattice of Cu(110). The image was obtained at $V_S = 50$ mV and $I = 1$ nA (28 × 28 Å^2). (b) The tunnel current during the approach (black) and retraction (red) of the tip along the surface normal. The tip was first positioned over the protrusion of the top molecule in (a) at a height corresponding to $V_S = 50$ mV and $I = 1$ nA, and the feedback loop was turned off. Then the tip was laterally displaced in the [001] direction by 2 Å (indicated by the cross) and moved toward the molecule. The origin of the abscissa ($\Delta z = 0$) is the initial tip height and the increase in Δz corresponds to the approach to the molecule, as shown in the inset. Data adapted from [12].

complete retraction of the tip, we confirm that the molecule returns to its original position by imaging the area. Also we can repeat the lift and release without changing the condition of the tip apex. Thus, the molecular junction can be reversibly switched by mechanical motion of a phenyl ring. As shown in [12] this switching mechanism is also supported by the calculated potential energy landscape as a function of tip approach.

The switch can also be actuated by a bias voltage with the tip position fixed (Figure 2). The sample bias was increased from −0.3 to 0.3 V and subsequently decreased to −0.3 V (blue lines in Figure 2a) while the tip was fixed over the molecule. The tunnel current during the voltage ramp (red lines) shows voltage-dependent two-state switching. The junction was in the off-state at first ($t = 0$, $V_S = -0.3$ mV), but immediately switched to the on-state. It was maintained until the voltage reached 0.1 V ($t = 80$ s), where the junction returned to the off-state. The off-state dominates until the voltage decreases to −0.1 V ($t = 210$ s), where the switch was again turned on. As a whole, the junction prefers the on and off states at negative and positive voltage, respectively. Using this voltage-dependent preference, we tried to toggle the switch by applying positive/negative pulse voltages with the electrode distance fixed (Figure 2b). By applying a short pulse of positive voltage to the

on-state junction, the molecule switched to the off-state. Conversely, switching to the on-state was achieved with a negative voltage pulse. This switching mechanism is particularly important for possible applications because no complete STM setup to control the tip height is needed.

The bias-dependent behavior was reproduced by our calculations of the induced atomic forces by applying a voltage across the junction (Figure 2c–f). These nonequilibrium forces are evaluated using the nonequilibrium density matrix and Hamiltonian in the equations for the equilibrium forces [19,22]. One observes repulsive (attractive) forces between the tip apex and nearest C-atom at positive (negative) sample voltages, consistent with the electrostatic force to be expected in the applied electric field with an overall negative charge associated with the C-atom. To further investigate this, we computed the following Hirshfeld (Voronoi) atomic charges [28] for the lifted PhO ($x = 1.4$ Å and $h = 13.9$ Å) in equilibrium $V_S = 0$: −0.043 (−0.038) for C, 0.032 (0.042) for H, −0.234 (−0.274) for O, and 0.105 (0.073) for the Cu apex atom (in units of $|e|$). These atomic charges were further found not to significantly change with applied voltage $V_S = \pm 0.5$ V. We thus conclude that the direction of the nonequilibrium force can be rationalized by electrostatics.
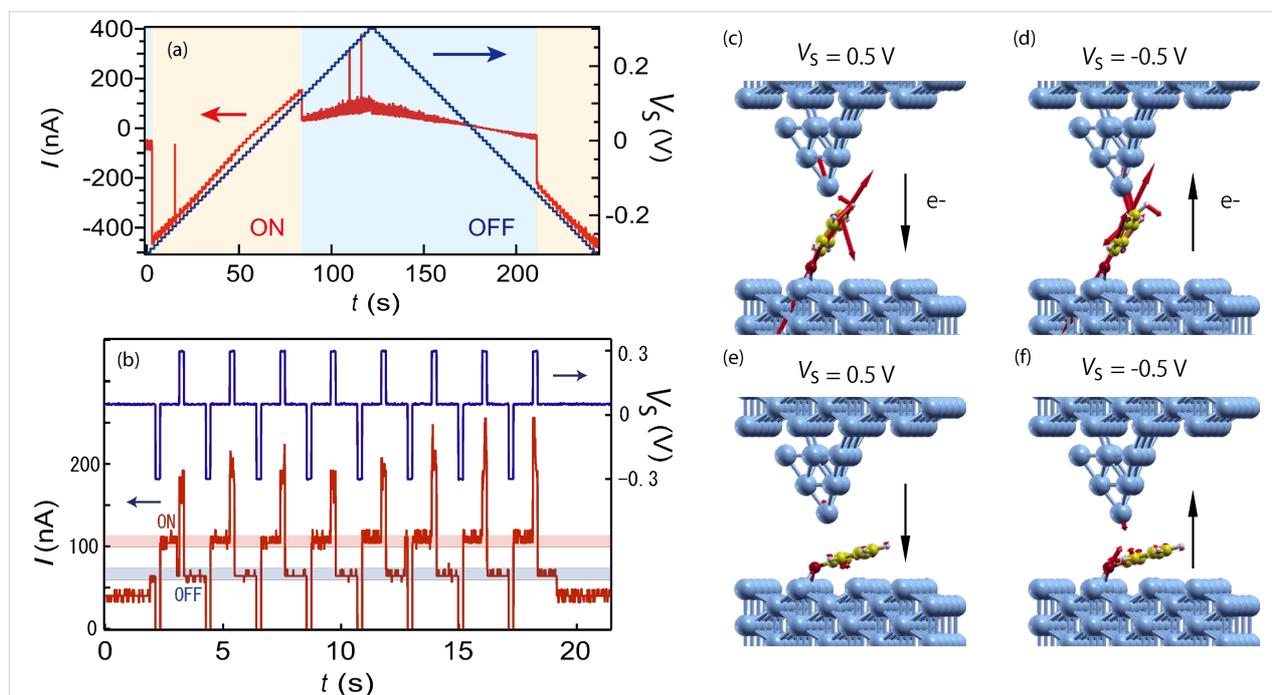
Figure 2: (a) The control of the switch by application of a bias voltage for PhO. The sample voltage V_S was ramped (blue lines) with the tip fixed over the molecule, during which the tunnel current was recorded (red lines). The on-state (lifted) is favorable at a negative sample bias, whereas the off-state (flat) is favorable at a positive bias. (b) Repeated switching of the molecular junction by using a sequence of voltage pulses. The molecule lifts up and lies down when negative and positive voltages are applied to the substrate (Cu surface), respectively. The atomic forces acting on the molecule in the junction were calculated for the lift-up configuration ($x = 1.4$ Å; $h = 13.9$ Å) with (c) positive and (d) negative sample voltages. Likewise the atomic forces for the lying-down configuration ($x = 1.4$ Å; $h = 11.9$ Å) were calculated with (e) positive and (f) negative sample voltage. The black arrows indicate the direction of the electron flow.

The current plateau that appears just before cleavage of the junction by tip retraction (Figure 1b) provides a well-defined measure of the direct current through the molecule. To investigate the influence of the anchoring group on the conductance, we also prepared PhS on the surface. This molecule is imaged as a protrusion with a tail which is ascribed to the sulfur atom (Figure 3a). The local structure is similar with that of PhO with the phenyl ring oriented along [001] and the sulfur atom bonded to the short-bridge site [13]. The controlled switching of the molecular junction is feasible with PhS as well as PhO, and the conductance values for different molecules are compared with the same tip apex (Figure 3b). As mentioned above, the initial tip height ($\Delta z = 0$) was defined by the set point of 50 mV and 1 nA over the protrusion of a PhO molecule. The difference in the set point for different species is calibrated by their topographic height. Thus, the tip–electrode distance is the same between two different junctions at the same Δz. The junction switching was conducted for PhO and PhS molecules placed near each other (Figure 3a) with the same tip apex. The measurement was repeated ten cycles for each molecule, and

the current jumps during the retraction were recorded. The height of the plateau, corresponding to the conductance for each molecule, is robust between repeated measurements and is larger by a factor of ≈2 for PhS. This demonstrates that the conductance is modified by chemical substitution of the anchoring atom from oxygen to sulfur.

To investigate the dependence of tip–molecule contact geometry on the molecular conductance, we obtained data for PhO and PhS with modified tip apexes. First, we recorded the conductance for each of the two molecules before the tip apex was modified by a gentle touch to the surface to change the tip–molecule contact geometry. We performed such conductance measurements with 85 modified tip apexes and obtained the distribution shown in Figure 4. The conductance values, which depend on the tip apex, are distributed at $(1.0 \pm 0.3) \times 10^{-2} G_0$ and $(2.2 \pm 0.5) \times 10^{-2} G_0$, for PhO and PhS molecules, respectively, where G_0 is the quantum of conductance. The variation of the conductance results from the difference in the tip–molecule contact geometry. Nevertheless,

Figure 3: (a) STM image of coadsorbed PhO (left) and PhS (right) obtained at V_S = 50 mV and I = 1 nA (52 × 52 Å²). (b) Measured I–Δz curves for PhO and PhS (offset). The switching was repeated for 10 cycles for each molecule with the identical tip apex. The height of the plateau (current jump at the cleavage) is defined as the on-state conductance of the molecular switches.

Figure 4: The dependence of the tip–molecule contact on the conductance. For a given tip apex, the conductance is recorded sequentially for each of the two molecules, generating a data point (green diamond) in the plot. Then the tip apex is modified by a gentle touch to the surface and the measurement procedure is repeated. The 85 different tip apexes were employed. Thus, the distribution of the conductance results from the variation of the tip–molecule contact. The solid line shows a linear fit that reveals $G_{PhS} = 2.1 \cdot G_{PhO}$, suggesting that the PhS molecule is more conductive than the PhO molecule by a factor of ≈2.1, irrespective of the tip–molecule contact geometry.

the linear relation in Figure 4 indicates that PhS is more conductive than PhO by a factor of 2.1, irrespective of the details of the tip–molecule contact.

The role of the anchoring group (O vs S) on the junction geometry was also computed. Figure 5 compares the total energy differences and molecular tilt angles for PhO [12] and PhS junctions in flat and tilted configurations. While the energy difference is rather similar, the tilt angle is generally lower for PhS than for PhO for the same tip height. This difference is due to different binding patterns to the Cu(110) surface (Figure 5c,d). For PhS the sp^3 hybridization of the S-atom results in a rather perfect tetrahedral bonding motif with the Cu–S–C bond angle being 111° (h = 13.9 Å). In the case of PhO, the sp^3 hybridization of the O-atom is more distorted and the corresponding Cu–O–C bond angle is found to be 135° (h = 13.9 Å).

Our transport simulations for the PhO and PhS junctions are summarized in Figure 6. The low-bias conductance is obtained from the Landauer formula, $G = G_0 T(E_F)$, where $G_0 = 2e^2/h$ is the conductance quantum and $T(E_F)$ is the transmission probability for electrons at the Fermi energy E_F. Considering

two different tip positions (h = 13.9 Å or h = 14.4 Å; x = 1.4 Å) we find conductance values of 3.7–4.7 × 10^{-2}G_0 (6.1–9.3 × 10^{-2}G_0) for the lifted PhO (PhS) molecule oriented along [001]. While the computed absolute conductances are overestimated by a factor of ≈3–4, the conductance ratio, 1.6–2.0, between the two species is in excellent agreement with the experiment. The slightly higher conductance for PhS (i.e., enhanced transmission around E_F, Figure 6a,c), is ascribed to a stronger hybridization with the substrate states as revealed by the increased projected density of states (PDOS) onto the chalcogen atom near E_F (Figure 6b,d; more extended atomic orbitals of S than of O) as well as by the larger width of the lowest unoccupied molecular orbital (LUMO) resonance around 2.0–2.4 eV above E_F (Figure 6b,d).

The chemical manipulation of the on-state conductance is also feasible by introducing functional groups into the phenyl ring, which increases or decreases the energy of the electronic level of the molecule responsible for the electron conduction. While the effect of an anchoring group on the molecular conductance has been intensively studied [29-31], that of the side group to the molecular backbone has received less attention [32-34].

Figure 5: Stability diagram and structure for PhO and PhS switching. (a) Total energy difference and (b) molecular tilt angle with the optPBE-vdW functional as a function of tip height with the lateral position fixed at x = 1.4 Å (black: PhO adapted from [12]; green: PhS; down-facing triangles: molecule flat, upright triangles: molecule lifted up). Vertical dashed lines indicate the tip height where flat and lifted configurations are energetically equal. (c) PhO (adapted from [12]) and (d) PhS molecules in the lifted configuration (h = 13.9 Å).

Figure 6: (a) Transmission and (b) projected density of states (PDOS) onto the Cu apex atom as well as onto the atoms in the PhO molecule (adapted from [12]). (c,d) Similar results for the PhS molecule. The tip height was *h* = 13.9 Å (solid lines) or *h* = 14.4 Å (dashed lines) and the lateral position was *x* = 1.4 Å. The conducting molecule is in the lifted configuration. The horizontal arrows guide the eye to the differences between PhO to PhS around E_F, mainly observed in the transmission and chalcogen-site PDOS.

This is probably due to the fact that the latter is much smaller than the former. Here we explore the effect of introducing one or two methyl groups into the phenyl ring at the *meta* positions (*m*-cresoxy and 3,5-xylenoxy, respectively). The corresponding STM images are shown in Figure 7a–c along with that of PhO for comparison. The methyl group on the phenyl ring appears bright, and the molecules coexisting on the surface can therefore be discriminated by their images. Figure 7d and Figure 7e compare typical *I*–Δ*z* curves for these molecules with those obtained on PhO with an identical tip apex, clearly demonstrating the impact of the methyl groups on the conductance, which increases as much as ≈20% and ≈35% for *m*-cresoxy and 3,5-xylenoxy, respectively (Figure 7f). This effect can be understood as an electrostatic consequence of electron-donating methyl groups that push up the π orbitals, resulting in an increased conductance because of a negative slope in the transmission around E_F (Figure 6a). Thus, an increase/decrease of the on-state conductance could be rationally achieved by substituting the phenyl ring with electron donating/withdrawing functional groups [32-34].

Conclusion

We have demonstrated a molecular switch that derives its function from the mechanical motion of a phenyl ring. The tip of a low-temperature STM was used to image and manipulate individual phenoxy (PhO) and thiophenoxy (PhS) molecules on Cu(110). These species are strongly bonded to the surface via the chalcogen atom in a nearly flat configuration. By moving the STM tip towards a target molecule or by applying a voltage pulse over it, the molecule can be lifted up to make contact to the tip apex while remaining firmly anchored to the Cu surface with the chalcogen atom acting as a hinge. Because the tip–phenyl π-bonding interaction is relatively weak compared with the covalent bond to the surface, the molecule can be released to the original position by tip retraction or by application of a reverse voltage pulse. The reversible and non-destructive operation of the switches allowed us to quantify the impact of the tip–molecule contact geometry and the chemical nature of functional groups on the molecular conductance. We observed that PhS is more conductive than PhO by a factor of 2.1, irrespective of the tip–molecule contact details. Similarly,
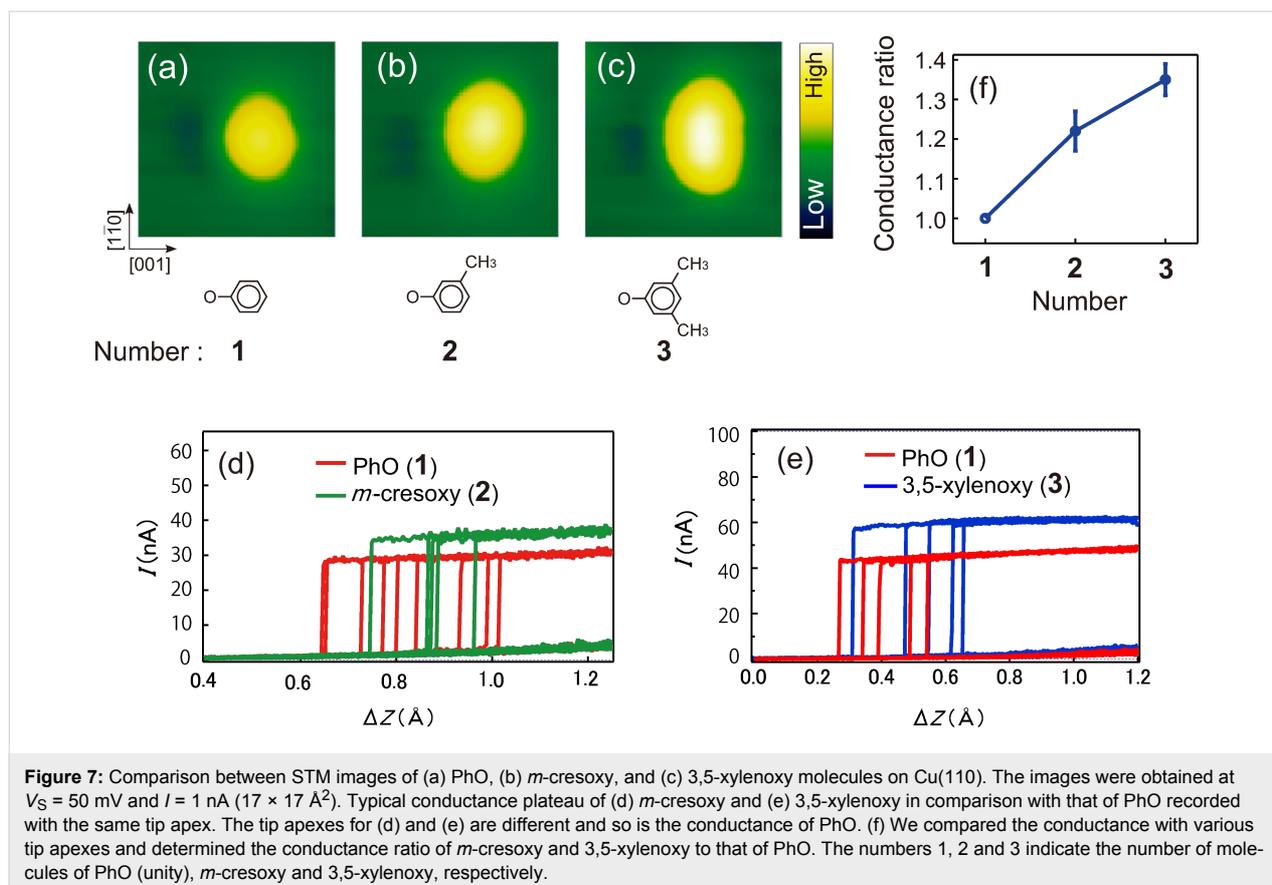
Figure 7: Comparison between STM images of (a) PhO, (b) *m*-cresoxy, and (c) 3,5-xylenoxy molecules on Cu(110). The images were obtained at V_S = 50 mV and I = 1 nA (17 × 17 Å^2). Typical conductance plateau of (d) *m*-cresoxy and (e) 3,5-xylenoxy in comparison with that of PhO recorded with the same tip apex. The tip apexes for (d) and (e) are different and so is the conductance of PhO. (f) We compared the conductance with various tip apexes and determined the conductance ratio of *m*-cresoxy and 3,5-xylenoxy to that of PhO. The numbers 1, 2 and 3 indicate the number of molecules of PhO (unity), *m*-cresoxy and 3,5-xylenoxy, respectively.

we also studied the effect of introducing methyl groups into the phenyl ring and found that the on-state conductance could be increased by ≈35%.

The operation of these phenyl-based switches was studied by first-principles simulations, revealing the relative stabilities of the flat and lifted molecular configurations. Finite-bias calculations showed consistency with the observed tendency for the junction to prefer the on (off) state at negative (positive) sample voltages. The low-bias conductance ratio between PhO and PhS was also reproduced and ascribed to different hybridization strengths with the substrate states.

In summary, we propose that phenyl rings are promising as versatile units for molecular electronic devices, whose mechanics can be controlled by different triggers such as electric field or electrode displacement. This controlled switching can be extended to other substituted phenyl groups, allowing for rational control of the on-state conductance through chemical modification.

Acknowledgements

References

1. Donhauser, Z. J.; Mantooth, B. A.; Kelly, K. F.; Bumm, L. A.; Monnell, J. D.; Stapleton, J. J.; Price, D. W., Jr.; Rawlett, A. M.; Allara, D. L.; Tour, J. M.; Weiss, P. S. *Science* **2001,** *292,* 2303–2307. doi:10.1126/science.1060294

2. Blum, A. S.; Kushmerick, J. G.; Long, D. P.; Patterson, C. H.; Yang, J. C.; Henderson, J. C.; Yao, Y.; Tour, J. M.; Shashidhar, R.; Ratna, B. R. *Nat. Mater.* **2005,** *4,* 167–172. doi:10.1038/nmat1309

3. Lörtscher, E.; Ciszek, J. W.; Tour, J.; Riel, H. *Small* **2006,** *2,* 973–977. doi:10.1002/smll.200600101

4. van der Molen, S. J.; Liljeroth, P. *J. Phys.: Condens. Matter* **2010,** *22,* 133001. doi:10.1088/0953-8984/22/13/133001

5. Sun, L.; Diaz-Fernandez, Y. A.; Gschneidtner, T. A.; Westerlund, F.; Lara-Avila, S.; Moth-Poulsen, K. *Chem. Soc. Rev.* **2014,** *43,* 7378–7411. doi:10.1039/C4CS00143E

6. Eigler, D. M.; Lutz, C. P.; Rudge, W. E. *Nature (London)* **1991,** *352,* 600–603. doi:10.1038/352600a0

7. Martin, C. A.; Smit, R. H. M.; van der Zant, H. S. J.; van Ruitenbeek, J. M. *Nano Lett.* **2009,** *9,* 2940–2945. doi:10.1021/nl901355y

8. Schirm, C.; Matt, M.; Pauly, F.; Cuevas, J. C.; Nielaba, P.; Scheer, E. *Nat. Nanotechnol.* **2013,** *8,* 645–648. doi:10.1038/nnano.2013.170

9. Karthäuser, S. *J. Phys.: Condens. Matter* **2011,** *23,* 013001. doi:10.1088/0953-8984/23/1/013001

10. Andrews, D. Q.; Solomon, G. C.; Van Duyne, R. P.; Ratner, M. A. *J. Am. Chem. Soc.* **2008,** *130,* 17309–17319. doi:10.1021/ja804399q

11. Guédon, C. M.; Valkenier, H.; Markussen, T.; Thygesen, K. S.; Hummelen, J. C.; van der Molen, S. J. *Nat. Nanotechnol.* **2012,** *7,* 305–309. doi:10.1038/nnano.2012.37

12. Kitaguchi, Y.; Habuka, S.; Okuyama, H.; Hatta, S.; Aruga, T.; Frederiksen, T.; Paulsson, M.; Ueba, H. *Sci. Rep.* **2015,** *5,* 11796. doi:10.1038/srep11796

13. Kitaguchi, Y.; Habuka, S.; Mitsui, T.; Okuyama, H.; Hatta, S.; Aruga, T. *J. Chem. Phys.* **2013,** *139,* 044708. doi:10.1063/1.4815968

14. Atodiresei, N.; Caciuc, V.; Blügel, S.; Hölscher, H. *Phys. Rev. B* **2008,** *77,* 153408. doi:10.1103/PhysRevB.77.153408

15. Kresse, G.; Furthmüller, J. *Phys. Rev. B* **1996,** *54,* 11169. doi:10.1103/PhysRevB.54.11169

16. Kresse, G.; Joubert, D. *Phys. Rev. B* **1999,** *59,* 1758. doi:10.1103/PhysRevB.59.1758

17. Klimeš, J.; Bowler, D. R.; Michaelides, A. *Phys. Rev. B* **2011,** *83,* 195131. doi:10.1103/PhysRevB.83.195131

18. Soler, J. M.; Artacho, E.; Gale, J. D.; García, A.; Junquera, J.; Ordejón, P.; Sánchez-Portal, D. *J. Phys.: Condens. Matter* **2002,** *14,* 2745–2779. doi:10.1088/0953-8984/14/11/302

19. Brandbyge, M.; Mozos, J. L.; Ordejón, P.; Taylor, J.; Stokbro, K. *Phys. Rev. B* **2002,** *65,* 165401. doi:10.1103/PhysRevB.65.165401

20. The Inelastica software is freely available at http://sourceforge.net/projects/inelastica.

21. Perdew, J. P.; Burke, K.; Ernzerhof, M. *Phys. Rev. Lett.* **1996,** *77,* 3865–3868. doi:10.1103/PhysRevLett.77.3865

22. Todorov, T. N.; Hoekstra, J.; Sutton, A. P. *Philos. Mag.* **2000,** *80,* 421–455. doi:10.1080/13642810008208601

23. Haiss, W.; Wang, C.; Grace, I.; Batsanov, A. S.; Schiffrin, D. J.; Higgins, S. J.; Bryce, M. R.; Lambert, C. J.; Nichols, R. J. *Nat. Mater.* **2006,** *5,* 995–1002. doi:10.1038/nmat1781

24. Temirov, R.; Lassise, A.; Anders, F. B.; Tautz, F. S. *Nanotechnology* **2008,** *19,* 065401. doi:10.1088/0957-4484/19/6/065401

25. Kockmann, D.; Poelsema, B.; Zandvliet, H. J. W. *Nano Lett.* **2009,** *9,* 1147–1151. doi:10.1021/nl803767c

26. Lafferentz, L.; Ample, F.; Yu, H.; Hecht, S.; Joachim, C.; Grill, L. *Science* **2009,** *323,* 1193–1197. doi:10.1126/science.1168255

27. Leary, E.; González, M. T.; van der Pol, C.; Bryce, M. R.; Filippone, S.; Martín, N.; Rubio-Bollinger, G.; Agraït, N. *Nano Lett.* **2011,** *11,* 2236–2241. doi:10.1021/nl200294s

28. Fonseca Guerra, C.; Handgraaf, J.-W.; Baerends, E. J.; Bickelhaupt, F. M. *J. Comput. Chem.* **2004,** *25,* 189–201. doi:10.1002/jcc.10351

29. Chen, F.; Li, X.; Hihath, J.; Huang, Z.; Tao, N. J. *J. Am. Chem. Soc.* **2006,** *128,* 15874–15881. doi:10.1021/ja065864k

30. Venkataraman, L.; Klare, J. E.; Tam, I. W.; Nuckolls, C.; Hybertsen, M. S.; Steigerwald, M. L. *Nano Lett.* **2006,** *6,* 458–462. doi:10.1021/nl052373+

31. Arroyo, C. R.; Leary, E.; Castellanos-Gómez, A.; Rubio-Bollinger, G.; González, M. T.; Agraït, N. *J. Am. Chem. Soc.* **2011,** *133,* 14313–14319. doi:10.1021/ja201861k

32. Venkataraman, L.; Park, Y. S.; Whalley, A. C.; Nuckolls, C.; Hybertsen, M. S.; Steigerwald, M. L. *Nano Lett.* **2007,** *7,* 502–506. doi:10.1021/nl062923j

33. Mowbray, D. J.; Jones, G.; Thygesen, K. S. *J. Chem. Phys.* **2008,** *128,* 111103. doi:10.1063/1.2894544

34. Jin, C.; Strange, M.; Markussen, T.; Solomon, G. C.; Thygesen, K. S. *J. Chem. Phys.* **2013,** *139,* 184307. doi:10.1063/1.4829520

License and Terms

Light-powered, artificial molecular pumps: a minimalistic approach

Giulio Ragazzon[1], Massimo Baroncini[1], Serena Silvi[1,2], Margherita Venturi[1,2,3] and Alberto Credi[*1,2]

Abstract

The realization of artificial molecular motors capable of converting energy into mechanical work is a fascinating challenge of nanotechnology and requires reactive systems that can operate away from chemical equilibrium. This article describes the design and construction of a simple, supramolecular ensemble in which light irradiation causes the directional transit of a macrocycle along a nonsymmetric molecular axle, thus forming the basis for the development of artificial molecular pumps.

Review
Introduction

Since ancient times, man has tried to construct devices that facilitate life. With the advent of nanoscience and nanotechnology, which aim at controlling matter on the nanometer scale, chemists have started to develop devices of molecular size capable of performing simple functions [1]. In this regard, an important source of inspiration and knowledge is represented by the natural world [2]. Indeed, owing to the progress in molecular biology, we know that living beings are endowed with

biomolecules that can replicate genetic material, transport substances inside cells or across membranes, and can be switched on and off in response to external stimuli [3]. Other classes of proteins, appropriately organized in arrays such as muscle fibers, take care of the macroscopic movements of organisms. Albeit still far from the complexity and functionality of biological systems, chemists have begun to undertake the design and construction of simple molecular devices, and to

understand their operational mechanisms [4-7], particularly with regard to the use of light as the source of energy [8,9]. As a matter of fact, molecular machines cannot be viewed merely as miniaturized versions of the corresponding macroscopic devices because several intrinsic properties of nanoscale systems are radically different from those of the macroscopic objects that we deal with in everyday life [10].

The research field of artificial molecular machines, which began in the early 1990s [11], has rapidly grown and has currently reached a significant degree of maturity, as witnessed by the publication of monographies [4], books [12], many review articles [5-8,10], and hundreds of scientific papers. In the past decade, the device-driven ingenuity of chemists and the use of increasingly sophisticated methodologies for molecular synthesis and characterization allowed the realization of a wide range of nanoscale devices, including mechanical switches [13,14], tweezers [15], valves [16], gyroscopes [17], elevators [18], and linear [19] and rotary [20] motors.

Multicomponent molecular systems such as rotaxanes and related species are frequently used to realize molecular devices and machines [4-8]. In their simplest form, rotaxanes are composed of a thread-like molecule (the axle) surrounded by a macrocyclic molecule (the ring) and terminated at both ends with bulky groups (the stoppers) that prevent the components

from disassembling. If the thread-like component does not have stoppers, the resulting ring–axle complex, termed pseudorotaxane, is in equilibrium with the separated molecular components in solution. The formation of the pseudorotaxane is enabled by the presence of noncovalent interactions between the ring and the axle, which can be modulated by an external stimulus, such that the threading and dethreading of the molecular components can be controlled (Figure 1a). Studies on switchable pseudorotaxanes form the basis of the field of artificial molecular machines and are a necessary premise for the realization of more sophisticated systems.

Today, the stimulus-controlled threading and dethreading of pseudorotaxanes are well known processes that have been realized with a wide variety of chemical structures [4-8]. They involve the ability to adjust the thermodynamic stability of the complex with respect to the separated molecular components. This, in turn, is related to the modulation of the noncovalent intercomponent interactions. Far less investigated are strategies that cause the threading/dethreading to occur along a specific direction, that is, to obtain the unidirectional transit of the ring along a nonsymmetric molecular axle, as shown in Figure 1b [21]. Such strategies require both thermodynamic and kinetic control over the threading and dethreading processes and are the basis of the construction of linear (Figure 1c) and rotary (Figure 1d) molecular motors.

Figure 1: Schematic representation of the threading/dethreading of a pseudorotaxane (a) and of the relative unidirectional transit of a macrocycle along a nonsymmetric molecular axle (b). By incorporating the system shown in (b) in a rotaxane or a catenane, linear (c) or rotary (d) motors may be obtained, respectively.
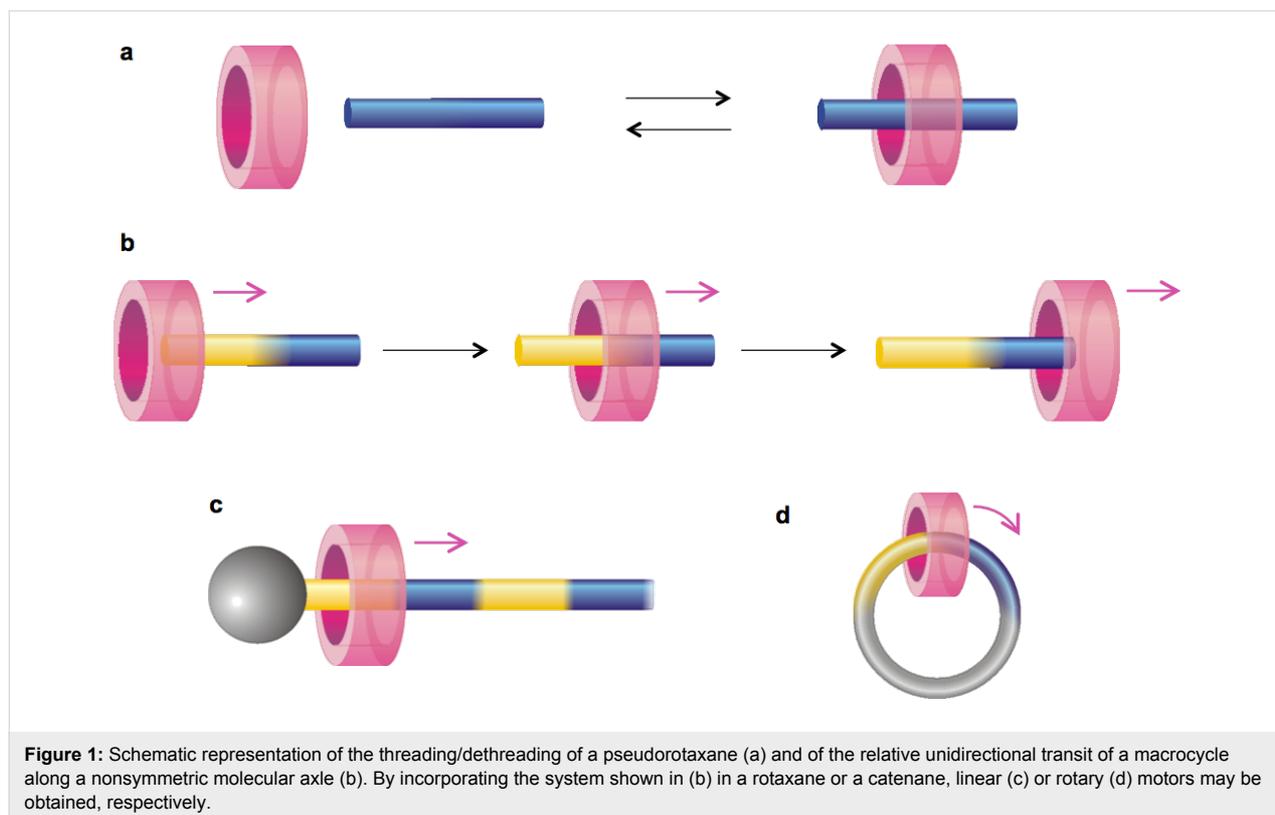
Our group recently developed a simple, self-assembling system in which a macrocycle is displaced unidirectionally along a nonsymmetric molecular axle in a repetitive fashion using light as the sole energy source [22]. The system, which operates autonomously (that is, under continuous experimental conditions and without external intervention, as long as the light source is on) and does not generate byproducts, is the first example of an artificial molecular pump operated by light. A pseudorotaxane-based supramolecular pump operated by redox reactions in solution was recently reported [23,24]; this system, however, is not autonomous and consumes chemical fuels. The scope of this article is to introduce the concept of the autonomous molecular motor, to discuss the design principles for the continuous conversion of light energy into directed motion, and to illustrate the experimental steps that led to the realization of a photochemical molecular pump.

From molecular switches to autonomous molecular motors

The vast majority of molecular devices studied so far belong to the class of molecular switches. A molecular or supramolecular system behaves as a switch if it can exist in at least two different forms, each characterized by given physical and chemical properties, which can be reversibly converted into one another in consequence of the application of an external stimulus. In a switch, the transformation that leads from state 1 to form 2 follows a path that is the exact reverse of the transformation from 2 to 1 (Figure 2a). This feature has an important physical implication, that is, the cyclic interconversion between the states of a molecular switch cannot be exploited to perform work on the system such that it will be pushed progressively away from equilibrium.

To understand the meaning of this statement we can use an example from everyday life. Let us imagine a person using a pulley to lift a weight by repeatedly exchanging the relative position of the hands with respect to the rope between state 1 (left hand ahead, right hand behind) and state 2 (right ahead, left behind). The operation of the switch can be compared to the situation in which the person has one hand bound to the rope: irrespective of the exerted force, the weight will not be lifted because the exchange in the position of the hands will put down the load by the same amount that has just been pulled up. To reach the goal the operator needs to pull the rope with one hand and move the other hand forward, alternating hands such that the work previously done is not cancelled out. This means that the conversion between states 1 and 2, each corresponding to a different hand configuration relative to the rope, must take place by following nonequivalent routes. Similarly, in a molecular motor, the transformation between the two mechanical states occurs through different configurations (Figure 2b) so that the work done in the first part of the cycle is not canceled in the second part.

Molecular motors, like macroscopic ones, need an energy source to operate. In reference to Figure 2, the transformation from state 1 to 2 requires an energy input; the same applies to the transformation from state 2 to 1, whose energy input should be alternated with the previous one so that the system can work cyclically. Such transformations can be caused by pH changes obtained by addition of acids and bases, or by redox reactions performed by adding oxidants and reductants. In these cases, the cyclical operation involves the repeated addition of reactants with the concomitant generation of waste products. At some point, this may compromise the integrity of the system

Figure 2: In a switch (a) the interconversion between states 1 and 2 takes place through the same transformation performed in opposite directions. In a motor (b) the conversion from 1 to 2 and from 2 to 1 occurs by following different routes.
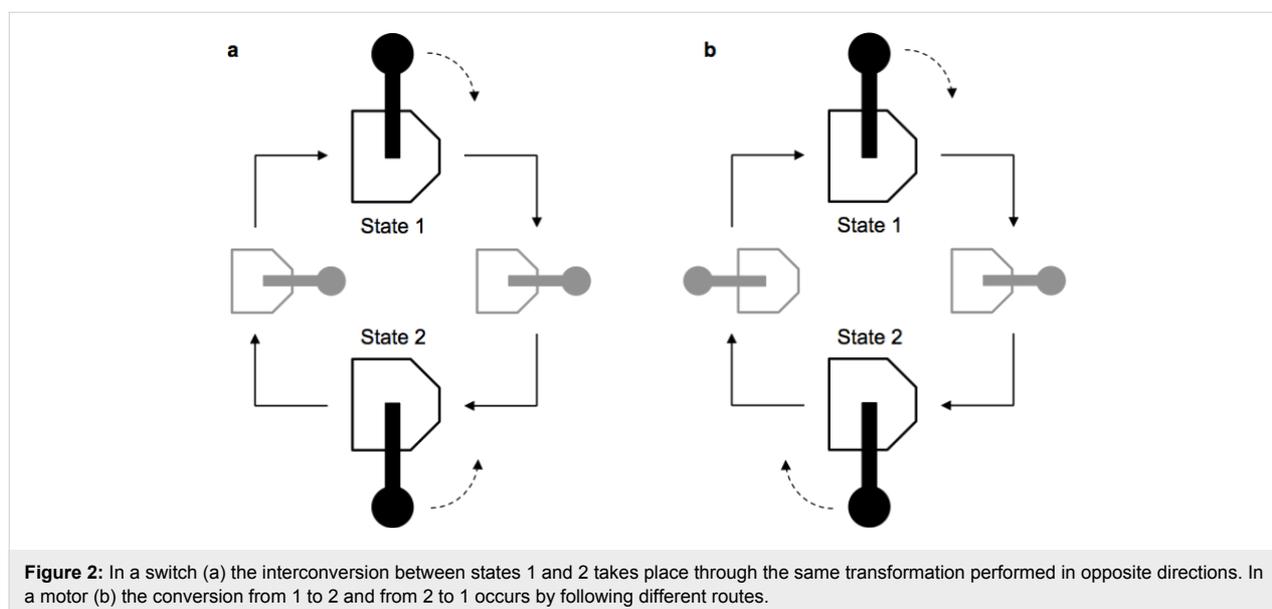
unless they are removed, as occurs in natural molecular motors as well as in conventional combustion engines.

Light is an energy source of great interest for use with molecules that has been widely exploited to operate molecular switches for a long time. For example, in photochromic compounds [25], the transformations between the two states can be caused by light of different wavelengths, or one transformation is caused by light while the other takes place in the absence of light. Light has a number of advantages compared with other types of stimuli in the context of molecular devices [26]. Since light is a "reactant" that contains energy but no mass, it is capable of transforming substances in a clean manner, that is, without generating byproducts. Moreover, in some instances, the same photons can induce both the conversion from state 1 to 2 and its reverse. A molecular machine exhibiting this property is of high interest because it can operate in an autonomous fashion, that is, under stationary experimental conditions and with no external intervention, as long as the light energy is supplied.

Modulation of the potential energy profiles

This work was developed with the goal of obtaining the relative, unidirectional transit of a macrocycle along a molecular thread using a minimalistic approach; in other words, to identify the simplest molecular structures capable of realizing a mechanism based on minimal functional requirements. The developed strategy relies on the use of a crown ether as the macrocyclic ring and a nonsymmetric molecular axle with three units: a terminal, photosensitive azobenzene group (A), an ammonium ion that performs as the recognition site (R) for the macrocycle, and a nonphotoactive unit (S). Azobenzene, which is stable in its *trans* configuration, can be temporarily converted in a photochemical manner into the metastable *cis* isomer, endowed with significantly different steric and electronic properties [27]. In particular, the threading of the *trans*-A unit through the crown ether ring is much faster than that of the *cis*-A unit [28]. The S moiety is chosen so that its hindrance for the passage of the macrocycle falls in between that of the *trans*-A (linear) and *cis*-A (bent) units.

The investigated strategy is shown in Figure 3. Because of the hydrogen bonds established between the molecular ring and the R unit located on the axle, a pseudorotaxane is formed in solution [29,30]. This process involves the passage of the ring on the *trans*-A unit because it is less hindered in comparison with the S unit. At this point, light irradiation in the ultraviolet or blue regions converts azobenzene into the *cis* form. This transformation causes, on the one hand, the destabilization of the pseudorotaxane by weakening the ring–axle interactions (increase of the energy minimum) and, on the other hand, the

increase of the barrier that the ring has to overcome to pass along the *cis*-A unit, which has now become larger than that associated with the passage on the S unit (Figure 3). The thermal or photochemical transformation of *cis*-azobenzene into the stable *trans* form, which is clean and efficient, completes the cycle, regenerating the starting pseudorotaxane.

A literature search [31] and molecular modelling experiments suggested that a good candidate for the critical role of the photoinactive pseudo-stopper S is the cyclopentyl moiety. The nonsymmetric molecular axle $1H^+$ (Figure 4) was thus synthesized, and the photoinduced transit of the dibenzo-24-crown-8 ether **2** was investigated in acetonitrile at room temperature by steady state and time-resolved ^{1}H NMR spectroscopy and UV–vis absorption experiments [32]. The kinetic measurements demonstrated that the photoisomerization of the A unit of $1H^+$ determines the threading/dethreading side (i.e., the height of the energy maximum) but, unfortunately, it does not affect the affinity of the axle for the macrocycle (i.e., the energy minimum). In other words, for these compounds under the employed conditions, the dissociation of the ring from the macrocycle cannot be obtained by light irradiation.

To overcome this problem, a second stimulus was used, namely, the addition of K^+ ions capable of competing with $1H^+$ for the cavity of macrocycle **2**. Indeed, the experimental data showed that the addition of an excess of KPF_6 to a solution of the $[1H \subset 2]^+$ pseudorotaxane caused the extrusion of the ring from the S extremity of the axle, thus completing the directionally controlled threading/dethreading cycle [29]. Interestingly, the ring–axle interactions in $[1H \subset 2]^+$ can also be switched off by deprotonating the ammonium site R with a base. This process, however, causes a significant increase of the energy of the system, such that the consequent dethreading is very fast, even if the ring has to pass along the azobenzene in the *cis* configuration [22].

Autonomous operation under the effect of light

Building on these encouraging results, we improved the system so that the directional transit could be caused solely by light irradiation [18]. To this aim, the benzene units of macrocycle **2** were replaced with naphthalene ones (ring **3**, Figure 4). Such naphthalene units are strongly fluorescent and thus enable the use of luminescence spectroscopy (a more sensitive technique than the NMR methods used in earlier experiments) to study the threading and dethreading processes. We also anticipated that the presence of larger aromatic units in the molecular ring could amplify the difference in affinity of **3** for the two isomeric forms of the axle $1H^+$ by exploiting the different ability of the *trans*- and *cis*-azobenzene units to interact with the naphthalene
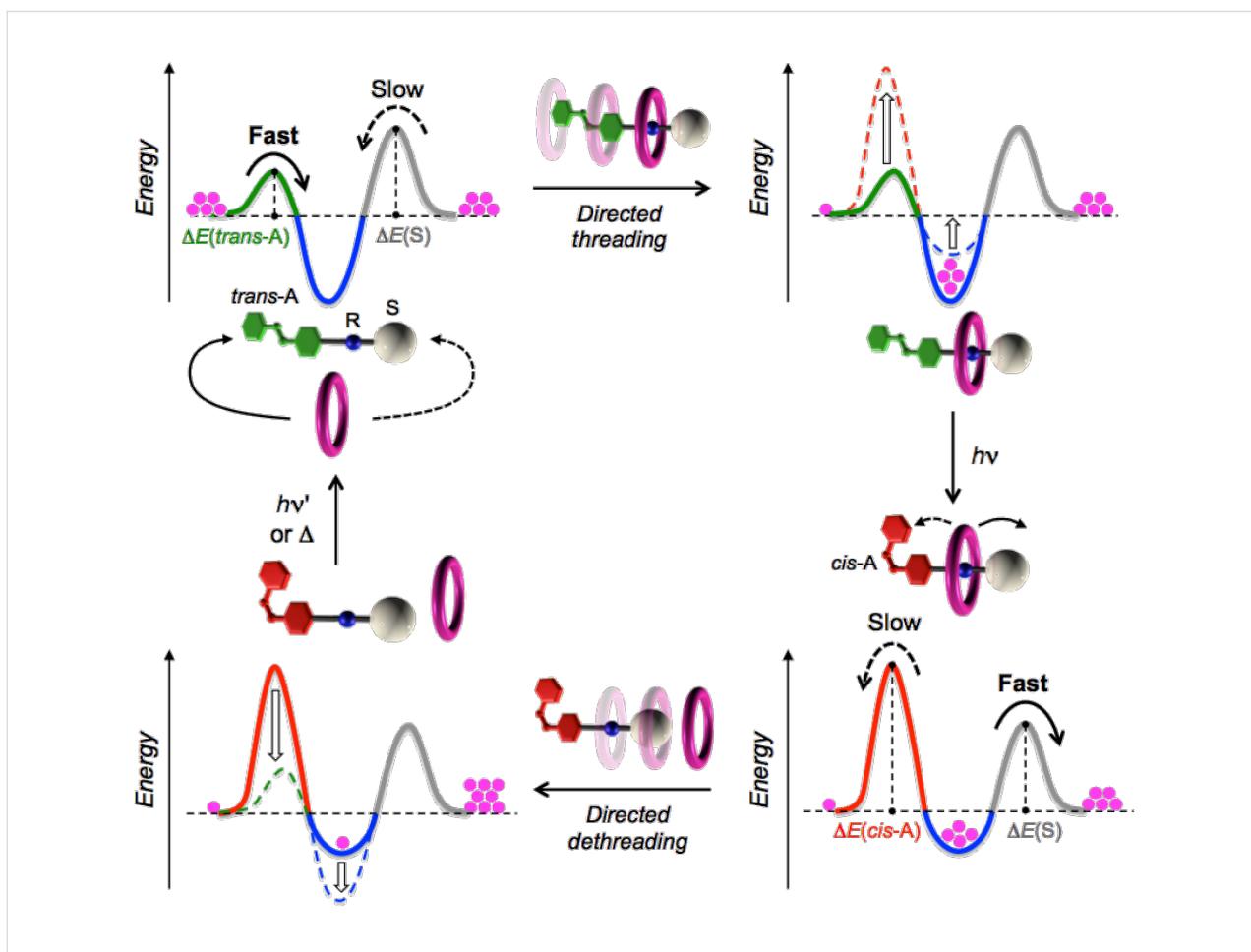
Figure 3: A minimalistic strategy for the photoinduced transit of a macrocycle along a nonsymmetric molecular axle. A simplified representation of the potential energy profile as a function of the ring–axle distance is shown for each state of the cycle. The periodic modulation of the potential energy maxima and minima, induced by light, enables the directionally controlled threading and dethreading of the molecular components.
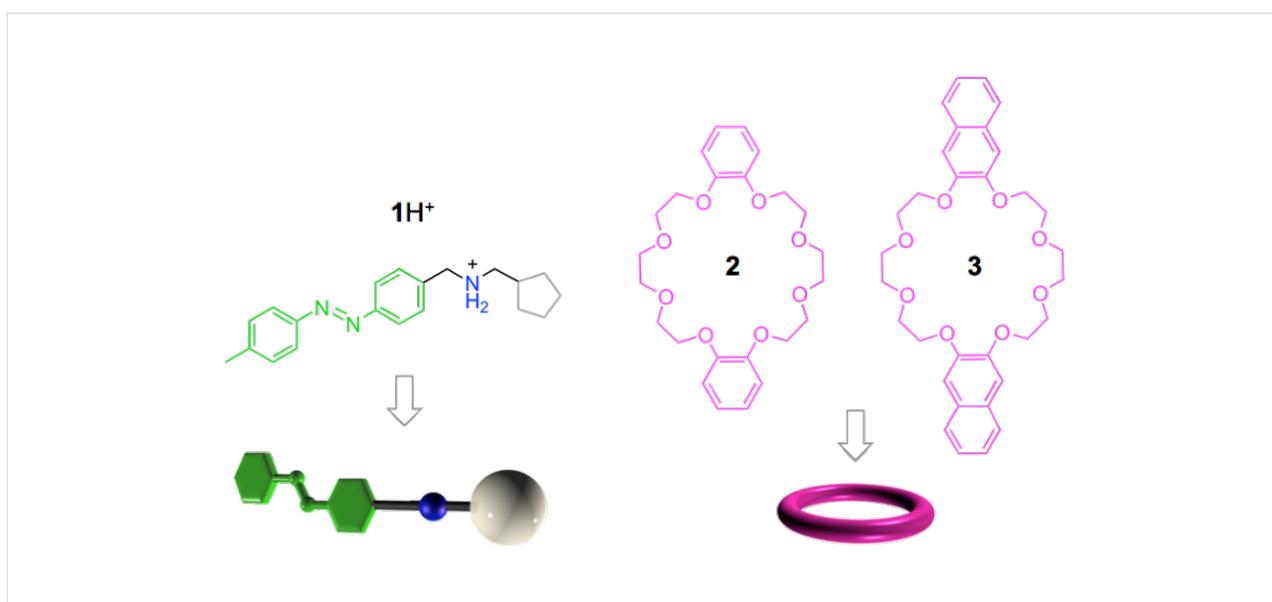
Figure 4: Structure formula and schematic representation of the examined molecular components.

moieties by π-stacking. Finally, in order to enhance the ring–axle interactions, dichloromethane was used as the solvent in the place of acetonitrile. Indeed, spectrophotometric and fluorimetric titrations showed that the ring–axle association constants increased by almost three orders of magnitude in comparison to the values found in acetonitrile. Moreover, the association constant (K) of macrocycle **3** with axle *trans*-**1**H$^+$ (K_{trans} = 6.3 × 10^5 M^{-1}) resulted to be about four times larger than that with the *cis*-axle (K_{cis} = 1.7 × 10^5 M^{-1}). At the same time, the correct order of the rate constants (k) and, thus, the energy barriers (ΔE) associated with the passage of the macrocycle on the *trans*-A ($k_{trans\text{-}A}$ = 54 M^{-1} s^{-1}, $\Delta E_{trans\text{-}A}$ = 14.8 kcal mol^{-1}), S (k_S = 0.81 M^{-1} s^{-1}, ΔE_S = 16.7 kcal mol^{-1}) and *cis*-A ($k_{cis\text{-}A}$ = 3.9 × 10^{-2} M^{-1} s^{-1}, $\Delta E_{cis\text{-}A}$ = 19.0 kcal mol^{-1}) units was maintained, in agreement with the fact that the cavities of macrocycles **2** and **3** have an identical size [22].

Hence, in the new generation system, photoisomerization controls both the height of the kinetic barrier and the stability of the pseudorotaxane, as required for the strategy illustrated in Figure 3. The processes that describe the behavior of the device are represented in Figure 5, which highlights the correlation between the chemical threading/dethreading equilibria (horizontal processes) and the photoisomerization reactions (vertical processes). Our measurements demonstrated that under continuous light irradiation, the cycle shown in Figure 5 is travelled with higher probability in the clockwise direction than in the counterclockwise one. As is well known, the principle of microscopic reversibility states that in any closed path of chemical reactions, the cycling probability is the same in both directions, unless energy is introduced into the system, as it happens in the present case in the form of light [33]. The supply of energy, however, is not a sufficient condition to bring the system out of equilibrium.

In the next section we will provide an intuitive explanation on how this system can operate autonomously and how it can use (or, more precisely, dissipate) light energy to reach a nonequilibrium state. For this purpose, it is important to note that in a photoisomerization process (such as that of azobenzene), once a steady state is reached under light irradiation (photostationary state), the ratio between the amounts of the two isomers is constant. The composition of the system at the photostationary state can be expressed with the ratio of the concentrations of the two isomers ($K_{2,hv}$ and $K_{4,hv}$ in Figure 5). This represents a quantity mathematically equivalent to the equilibrium constant but with a different physical meaning, because it is not referred to a thermodynamic equilibrium state.

By analyzing the reaction cycle shown in Figure 5, one can notice that the transition from the state in which the ring and *trans*-axle are separated (top left) to that in which the ring and *cis*-axle are associated (bottom right) can be performed by following two alternative paths. The first one (clockwise half-cycle) corresponds to the formation of the *trans*-complex and its
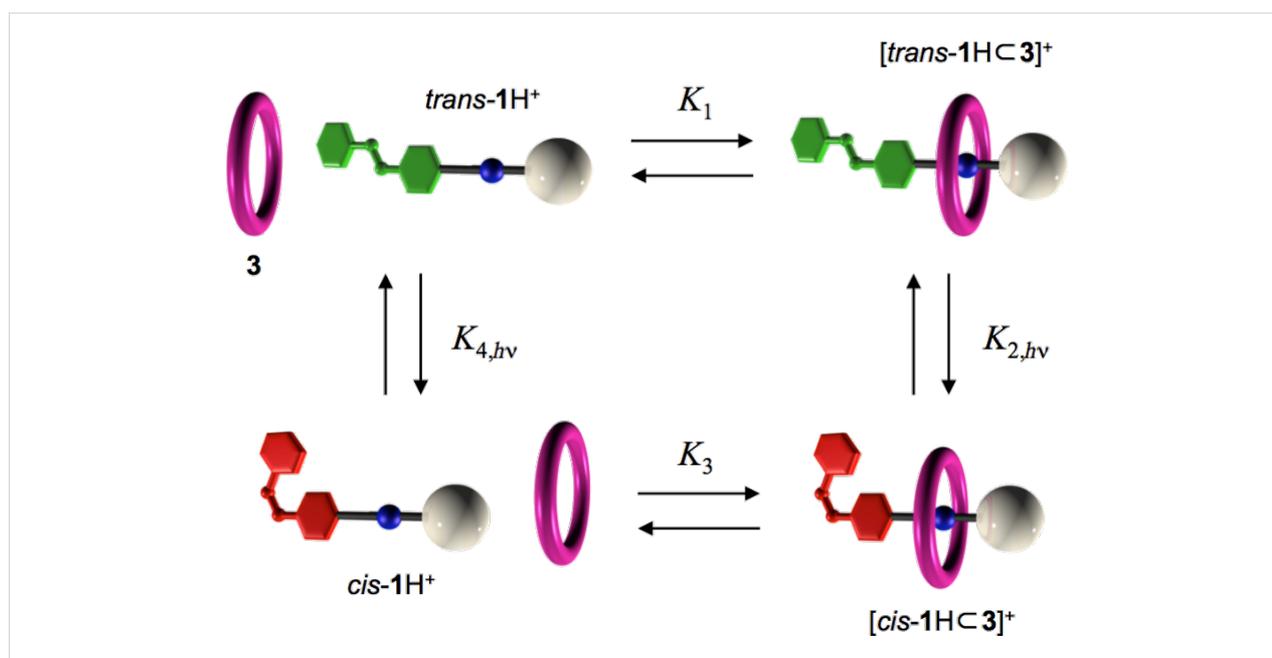
Figure 5: Self-assembly chemical reactions (horizontal processes) and photochemical isomerization reactions (vertical processes) that describe the operation of the molecular pump. The chemical or photochemical equilibrium constants refer to reactions read from left to right and from top to bottom. Figure adapted with permission from [18], copyright 2006 American Chemical Society.

conversion to the *cis* form, whereas the second one (counterclockwise half-cycle) corresponds to the conversion of the free axle from *trans* to *cis* and subsequent formation of the complex. In a cycle of reactions at thermal equilibrium, the relative stability of the initial and final states is expressed by the product of the thermodynamic constants of the reactions that link the two states and must be independent on the followed path. This condition, with respect to the cycle presented in Figure 5, would result in the following expression:

$$K_1 K_{2,h\nu} = K_{4,h\nu} K_3 \qquad (1)$$

The experimental results indicate that under light irradiation at $\lambda > 400$ nm, the photostationary states of $1H^+$ in the presence or in the absence of ring **3** have the same composition. In other words, $K_{2,h\nu} = K_{4,h\nu}$. Since the titrations experiments show that $K_1 > K_3$, Equation 1 cannot be fulfilled and the *cis* complex is apparently more stable when it is generated through the clockwise half-cycle. Consequently, under steady light irradiation, the system reaches a stationary state (that is, a state in which the concentrations of all species are constant) corresponding to the cycle of Figure 5 preferentially travelled clockwise.

The direct experimental observation of photostationary cycling is not straightforward because the physico-chemical properties of the ensemble are constant at steady state. As discussed above, however, a net flux around the cycle should be established by the supply of light energy even if the concentration of each species remains static, thus bringing the system out of equilibrium. Hence, the fact that the photostationary concentration for any species involved in the cycle is not consistent with its expected equilibrium value constitutes proof of autonomous, light-powered cycling. In this context, it is worth noting that the fluorescence intensity of **3** is completely quenched when it is complexed by either *trans*- or *cis*-$1H^+$; therefore, the amount of uncomplexed macrocycle can be determined from the fluorescence intensity of the solution, measured under suitable spectral conditions [34]. Indeed, we found that upon light irradiation the concentration of the uncomplexed ring **3** shifts away from the range of values compatible with thermal equilibrium. When the light is switched off, the concentration of **3** slowly goes back to the same equilibrium value measured before illumination.

In summary, on the basis of the previous discussion (Figure 3 and Figure 5), the absorption of photons promotes the unidirectional, repetitive and autonomous transit of macrocycle **3** along axle $1H^+$, thus realizing the first example of an artificial molecular pump activated by light. As already evidenced, the element that breaks the symmetry and enables the autonomous operation is the different stability of the ring–axle complexes in the two isomeric forms ($K_1 > K_3$). Furthermore, detailed measurements showed that for specific irradiation wavelengths, the photoisomerization efficiency is affected by complexation, namely, the photoreactivity of the axle depends on whether it is surrounded by the ring or not.

For example, the photostationary *cis/trans* ratio upon 365 nm irradiation is slightly larger for the complex than for the free axle, which means that $K_{2,h\nu} > K_{4,h\nu}$. On the other hand, we observed that the photoisomerization quantum yield values are the same for the free and complexed axle. Thus, the larger *trans→cis* conversion in the complex must be due to the fact that its molar absorption coefficient at 365 nm is higher than that of the free axle. When the irradiation light is also absorbed by the ring component (e.g., at $\lambda = 287$ nm), the situation becomes even more interesting. Irradiation of the ring–axle mixture at 287 nm generates a photostationary state with a larger *cis/trans* ratio than for the axle alone ($K_{2,h\nu} > K_{4,h\nu}$), as discussed above for excitation at 365 nm. Also, upon irradiation at 287 nm, the photoisomerization quantum yield of the axle is not affected by the presence of the ring. Thus, the reason why $K_{2,h\nu}$ is larger than $K_{4,h\nu}$ is because the excitation energy of **3** is effectively transferred to *trans*-$1H^+$ but not to *cis*-$1H^+$ in their respective complexes. This is due to a much better spectral overlap in the [*trans*-$1H \subset 3$]$^+$ complex than in the [*cis*-$1H \subset 3$]$^+$ one.

These data enable an insightful discussion about the mechanisms used by this system to rectify Brownian fluctuations [10]. If irradiation is carried out with $\lambda > 400$ nm ($K_{2,h\nu} = K_{4,h\nu}$), the mechanism is energy ratcheting, whereas upon irradiation at 365 or 287 nm, information ratcheting is also present. Different physical phenomena, however, account for the information ratcheting effect at these two wavelengths. The 365 nm light is not absorbed by the ring, but the presence of the latter enhances the absorption of the *trans*-axle, causing the preferential, photoinduced closure of the azobenzene gate in the pseudorotaxane with respect to the axle. The excitation of the ring with 287 nm light is followed by energy transfer to the *trans*-axle, a process that can effectively take place only if the components are associated, and causes the *trans→cis* isomerization. Hence, upon irradiation at either 287 or 365 nm, the information about the relative position of the ring and axle components (i.e., whether they are associated or not) contributes to the gating.

From the analysis of the free energy change of the system, it can be estimated that the maximum amount of work that could be performed by the pump in a cycle under the employed conditions is $5.1 \cdot k_B T$ (3.0 kcal mol^{-1} at 20 °C), which is about one fourth of the energy of ATP hydrolysis utilized by natural mole-

cular motors. It can also be calculated that the system consumes on average 430 photons of 365 nm light (78 kcal mol^{-1}) to complete a cycle, corresponding to an upper limit for the energy conversion efficiency of 9×10^{-5}. Despite such a low conversion efficiency, this study clearly demonstrates that the synergy between photochemical reactions and self-assembly processes can lead to innovative methods for the conversion of sunlight into chemical energy [35].

Conclusion

The most recent progress in the area of molecular machines has revealed the importance of designing and realizing molecular and supramolecular systems that can operate continuously away from equilibrium. The development of an artificial molecular pump powered by light following a minimalistic approach is an important step towards this goal and enabled the study and detailed understanding of some fundamental principles underlying the operation of molecular motors.

The structural simplicity and synthetic accessibility of the employed components are indeed important elements to favor the progress of this research and its possible applications. The present system, however, has a few important limitations. For example, because of the symmetry of the crown ether used as the macrocycle, it is impossible to establish which side of the ring cavity is pierced by the axle. Moreover, the device in its current form does not perform work but merely dissipates the light energy input into heat. The main challenge for this research is to modify the system so that the molecular movements can be used to generate concentration gradients or to transport chemical species along predetermined directions for significant distances in comparison with typical diffusive paths in solution.

Acknowledgements

References

1. Browne, W. R.; Feringa, B. L. *Nat. Nanotechnol.* **2006,** *1,* 25–35. doi:10.1038/nnano.2006.45
2. Jones, R. A. L. *Soft machines: nanotechnology and life;* Oxford University Press: Oxford, USA, 2008.
3. Mann, S. *Angew. Chem., Int. Ed.* **2008,** *47,* 5306–5320. doi:10.1002/anie.200705538
4. Balzani, V.; Credi, A.; Venturi, M. *Molecular devices and machines: Concepts and perspectives for the nanoworld,* 2nd ed.; Wiley-VCH: Weinheim, Germany, 2008. doi:10.1002/9783527621682
5. Kay, E. R.; Leigh, D. A.; Zerbetto, F. *Angew. Chem., Int. Ed.* **2007,** *46,* 72–191. doi:10.1002/anie.200504313
6. Abendroth, J. M.; Bushuyev, O. S.; Weiss, P. S.; Barrett, C. J. *ACS Nano* **2015,** *9,* 7746–7768. doi:10.1021/acsnano.5b03367
7. Kay, E. R.; Leigh, D. A. *Angew. Chem., Int. Ed.* **2015,** *54,* 10080–10088. doi:10.1002/anie.201503375
8. Silvi, S.; Venturi, M.; Credi, A. *Chem. Commun.* **2011,** *47,* 2483–2489. doi:10.1039/C0CC03829F
9. Raiteri, P.; Bussi, G.; Cucinotta, C. S.; Credi, A.; Stoddart, J. F.; Parrinello, M. *Angew. Chem., Int. Ed.* **2008,** *47,* 3536–3539. doi:10.1002/anie.200705207
10. Astumian, R. D. *Phys. Chem. Chem. Phys.* **2007,** *9,* 5067–5083. doi:10.1039/b708995c
11. Anelli, P. L.; Spencer, N.; Stoddart, J. F. *J. Am. Chem. Soc.* **1991,** *113,* 5131–5133. doi:10.1021/ja00013a096
12. Credi, A.; Silvi, S.; Venturi, M., Eds. *Molecular Machines and Motors: Recent Advances and Perspectives;* Springer International Publishing: Switzerland, 2014. doi:10.1007/978-3-319-08678-1
13. Avellini, T.; Li, H.; Coskun, A.; Barin, G.; Trabolsi, A.; Basuray, A. N.; Dey, S. K.; Credi, A.; Silvi, S.; Stoddart, J. F.; Venturi, M. *Angew. Chem., Int. Ed.* **2012,** *51,* 1611–1615. doi:10.1002/anie.201107618
14. Bleve, V.; Schäfer, C.; Franchi, P.; Silvi, S.; Mezzina, E.; Credi, A.; Lucarini, M. *ChemistryOpen* **2015,** *4,* 18–21. doi:10.1002/open.201402073
15. Leblond, J.; Petitjean, A. *ChemPhysChem* **2011,** *12,* 1043–1051. doi:10.1002/cphc.201001050
16. Saha, S.; Leug, K. C.-F.; Nguyen, T. D.; Stoddart, J. F.; Zink, J. I. *Adv. Funct. Mater.* **2007,** *17,* 685–693. doi:10.1002/adfm.200600989
17. Garcia-Garibay, M. A. *Proc. Natl. Acad. Sci. U. S. A.* **2005,** *102,* 10771–10776. doi:10.1073/pnas.0502816102
18. Badjic, J. D.; Ronconi, C. M.; Stoddart, J. F.; Balzani, V.; Silvi, S.; Credi, A. *J. Am. Chem. Soc.* **2006,** *128,* 1489–1499. doi:10.1021/ja0543954
19. von Delius, M.; Geertsema, E. M.; Leigh, D. A. *Nat. Chem.* **2010,** *2,* 96–101. doi:10.1038/nchem.481
20. Conyard, J.; Addison, K.; Heisler, I. A.; Cnossen, A.; Browne, W. R.; Feringa, B. L.; Meech, S. R. *Nat. Chem.* **2012,** *4,* 547–551. doi:10.1038/nchem.1343
21. Arduini, A.; Bussolati, R.; Credi, A.; Monaco, S.; Secchi, A.; Silvi, S.; Venturi, M. *Chem. – Eur. J.* **2012,** *18,* 16203–16213. doi:10.1002/chem.201201625
22. Ragazzon, G.; Baroncini, M.; Silvi, S.; Venturi, M.; Credi, A. *Nat. Nanotechnol.* **2015,** *10,* 70–75. doi:10.1038/nnano.2014.260
23. Cheng, C.; McGonigal, P. R.; Schneebeli, S. T.; Li, H.; Vermeulen, N. A.; Ke, C.; Stoddart, J. F. *Nat. Nanotechnol.* **2015,** *10,* 547–553. doi:10.1038/nnano.2015.96
24. Cheng, C.; McGonigal, P. R.; Stoddart, J. F.; Astumian, R. D. *ACS Nano* **2015,** *9,* 8672–8688. doi:10.1021/acsnano.5b03809
25. Irie, M., Ed. Photochromism: Memories and Switches. *Chem. Rev.* **2000,** *100,* 6–1890. doi:10.1021/cr980068l
26. Ceroni, P.; Credi, A.; Venturi, M. *Chem. Soc. Rev.* **2014,** *43,* 4068–4083. doi:10.1039/c3cs60400d
27. Bandara, H. M. D.; Burdette, S. C. *Chem. Soc. Rev.* **2012,** *41,* 1809–1825. doi:10.1039/C1CS15179G
28. Baroncini, M.; Silvi, S.; Venturi, M.; Credi, A. *Chem. – Eur. J.* **2010,** *16,* 11580–11587. doi:10.1002/chem.201001409
29. Ashton, P. R.; Campbell, P. J.; Glink, P. T.; Philp, D.; Spencer, N.; Stoddart, J. F.; Chrystal, E. J. T.; Menzer, S.; Williams, D. J.; Tasker, P. A. *Angew. Chem., Int. Ed. Engl.* **1995,** *34,* 1865–1869. doi:10.1002/anie.199518651

30. Rogez, G.; Ribera, B. F.; Credi, A.; Ballardini, R.; Gandolfi, M. T.;
    Balzani, V.; Liu, Y.; Northrop, B. H.; Stoddart, J. F. *J. Am. Chem. Soc.*
    2007, *129,* 4633–4642. doi:10.1021/ja067739e
31. Ashton, P. R.; Baxter, I.; Fyfe, M. C. T.; Raymo, F. M.; Spencer, N.;
    Stoddart, J. F.; White, A. J. P.; Williams, D. J. *J. Am. Chem. Soc.* **1998,**
    120, 2297–2307. doi:10.1021/ja9731276
32. Baroncini, M.; Silvi, S.; Venturi, M.; Credi, A. *Angew. Chem., Int. Ed.*
    2012, *51,* 4223–4226. doi:10.1002/anie.201200555
33. Astumian, R. D. *Nat. Nanotechnol.* **2012,** *7,* 684–688.
    doi:10.1038/nnano.2012.188
34. Credi, A.; Prodi, L. *J. Mol. Struct.* **2014,** *1077,* 30–39.
    doi:10.1016/j.molstruc.2014.03.028
35. Balzani, V.; Credi, A.; Venturi, M. *ChemSusChem* **2008,** *1,* 26–58.
    doi:10.1002/cssc.200700087

Thermoelectricity in molecular junctions with harmonic and anharmonic modes

Bijay Kumar Agarwalla[1], Jian-Hua Jiang[2] and Dvira Segal[*1]

Abstract

We study charge and energy transfer in two-site molecular electronic junctions in which electron transport is assisted by a vibrational mode. To understand the role of mode harmonicity/anharmonicity in transport behavior, we consider two limiting situations: (i) the mode is assumed harmonic, (ii) we truncate the mode spectrum to include only two levels, to represent an anharmonic mode. Based on the cumulant generating functions of the models, we analyze the linear-response and nonlinear performance of these junctions and demonstrate that while the electrical and thermal conductances are sensitive to whether the mode is harmonic/anharmonic, the Seebeck coefficient, the thermoelectric figure-of-merit, and the thermoelectric efficiency beyond linear response, conceal this information.

Introduction

Molecular electronic junctions offer a rich playground for exploring basic and practical questions in quantum transport, such as the interplay between electronic and nuclear dynamics in nonequilibrium situations. Theoretical and computational efforts based on minimal model Hamiltonians are largely focused on the Anderson impurity dot model which consists a single molecular electronic orbital directly coupled to biased metal leads, as well as to a particular vibrational mode [1]. Since the same molecular orbital is assumed to extend both

contacts, the model allows for simulations of transport characteristics in conjugated molecular junctions with delocalized electrons.

In this work, we focus on a different class of molecular junctions as depicted in Figure 1. In such systems, two electronic levels are coupled via a weak tunneling element, but electrons may effectively hop between these electronic states when interacting with a vibrational mode. This could e.g., correspond to a

Figure 1: Scheme of the D–A model considered in this work. A two-site (D, A) electronic junction is coupled to either (a) a harmonic molecular mode, or (b) an anharmonic mode, represented by a two-state system. The molecular mode may further relax its energy to a phononic thermal reservoir (not depicted here), maintained at temperature T_{ph}.
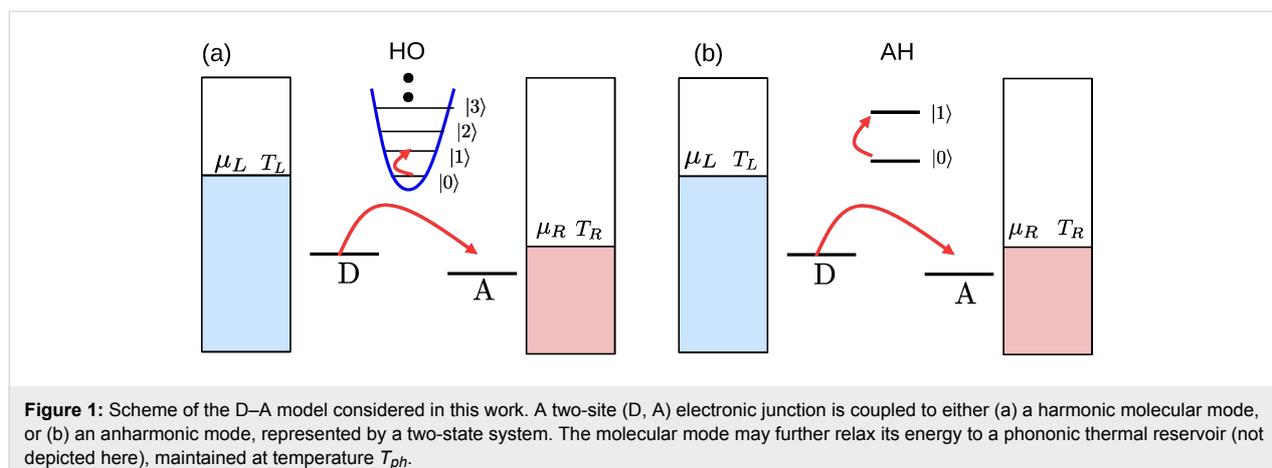
torsional motion bringing orthogonal π systems into an overlap as in the 2,2'-dimethylbiphenyl (DMBP) molecule recently examined in [2-4].

This model is related to the original Aviram–Ratner construction for a donor–acceptor molecular rectifier [5]. Thus, we identify the two states here as "D" and "A", see Figure 1, and refer to the model as the "D–A junction". More recently, this construction was employed for exploring vibrational heating and instability under a large bias voltage [6-8]. The system is also referred to as the "dimer molecular junction" [9], or an "open spin–boson model" [10] (where the spin here represents the D and A states, the bosons correspond to the molecular vibrational modes, and the system is open, i.e., coupled to metal leads). It was utilized to study charge transfer in donor–bridge–acceptor organic molecules [11] and organic molecular semiconductors [12], as well as thermoelectric effects in quantum dot devices [13,14].

Recently, Erpenbeck et al. had provided a thorough computational study of transport characteristics with nondiagonal (or nonlocal) as well as diagonal (local) electron–vibration interactions [15]. Here, in contrast, we simplify the junction model and omit the contribution of direct tunneling between the D and A units. This simplification allows us to derive a closed (perturbative) expression for the cumulant generating function (CGF) of the model, which contains comprehensive information over transport characteristics.

Measurements of charge current and electrical conductance in single molecules hand over detailed energetic and dynamical information [16]. Complementing electrical conductance measurements, the thermopower, a linear response quantity, also referred to as the Seebeck coefficient, is utilized as an independent tool for probing the energetics of molecular junctions [17-24]. Experimental efforts identified orbital hybridization,

contact-molecule energy coupling and geometry, and whether the conductance is HOMO or LUMO dominated. More generally, the thermoelectric performance beyond linear response is of interest, with the two metal leads maintained at (largely) different temperatures and chemical potentials.

What information can linear and nonlinear thermoelectric transport coefficients reveal on molecular junctions? Specifically, can they expose the underlying electron–phonon interactions and the characteristics of the vibrational modes participating in the process? Focusing on the challenge of efficient thermoelectric systems, how should we tune molecular parameters to improve heat to work conversion efficiency? These questions were examined in recent studies, a non-exhaustive list includes [13,14,25-36].

We focus here on the effect of vibrational anharmonicity on thermoelectric transport within the D–A model. To explore this issue, two limiting variants of the basic construction are examined, as displayed in Figure 1: (a) The vibration is harmonic in the so-called "harmonic oscillator" (HO) model. (b) To learn about deviations from the harmonic picture, we truncate the vibrational spectrum to include only its two lowest levels, constructing the "anharmonic" (AH) mode model. In a different context, the AH model could represent transport through molecular magnets, in which electron transfer is controlled by a spin impurity [37].

The complete information over transport behavior is contained in the respective cumulant generating functions, which we provide here for the HO and the AH models, valid under the approximation of weak electron–vibration interactions. From the CGFs, we derive expressions for charge and heat currents, and study the linear and nonlinear thermoelectric performance of the junctions. Focusing on the role of vibrational anharmonicity, we find that while it significantly influences the elec-

trical and thermal conductances, nevertheless in the present model it does not affect heat-to-work conversion efficiency.

Model

We consider a two-site junction, where electron hopping between the D and A electronic states (creation operators $c_d^\dagger$ and $c_a^\dagger$, respectively) is assisted by a vibrational mode. The total Hamiltonian is written as

$$
\begin{aligned}
H = {} & \varepsilon_d c_d^\dagger c_d + \varepsilon_a c_a^\dagger c_a + H_{vib} + H_{el-vib} \\
& + \sum_{l \in L} \varepsilon_l c_l^\dagger c_l + \sum_{r \in R} \varepsilon_r c_r^\dagger c_r + \sum_{l \in L} v_l \left(c_l^\dagger c_d + c_d^\dagger c_l \right) \\
& + \sum_{r \in R} v_r \left(c_r^\dagger c_a + c_a^\dagger c_r \right).
\end{aligned}
\tag{1}
$$

The molecular electronic states of energies $\varepsilon_{d,a}$ are hybridized with their adjacent metals, collection of noninteracting electrons, by hopping elements v_l and v_r. Here $c_j^\dagger$ (c_j) is a fermionic creation (annihilation) operator. The electronic Hamiltonian (Equation 1, excluding $H_{vib} + H_{el-vib}$) can be diagonalized and expressed in terms of new fermionic operators a_l and a_r,

$$
H_{el} = \sum_l \varepsilon_l a_l^\dagger a_l + \sum_r \varepsilon_r a_r^\dagger a_r .
\tag{2}
$$

The molecular operators can be expanded in the new basis as,

$$
c_d = \sum_l \gamma_l a_l, \quad c_a = \sum_r \gamma_r a_r .
$$

The $\gamma_{l,r}$ coefficients satisfy [7]

$$
\gamma_l = v_l \Bigg/ \left(\varepsilon_l - \varepsilon_d - \sum_{l'} \frac{v_{l'}^2}{\varepsilon_l - \varepsilon_{l'} + i\delta} \right).
$$

δ is a positive infinitesimal number, introduced to maintain causuality.

The operators c_l and c_r can be expressed in terms of the new basis as

$$
c_l = \sum_{l'} \eta_{ll'} a_{l'}, \text{with } \eta_{ll'} = \delta_{ll'} - \frac{v_l \gamma_{l'}}{\varepsilon_l - \varepsilon_{l'} + i\delta} .
$$

Similar expressions hold for the r set.

Back to Equation 1, H_{vib} and H_{el-vib} represent the Hamiltonians of the molecular vibrational mode and its coupling to electrons, respectively. We assume an "off-diagonal" interaction with electron hopping between local sites assisted by the vibrational mode. Assuming a local harmonic mode we write

$$
\begin{aligned}
H_{vib} &= \omega_0 b_0^\dagger b_0 , \\
H_{el-vib} &= g \left[c_d^\dagger c_a + c_a^\dagger c_d \right] \left(b_0^\dagger + b_0 \right),
\end{aligned}
\tag{3}
$$

with b_0 ($b_0^\dagger$) as the annihilation (creation) operator for the vibrational mode of frequency ω_0, g is the coupling parameter. The Hamiltonian (Equation 1) then becomes

$$
H_{HO} = H_{el} + \omega_0 b_0^\dagger b_0 + g \sum_{l \in L, r \in R} \left[\gamma_l^* \gamma_r a_l^\dagger a_r + h.c. \right] \left(b_0^\dagger + b_0 \right).
\tag{4}
$$

The second model considered here includes an anharmonic two-state mode. It is convenient to represent it with the Pauli matrices $\sigma_{x,y,z}$, and to write the total Hamiltonian for the junction as

$$
H_{AH} = H_{el} + \frac{\omega_0}{2} \sigma_z + g \sum_{l \in L, r \in R} \left[\gamma_l^* \gamma_r a_l^\dagger a_r + h.c. \right] \sigma_x .
\tag{5}
$$

The two models, Equation 4 and Equation 5, describe electron–hole pair generation/annihilation by de-excitation/excitation of an "impurity" (vibrational mode). The left and right reservoirs defining H_{el} in Equation 2 are characterized by a structured density of states since we had absorbed the D state in the L terminal, and similarly, the A level in the R metal. These electronic reservoirs are prepared in a thermodynamic state of temperature $T_\nu = 1/(k_B \beta_\nu)$ and chemical potential μ_ν, $\nu = L,R$, set relative to the equilibrium chemical potential $\mu_F = 0$. In our description we work with $\hbar = 1$ and $e = 1$. Units are revived in simulations.

Transport

The complete information over steady-state charge and energy transport properties of molecular junctions is delivered by the so-called cumulant generating function $\mathcal{G}$, defined in terms of the characteristic function $\mathcal{Z}$ as

$$
\mathcal{G}\left(\lambda_e, \lambda_p \right) = \lim_{t \to \infty} \frac{1}{t} \ln \mathcal{Z}\left(\lambda_e, \lambda_p \right)
$$

with

$$
\mathcal{Z}\left(\lambda_e, \lambda_p \right) = \left\langle e^{i\lambda_e H_R + i\lambda_p N_R} e^{-i\lambda_e H_R^H(t) - i\lambda_p N_R^H(t)} \right\rangle.
$$

Here λ_e, λ_p are counting fields for energy and particles, respectively, defined for the right lead measurement, t is the final measurement time. The operators in this definition are $N_R = \sum_r a_r^\dagger a_r$, the number operator for the total charge in the right lead, and similarly $H_R = \sum_r \varepsilon_r a_r^\dagger a_r$ as the total energy in the same compartment. The superscript H identifies the Heisenberg picture, with operators evolving with respect to the full Hamiltonian. While closed results for the CGF can be derived for junctions of noninteracting particles [38], it is challenging to calculate this function analytically for models with interactions, see for example [39]. Our simplified D–A model is one of the very few many-body models that can be solved analytically.

The CGF of the harmonic-mode junction (Equation 4) can be derived using the nonequilibrium Green's function (NEGF) technique [40,41] assuming weak interaction between electrons and the particular vibration, employing the random phase approximation (RPA) [39,42]. This scheme involves a summation over a particular set (infinite) of diagrams (ring type) in the perturbative series, taking into account all electron scattering processes that are facilitated by the absorption or emission of a *single* quantum ω_0. Physically, this summation collects not only sequential tunneling electrons, but all coordinated multi-tunneling processes, albeit with each electron interacting with the mode to the lowest order. The derivation of the CGF is nontrivial, and it is included in a separate communication [43]. Here we provide the final result

$$\mathcal{G}_{HO}\left(\lambda_e, \lambda_p\right) = \frac{1}{2}\left(k_d - k_u\right) - \frac{1}{2}\sqrt{\left(k_u + k_d\right)^2 - 4 k_u^\lambda k_d^\lambda}. \quad (6)$$

The CGF of the AH model (Equation 5) can be derived based on a counting-field dependent master equation approach [7,43],

$$\mathcal{G}_{AH}\left(\lambda_e, \lambda_p\right) = -\frac{1}{2}\left(k_u + k_d\right) + \frac{1}{2}\sqrt{\left(k_u - k_d\right)^2 + 4 k_u^\lambda k_d^\lambda}. \quad (7)$$

Both expressions are correct to second-order in the electron-vibration coupling g. It is remarkable to note on the similarity of these expressions, which were derived from separate approaches. We use the short notation $\lambda = (\lambda_p, \lambda_e)$, where the counting fields are defined for right-lead measurements. It can be proved that our CGFs satisfy the fluctuation symmetry [44]

$$\mathcal{G}\left(\lambda_e, \lambda_p\right) = \mathcal{G}\left(-\lambda_e - i\Delta\beta, -\lambda_p - i\left(\beta_L \mu_L - \beta_R \mu_R\right)\right), \quad (8)$$

with $\Delta\beta = \beta_R - \beta_L$. This result is not trivial: Schemes involving truncation of interaction elements may leave out terms inconsistently with the fluctuation symmetry.

Equation 6 and Equation 7 are expressed in terms of an upward (excitation) k_u^λ and a downward (de-excitation) k_d^λ rates between vibrational states. The rates are additive in the two baths,

$$k_d^\lambda = \left[k_d^\lambda\right]^{L \to R} + \left[k_d^\lambda\right]^{R \to L}, \quad (9)$$

and obey the relation $k_u^\lambda = k_d^\lambda\left[\omega_0 \to -\omega_0\right]$. They are given by Equation 10 [7,43].

The rates k_d and k_u are evaluated from these expressions at $\lambda = 0$; $f_\nu(\varepsilon) = [\exp(\beta_\nu(\varepsilon - \mu_\nu)) + 1]^{-1}$ is the Fermi–Dirac distribution function of the $\nu = L, R$ lead. The properties of the molecular junction are embedded within the spectral density functions, peaked around the molecular electronic energies $\varepsilon_{d,a}$ with the broadening $\Gamma_{L,R}$ satisfying, e.g., $\Gamma_\nu(\varepsilon) = 2\pi \sum_{k \in \nu} v_k^2 \delta(\varepsilon - \varepsilon_k)$,

$$J_L(\varepsilon) = g \frac{\Gamma_L(\varepsilon)}{\left(\varepsilon - \varepsilon_d\right)^2 + \left(\Gamma_L(\varepsilon)/2\right)^2},$$
$$J_R(\varepsilon) = g \frac{\Gamma_R(\varepsilon)}{\left(\varepsilon - \varepsilon_a\right)^2 + \left(\Gamma_R(\varepsilon)/2\right)^2}. \quad (11)$$

These expressions are reached through the diagonalization procedure of the electronic Hamiltonian while ignoring the real principal value term, responsible for a small energy shift of $\varepsilon_{d,a}$ [7]. In what follows we take Γ_ν as a constant independent of energy and assume broad bands with a large cutoff $\pm D$, the largest energy scale in the problem.

We obtain currents and high order cumulants by taking derivatives of the CGF with respect to the counting fields. The particle $\langle I_p \rangle$ and energy $\langle I_e \rangle$ current are given by Equation 12

$$\left[k_d^\lambda\right]^{L \to R} = \int_{-\infty}^{\infty} \frac{d\varepsilon}{2\pi} f_L(\varepsilon)\left(1 - f_R\left(\varepsilon + \omega_0\right)\right) J_L(\varepsilon) J_R\left(\varepsilon + \omega_0\right) e^{-i\lambda_p - i(\varepsilon + \omega_0)\lambda_e},$$

$$\left[k_d^\lambda\right]^{R \to L} = \int_{-\infty}^{\infty} \frac{d\varepsilon}{2\pi} f_R(\varepsilon)\left(1 - f_L\left(\varepsilon + \omega_0\right)\right) J_R(\varepsilon) J_L\left(\varepsilon + \omega_0\right) e^{i\lambda_p + i\varepsilon\lambda_e}. \quad (10)$$

$$\langle I_p \rangle \equiv \frac{\langle N \rangle}{t} = \left. \frac{\partial \mathcal{G}(\lambda_e, \lambda_p)}{\partial (i\lambda_p)} \right|_{\lambda_e = \lambda_p = 0} ,$$

$$\langle I_e \rangle \equiv \frac{\langle Q \rangle}{t} = \left. \frac{\partial \mathcal{G}(\lambda_e, \lambda_p)}{\partial (i\lambda_e)} \right|_{\lambda_e = \lambda_p = 0} . \qquad (12)$$

After some manipulations we reach the compact form for the harmonic (−) and anharmonic (+) models,

$$\left\langle I_p^{AH/HO} \right\rangle = 2 \frac{k_d^{R\to L} k_u^{R\to L} - k_d^{L\to R} k_u^{L\to R}}{k_d \pm k_u} ,$$

$$\left\langle I_e^{AH/HO} \right\rangle = \frac{k_d \left[\partial_{(i\lambda_e)} k_u^\lambda \, |_{\lambda_e = 0} \right] + k_u \left[\partial_{(i\lambda_e)} k_d^\lambda \, |_{\lambda_e = 0} \right]}{k_d \pm k_u} . \qquad (13)$$

The rates are given by Equation 10 with $\lambda = 0$. It is notable that the only difference between the HO and AH models is the sign in the denominator. Note that we did not simplify the expression for the energy current $\langle I_e^{AH/HO} \rangle$ above; the derivatives return energy transfer rates analogous to Equation 10, only with an additional energy variable in the integrand.

While figures below only display quantities related to charge and energy currents, it is useful to emphasize that the CGF contains information on fluctuations of these currents. For example, the zero-frequency noise for charge current is given from

$$\langle S_p \rangle \equiv \frac{\langle\langle N^2 \rangle\rangle}{t} = \left. \frac{\partial^2 \mathcal{G}(\lambda_e, \lambda_p)}{\partial (i\lambda_p)^2} \right|_{\lambda_e = \lambda_p = 0} , \qquad (14)$$

where $\langle\langle N^2 \rangle\rangle = \langle N^2 \rangle - \langle N \rangle^2$ is the second cumulant.

Our derivation is based on the diagonal representation of the electronic Hamiltonian, thus the occupations of the molecular electronic states D and A follow the Fermi function by construction. In the weak coupling limit employed here, the back-action of the vibrational degrees of freedom on the electronic distribution is not included. While in other models [45] this back-action may be significant, here we argue that its role is rather small: Recent numerically exact path integral simulations [8] testify that this type of quantum master equation performs very well at weak to intermediate electron–vibration coupling, justifying our scheme. Note that in path integral simu-

lations [8] the states D and A were absorbed into the metal leads as well, yet the electronic distribution was allowed to evolve in time, naturally incorporating the back-effect of vibrations on the electronic distribution in the steady-state limit.

Results

We are interested in identifying signatures of mode harmonicity in transport characteristics. We set the right contact as hot, $T_R > T_L$, and write the electronic heat current extracted from the hot bath by $\langle I_h \rangle = \langle I_e \rangle - \mu_R \langle I_p \rangle$. The bias is applied such that $\mu_L > \mu_R$, thus the macroscopic efficiency of a thermoelectric device, converting heat to work, is given by

$$\eta \equiv \frac{-\langle W \rangle}{\langle I_h \rangle} = \frac{(\mu_L - \mu_R)\langle I_p \rangle}{\langle I_h \rangle} . \qquad (15)$$

The device is operating as a thermoelectric engine when both charge and energy current flow from the hot (right) bath to the cold one. Note that according to our conventions the currents are positive when flowing from the right contact to the left.

Linear response coefficients

In linear response, i.e., close to equilibrium, the charge current $\langle I_p \rangle$ and heat current $\langle I_h \rangle$ as obtained from Equation 13 can be expanded to lowest order in the bias voltage $\Delta\mu = \mu_R - \mu_L = eV$ and temperature difference $\Delta T = T_R - T_L$. To re-introduce physical dimensions, we multiply the charge current by $e/\hbar$ and the heat current by $1/\hbar$. The resulting expansions are cumbersome thus we write them formally in terms of the coefficients $a_{i,j}$, $(i,j = h,p)$,

$$\langle I_p \rangle = \frac{e}{\hbar} a_{p,p} \Delta\mu + \frac{e}{\hbar} a_{p,h} k_B \Delta T ,$$

$$\langle I_h \rangle = \frac{1}{\hbar} a_{h,p} \Delta\mu + \frac{1}{\hbar} a_{h,h} k_B \Delta T . \qquad (16)$$

For $\langle I_p \rangle = GV + GS\Delta T$ and $\langle I_h \rangle = G\Pi V + (\Sigma + GS\Pi)\Delta T$ with Π being the Peltier coefficient [46,47], we identify the electrical conductance

$$G = \frac{e^2}{\hbar} a_{p,p} ,$$

the thermopower

$$S = \frac{k_B}{e} \frac{a_{p,h}}{a_{p,p}} ,$$

the electron contribution to the thermal conductance

$$\Sigma = \frac{k_{\mathrm{B}}}{\hbar}\left(a_{h,h} - \frac{a_{p,h}a_{h,p}}{a_{p,p}}\right)$$

and the (dimensionless) thermoelectric figure of merit

$$ZT = \frac{GS^2}{\Sigma}T,$$

which determine the linear response thermoelectric efficiency. We obtain these coefficients numerically, by simulating Equation 13 under small biases.

Figure 2–Figure 4 below display the behavior of *G, S,* Σ and *ZT* at room temperature *T* = 300 K for the harmonic and anharmonic-mode junctions. In the numerical simulations below the phononic contribution to the thermal conductance is ignored, assuming it to be small compared to its electronic counterpart. A quantitative analysis of the contribution of the phononic thermal conductance is included in the Discussion section. In addition, for simplicity, the junction is made spatially symmetric with Γ = Γ$_{L,R}$ and ε$_0$ = ε$_{d,a}$. The currents are given by Equation 13, and we make the following observations: (i) The harmonic-mode model supports higher currents relative to the two-state case, but at low temperatures, ω$_0$/*T* >> 1, when the excitation rate is negligible relative to the relaxation rate, the two models provide the same results. (ii) Since the expressions for the currents in the HO and the AH models are proportional to each other, the resulting thermopower and figure of merit are identical.

Figure 2 displays transport coefficients as a function of metal–molecule hybridization assuming a resonance situation $k_{\mathrm{B}}T > \varepsilon_0$. The conductances show a turnover behavior in accord with Equation 11, growing with Γ for small values Γ < ε$_0$, then falling down approximately as $G, \Sigma \propto \Gamma^{-2}$. The figure of merit shows a monotonic behavior, increasing when the broadening of levels becomes small Γ << *T* as we approach the so called "tight coupling" limit in which charge and heat currents are (optimally) proportional to each other.

ZT can be significantly enhanced by tuning the molecule to an off-resonance situation, ε$_0$ > $k_{\mathrm{B}}T$, Γ (Figure 3). We find that the electrical and thermal conductances strongly fall off with ε$_0$, but the Seebeck coefficient displays a non-monotonic structure, with a maximum showing up off-resonance [48], resulting in a similar enhancement of *ZT* around ε$_0$ = 0.2. It can be proven that the conductances are even functions in gate voltage, $G(\varepsilon_0) = G(-\varepsilon_0)$, $\Sigma(\varepsilon_0) = \Sigma(-\varepsilon_0)$ while $S(\varepsilon_0) = -S(-\varepsilon_0)$, resulting in an even symmetry for *ZT* with gate voltage.
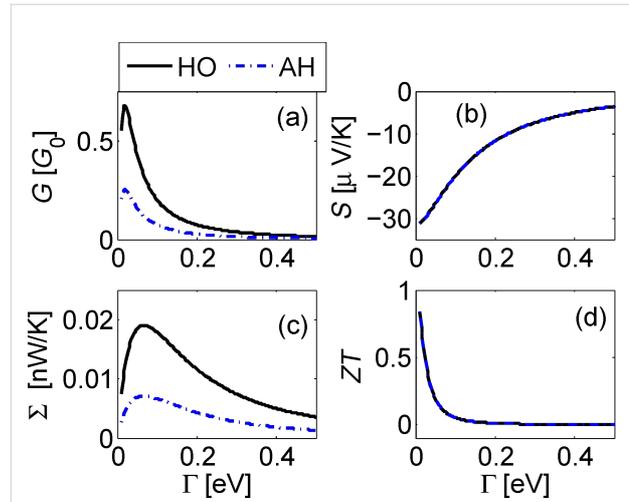
Figure 2: Linear response behavior of the donor–acceptor junction as a function of molecule–metal hybridization with a harmonic mode (full) and an anharmonic two-state system mode (dashed). (a) Normalized electrical conductance G/G_0 with $G_0 = e^2/h$, the quantum of conductance per channel per spin. (b) Seebeck coefficient *S*. (c) Electronic thermal conductance Σ, and (d) the figure of merit *ZT*. Parameters are ε$_0$ = 0.01, ω$_0$ = 0.02, *g* = 0.01 in eV, room temperature *T* = 300 K. We assumed flat bands with a constant density of states.
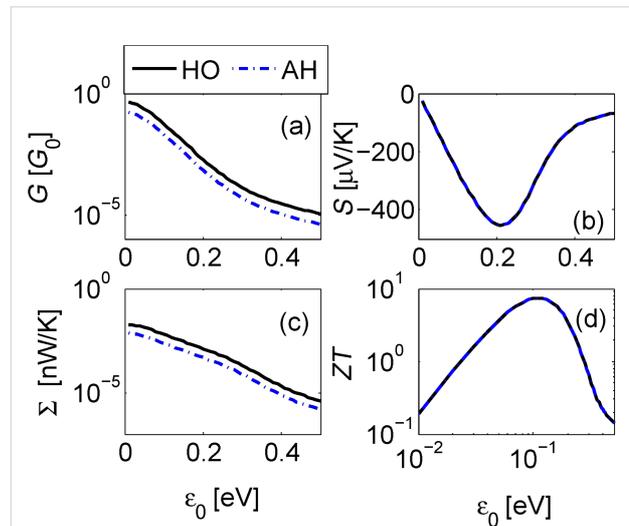
Figure 3: Linear response behavior of the donor–acceptor junction as a function of gate voltage. (a) Electrical conductance, (b) Seebeck coefficient, (c) electronic thermal conductance, and (d) figure of merit *ZT*. Parameters are the same as Figure 2 for Γ = 0.05 eV.

In Figure 4 we show transport coefficients as a function of the vibrational frequency. Parameters correspond to a resonant situation ε$_0$/Γ = 1. Both *G* and Σ decay exponentially with ω$_0$ when ω$_0$ > $k_{\mathrm{B}}T$. However, the figure of merit only modestly increases with ω$_0$ in the analyzed range due to the enhancement of *S* in this region. The values reported for *ZT* in Figure 4 can be increased by weakening the metal–molecule coupling energy Γ.
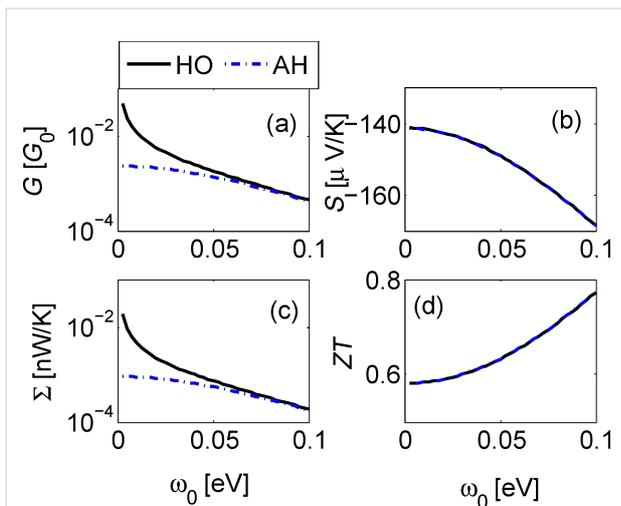
Figure 4: Linear response behavior of the donor–acceptor junction as a function of vibrational frequency ω_0 for ε_0 = 0.2 eV, Γ = 0.2 eV, g = 0.01 eV, and T = 300 K. (a) Electrical conductance, (b) Seebeck coefficient, (c) electronic thermal conductance, and (d) figure of merit ZT.

The maximal efficiency,

$$\eta_{\max} = \eta_C \frac{\sqrt{ZT+1}-1}{\sqrt{ZT+1}+1},$$

and the efficiency at maximum power [46],

$$\eta\left(P_{\max}\right) = \frac{\eta_C}{2} \frac{ZT}{ZT+2},$$

are shown in Figure 5 as a function of ε_0 and Γ for a fixed molecular frequency ω_0 = 0.02 eV and temperature T = 300 K. Here, $\eta_C = 1 - T_{\text{cold}}/T_{\text{hot}}$ corresponds to the Carnot efficiency. By tuning the gate voltage and the molecule–lead hybridization we

approach the bounds $\eta_{\max}/\eta_C \rightarrow 1$, $\eta(P_{\max})/\eta_C \rightarrow 1/2$ [46]. Particularly, for $\Gamma \approx 0.01$ eV we obtain $\eta_{\max}/\eta_C = 0.8$ at the energy $\varepsilon_0 = 0.15$.

Nonlinear performance

Nonlinear thermoelectric phenomena are anticipated to enhance thermoelectric response [49]. Elastic scattering theories of nonlinear thermoelectric transport have been developed, e.g., in [50-53], accounting for many-body effects in a phenomenological manner. Only few studies had considered this problem with explicit electron–phonon interactions, based on the Anderson–Holstein model [54] or Fermi Golden rule expressions [14].

In Figure 6 we simulate the current–voltage characteristics and the resulting efficiency of the D–A junction beyond linear response, by directly applying Equation 13. As discussed in previous investigations [6-8], the molecular junction may break
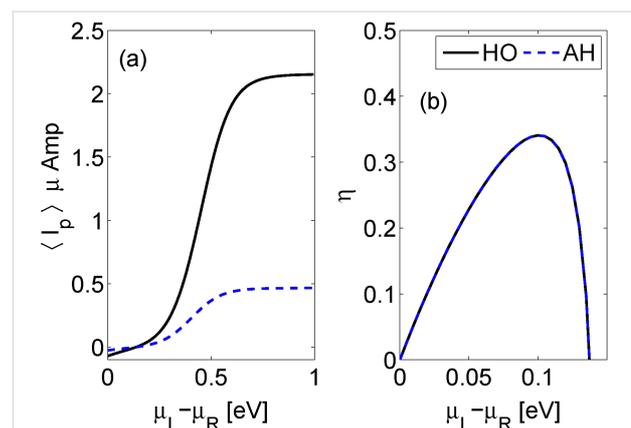
Figure 6: Transport beyond linear response. (a) current voltage characteristics for the harmonic (full) and anharmonic (dashed) mode models. (b) Heat to work conversion efficiency (Equation 15). Parameters are ω_0 = 0.02, ε_0 = 0.2, g = 0.01, Γ = 0.1, Γ_{ph} = 0.002 in units of eV, and T_L = 300 K, T_R = 800 K and T_{ph} = 300 K.
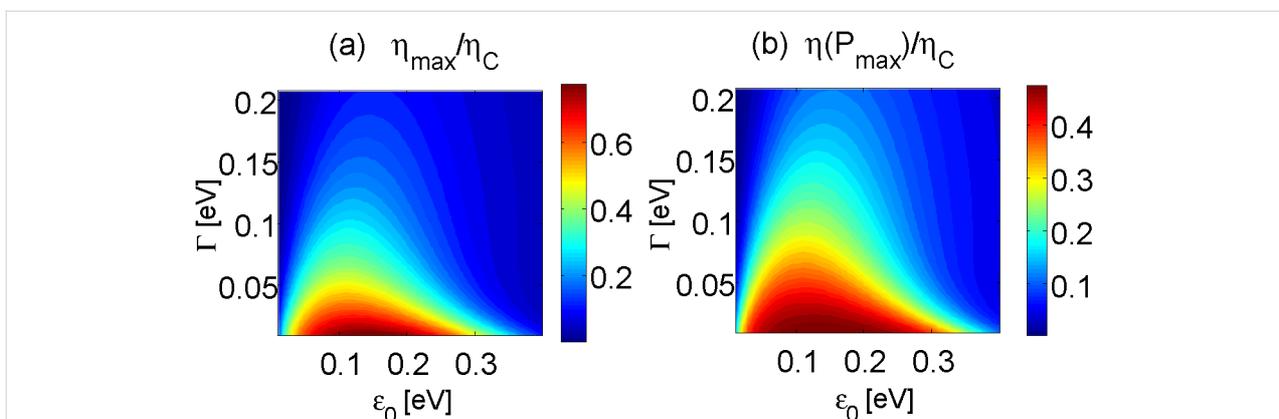
Figure 5: Contour plot of linear response efficiencies as a function of hybridization Γ and electronic energies (or gate voltage) ε_0. (a) Maximum efficiency. (b) Efficiency at maximum power. Parameters are ω_0 = 0.02 eV and T = 300 K.

down far from equilibrium due to the development of "vibrational instability". This over-heating effect occurs when (electron-induced) vibrational excitation rates exceed relaxation rates. To cure this physical problem, we allow the particular vibrational mode of frequency ω_0 to relax its excess energy to a secondary phonon bath of temperature T_{ph}. This can be done rigorously at the level of the quantum master equations and within the NEGF technique [7,43] to yield the rates

$$k_d = k_d^{L \to R} + k_d^{R \to L} + \Gamma_{ph}(\omega_0)\left[n_{ph}(\omega_0)+1\right],$$

$$k_u = k_u^{L \to R} + k_u^{R \to L} + \Gamma_{ph}(\omega_0)n_{ph}(\omega_0),$$

with $n_{ph}(\omega_0) = [e^{\omega_0/k_B T_{ph}}-1]^{-1}$ and a damping term $\Gamma_{ph}(\omega_0)$. Interestingly, we confirmed (not shown) that this additional energy relaxation process does not modify the thermoelectric efficiency displayed in Figure 6b.

Discussion and Prospect

We focused on two-site electronic junctions in which electron transfer between sites is assisted by a particular mode, harmonic or anharmonic (two-state system). The complete information over steady state transport behavior is catered by the cumulant generating function, which we provide here for the HO and the AH mode models, valid under the approximation of weak electron–vibration interaction. We explored linear-response properties, the electrical and thermal conductances G and Σ, as well as the Seebeck coefficient S, the thermoelectric figure of merit ZT, and the resulting efficiency. We further examined current–voltage behavior and the heat-to-work conversion efficiency far-from-equilibrium. We found that G and Σ (more generally, the charge and energy currents) are sensitive to the properties of the mode, while S and ZT are insensitive to whether we work with a harmonic mode or a truncated two-state model.

Several comments are now in place:

(i) **Genuine anharmonicity.** We examined the role of mode anharmonicity by devising a two-state impurity model. It should be emphasized that in the context of molecules, the two-state impurity does not well represent vibrational anharmonicity at high temperatures, as many states should then contribute. Furthermore, it misses an explicit parameter tuning the potential anharmonicity. However, the AH model allows for a first indication on how deviations from harmonicity reflect in transport behavior. The HO and AH models have similar CGFs, yielding currents which are proportional, thus an identical thermoelectric efficiency. It can be readily shown that an n-state truncated HO provides a figure of merit identical to the infinite-level HO model, but it is interesting to perform more realistic calculations and consider, e.g., a morse potential to represent a

physical anharmonic molecular vibration. In this case, an analytical form for the CGF is missing, but one could still derive the charge current directly from a quantum master equation formalism, to obtain the performance of the system. We expect that with a genuine anharmonic potential, S and ZT would show deviations from the harmonic limit, as different pathways for transport open up. Overall, we believe that our results here indicate on the minor role played by mode anharmonicity in determining heat-to-work conversion efficiency.

(ii) **Direct tunneling.** Our analysis was performed while neglecting direct electron tunneling between the D and A sites. This effect could be approximately re-instituted by assuming that coherent transport proceeds in parallel to phonon-assisted conduction, accounting for the coherent contribution using a Landauer expression, see, e.g., [3,14]. Indeed, path integral simulations indicted that in the D–A model, coherent and the incoherent contributions are approximately additive [8].

(iii) **Strong electron-phonon interaction.** The CGFs (Equation 6 and Equation 7) are exact to all orders in the metal–molecule hybridization but perturbative (to the lowest nontrivial order) in the electron phonon coupling g. This is evident from the structure of the rate constants in Equation 10, as electron transfer is facilitated by the absorption/emission of a single quantum ω_0. In numerical simulations we typically employed $g = 0.01$ eV and $\omega_0 = 0.02$ eV. This value for g may seem large given the perturbative nature of our treatment requiring $g/\omega_0 \ll 1$. However, since in the present weak-coupling limit the current simply scales as g^2, Equation 13, our simulations in this work are representative, and can be immediately translated for other values for g. It is of interest to generalize our results and study the performance of the junction with strong electron–phonon interaction, e.g., by using a polaronic transformation [55-59].

(iv) **Phononic thermal conductance.** We studied here electron transfer through molecular junctions, but did not discuss phonon transport characteristics across the junction, mediated by molecular vibrational modes. Consideration of the phononic thermal conductance κ_{ph} is particularly important for a reliable estimate of ZT, as the thermal conductance Σ should include contributions from both electrons and phonons. We now estimate κ_{ph}. The quantum of thermal conductance, an upper bound for ballistic conduction, is given by $\kappa_Q \equiv \pi k_B^2 T/6\hbar$ [60]. At room temperature, this yields $\kappa_Q = 0.28$ nW/K, which exceeds the electronic thermal conductance obtained in our simulations, to dominate the total thermal conductance and predict (significantly) lower values for the figure of merit. However, one should recognize that at high temperatures the ballistic bound for phonon thermal conductance is far from being saturated as

was recently demonstrated in [61]. In particular, the phononic thermal conductance of a two-level junction was evaluated exactly in [62], and it significantly falls below the harmonic bound [61].

For a concrete estimate, we adopt the perturbative (weak mode–thermal bath) expression for the phononic current through a two-state junction developed in [63] and further examined in [64],

$$ j_{ph}^{AH} = g_{ph}\omega_0 \frac{\left[n_R\left(\omega_0\right) - n_L\left(\omega_0\right) \right]}{\left[2 + 2n_R\left(\omega_0\right) + 2n_L\left(\omega_0\right) \right]}. \qquad (17) $$

Here, g_{ph} is the interaction strength of the local vibrational mode to the phononic environments at the two terminals (assuming identical interaction strengths). The baths are characterized by their Bose–Einstein distribution functions $n_\nu(\omega)$. In the case of a local harmonic mode, Equation 17 holds, only missing its denominator. Using $\omega_0 = 0.02$ eV, we receive an estimate for the phononic thermal conductance $\kappa_{ph}^{AH} \equiv j_{ph}^{AH}/\Delta T$, $\kappa_{ph}^{AH} \approx 3.5 \times g_{ph}$ nW/K. Thus, as long as the mode-bath coupling g_{ph} is taken as weak, for example, g_{ph} <5 meV for the data of Figure 2, the electronic contribution to the thermal conductance dominates the total thermal conductance and our simulations are intact. Similar considerations hold for harmonic-mode junctions. Proposals to reduce the coherent phononic thermal conductance by quantum interference effects [65] and through-space designs [66] could be further considered.

(v) **High order cumulants.** The cumulant generating functions, Equation 6 and Equation 7, contain significant information. For example, one could examine the (zero-frequency) current noise, to find out to what extent it can reveal microscopic molecular information.

(vi) **Methodology development.** The cumulant generating function of the HO model was derived from an NEGF approach [43]. The corresponding function for the AH model was reached from a master equation calculation [7,43]. Both treatments are perturbative to second order in the electron–vibration interaction. We take into account all electron scattering processes that are facilitated by the absorption or emission of a *single* quantum ω_0. It is yet surprising to note on the direct correspondence between NEGF and master equation results, as derivations proceeded on completely different lines. In particular, the NEGF approach was done at the level of the RPA approximation to guarantee the validity of the fluctuation theorem. The master equation approach has been employed before to study currents (first cumulants) in the HO model [7],

showing exact agreement with NEGF expressions presented here. This agreement, as well as supporting path integral simulations [8], indicate on the accuracy and consistency of the master equation in the present model. Given its simplicity and transparency, it is of interest to extend this method and examine higher order processes in perturbation theory, to gain further insight on the role of electron–vibration interaction in molecular conduction.

(vii) **Efficiency fluctuations.** We focused here only on averaged-macroscopic quantities. However, in small systems fluctuations in input heat and output power are significant, resulting in "second law violations" as predicted from the fluctuation theorem [44], to, e.g., grant efficiencies exceeding the thermodynamic bound. To analyze the distribution of efficiency, the concept of "stochastic efficiency" has been recently coined and examined [67,68]. In a separate contribution [43] we extend the present analysis and describe the characteristics of the stochastic efficiency in our model, particularly, we explore signatures of mode anharmonicity in the statistics of efficiency.

(viii) **Molecular calculations.** It is of interest to employ our expressions and examine heat-to-work conversion efficiency in realistic molecular junctions. Our results demonstrate that the conversion efficiency can be improved by working in the off-resonant limit, $\Gamma/\varepsilon_0 \ll 1$, as well, when tuning ε_0 through a gate voltage to $\varepsilon_0/k_B T \approx 5$. In such situations, the figure of merit ZT can be made large since one can tune S to large values (though the conductances are small). This suggests that in the D–A class of molecules one should focus on enhancing the thermopower as a promising mean for making an overall improvement in efficiency.

In our ongoing work we are pursuing some of these topics. The derivation of the CGFs employed here and the behavior of efficiency fluctuations in linear response, and beyond that, are detailed in [43]. In [14] we derive thermoelectric transport coefficients for the dissipative D–A model, beyond linear response, and describe the operation of thermoelectric diodes and transistors.

Acknowledgements

References

1. Galperin, M.; Ratner, M. A.; Nitzan, A. *J. Phys.: Condens. Matter* **2007,** *19,* 103201. doi:10.1088/0953-8984/19/10/103201

2. Ballmann, S.; Härtle, R.; Coto, P. B.; Elbing, M.; Mayor, M.; Bryce, M. R.; Thoss, M.; Weber, H. B. *Phys. Rev. Lett.* **2012,** *109,* 056801. doi:10.1103/PhysRevLett.109.056801

3. Markussen, T.; Thygesen, K. S. *Phys. Rev. B* **2014,** *89,* 085420. doi:10.1103/PhysRevB.89.085420

4. Simine, L.; Chen, W. J.; Segal, D. *J. Phys. Chem. C* **2015,** *119,* 12097–12108. doi:10.1021/jp512648f

5. Aviram, A.; Ratner, M. A. *Chem. Phys. Lett.* **1974,** *29,* 277–283. doi:10.1016/0009-2614(74)85031-1

6. Lü, J.-T.; Hedegård, P.; Brandbyge, M. *Phys. Rev. Lett.* **2011,** *107,* 046801. doi:10.1103/PhysRevLett.107.046801

7. Simine, L.; Segal, D. *Phys. Chem. Chem. Phys.* **2012,** *14,* 13820–13834. doi:10.1039/c2cp40851a

8. Simine, L.; Segal, D. *J. Chem. Phys.* **2013,** *138,* 214111. doi:10.1063/1.4808108

9. Santamore, D. H.; Lambert, N.; Nori, F. *Phys. Rev. B* **2013,** *87,* 075422. doi:10.1103/PhysRevB.87.075422

10. Aguado, R.; Brandes, T. *Phys. Rev. Lett.* **2004,** *92,* 206601. doi:10.1103/PhysRevLett.92.206601

11. Berlin, Y. A.; Grozema, F. C.; Siebbeles, L. D. A.; Ratner, M. A. *J. Phys. Chem. C* **2008,** *112,* 10988–11000. doi:10.1021/jp801646g

12. Coropceanu, V.; Sánchez-Carrera, R. S.; Paramonov, P.; Day, G. M.; Brédas, J.-L. *J. Phys. Chem. C* **2009,** *113,* 4679–4686. doi:10.1021/jp900157p

13. Jiang, J.-H.; Entin-Wohlman, O.; Imry, Y. *Phys. Rev. B* **2012,** *85,* 075412. doi:10.1103/PhysRevB.85.075412

14. Jiang, J.-H.; Kulkarni, M.; Segal, D.; Imry, Y. *Phys. Rev. B* **2015,** *92,* 045309. doi:10.1103/PhysRevB.92.045309

15. Erpenbeck, A.; Härtle, R.; Thoss, M. *Phys. Rev. B* **2015,** *91,* 195418. doi:10.1103/PhysRevB.91.195418

16. Aradhya, S. V.; Venkataraman, L. *Nat. Nanotechnol.* **2013,** *8,* 399–410. doi:10.1038/nnano.2013.91

17. Reddy, P.; Jang, S.-Y.; Segalman, R. A.; Majumdar, A. *Science* **2007,** *315,* 1568–1571. doi:10.1126/science.1137149

18. Malen, J. A.; Doak, P.; Baheti, K.; Tilley, T. D.; Segalman, R. A.; Majumdar, A. *Nano Lett.* **2009,** *9,* 1164–1169. doi:10.1021/nl803814f

19. Tan, A.; Sadat, S.; Reddy, P. *Appl. Phys. Lett.* **2010,** *96,* 013110. doi:10.1063/1.3291521

20. Tan, A.; Balachandran, J.; Sadat, S.; Gavini, V.; Dunietz, B. D.; Jang, S.-Y.; Reddy, P. *J. Am. Chem. Soc.* **2011,** *133,* 8838–8841. doi:10.1021/ja202178k

21. Guo, S.; Zhou, G.; Tao, N. *Nano Lett.* **2013,** *13,* 4326–4332. doi:10.1021/nl4021073

22. Baheti, K.; Malen, J. A.; Doak, P.; Reddy, P.; Jang, S.-Y.; Tilley, T. D.; Majumdar, A.; Segalman, R. A. *Nano Lett.* **2008,** *8,* 715–719. doi:10.1021/nl072738l

23. Widawsky, J. R.; Chen, W.; Vázquez, H.; Kim, T.; Breslow, R.; Hybertsen, M. S.; Venkataraman, L. *Nano Lett.* **2013,** *13,* 2889–2894. doi:10.1021/nl4012276

24. Kim, Y.; Jeong, W.; Kim, K.; Lee, W.; Reddy, P. *Nat. Nanotechnol.* **2014,** *9,* 881–885. doi:10.1038/nnano.2014.209

25. Koch, J.; von Oppen, F.; Oreg, Y.; Sela, E. *Phys. Rev. B* **2004,** *70,* 195107. doi:10.1103/PhysRevB.70.195107

26. Segal, D. *Phys. Rev. B* **2005,** *72,* 165426. doi:10.1103/PhysRevB.72.165426

27. Walczak, K. *Physica B* **2007,** *392,* 173–179. doi:10.1016/j.physb.2006.11.013

28. Hsu, B. C.; Liu, Y.-S.; Lin, S. H.; Chen, Y.-C. *Phys. Rev. B* **2011,** *83,* 041404. doi:10.1103/PhysRevB.83.041404

29. Wang, Y.; Liu, J.; Zhou, J.; Yang, R. *J. Phys. Chem. C* **2013,** *117,* 24716–24725. doi:10.1021/jp4084019

30. Perroni, C. A.; Ninno, D.; Cataudella, V. *Phys. Rev. B* **2014,** *90,* 125421. doi:10.1103/PhysRevB.90.125421

31. Ren, J.; Zhu, J.-X.; Gubernatis, J. E.; Wang, C.; Li, B. *Phys. Rev. B* **2012,** *85,* 155443. doi:10.1103/PhysRevB.85.155443

32. Zhou, H.; Thingna, J.; Wang, J.-S.; Li, B. *Phys. Rev. B* **2015,** *91,* 045410. doi:10.1103/PhysRevB.91.045410

33. Arrachea, L.; Bode, N.; von Oppen, F. *Phys. Rev. B* **2014,** *90,* 125450. doi:10.1103/PhysRevB.90.125450

34. Entin-Wohlman, O.; Imry, Y.; Aharony, A. *Phys. Rev. B* **2010,** *82,* 115314. doi:10.1103/PhysRevB.82.115314

35. Entin-Wohlman, O.; Imry, Y.; Aharony, A. *Phys. Rev. B* **2015,** *91,* 054302. doi:10.1103/PhysRevB.91.054302

36. Lü, J.-T.; Zhou, H.; Jiang, J.-W.; Wang, J.-S. *AIP Adv.* **2015,** *5,* 053204. doi:10.1063/1.4917017

37. Thiele, S.; Balestro, F.; Ballou, R.; Klyatskaya, S.; Ruben, M.; Wernsdorfer, W. *Science* **2014,** *344,* 1135–1138. doi:10.1126/science.1249802

38. Levitov, L. S.; Lee, H.; Lesovik, G. B. *J. Math. Phys. (Melville, NY, U. S.)* **1996,** *37,* 4845–4866. doi:10.1063/1.531672

39. Utsumi, Y.; Entin-Wohlman, O.; Ueda, A.; Aharony, A. *Phys. Rev. B* **2013,** *87,* 115407. doi:10.1103/PhysRevB.87.115407

40. Wang, J.-S.; Agarwalla, B. J.; Li, H.; Thingna, J. *Front. Phys.* **2014,** *9,* 673–697. doi:10.1007/s11467-013-0340-x

41. Agarwalla, B. K.; Li, B.; Wang, J.-S. *Phys. Rev. E* **2012,** *85,* 051142. doi:10.1103/PhysRevE.85.051142

42. Altland, A.; Simons, D. B. *Condensed Matter Field Theory,* 2nd ed.; Cambridge University Press: Cambridge, United Kingdom, 2010. doi:10.1017/CBO9780511789984

43. Agarwalla, B. K.; Jiang, J.-H.; Segal, D. *arXiv* **2015,** No. 1508.02475.

44. Evans, D. J.; Searles, D. J. *Adv. Phys.* **2002,** *51,* 1529–1585. doi:10.1080/00018730210155133

45. Park, T.-H.; Galperin, M. *Phys. Rev. B* **2011,** *84,* 205450. doi:10.1103/PhysRevB.84.205450

46. Benenti, G.; Casati, G.; Prosen, T.; Saito, K. *arXiv* **2013,** No. 1311.4430.

47. Onsager, L. *Phys. Rev.* **1931,** *37,* 405–426. doi:10.1103/PhysRev.37.405

48. Paulsson, M.; Datta, S. *Phys. Rev. B* **2003,** *67,* 241403. doi:10.1103/PhysRevB.67.241403

49. Vashaee, D.; Shakouri, A. *Phys. Rev. Lett.* **2004,** *92,* 106103. doi:10.1103/PhysRevLett.92.106103

50. Meair, J.; Jacquod, P. *J. Phys.: Condens. Matter* **2013,** *25,* 082201. doi:10.1088/0953-8984/25/8/082201

51. Sánchez, D.; López, R. *Phys. Rev. Lett.* **2013,** *110,* 026804. doi:10.1103/PhysRevLett.110.026804

52. Svensson, S. F.; Hoffmann, E. A.; Nakpathomkun, N.; Wu, P. M.; Xu, H. Q.; Nilsson, H. A.; Sánchez, D.; Kashcheyevs, V.; Linke, H. *New J. Phys.* **2013,** *15,* 105011. doi:10.1088/1367-2630/15/10/105011

53. Whitney, R. S. *Phys. Rev. B* **2013,** *88,* 064302. doi:10.1103/PhysRevB.88.064302

54. Leijnse, M.; Wegewijs, M. R.; Flensberg, K. *Phys. Rev. B* **2010,** *82,* 045412. doi:10.1103/PhysRevB.82.045412

55. Maier, S.; Schmidt, T. L.; Komnik, A. *Phys. Rev. B* **2011,** *83,* 085401. doi:10.1103/PhysRevB.83.085401

56. Koch, J.; Semmelhack, M.; von Oppen, F.; Nitzan, A. *Phys. Rev. B* **2006,** *73,* 155306. doi:10.1103/PhysRevB.73.155306

57. Härtle, R.; Thoss, M. *Phys. Rev. B* **2011,** *83,* 125419.
    doi:10.1103/PhysRevB.83.125419
58. Schaller, G.; Krause, T.; Brandes, T.; Esposito, M. *New J. Phys.* **2013,**
    15, 033032. doi:10.1088/1367-2630/15/3/033032
59. Dong, B.; Ding, G. H.; Lei, X. L. *Phys. Rev. B* **2013,** *88,* 075414.
    doi:10.1103/PhysRevB.88.075414
60. Rego, L. G. C.; Kirczenow, G. *Phys. Rev. Lett.* **1998,** *81,* 232–235.
    doi:10.1103/PhysRevLett.81.232
61. Taylor, E.; Segal, D. *Phys. Rev. Lett.* **2015,** *114,* 220401.
    doi:10.1103/PhysRevLett.114.220401
62. Saito, K.; Kato, T. *Phys. Rev. Lett.* **2013,** *111,* 214301.
    doi:10.1103/PhysRevLett.111.214301
63. Segal, D.; Nitzan, A. *Phys. Rev. Lett.* **2005,** *94,* 034301.
    doi:10.1103/PhysRevLett.94.034301
64. Boudjada, N.; Segal, D. *J. Phys. Chem. A* **2014,** *118,* 11323–11336.
    doi:10.1021/jp5091685
65. Markussen, T. *J. Chem. Phys.* **2013,** *139,* 244101.
    doi:10.1063/1.4849178
66. Kiršanskas, G.; Li, Q.; Flensber, K.; Solomon, G. C.; Leijnse, M.
    Appl. Phys. Lett. **2014,** *105,* 233102. doi:10.1063/1.4903340
67. Verley, G.; Willaert, T.; Van den Broeck, C.; Esposito, M.
    Nat. Commun. **2014,** *5,* No. 4721. doi:10.1038/ncomms5721
68. Verley, G.; Willaert, T.; Van den Broeck, C.; Esposito, M. *Phys. Rev. E*
    2014, *90,* 052145. doi:10.1103/PhysRevE.90.052145

Nonconservative current-driven dynamics: beyond the nanoscale

Brian Cunningham[*], Tchavdar N. Todorov and Daniel Dundas

Abstract

Long metallic nanowires combine crucial factors for nonconservative current-driven atomic motion. These systems have degenerate vibrational frequencies, clustered about a Kohn anomaly in the dispersion relation, that can couple under current to form nonequilibrium modes of motion growing exponentially in time. Such motion is made possible by nonconservative current-induced forces on atoms, and we refer to it generically as the waterwheel effect. Here the connection between the waterwheel effect and the stimulated directional emission of phonons propagating along the electron flow is discussed in an intuitive manner. Nonadiabatic molecular dynamics show that waterwheel modes self-regulate by reducing the current and by populating modes in nearby frequency, leading to a dynamical steady state in which nonconservative forces are counter-balanced by the electronic friction. The waterwheel effect can be described by an appropriate effective nonequilibrium dynamical response matrix. We show that the current-induced parts of this matrix in metallic systems are long-ranged, especially at low bias. This nonlocality is essential for the characterisation of nonconservative atomic dynamics under current beyond the nanoscale.

Introduction

The development of electronic devices at the nanoscale is a challenging avenue of research with the aim of improving their efficiency and performance. This requires an understanding of the mechanisms for energy transfer from current carriers into atomic motion. Large current densities can generate significant additional forces on atomic nuclei [1-3], resulting in a class of phenomena known as electromigration: atomic rearrangements and mass transport driven by current flow [4,5]. Recent work has drawn attention to another aspect of these forces, anticipated in a visionary argument by Sorbello [5]: unlike equilib-

rium interatomic forces, they are nonconservative (NC), enabling the current to do work on atoms around closed paths [6-9].

This mechanism for energy conversion from current into atomic motion, which we refer to as the waterwheel effect, differs from Joule heating [10,11] in two key respects. First, the growth in atomic kinetic energy is exponential. Second, it is not stochastic: the energy transferred in the waterwheel effect is stored in directional motion, specifically as generalised angular momentum [12].

In the early work above, it seemed that the waterwheel effect might require rather specialised conditions. The effect operates fundamentally through the coupling of pairs of normal modes to form generalised rotors driven by the current. This requires modes that are close in frequency and are, furthermore, strongly coupled by the NC current-induced forces.

A class of systems where these requirements are met are long, low-dimensional metallic wires [13]. They have a dense frequency spectrum providing the desired degeneracies. In addition, frequency renormalisation by the current (which in general can ruin the degeneracies) is small in these quasi-ballistic systems. Finally, electrons couple strongly to extended phonon modes with the wavevectors needed for momentum conservation under backscattering [14]. Simulations under current indeed show NC dynamics in long atomic wires on a grand scale [13].

This study revisits the waterwheel effect in long wires, and reports on two further aspects of this problem. The first is the physical interpretation of the effect. Originally the effect was demonstrated for a system with just two degrees of freedom – the corner atom in an atomic wire with a bend [6]. Under the right conditions, current drives the atom around an expanding orbit in analogy with a real waterwheel, enabling an intuitive picture of how NC forces work. We will see that an intuitive analogy at the other end of the spectrum, that is, in extended systems, is also possible: it is how strong winds generate forward-travelling ripples on a lake, or the uncompensated stimulated emission of directional phonons [12,15].

However, this process hinges on momentum conservation, and for waves, this information requires a sufficiently long-ranged physical property. For atomic motion under current, this property is the nonequilibrium dynamical response matrix, whose antisymmetric part (induced by the current) describes the NC forces [8,16]. The second advance reported here is the quantitative analysis of this property of long metallic nanoconductors. We show that in long nanowires this antisymmetric part

becomes very long-ranged. This nonlocality is essential for the characterisation of NC dynamics under current beyond the nanoscale.

Methods

The system investigated is illustrated in Figure 1. A central region, *C*, whose middle section containing 200 atoms will be treated dynamically, and two electrodes, *L* and *R*, are used to generate current flow.

Figure 1: Long one-dimensional (1D) atomic chain. Region *C* (red) is composed of 200 mobile atoms sandwiched between 50-atom long rigid regions on the ends. *C* is then connected to electrodes *L* and *R* (blue). Electrons are injected into the electrodes by sources held at different electrochemical potentials, μ_L and μ_R. For $\mu_L > \mu_R$, net particle current flows from left to right.
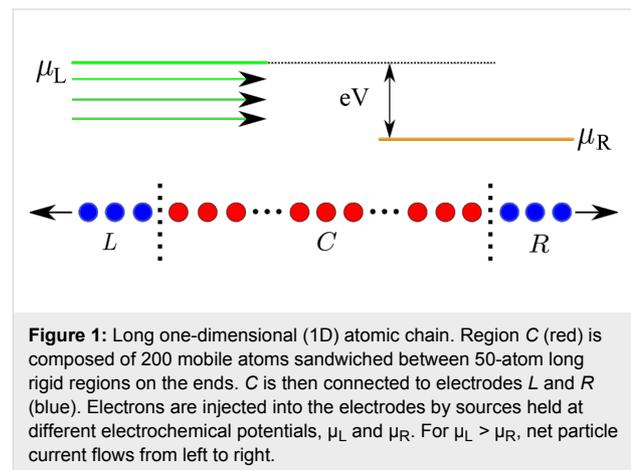
We are interested in the behaviour of the ions (nuclei and core electrons) in these systems under current, and in particular, the gain in atomic kinetic energy due to work done by the current. The force we are considering is the mean force exerted by electrons on ions. It is determined by the rate of change of the expectation value of the ionic momentum. Using the Ehrenfest approximation, the force on an atomic degree of freedom *n* is given by

$$F_n = -\text{Tr}\left\{\hat{\rho}_e \nabla_n \hat{H}_e(\vec{R})\right\}, \tag{1}$$

where $\hat{\rho}_e$ is the one-electron density matrix and $\hat{H}_e(\vec{R})$ is the one-electron Hamiltonian as a parametric function of the atomic position $\vec{R}$.

We will employ two different approaches to determine $\hat{\rho}_e$: an adiabatic steady-state approach, where $\hat{\rho}_e = \hat{\rho}_e(V, \vec{R})$ is a function of the bias *V* and the geometry $\vec{R}$, and a nonadiabatic dynamical approach (within the mixed quantum-classical Ehrenfest method), where $\hat{\rho}_e = \hat{\rho}_e(t)$ is obtained from an open-boundary quantum Liouville equation [17]. These approaches will be discussed in more detail later.

Electrons are described within a spin-degenerate single-orbital orthogonal nearest-neighbour tight-binding model with parame-

ters fitted to the elastic properties of bulk gold [18]. The nearest-neighbour Hamiltonian matrix elements have the form

$$H_{e,mn} = -\frac{\varepsilon c}{2}\left(\frac{a}{R_{mn}}\right)^q , \qquad (2)$$

where R_{mn} is interatomic distance, $\varepsilon = 0.007868$ eV, $a = 4.08$ eV, $c = 139.07$, and $q = 4$. In addition, the model includes a repulsive pair potential of the form

$$P_{mn} = \varepsilon\left(\frac{a}{R_{mn}}\right)^p , \qquad (3)$$

with $p = 11$. The onsite elements of the Hamiltonian are set to zero, and the electron band filling is $v = 0.36361$. Noninteracting electrons are considered throughout. As in [13], we compress the chain to a lattice spacing of $R = 2.373$ Å to suppress a Peierls distortion and resultant band gap that form after geometry relaxation.

Landauer steady state

In the adiabatic steady-state method for the electronic structure, we employ the Landauer picture of conduction. Here the electrodes are infinite, and electrons populate sets of stationary Lippmann–Schwinger scattering states, arriving from either side. The respective population functions, $f_L(E)$ and $f_R(E)$, correspond to the electrochemical potentials of the left and right source reservoirs. The steady-state electron density matrix is then given by [19]

$$\hat{\rho}_e = \int_{-\infty}^{+\infty}\left\{f_L(E)\hat{D}_L(E) + f_R(E)\hat{D}_R(E)\right\}dE, \qquad (4)$$

where $\hat{D}_i(E)$, $i = L,R$ are the density of state operators (subsuming spin degeneracy) for the two sets of scattering states. We work at zero electronic temperature where the occupations are step functions. The density of states operators are generated by Green's function techniques.

We can now calculate the forces on ions about a chosen reference geometry, $\vec{R}_0$. Under small displacements, $d\vec{R}_0$,

$$F_n(\vec{R}) \approx F_n(\vec{R}_0) - \sum_m K_{nm}dR_m , \qquad (5)$$

where $K_{nm} = -\partial F_n(\vec{R}_0)/\partial R_m$ are the elements of the dynamical response matrix.

The dynamical response matrix determines the vibrational frequencies and corresponding collective modes of motion of the ions. We ignore velocity-dependent forces in the present steady-state description (although they will be present in the nonadiabatic dynamical simulations later). These forces can be included perturbatively [8,20] and tend to dampen the atomic motion, and introduce a contribution arising from the Berry phase [8]. Force noise is also excluded here.

The vector containing the atomic displacements can then be expressed as

$$d\vec{R}(t) = \sum_j \vec{p}_j\left\{A_j e^{i\omega_j t} + B_j e^{-i\omega_j t} + \tilde{f}_j\right\}, \qquad (6)$$

where $\{\vec{p}_j\}$ are the eigenvectors of the dynamical response matrix, with frequencies $\{\omega_j\}$, and the static contribution $\{\tilde{f}_j\}$ is determined by any residual forces present in the chosen reference geometry. $\{A_j\}$ and $\{B_j\}$ are set by initial conditions.

The dynamical response matrix can be separated into an equilibrium and a current-induced part:

$$K = K_{eq} + \Delta K. \qquad (7)$$

The current-induced part, in turn, is separated into a symmetric and antisymmetric part [16], $\Delta K = S + A$, with

$$S_{nm} = \frac{\Delta K_{nm} + \Delta K_{mn}}{2} \qquad (8)$$

$$A_{nm} = \frac{\Delta K_{nm} - \Delta K_{mn}}{2}. \qquad (9)$$

The antisymmetric part, present only under bias, is a generalisation of the curl of the force on an ion [13,16]. The resultant nonhermiticity of the dynamical response matrix under current in general generates complex frequencies. The complex modes come in complex conjugate pairs. Via Equation 6 these modes give rise to solutions that grow or decay exponentially in time. These are the waterwheel mode pairs investigated in [6,12,13,16].

Within this steady-state approach, current is determined from the bias and the reference geometry, and is not allowed to respond to the subsequent motion of the ions. This approach is accurate for small atomic displacements and large atomic mass (suppressing the velocity-dependent forces relative to the nonconservative forces, and also the work rate due to inelastic scattering [21]), and in systems where fluctuations in the current

due to deviations from ideal steady-state behaviour are not too large [13].

Dynamical simulations

To simulate departures from the above ideal conditions, we use the nonequilibrium nonadiabatic molecular dynamics method of [17]. Now the leads are finite and embedded in external electron bath supplying carriers. The leads in the present simulations will be 250 atoms long, with open-boundary parameters, $\Gamma = 0.5$ eV and $\Delta = 0.0005$ eV [17]. The electron density matrix then evolves according to the open-boundary equation of motion with the source and sink terms present [17] in the presence of the atomic motion. Atoms obey Newtonian equations, with forces found from the time-evolving density matrix via Equation 1. This form of electron-ion dynamics is known as Ehrenfest dynamics. It captures all forces, equilibrium and nonequilibrium, with the exception of the force noise associated with spontaneous phonon emission and Joule heating [20]. By contrast with the Landauer method above, the dynamical simulations accommodate departures from steady-state conditions and allow the current to respond to changes in the vibrational amplitudes.

To compare the two methods we will further perform a short-time Fourier transform on the ion trajectories $\vec{R}(t)$ from the dynamical simulations and examine the evolution of the energy distribution across the phonon band. The Fourier transform uses a Blackman window, effectively suppressing data outside a particular time interval, while ensuring the data remains continuous. The frequency spectrum of the total ionic kinetic energy (for all N ions) is then

$$E(\omega) \propto \omega^2 \sum_{n=1}^{N} \left| A_n(\omega) \right|^2, \qquad (10)$$

where $\{A_n(\omega)\}$ is a Fourier component of $\{R_n(t)\}$. The window is then moved along in time.

Results and Discussion
Landauer steady-state calculations

First we analyse the equilibrium vibrational modes determined from the dynamical response matrix for a long metallic wire. The mode analysis is then performed under bias, where complex frequencies are present. Long-range interactions in the dynamical response matrix are investigated.

Equilibrium mode analysis

We analyse the equilibrium eigenfrequencies and eigenmodes for longitudinal phonons in a chain with 200 mobile atoms of mass $M = 10$ amu. The 200 eigenvalues $\{k_j\}$ of the 200×200

dynamical response matrix give rise to 2×200 eigenfrequencies: positive and negative square roots of the eigenvalues divided by mass, $\omega_j = \pm\sqrt{k_j / M}$. Each eigenvector of the dynamical response matrix is of length 200. Its elements give the relative amplitudes of the atoms in the given mode. These real-space eigenmodes are normalised to unity and Fourier transformed into momentum space. Figure 2 presents the mode frequencies (vertical axis), together with the modulus (colour) of the Fourier components (k, horizontal axis) of the corresponding eigenvector.

Figure 2: The equilibrium frequencies of each vibrational mode (vertical axis). For each eigenfrequency, the moduli of the k-space components (horizontal axis) of the corresponding eigenvector (normalised to unity) are represented by colour. The system consists of 200 atoms (relaxed) of mass 10 amu sandwiched between two semi-infinite perfect leads.
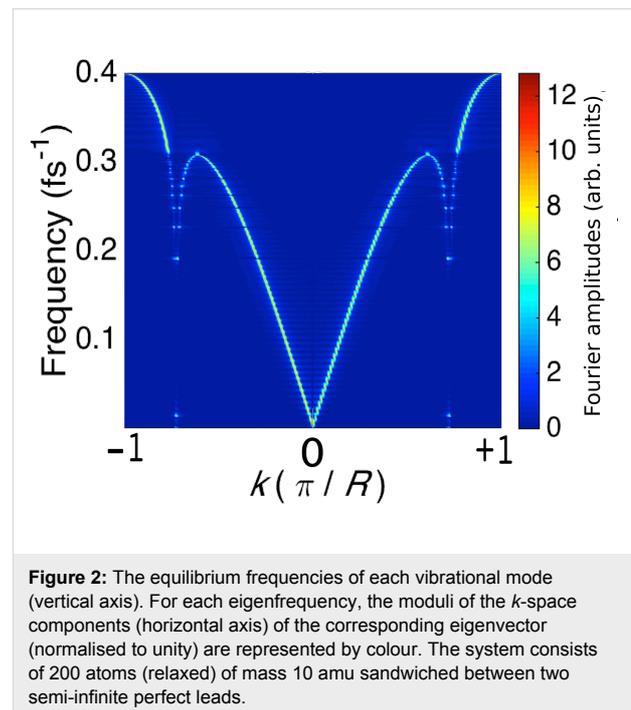
Notice the dip around $k = \pm 0.73\pi/R$. It arises due to the long range behaviour of the dynamical response matrix. To check this, we have determined the dispersion relation by truncating the dynamical response matrix beyond a chosen cut-off range. The dip appears when the range includes at least third or fourth neighbours. The overall shape of the curve in Figure 2 is also sensitive to the truncation range, with the shape in the figure emerging at about 20 lattice spacings. The dip in Figure 2 is qualitatively similar to experiment [22], and occurs at a wavevector of about $\pm 0.73\pi/R$. This is twice the Fermi wavevector $\kappa_F = \nu\pi/R$. We conclude that this dip is the result of a Kohn anomaly [23].

Mode analysis under bias

The key difference between the equilibrium and nonequilibrium dynamical response matrices is the antisymmetric part of the latter. For an infinite perfect chain it can be evaluated analytically:

$$A_{mn} = \frac{8q^2\beta}{\pi R^2 (4(m-n)^2 - 1)} \Big[\cos\phi_L \sin(2(m-n)\phi_L) \tag{11}$$
$$-2(m-n)\sin\phi_L \cos(2(m-n)\phi_L) - f(\phi_R) \Big]$$

where β is the hopping integral, $\phi_{L(R)} = \cos^{-1}(\mu_{L(R)}/2\beta)$, and $f(\phi_R)$ denotes the whole preceding expression in the square brackets with ϕ_L replaced by ϕ_R. The upper panel in Figure 3 shows the relative values of the antisymmetric contribution as a function of site separation and bias.

We see that A_{mn} is oscillatory and long-ranged and, at small bias, becomes infinitely long-ranged. The lower panel in

Figure 3 shows the number of waterwheel pairs formed under bias for different truncations of the dynamical response matrix. We see (main panel) that the data deviates from the plateau by a chosen fractional amount, for longer truncations at low bias; consistent with the upper panel. The inset then shows that the sensitivity to truncation is set by the nonequilibrium, antisymmetric part of the dynamical response matrix.

We now turn to chains relaxed at zero bias as the reference geometry (which remain close to the perfect chain). Figure 4 presents the eigenvector of the dynamical response matrix, under a bias of 0.5 V, for the waterwheel mode with the largest negative imaginary part to its eigenfrequency, $\omega = 0.237 - 0.083$ fs^{-1} i, for a wire with 200 mobile atoms

Figure 3: Upper panel: for each bias (vertical axis) the elements of the antisymmetric part of the dynamical response matrix, relative to the maximum element (for the given bias), are presented as a function of site separation. Lower panel: number of waterwheel pairs with imaginary part above 10% of the maximum, as a function of the truncation of the dynamical response matrix. The main panel truncates the whole matrix, *K*, whereas the inset truncates either just the antisymmetric part (black), or both the equilibrium and nonequilibrium symmetric parts (pink). The system is an infinite perfect wire with 200 mobile atoms.

Figure 4: Main panel: Fourier components (moduli) of the eigenmode with the largest (negative) imaginary part to its frequency under 0.5 V. The system consists of 200 mobile atoms, relaxed under zero bias. Inset: real-space components (moduli) of the eigenmode (blue), and of their real (turquoise) and imaginary (violet) parts.

(mass 10 amu). The inset shows the real and imaginary parts of the eigenvector (now complex), together with its modulus; the main panel displays the moduli of the Fourier components of the mode in *k*-space. (The Fourier picture is qualitatively similar for other waterwheel modes.)

First, what motion does this mode describe? Given $\omega = \omega' + \omega''$ i as the frequency (with ω' and ω'' real) and v_n the mode component at site *n*, the corresponding physical displacement is of the form

$$R_n(t) = Cv_n e^{i\omega t} + C^* v_n^* e^{-i\omega^* t}, \qquad (12)$$

with an amplitude of *C*. The Fourier spectrum shows that the mode is dominated by a negative *k*-component (close in magnitude to the value $2\kappa_F$ required for momentum conservation in electron–phonon interactions, where the Kohn anomaly occurs). Since $\omega' > 0$ and $\omega'' < 0$, we obtain a right-travelling wave that grows in time. The small contribution in the Fourier spectrum at the corresponding positive $k \approx 2\kappa_F$ describes phonon waves travelling the other way, which are attenuated by the electron particle current (flowing to the right).

These observations can be summarised by the physical picture in the Introduction: NC forces in long metallic systems generate modes of motion, in which the current-carrying electrons close

to the Fermi level emit a directed shower of forward-travelling phonons, in analogy with how a breeze creates waves on a lake.

In addition to the features at $\pm 2\kappa_F$, Figure 4 shows a weak background of other Fourier components. By mixing in these other wavevectors, the mode redirects some of the energy gained from the electron "wind" to phonon momenta that can no longer interact directly with the Fermi electrons, and be reabsorbed. This enables the mode energy to grow in time.

We can use Equation 6 to simulate the atomic motion. We calculate the forces under bias for the zero-bias relaxed geometry and use them with zero initial displacements and velocities to set the coefficients $\{A_j\}$ and $\{B_j\}$. We do not include the friction forces here, but we cut the imaginary parts of the frequencies by a factor of 5 to stretch out the growth of the amplitudes in time. Figure 5 shows the displacements of the ions as a function of position and time for a bias of 0.2 V.

The right-travelling phonons generated by the current are evident. The velocity of the peaks and troughs is about 2.5×10^4 ms^{-1}, which is approximately equal to $\omega/2\kappa_F$, with $\omega \approx 0.25$ fs^{-1}. This representative frequency is close to: the Einstein frequency for this system; the typical real part of the (closely-clustered) waterwheel modes; the frequency where the dispersion relation (Figure 2) starts to flatten out; and as we will see, the dominant frequency observed in the dynamical simulations (below).

Nonadiabatic nonequilibrium dynamical simulations

The dynamical simulations under bias are performed for atoms initially at rest in the zero-bias relaxed geometry. The bias is then ramped up at the start. The NC forces cause the ionic kinetic energies to rapidly increase. Unlike the steady-state analysis above, the current now responds and is suppressed by the atomic motion. The system eventually settles at a dynamical steady state, where the velocity-dependent friction forces balance out (on average) the driving NC forces. This interpretation is supported by the fact that balancing these forces leads to analytical predictions that agree with the nonadiabatic simulations [13]. A further, independent verification of this balance is given below. In the simulation below the applied bias is 0.5 V; in the long-time dynamical steady state the current settles at a value corresponding to an effective reduced bias of about 0.2 V (the bias used in the adiabatic visualisation in Figure 5).

Figure 6 presents the temporal Fourier composition of the ionic kinetic energy, as in Equation 10, for the first 6 ps of the simulation. Initially, the growing energy is stored in a narrow frequency range, clustered around the representative frequency
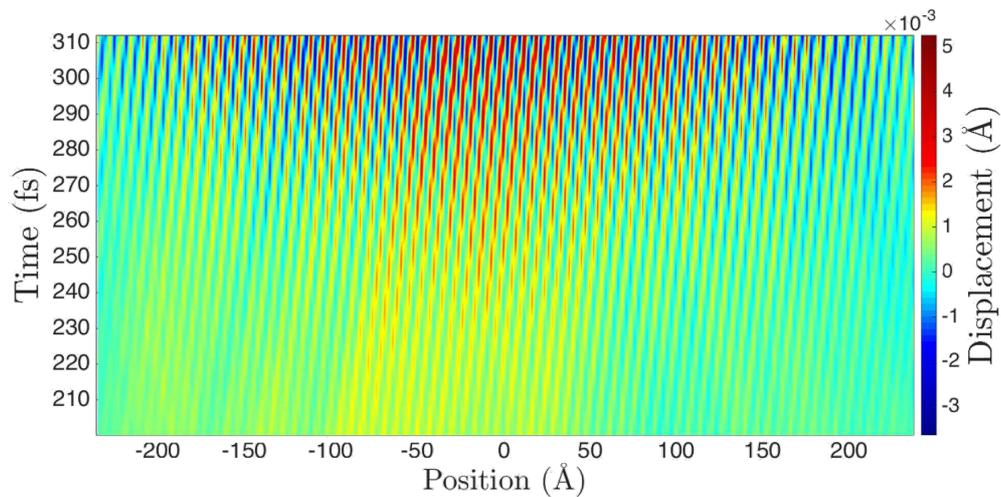
Figure 5: Longitudinal atomic displacements in a wire with 200 dynamical atoms as a function of position (horizontal axis) and time (vertical axis), for an applied bias of 0.2 V, starting from the zero-bias relaxed geometry. The simulation employs the small-amplitude adiabatic steady-state description of Equation 6. The atomic mass is 10 amu.
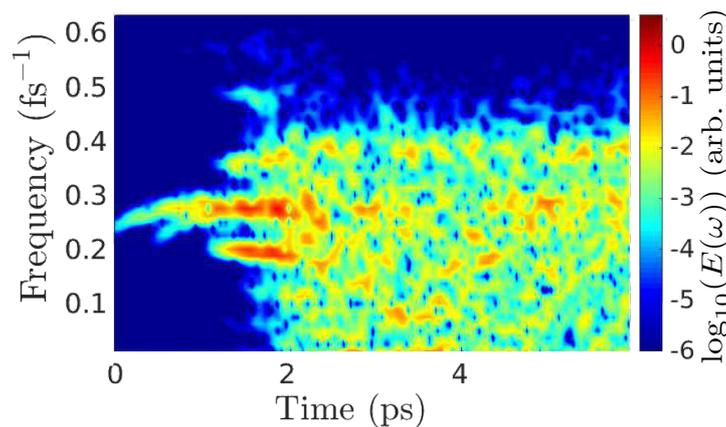
Figure 6: Fourier-decomposed total ionic kinetic energy (colour) across the phonon band, determined using Equation 10, during the nonadiabatic dynamical simulation under a bias of 0.5 V, for 200 mobile atoms of mass 10 amu. A time window of 0.5 ps was applied in increments of 10 fs in the Fourier transform.

above. As the amplitudes increase, phonon–phonon scattering eventually redistributes the energy across the phonon band, resulting in approximate energy equipartioning among available frequencies [13].

The dynamical simulations can be used to give a measure of the efficiency [24] with which the NC forces convert electrical energy into atomic motion. From [13] we can estimate the average imaginary part, Φ, of mode frequencies at a given current. E_0 is the total atomic kinetic energy in the dynamical steady state (beyond about 2 ps in Figure 6). The rate of work by the NC forces is then $W_{NC} \approx 2E_0 2\Phi$ (a factor of 2 to give total, as opposed to just kinetic, vibrational energy, and

another to convert amplitude to intensity). For the simulation in Figure 6, the current in the dynamical steady state is $I \approx 14.2$ µA and $E_0 \approx 17.5$ eV, giving $\Phi \approx 10^{-3}$ fs^{-1} and $W_{NC} \approx 0.07$ eV fs^{-1}. This can be compared against the power, $W = IV$, due to the transfer of electrons between reservoirs, $W \approx 0.04$ eV fs^{-1}. Thus, for the present systems, these two quantities are comparable. A more detailed investigation of this comparison, including its system-dependence, is clearly an important direction for further work.

We can also use the above estimates to independently verify the balance between friction and NC forces in the dynamical steady state. For estimation purposes, we use the analytical result for

the friction coefficient, and corresponding energy relaxation time, τ_{frict}, for atomic Einstein oscillators [17]: $1/\tau_{\text{frict}} = (4\hbar/M\pi)(H'/H)^2$, for a nearest-neighbour tight-binding chain, where H and H' are the hopping integral and its derivative with distance. For the present parameters, and for the above steady-state kinetic energy, the power lost to friction is $W_{\text{frict}} = 2E_0/\tau_{\text{frict}} \approx 0.08$ eV fs^{-1}, in agreement with the (independent) estimate of W_{NC} above.

Conclusion

Long low-dimensional metallic systems are a promising testbed for NC current-driven atomic dynamics. We have highlighted two aspects of these effects here: the physical interpretation of NC motion as "ripples" driven by the electron "wind", and the long-ranged character of the nonequilibrium parts of the dynamical response matrix, responsible for NC dynamics. The inclusion of Joule heating (suppressed in Ehrenfest dynamics) and its interplay with the NC forces is an attractive direction for further work, as is the current-driven dynamical behaviour in the presence of the Peierls instability that occurs under compression-free conditions. We hope that this work will motivate further research into some of these questions.

Acknowledgements

References

1. Brandbyge, M.; Stokbro, K.; Taylor, J.; Mozos, J.-L.; Ordejón, P. *Phys. Rev. B* **2003,** *67,* 193104. doi:10.1103/PhysRevB.67.193104
2. Di Ventra, M.; Pantelides, S. T.; Lang, N. D. *Phys. Rev. Lett.* **2002,** *88,* 046801. doi:10.1103/PhysRevLett.88.046801
3. Todorov, T. N.; Hoekstra, J.; Sutton, A. P. *Phys. Rev. Lett.* **2001,** *86,* 3606–3609. doi:10.1103/PhysRevLett.86.3606
4. Landauer, R.; Woo, J. W. F. *Phys. Rev. B* **1974,** *10,* 1266. doi:10.1103/PhysRevB.10.1266
5. Sorbello, R. S. Theory of Electromigration. In *Solid State Physics;* Ehrenreich, H.; Spaepen, F., Eds.; Academic Press, 1997; Vol. 51, pp 159–231.
6. Dundas, D.; McEniry, E. J.; Todorov, T. N. *Nat. Nanotechnol.* **2009,** *4,* 99–102. doi:10.1038/nnano.2008.411
7. Stamenova, M.; Sanvito, S.; Todorov, T. N. *Phys. Rev. B* **2005,** *72,* 134407. doi:10.1103/PhysRevB.72.134407
8. Lü, J.-T.; Brandbyge, M.; Hedegård, P. *Nano Lett.* **2010,** *10,* 1657–1663. doi:10.1021/nl904233u
9. Bode, N.; Kusminskiy, S. V.; Egger, R.; von Oppen, F. *Phys. Rev. Lett.* **2011,** *107,* 036804. doi:10.1103/PhysRevLett.107.036804
10. Horsfield, A. P.; Bowler, D. R.; Fisher, A. J.; Todorov, T. N.; Montgomery, M. J. *J. Phys.: Condens. Matter* **2004,** *16,* 3609–3622. doi:10.1088/0953-8984/16/21/010
11. Galperin, M.; Ratner, M. A.; Nitzan, A. *J. Phys.: Condens. Matter* **2007,** *19,* 103201. doi:10.1088/0953-8984/19/10/103201
12. Todorov, T. N.; Dundas, D.; Paxton, A. T.; Horsfield, A. P. *Beilstein J. Nanotechnol.* **2011,** *2,* 727–733. doi:10.3762/bjnano.2.79
13. Cunningham, B.; Todorov, T. N.; Dundas, D. *Phys. Rev. B* **2014,** *90,* 115430. doi:10.1103/PhysRevB.90.115430
14. Agraït, N.; Untiedt, C.; Rubio-Bollinger, G.; Vieira, S. *Phys. Rev. Lett.* **2002,** *88,* 2168031–2168034. doi:10.1103/PhysRevLett.88.216803
15. Lü, J.-T.; Christensen, R. B.; Wang, J.-S.; Hedegård, P.; Brandbyge, M. *Phys. Rev. Lett.* **2015,** *114,* 096801. doi:10.1103/PhysRevLett.114.096801
16. Dundas, D.; Cunningham, B.; Buchanan, C.; Terasawa, A.; Paxton, A. T.; Todorov, T. N. *J. Phys.: Condens. Matter* **2012,** *24,* 402203. doi:10.1088/0953-8984/24/40/402203
17. McEniry, E. J.; Bowler, D. R.; Dundas, D.; Horsfield, A. P.; Sánchez, C. G.; Todorov, T. N. *J. Phys.: Condens. Matter* **2007,** *19,* 196201. doi:10.1088/0953-8984/19/19/196201
18. Sutton, A. P.; Todorov, T. N.; Cawkwell, M. J.; Hoekstra, J. *Philos. Mag. A* **2001,** *81,* 1833–1848. doi:10.1080/01418610108216639
19. Todorov, T. N. *J. Phys.: Condens. Matter* **2002,** *14,* 3049. doi:10.1088/0953-8984/14/11/314
20. Todorov, T. N.; Dundas, D.; Lü, J.-T.; Brandbyge, M.; Hedegård, P. *Eur. J. Phys.* **2014,** *35,* 065004. doi:10.1088/0143-0807/35/6/065004
21. Montgomery, M. J.; Todorov, T. N.; Sutton, A. P. *J. Phys.: Condens. Matter* **2002,** *14,* 5377. doi:10.1088/0953-8984/14/21/312
22. Renker, B.; Rietschel, H.; Pintschovius, L.; Gläser, W.; Brüesch, P.; Kuse, D.; Rice, M. J. *Phys. Rev. Lett.* **1973,** *30,* 1144–1147. doi:10.1103/PhysRevLett.30.1144
23. Kohn, W. *Phys. Rev. Lett.* **1959,** *2,* 393–394. doi:10.1103/PhysRevLett.2.393
24. Bustos-Marún, R.; Refael, G.; von Oppen, F. *Phys. Rev. Lett.* **2013,** *111,* 060802. doi:10.1103/PhysRevLett.111.060802

License and Terms

Virtual reality visual feedback for hand-controlled scanning probe microscopy manipulation of single molecules

Philipp Leinen[1,2], Matthew F. B. Green[1,2], Taner Esat[1,2], Christian Wagner[1,2], F. Stefan Tautz[1,2] and Ruslan Temirov[*1,2]

Abstract

Controlled manipulation of single molecules is an important step towards the fabrication of single molecule devices and nanoscale molecular machines. Currently, scanning probe microscopy (SPM) is the only technique that facilitates direct imaging and manipulations of nanometer-sized molecular compounds on surfaces. The technique of hand-controlled manipulation (HCM) introduced recently in *Beilstein J. Nanotechnol.* **2014,** *5,* 1926–1932 simplifies the identification of successful manipulation protocols in situations when the interaction pattern of the manipulated molecule with its environment is not fully known. Here we present a further technical development that substantially improves the effectiveness of HCM. By adding Oculus Rift virtual reality goggles to our HCM set-up we provide the experimentalist with 3D visual feedback that displays the currently executed trajectory and the position of the SPM tip during manipulation in real time, while simultaneously plotting the experimentally measured frequency shift (Δf) of the non-contact atomic force microscope (NC-AFM) tuning fork sensor as well as the magnitude of the electric current (I) flowing between the tip and the surface. The advantages of the set-up are demonstrated by applying it to the model problem of the extraction of an individual PTCDA molecule from its hydrogen-bonded monolayer grown on Ag(111) surface.

Introduction

The recently introduced scanning probe microscopy (SPM) technique of hand controlled manipulation (HCM) allows the operator of the SPM to manipulate single molecules on surfaces by coupling the motion of the microscope tip to the movements of the hand of the operator in 3D space [1]. The possibility to control the position of the SPM tip by hand is especially advantageous when the manipulation is performed in an environment where the forces acting on the manipulated molecule are a priori

not fully known. In such cases, a hand-controlled trial and error search for successful manipulation protocols is more efficient than model-based simulation approaches, simply because in HCM tests of various manipulation protocols can be performed very quickly by execution and comparison of many alternative tip trajectories.

For its initial demonstration HCM was applied to the problem of extraction of single PTCDA molecules out of their commensurate monolayer grown on the Ag(111) surface [1-3]. Similar to the current study those experiments were performed with a commercial, combined qPlus tuning fork [4] non-contact atomic force/scanning tunnelling microscope (NC-AFM/STM) operated at 5 K under ultra-high vacuum conditions. Each extraction attempt started with positioning the tip over one of the four carboxylic oxygen atoms (marked by red circles in Figure 1) of the PTCDA molecule. The tip was then approached to the surface until the operator observed a sudden jump in the I and Δf signals. Here the oxygen atom under the tip flipped up toward the tip apex, thereby establishing a chemical bond between the tip and the molecule [5,6]. Through this bond the molecule can be lifted from the surface by pulling it with the tip as it is retracted away from the surface. When the contacted molecule rests isolated on the surface, retracting the tip on a straight line away from the surface allows for the successful lifting of the molecule [7,8]. However if the contacted molecule resides inside an ordered PTCDA monolayer, most of the attempts of pulling it straight up fail [1], because intermolecular interactions in the monolayer hold the molecules together [9]. When the force exerted by the intermolecular bonds overcomes the strength of the tip–molecule bond, the latter breaks and the molecule being lifted drops back to the surface.

Previously, we employed HCM to identify tip retraction trajectories which minimize the instances of tip–molecule bond breaking that prematurely end the manipulation procedure [1]. The task was accomplished by extracting 48 PTCDA molecules one by one. The experiment started without any prior training of the operator and lasted for about 50 working hours. In the course of the experiment an average time between successful manipulation attempts decreased from 40 to 13 minutes, which suggested that the operator learned how to move the tip in order to extract the molecule successfully. The learning was achieved by observing and intuitively interpreting the real-time $I(t)$ and $\Delta f(t)$ signals displayed during the manipulation on the screen of the oscilloscope, where a premature break of the tip–molecule contact was revealed as a simultaneous sharp drop of both $I(t)$ and $\Delta f(t)$ signal values.

Experimental

While in its present form HCM is able to generate many tip trajectories in a fast and intuitive manner, it does not yet allow for a convenient visual inspection of the generated data in real time. Having such a possibility would make the analysis of manipulation trajectory data much simpler. It would also help to transfer knowledge between different users and/or experiments, thus facilitating systematic learning during which manipulation protocols are refined and corrected in multiple steps. Visualization of the manipulation trajectory data should therefore greatly increase the effectiveness of HCM and extend the range of its possible applications. Here we introduce a system that visualizes HCM data in real time by displaying the actual tip position as well as the history of its movements in 3D using Oculus Rift DK 2 (ORt) virtual reality goggles. A scheme of the set-up is shown in Figure 2. As before we use two VICON Bonita
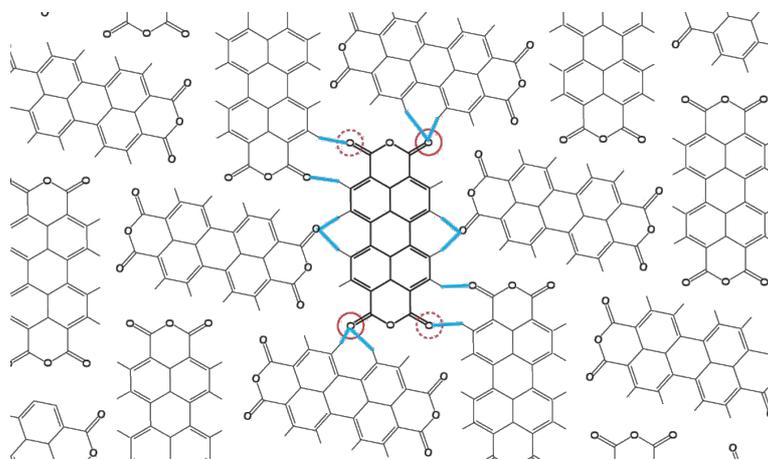
Figure 1: Structural model of a fragment of the commensurate PTCDA monolayer grown on an Ag(111). Blue lines mark the expected positions of intermolecular hydrogen bonds. Red circles mark positions of carboxylic oxygen atoms that may be used for contacting the molecule by the tip. Here we only contact the oxygen atoms marked by solid circles.

Figure 2: Scheme of the set-up used for HCM with a visual feedback using Oculus Rift virtual reality goggles (ORt). VICON 3D tracking system with two IR cameras follows the position of the VICON Apex device. VICON Apex has a dodecahedral shape, on the surface of which multiple sources of IR light are installed. The emitted IR light is registered by the cameras that compose an image from which the VICON software reconstructs the position and the orientation (not used in the experiment) of the Apex device in 3D space. The obtained coordinates *x,y,z* are used to set the position of the AFM/STM tip. The same coordinates are used to plot 3D trajectories in the virtual space of (ORt).

cameras for 3D tracking of the position of the operator's hand. In contrast to our previous work [1] where we tracked a single reflective marker we now use a VICON Apex device. Due to its shape and multiple active sources of infra-red (IR) light on its surface, tracking of the Apex device is more reliable [10]. Moreover, it allows for the implementation of additional service functions that help the operator to perform manipulation experiments without the use of a PC keyboard.

3D trajectories of the tip are visualised in ORt by intercepting the coordinates of the Apex device $\vec{r}(t) \equiv (x(t), y(t), z(t))$ that are sent to the SPM electronics to position the tip [1] and forwarding them to ORt where a dot is plotted at each $\vec{r}$, thus generating a 3D image of the tip trajectory. In addition, each dot is coloured to exhibit values of $\log(I(\vec{r}(t)))$ or $\Delta f(\vec{r}(t))$ as obtained from the SPM. Switching between the $\log(I)$ and Δf color-codes can be performed by pressing a custom-defined action button on the Apex device.

Results and Discussion

We begin the discussion of our results by characterising the precision of the implemented visual feedback system. The characterisation was performed in the following manner: First, a circle with a diameter of 7 Å oriented arbitrarily in 3D space was visualized in ORt. The operator, wearing ORt, tried to follow the drawn circle by moving the Apex device held in their hand. Four of such attempts are exhibited in Figure 3. Superimposing the original circle with a torus of minimal volume that encloses all hand-drawn trajectories we find that the maximum error of trajectory tracking was approx. 0.4 Å. The accuracy of the manual trajectory tracking depends on the movement speed of the operator's hand and thus can be improved further. Note, however, that the oscillation amplitude of the NC-AFM tuning fork sensor (approx. 0.4 Å) directly adds to the error of trajectory tracking and thus limits the achievable accuracy.

Figure 3: Precision of an arbitrary trajectory tracking in HCM with the visual feedback. The operator followed a circle with HCM for four times. Each attempt took one minute and the maximum deviation from the cycle was approx. 0.4 Å. Further details in text.
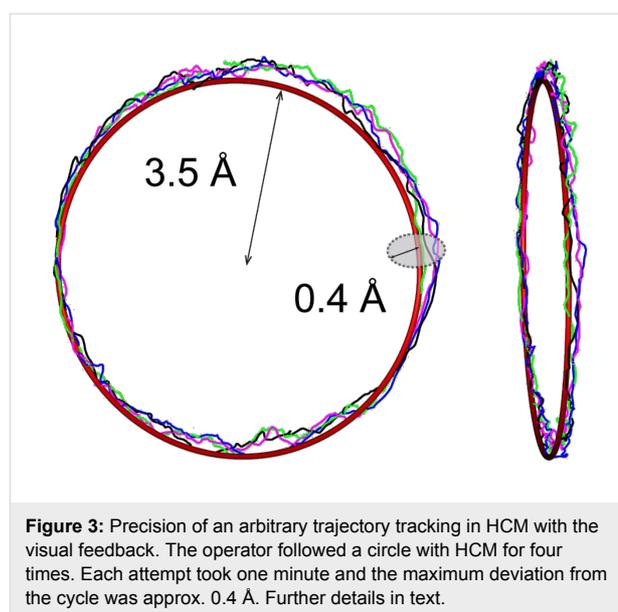
Further, we applied the extended HCM set-up to our model manipulation problem of [1], i.e., extraction of PTCDA from a monolayer adsorbed on Ag(111). First, by averaging all the successful tip trajectories from [1] we composed a single 3D trajectory. The averaged trajectory that is shown in Figure 4 was then plotted in ORt to serve as a guide for the operator. The plotted trajectory was rotated around the *z*-axis (perpendicular to the surface) to match the ORt view to the real azimuthal orientation of the chosen PTCDA molecule on the sample surface. As shown in Figure 4, in the correct orientation the projection of the averaged trajectory roughly follows the diagonal of the rectangular molecular backbone (for 3D images see Supporting Information File 2).

After the alignment of the ORt image, the manipulation process was started. First, using the standard options of our SPM soft-

Figure 4: Manipulation trajectories recorded using HCM with the visual feedback. The inset in (a) shows three manipulation attempts (numbered by the sequence of their appearance) performed by the operator in the search of the kinked trajectory shown in (a) and (b). Top and side views of a) $\log(I(x,y,z))$ and b) $\Delta f(x,y,z)$ trajectories recorded by pulling a single PTCDA molecule out of the PTCDA monolayer grown on Ag(111). Orientation of the molecule is shown in Figure 1. A section of the averaged trajectory obtained from [1] is shown in gray. Seven attempts following the averaged trajectory fail due to a premature loss of the tip–molecule contact. In contrast, eight attempts following a newly found kinked trajectory lift the molecule far from the surface without loosing the tip–molecule contact.

ware, we parked the tip directly above the oxygen atom of the PTCDA that was chosen for contacting (Figure 1). After the tip was stabilized, the STM current feedback loop was opened and the control over the tip position was passed to the operator. The operator contacted the molecule by moving the tip in a strictly vertical trajectory (x,y tip coordinates frozen) until a sharp jump of the I and Δf bar indicators in the ORt display indicated establishing of the contact between tip and PTCDA (see Supporting Information File 1). After the contact was established the tip control was switched from the 1D (only z) to full 3D (x,y,z) HCM mode.

Using HCM the operator made seven attempts to follow the average trajectory. As Figure 4 shows, in all cases the contact to the molecule was lost after about $r = 5$ Å of tip retraction. The breaking of the contact was recognized by an abrupt simultaneous drop of the I and Δf signals, which could be directly observed in the ORt display (see Supporting Information

File 1). The early rupture of the tip–PTCDA contact indicated that the chosen tip trajectory was not optimal. The deficiency of the averaged trajectory can be explained by the fact that it was generated by averaging the datasets obtained by the extraction of PTCDA molecules that had different numbers of nearest neighbours [1]. Since we expect the intermolecular interactions in the monolayer to play a significant role, the tip trajectories that extract molecules from different intermolecular configurations most likely deviate from each other substantially. Thus, averaging them could produce a trajectory that is not optimal for any particular configuration, such as the one chosen in our present experiment (Figure 1). Another argument for a poor performance of the averaged trajectory may be supplied by assuming different tip structures. In other words, the tip used here could form a weaker bond to the molecule than the tip employed in [1]. However, the fact that the failure of the averaged trajectory occurred also after several tip-forming procedures, makes the second argument less convincing.

The failure of the averaged trajectory challenged us with the problem of identification of a new tip trajectory that is able to extract a PTCDA molecule from the chosen configuration. We show that HCM with ORt visual feedback allows the operator to identify the necessary tip trajectory very efficiently, making only a few manipulation attempts. The inset of Figure 4a exhibits three steps of the search process: In the first attempt (trajectory 1) the operator deviated laterally from the unsuccessful averaged trajectory. The first attempt failed and the contact to the molecules was lost rather early. The second attempt (trajectory 2) however took a different direction and there the contact to the tip was kept longer. In the third attempt (trajectory 3) the operator first followed trajectory 2 but then made another twist which finally enabled further lifting. Following trajectory 3, the operator sequentially lifted the molecule eight times, each time retracting the tip by up to 12 Å from the surface without a single failure of the tip–molecule bond.

It is important to note that in the course of the manipulation experiments in Figure 4 the molecule was never fully detached from the surface in order to prevent a tip structure change from happening, e.g., due to a jump of the extracted molecule onto the tip apex. After retracting the tip by 11–12 Å it was approached back to the surface and the tip–molecule bond was cleaved by carefully raising the junction bias to 0.1–0.5 V. In all cases after this voltage increase the molecule was re-deposited back to the substrate, precisely into its previous configuration within the monolayer. Using the described procedure we were able to contact and lift the same molecule with the same tip which, as Figure 4 shows (see also the interactive 3D models provided in Supporting Information File 2), resulted in a highly reproducible behaviour of $I(x,y,z)$ and $\Delta f(x,y,z)$.

Conclusion

In summary, we have extended our SPM HCM set-up by adding a visual feedback system based on Oculus Rift virtual reality goggles. Visual feedback helps the operator performing HCM to control their actions in real time by directly observing the executed tip trajectory in 3D. The system also allows the operator to follow any arbitrary preset 3D trajectories and execute controlled deviations from them. The typical error of the trajectory following was found to be about 0.4Å. The extended SPM HCM set-up was applied to the model problem of extracting of a single PTCDA molecule out of a PTCDA/Ag(111) monolayer. We demonstrated that the added visual feedback facilitates the systematic search for optimal manipulation trajectories. The kinked manipulation trajectory that was found in this work aided the uninterrupted lifting of the molecule from the surface. The stability of the established manipulation protocol resulted in the collection of a very reproducible $I(x,y,z)$ and $\Delta f(x,y,z)$ data set that clearly exhibits interesting signatures of the molecular manipulation process and which opens up the prospect for systematic studies.

Supporting Information

Supporting Information File 1
Screenshot Oculus Rift movie showing different stages of manipulation (watch subtitles for additional information). [http://www.beilstein-journals.org/bjnano/content/supplementary/2190-4286-6-220-S1.mp4]

Supporting Information File 2
Interactive 3D models of the data shown in Figure 4. In order to view it unpack and open either 'df.html' (frequency shift) or 'I.html' (logarithm of the current) file. [http://www.beilstein-journals.org/bjnano/content/supplementary/2190-4286-6-220-S2.zip]

References

1. Green, M. F. B.; Esat, T.; Wagner, C.; Leinen, P.; Grötsch, A.; Tautz, F. S.; Temirov, R. *Beilstein J. Nanotechnol.* **2014**, *5*, 1926–1932. doi:10.3762/bjnano.5.203
2. Rohlfing, M.; Temirov, R.; Tautz, F. S. *Phys. Rev. B* **2007**, *76*, 115421. doi:10.1103/PhysRevB.76.115421
3. Kraft, A.; Temirov, R.; Henze, S. K. M.; Soubatch, S.; Rohlfing, M.; Tautz, F. S. *Phys. Rev. B* **2006**, *74*, 041402(R). doi:10.1103/PhysRevB.74.041402
4. Giessibl, F. J. *Rev. Mod. Phys.* **2003**, *75*, 949. doi:10.1103/RevModPhys.75.949
5. Temirov, R.; Lassise, A.; Anders, F. B.; Tautz, F. S. *Nanotechnology* **2008**, *19*, 065401. doi:10.1088/0957-4484/19/6/065401
6. Toher, C.; Temirov, R.; Greuling, A.; Pump, F.; Kaczmarski, M.; Cuniberti, G.; Rohlfing, M.; Tautz, F. S. *Phys. Rev. B* **2011**, *83*, 155402. doi:10.1103/PhysRevB.83.155402
7. Fournier, N.; Wagner, C.; Weiss, C.; Temirov, R.; Tautz, F. S. *Phys. Rev. B* **2011**, *84*, 035435. doi:10.1103/PhysRevB.84.035435
8. Wagner, C.; Fournier, N.; Tautz, F. S.; Temirov, R. *Phys. Rev. Lett.* **2012**, *109*, 076102. doi:10.1103/PhysRevLett.109.076102
9. Kilian, L.; Hauschild, A.; Temirov, R.; Soubatch, S.; Schöll, A.; Bendounan, A.; Reinert, F.; Lee, T.-L.; Tautz, F. S.; Sokolowski, M.; Umbach, E. *Phys. Rev. Lett.* **2008**, *100*, 136103. doi:10.1103/PhysRevLett.100.136103
10. Using ORt we found that it interfered with operation of the VICON system: In case a single point-marker is used with the VICON system and because ORt also uses multiple sources of infra-red light (fixed at a surface of the goggles) for positioning, the correct determination of the marker's position becomes complicated. To overcome that problem we used VICON Apex device that is recognised by the VICON software as a 3D object with a unique shape which allows the VICON software to distinguish it clearly from the shapes created by the light sources installed on ORt.

Negative differential electrical resistance of a rotational organic nanomotor

Hatef Sadeghi, Sara Sangtarash, Qusiy Al-Galiby, Rachel Sparks, Steven Bailey[*]
and Colin J. Lambert[*]

Abstract

A robust, nanoelectromechanical switch is proposed based upon an asymmetric pendant moiety anchored to an organic backbone between two C_{60} fullerenes, which in turn are connected to gold electrodes. Ab initio density functional calculations are used to demonstrate that an electric field induces rotation of the pendant group, leading to a nonlinear current–voltage relation. The nonlinearity is strong enough to lead to negative differential resistance at modest source–drain voltages.

Introduction

Biomotors utilising myosins, kinesins, and dyneins [1-4] have been utilised in several motor-protein-driven devices for cargo transportation [5,6], molecule sorting [7,8], imaging [9] and sensing [10,11]. In contrast to biological machines, which convert energy into directed motion by moving out of thermodynamic equilibrium [12-15], artificially designed nanoelectromechanical (NEM) motors operate by moving towards thermodynamic equilibrium. Many examples of artificial NEM devices use directed motion [16-26]. For example, oscillators with frequencies in excess of 1 GHz have been constructed from multiwalled carbon nanotubes (MWCNT), where the telescoping nature of the inner carbon nanotubes [27,28] with very

low interwall friction [29-34] lead to novel electrical properties [35-40]. These examples illustrate how an electric field can induce motion and also how a motion-induced change of geometry can affect electrical properties. In what follows, our aim is to demonstrate that this coupling between a controlled geometry and electrical properties can lead to desirable nonlinear current–voltage relations and negative differential resistance (NDR).

As a specific example that demonstrates the general principle, we analyse the molecular-scale NEM shown in Figure 1 whose conformation can be manipulated using an external electric field

and whose conformational changes feedback to produce a nonlinear current–voltage relation. This novel NEM consists of a pendant rotor attached by a single carbon bond to an aromatic backbone. The rotor is designed to possess a dipole moment aligned along its length such that an applied electric field will cause the rotor to turn relative to the aromatic backbone. Our aim is to examine the response of the device to an external electric field and determine the change in electrical conductance due to the associated conformational changes when the C_{60} molecules are attached to metallic electrodes. Our calculations will demonstrate that such conformation changes lead to NDR.

Results and Discussion

The dumbbell molecular switch shown in Figure 1 consists of three main sections, the backbone, the terminating groups and the branch. The backbone consists of five interconnected phenyl rings with attached methyl groups to prevent the backbone from twisting and is stabilized at either end by a fullerene, C_{60} terminating group. The C_{60} at either end not only stabilizes the molecule, but also allows the molecule to appear more clearly visible in STM images [41], therefore facilitating experimental STM measurements. The branch extends from the central ring of the backbone and is made up of three interlinked arene compounds; the central phenyl ring is capped by aniline at one end and terminated with a fluoro-toluene derivative at the other, where the hydrogens are replaced by fluorine. As fluorine is the most electronegative element, this design will enable the branch to possess a dipole moment. The dipole moment for the combined pendant group and backbone as an average of all the rotation angles of the pendant group relative to the backbone is approximately 9.4 debye over a length of 28.23 Å. The length of the pendant group alone is 20.4 Å. The variation in the dipole moment, over all rotation angles, is given in Supporting Information File 1, Figure S4 and the lengths are given in Supporting Information File 1, Figure S5.

This dipole moment of the branch facilitates the electric-field-induced rotation required to create a switch. By applying an external electric field, E_{ext}, across the molecule, the additional contribution to the total energy is $U = -p \cdot E_{ext}$, where p is the dipole. In the presence of a uniform electric field, the energy landscape of the system will change, with the possibility that the most stable rotation angle switches from one value to another. By computing the total energy as a function of rotation angle, we thereby obtain an estimate of the size of the electric field required to switch the molecule.

We use the SIESTA [42] implementation of the density functional theory (DFT) with a van der Waals density functional [43,44] and extended and corrected double-zeta-polarised basis sets of the pseudoatomic orbitals. The geometries were optimised by relaxing the atomic forces to less than 20 meV/Å. The van der Waals density functional allows long-range interactions to be taken into account. The total ground-state energy of the molecule is calculated to find the energy profile of the molecule with different confirmations. A basis set superposition correction is carried out to account for overlapping basis functions. This correction is calculated by taking the relaxed energy of the entire molecule and subtracting the energy of the structural relaxation of backbone and the branch separately: $U_{BSC} = U_{molecule} - U_{branch} - U_{backbone}$. Figure 2 shows the potential energy profile of the dumbbell molecule against the rotation angle of the rotor with respect to the backbone. The DFT-calculated energy profile yields an energy barrier to rotation of about 800 meV.

Figure 2 shows the energy landscape as a function of rotation angle for four magnitudes of electric field between 1.0 and 3.5 V/nm. Figure 2a–d corresponds to the directions $E^{(a)}$, $E^{(b)}$, $E^{(c)}$ and $E^{(d)}$, respectively, as shown in the left-most part of the figure. Only Figure 2a and Figure 2b are relevant to the two-

Figure 1: Schematic of the proposed molecular switch, where the asymmetric rotor blade is terminated at one end with nitrogen and at the other with three fluorine atoms with a single bond linking the rotor to the aromatic backbone. The two C_{60} molecules act as secure anchors for the device and could be connected to gold leads.

Figure 2: The potential energy profile, U_{BSC} (eV), calculated from the changes in the total energy of the system against the rotation angle of the rotor with respect to the backbone as shown in Figure 1 for four applied magnitudes of electric field between 1.0 and 3.5 V/nm. (a–d) correspond to the directions $E^{(a)}$, $E^{(b)}$, $E^{(c)}$ and $E^{(d)}$, respectively, shown in the left-most figure. The rotation angle is defined in Figure 1 and Supporting Information File 1, Figure S2. 240° corresponds to the pendant group being parallel to the backbone, as shown in Figure 2, whereas 60° (or equivalently 420°) corresponds to the pendant group making a 30° angle with the backbone. The zero-field energy minima are located at rotation angles of 60° and 240°. To sample all angles and compute these energy–angle curves, the pendant group was artificially rotated to a chosen angle and then the molecule was allowed to relax to a local energy minimum.

terminal device shown in Figure 3a. The plots in Figure 2c,d are relevant to a three-terminal device containing a gate electrode able to create a field perpendicular to the length of the molecule. In what follows, we focus on a two-terminal device only, since this is likely to be realised in the laboratory. At zero temperature, the rotation angle coincides with the global minimum of the energy curves. At a finite temperature, the above minima correspond to the most-probable rotation angles, but other angles can be sampled according to the Boltzmann factor (see Equation 4 below). At zero field, the energy minima occur at $\theta_A = 60°$ and $\theta_B = 240°$. In both positions, the branch is parallel to the backbone and there is a significant overlap between one of the phenyl rings on the backbone with the aniline capped end of the branch. This suggests that these positions are stabilised by the π–π interaction between the two aromatic rings. The rotor does not rotate at a uniform distance from the backbone and therefore the charge distribution of the branch interacts nonuniformly with the backbone. This effect is apparent at θ_B where one end of the branch is located closer to the backbone than the other.

When an electric field is applied parallel to the backbone in the direction of $E^{(a)}$ (Figure 2a), the global minimum at θ_B becomes a local minimum and the global minimum is then located at θ_A. This means that through application of an electric field parallel to the backbone, the most stable state of the molecule can be

manipulated, and the branch of the molecule will switch due to this electric field. One can also observe that by removing or reversing the direction of the electric field the branch can be switched back to θ_B. As shown in Figure 2c, by applying an external field $E^{(c)}$ orthogonal to the molecule, the global minimum of the energy curve can be switched to 0°, whereas a field of $E^{(d)}$ causes no such crossover.

To study the effect of the external electric field on transport properties of the dumbbell molecule, consider the molecule connected to two gold electrodes in a junction, as shown in Figure 3a. Since we are interested in a two-terminal switch, we focus on the effect of the source–drain electric field induced by gold electrodes (electric field parallel to the molecule, Figure 1a,b). By contacting the left and right C_{60} to gold electrodes, electrons entering the leads from external reservoirs have Fermi distributions given by $f_L(E)$ and $f_E(E)$ and the Landauer formula [45] gives:

$$I = \frac{2e}{h} \int_{-\infty}^{+\infty} dE\, T(E) \big(f_L(E) - f_R(E) \big), \qquad (1)$$

where the electronic charge $e = |e|$, h is Plank's constant and $T(E)$ is the transmission coefficient for electrons with energy E passing through the molecule from left (L) to right (R).

Figure 3: (a) The molecular structure within the junction. (b) A contour plot of the local density of states of the gas-phase molecule at θ = 60° (right) and θ = 0° (left). (c,d) A contour plot of the conductance G/G_0 and current I/I_0 ($I_0 = 2e^2/h \times 1$ V = 77 nA), respectively, through the dumbbell molecule between two gold electrodes against angle θ degrees and E_F (eV) at room temperature. A contour plot of the conductance G/G_0 and current I/I_0 at zero temperature is shown in Supporting Information File 1, Figure S3.

$$I = \frac{2e}{h} \int_{E_F - eV/2}^{E_F + eV/2} dE\, T(E). \qquad (2)$$

Therefore, the electrical conductance, $G = I / V$, is obtained by averaging $T(E)$ over an energy window of width eV centred upon the Fermi energy. The Fermi functions can then be Taylor expanded over the range eV to give the electrical conductance in the zero-voltage but finite temperature limit by

$$G = \frac{I}{V} = G_0 \int_{-\infty}^{+\infty} dE\, T(E) \left(-\frac{df(E)}{dE} \right), \qquad (3)$$

which represents a thermal average of $T(E)$ over an energy window of $k_B T$ where k_B is the Boltzmann constant. The normalised probability distribution, $-df(E)/dE$, has a width of approximately $k_B T$ so in the limit of zero voltage and zero temperature, $G = G_0 T(E_F)$. Figure 3c,d shows the changes in the conductance and current, respectively, of the dumbell molecule placed between two gold electrodes for different angles between the rotor and molecular backbone. The conductance (and therefore, the current) is reduced significantly at $\theta_A = 60°$ and $\theta_B = 240°$ where the minima of U_{BSC} occur.

To include the effect of the parallel electric field due to the source–drain voltage, V, and induced rotation of the rotor, we use the energy landscape, $U_{BSC}(\theta, V)$ to construct the probability function

$$p(\theta, V) = A \exp\left(-U_{BSC}(\theta, V)/k_B T \right) \qquad (4)$$

where A is a normalisation constant. The average current at voltage V can be computed using the relation:

$$\langle I \rangle = \frac{2e}{h} \int_{-\infty}^{\infty} dE \int_0^{2\pi} d\theta\, p(\theta, V) T(E, V) \left(f_L(E) - f_R(E) \right) \quad (5)$$

The blue curve in Figure 4 shows the weighted current at room temperature for applied biases between −1 and 1 V. By differentiating the current with respect to the bias voltage V, one obtains the differential conductance (Figure 4, green dashed line) of the device, which clearly shows regions of NDR behaviour arising from the change in the energy landscape. The higher NDR effect occurs in the bias interval of 0.6–0.7 V, although there is also a smaller NDR region at low bias voltage ≈0.05 V.

The transmission coefficients $T(E)$ were calculated using GOLLUM [46], which is a newly developed simulation tool for electron, thermal and spin transport using the approach described in [47]. Close to equilibrium, $f_{L,R}(E) = (1 + \exp(\mu_{L,R}))^{-1}$ where $\mu_{L,R} = E - E_F^{L,R}/k_B T$, E_F^L (E_F^R) is the Fermi energy of the left (right) reservoir and T is the temperature. As shown by the transmission curves in Supporting Information File 1, Figure S1, transport is HOMO-dominated. Figure 3b shows contour plots of the local density of states (LDOS) around the HOMO of the isolated molecule for two different rotation angles. These plots show that the HOMO is extended, but not symmetric. This demonstrates why the transmission coefficient does not approach unity on resonance, because it is well known that the transmission coefficient is less than unity in asymmetric systems, such as the structure in Figure 1 [47-49]. At zero temperature and finite voltage $E_F^L = E_F + eV/2$ and $E_F^R = E_F - eV/2$ the current could be calculated as

Figure 4: The weighted current (blue curve) from Equation 5 and the NDR (green curve, d*I*/d*V*) for applied bias between 0 and 1 V. The prominent NDR features are seen at a bias voltage between 0.0–0.1 V and 0.6–0.7 V for the device.

the backbone states and this gating is angle dependent. Such NDR behaviour is potentially of interest for molecular-scale electronic applications such as single-molecule Gunn oscillators. The device studied in this paper utilises C_{60} terminal groups attached to gold electrodes. These groups reduce the overall magnitude of the current, and therefore, for the future, it would be of interest to improve this proof of principle device. This could be accomplished by utilising alternative combinations of terminal groups and electrodes, which increase the current. One such possibility would be planar anchor groups on graphene electrodes, which are currently under development in a number of groups [50-52] and allow the imposition of an external electric field via a nearby gate.

At zero temperature, the rotation angle coincides with the global minimum of the energy curves. For example in Figure 2a, at zero bias (black curve), the energy minimum corresponds to an angle of 240°, whereas at for a field of 3.5 V/nm parallel to the backbone (blue curve), the energy minimum corresponds to 410°. This demonstrates that such a field can cause the pendant group to rotate through 170°. On the other hand, Figure 2b shows that a field in the opposite direction does not shift the global minimum and therefore does not cause the pendant group to rotate. Similarly, Figure 2c shows that a field perpendicular to the backbone can shift the minimum to 360°. It is these conformational changes which cause the NDR. This is because the gating of the backbone due to the dipole moment of the pendant group is angle dependent. It should be noted that the applied field does not rotate the pendant group by 360°. Nevertheless, the voltage-dependent energy landscape $U_{BSC}(\theta,V)$ shown in Figure 2 and the associated changes in the distribution of rotation angles $p(\theta,V)$ is sufficient to produce NDR. At finite temperature, the minima in $U_{BSC}(\theta,V)$ correspond to the most probable rotation angles, but other angles can be sampled according to the Boltzmann factor in Equation 4.

Conclusion

We have examined the change in conformation of a molecular-scale rotator attached via a backbone to two C_{60} anchor groups, which in turn are connected to gold electrodes. Our aim was to determine if an applied source–drain bias could cause the equilibrium angle of the rotator to change, leading to a nonlinear current–voltage relation. Our results confirm that such a nonlinearity indeed occurs and is strong enough to lead to a pronounced negative differential resistance region at relatively low bias in the range 0.6–0.7 V. The underlying mechanism is that the dipole moment of the pendant group electrostatically gates

Supporting Information

Supporting Information File 1
Additional theoretical information.
[http://www.beilstein-journals.org/bjnano/content/supplementary/2190-4286-6-240-S1.pdf]

Acknowledgement

References

1. Hiratsuka, Y.; Tada, T.; Oiwa, K.; Kanayama, T.; Uyeda, T. Q. P. *Biophys. J.* **2001,** *81,* 1555–1561. doi:10.1016/S0006-3495(01)75809-2
2. van den Heuvel, M. G.; Dekker, C. *Science* **2007,** *317,* 333–336. doi:10.1126/science.1139570
3. Fujimoto, K.; Kitamura, M.; Yokokawa, M.; Kanno, I.; Kotera, H.; Yokokawa, R. *ACS Nano* **2012,** *7,* 447–455. doi:10.1021/nn3045038
4. Aoyama, S.; Shimoike, M.; Hiratsuka, Y. *Proc. Natl. Acad. Sci. U. S. A.* **2013,** *110,* 16408–16413. doi:10.1073/pnas.1306281110
5. Taira, S.; Du, Y.-Z.; Hiratsuka, Y.; Uyeda, T. Q. P.; Yumoto, N.; Kodaka, M. *Biotechnol. Bioeng.* **2008,** *99,* 734–739. doi:10.1002/bit.21618
6. Song, W.; Möhwald, H.; Li, J. *Biomaterials* **2010,** *31,* 1287–1292. doi:10.1016/j.biomaterials.2009.10.026
7. Ionov, L.; Stamm, M.; Diez, S. *Nano Lett.* **2005,** *5,* 1910–1914. doi:10.1021/nl051235h
8. van den Heuvel, M. G. L.; de Graaff, M. P.; Dekker, C. *Science* **2006,** *312,* 910–914. doi:10.1126/science.1124258
9. Hess, H.; Clemmens, J.; Howard, J.; Vogel, V. *Nano Lett.* **2002,** *2,* 113–116. doi:10.1021/nl015647b
10. Bachand, G. D.; Hess, H.; Ratna, B.; Satir, P.; Vogel, V. *Lab Chip* **2009,** *9,* 1661–1666. doi:10.1039/B821055A
11. Fischer, T.; Agarwal, A.; Hess, H. *Nat. Nanotechnol.* **2009,** *4,* 162–166. doi:10.1038/nnano.2008.393
12. Schliwa, M.; Woehlke, G. *Nature* **2003,** *422,* 759–765. doi:10.1038/nature01601
13. Bruns, C. J.; Stoddart, J. F. *Acc. Chem. Res.* **2014,** *47,* 2186–2199. doi:10.1021/ar500138u

14. Kumar, K. R. S.; Kamei, T.; Fukaminato, T.; Tamaoki, N. *ACS Nano* **2014,** *8,* 4157–4165. doi:10.1021/nn5010342
15. Gao, W.; Wang, J. *Nanoscale* **2014,** *6,* 10486–10494. doi:10.1039/C4NR03124E
16. Browne, W. R.; Feringa, B. L. *Nat. Nanotechnol.* **2006,** *1,* 25–35. doi:10.1038/nnano.2006.45
17. Balzani, V.; Credi, A.; Venturi, M. *Molecular devices and machines: concepts and perspectives for the nanoworld;* John Wiley & Sons, Inc.: New York, NY, U.S.A., 2008.
18. Garcia-Garibay, M. A. *Proc. Natl. Acad. Sci. U. S. A.* **2005,** *102,* 10771–10776. doi:10.1073/pnas.0502816102
19. Karlen, S. D.; Garcia-Garibay, M. A. Amphidynamic crystals: Structural blueprints for molecular machines. *Molecular Machines;* Springer: Berlin, Germany, 2005; pp 179–227.
20. Davis, A. P. *Angew. Chem., Int. Ed.* **1998,** *37,* 909–910. doi:10.1002/(SICI)1521-3773(19980420)37:7<909::AID-ANIE909>3.0. CO;2-X
21. Kelly, T. R.; Sestelo, J. P.; Tellitu, I. *J. Org. Chem.* **1998,** *63,* 3655–3665. doi:10.1021/jo9723218
22. Hugel, T.; Holland, N. B.; Cattani, A.; Moroder, L.; Seitz, M.; Gaub, H. E. *Science* **2002,** *296,* 1103–1106. doi:10.1126/science.1069856
23. Liu, Y.; Flood, A. H.; Bonvallet, P. A.; Vignon, S. A.; Northrop, B. H.; Tseng, H.-R.; Jeppesen, J. O.; Huang, T. J.; Brough, B.; Baller, M.; Magonov, S.; Solares, S. D.; Goddard, W. A.; Ho, C.-M.; Stoddart, J. F. *J. Am. Chem. Soc.* **2005,** *127,* 9745–9759. doi:10.1021/ja051088p
24. Coskun, A.; Banaszak, M.; Astumian, R. D.; Stoddart, J. F.; Grzybowski, B. A. *Chem. Soc. Rev.* **2012,** *41,* 19–30. doi:10.1039/C1CS15262A
25. Bruns, C. J.; Stoddart, J. F. *Nat. Nanotechnol.* **2013,** *8,* 9–10. doi:10.1038/nnano.2012.239
26. Morin, J.-F.; Shirai, Y.; Tour, J. M. *Org. Lett.* **2006,** *8,* 1713–1716. doi:10.1021/ol060445d
27. Cumings, J.; Zettl, A. *Science* **2000,** *289,* 602–604. doi:10.1126/science.289.5479.602
28. Yu, M.-F.; Yakobson, B. I.; Ruoff, R. S. *J. Phys. Chem. B* **2000,** *104,* 8764–8767. doi:10.1021/jp002828d
29. Kolmogorov, A. N.; Crespi, V. H. *Phys. Rev. Lett.* **2000,** *85,* 4727–4730. doi:10.1103/PhysRevLett.85.4727
30. Zheng, Q.; Jiang, Q. *Phys. Rev. Lett.* **2002,** *88,* 045503. doi:10.1103/PhysRevLett.88.045503
31. Forró, L. *Science* **2000,** *289,* 560–561. doi:10.1126/science.289.5479.560
32. Williams, P. A.; Papadakis, S. J.; Patel, A. M.; Falvo, M. R.; Washburn, S.; Superfine, R. *Phys. Rev. Lett.* **2002,** *89,* 255502. doi:10.1103/PhysRevLett.89.255502
33. Rivera, J. L.; McCabe, C.; Cummings, P. T. *Nano Lett.* **2003,** *3,* 1001–1005. doi:10.1021/nl034171o
34. Sangtarash, S.; Sadeghi, H.; Ahmadi, M. T.; Ghadiry, M. H.; Anwar, S.; Ismail, R. *J. Comput. Theor. Nanosci.* **2012,** *9,* 1554–1557. doi:10.1166/jctn.2012.2243
35. Grace, I. M.; Bailey, S. W.; Lambert, C. J. *Phys. Rev. B* **2004,** *70,* 153405. doi:10.1103/PhysRevB.70.153405
36. Bailey, S. W. D.; Amanatidis, I.; Lambert, C. J. *Phys. Rev. Lett.* **2008,** *100,* 256802. doi:10.1103/PhysRevLett.100.256802
37. Cai, K.; Yin, H.; Qin, Q. H.; Li, Y. *Nano Lett.* **2014,** *14,* 2558–2562. doi:10.1021/nl5003608
38. Fennimore, A. M.; Yuzvinsky, T. D.; Han, W.-Q.; Fuhrer, M. S.; Cumings, J.; Zettl, A. *Nature* **2003,** *424,* 408–410. doi:10.1038/nature01823
39. Bourlon, B.; Glattli, D. C.; Miko, C.; Forró, L.; Bachtold, A. *Nano Lett.* **2004,** *4,* 709–712. doi:10.1021/nl035217g
40. Niguès, A.; Siria, A.; Vincent, P.; Poncharal, P.; Bocquet, L. *Nat. Mater.* **2014,** *13,* 688–693. doi:10.1038/nmat3985
41. Leary, E.; González, M. T.; van der Pol, C.; Bryce, M. R.; Filippone, S.; Martín, N.; Rubio-Bollinger, G.; Agraït, N. *Nano Lett.* **2011,** *11,* 2236–2241. doi:10.1021/nl200294s
42. Soler, J. M.; Artacho, E.; Gale, J. D.; García, A.; Junquera, J.; Ordejón, P.; Sánchez-Portal, D. *J. Phys.: Condens. Matter* **2002,** *14,* 2745. doi:10.1088/0953-8984/14/11/302
43. Dion, M.; Rydberg, H.; Schröder, E.; Langreth, D. C.; Lundqvist, B. I. *Phys. Rev. Lett.* **2004,** *92,* 246401. doi:10.1103/PhysRevLett.92.246401
44. Langreth, D. C.; Dion, M.; Rydberg, H.; Schröder, E.; Hyldgaard, P.; Lundqvist, B. I. *Int. J. Quantum Chem.* **2005,** *101,* 599–610. doi:10.1002/qua.20315
45. Landauer, R. *Z. Phys. B: Condens. Matter* **1987,** *68,* 217–228. doi:10.1007/BF01304229
46. Ferrer, J.; Lambert, C. J.; García-Suárez, V. M.; Manrique, D. Zs.; Visontai, D.; Oroszlany, L.; Rodríguez-Ferradás, R.; Grace, I.; Bailey, S. W. D.; Gillemot, K.; Sadeghi, H.; Algharagholy, L. A. *New J. Phys.* **2014,** *16,* 093029. doi:10.1088/1367-2630/16/9/093029
47. Sadeghi, H.; Mol, J. A.; Lau, C. S.; Briggs, G. A. D.; Warner, J.; Lambert, C. J. *Proc. Natl. Acad. Sci. U. S. A.* **2015,** *112,* 2658–2663. doi:10.1073/pnas.1418632112
48. Lambert, C. *Chem. Soc. Rev.* **2015,** *44,* 875–888. doi:10.1039/c4cs00203b
49. Martín, S.; Manrique, D. Zs.; García-Suárez, V. M.; Haiss, W.; Higgins, S. J.; Lambert, C. J.; Nichols, R. J. *Nanotechnology* **2009,** *20,* 125203. doi:10.1088/0957-4484/20/12/125203
50. Sadeghi, H.; Sangtarash, S.; Lambert, C. J. *Beilstein J. Nanotechnol.* **2015,** *6,* 1413. doi:10.3762/bjnano.6.146
51. Mol, J. A.; Lau, C. S.; Lewis, W. J. M.; Sadeghi, H.; Roche, C.; Cnossen, A.; Warner, J. H.; Lambert, C. J.; Anderson, H. L.; Briggs, G. A. D. *Nanoscale* **2015,** *7,* 13181–13185. doi:10.1039/C5NR03294F
52. Prins, F.; Barreiro, A.; Ruitenberg, J. W.; Seldenthuis, J. S.; Aliaga-Alcalde, N.; Vandersypen, L. M. K.; van der Zant, H. S. J. *Nano Lett.* **2011,** *11,* 4607–4611. doi:10.1021/nl202065x

Evidence for non-conservative current-induced forces in the breaking of Au and Pt atomic chains

Carlos Sabater[1], Carlos Untiedt[2] and Jan M. van Ruitenbeek[*1]

Abstract

This experimental work aims at probing current-induced forces at the atomic scale. Specifically it addresses predictions in recent work regarding the appearance of run-away modes as a result of a combined effect of the non-conservative wind force and a 'Berry force'. The systems we consider here are atomic chains of Au and Pt atoms, for which we investigate the distribution of break down voltage values. We observe two distinct modes of breaking for Au atomic chains. The breaking at high voltage appears to behave as expected for regular break down by thermal excitation due to Joule heating. However, there is a low-voltage breaking mode that has characteristics expected for the mechanism of current-induced forces. Although a full comparison would require more detailed information on the individual atomic configurations, the systems we consider are very similar to those considered in recent model calculations and the comparison between experiment and theory is very encouraging for the interpretation we propose.

Introduction

One of the great promises of nanotechnology is the prospect of constructing autonomous nanomachines. While this is still a far prospect, micromotors [1] and nanomotors [2,3] have already been demonstrated. A drawback of these nanomotors is that they require externally supplied cyclic driving. It would be very attractive if we could realize a nanomotor driven by a dc current flow, in analogy to the driving of a waterwheel by a waterflow. For this to work one would need a non-conservative force to act between the non-equilibrium electron bath and the position degrees of freedom of the ions that make up the nanoscale system.

Such a non-conservative force mechanism was recently proposed in works by Dundas et al. [4,5], and these ideas were further elaborated upon by Lü et al. [6] and by Bode et al. [7]. In these works the electron gas is treated fully quantum-mechanically, while the lattice degrees of freedom are described in a semi-classical approximation. The interaction between the

electrons and the lattice gives rise to two interesting contributions to the force on the ions, which appear only when the electron gas is driven out of equilibrium, such that a macroscopic current flows through the system. The first is a non-conservative force, in other words a force that can do work on the ions, and which is linked to the wind force often discussed in the context of electromigration [8]. The second is a force originating in the Berry phase of the electrons, which works just like a Lorentz force: it is directed perpendicular to the velocity of the ions, keeping them in periodic orbits.

This so-called 'Berry force' has never been demonstrated in experiment. In fact, also the first component of the non-equilibrium force is only known from electromigration experiments that detect mass transport of atoms or ions. Truly microscopic experiments probing the forces at the scale of atoms or molecules have not yet been reported. Such experiments are challenging, because high current densities are required and it would probably be needed that the detailed atomic configurations are known and can be monitored. A first promising experiment that fulfils many of these conditions was recently reported [9].

A concrete model system showing the action of the non-conservative force and the Berry force combined was analysed in the theoretical work of Lü et al. [6]. In this work they consider a short chain of metal atoms suspended between metallic leads of the same metal (Au or Pt). They observe that a pair of nearly-degenerate vibration modes becomes coupled by the action of the current-induced forces, leading to negative damping of the atomic motion. In other words, the amplitude of the motion keeps increasing as a result of the energy that is pumped into the motion by the non-conservative force. In practice this will ultimately lead to a breakup of the wire.

This model system closely resembles the experimental configuration in experiments that were performed by Smit et al. [10]. In the discussion of their model calculations Lü et al. refer to these experiments and propose an alternative interpretation of the main peak in the experimental data in terms of their model of current-induced forces. Here we extend these experiments and argue that the main peak is still best described by regular thermally induced breaking as originally proposed by Smit et al. However, the pieces of the puzzle may fit better when considering the interpretation of an anomalous peak at low voltage that is observed in the experimental data. In the analysis by Smit et al. this peak was set aside as unexplained, and ignored in the analysis of the main results. We propose here that this unexplained peak may be the hallmark of the non-conservative forces acting at high current densities, and that it may provide the first experimental evidence for these effects. We extend the

experimental data of [10] and focus our attention here on the analysis of the peak at low-bias voltage.

Experimental

For details of the experimental techniques we refer to Smit et al. [10]. Briefly, the experiment is based on the formation of chains of metal atoms by the mechanically controllable break junction (MCBJ) technique [11,12]. As schematically illustrated in Figure 1 we start from a macroscopic metallic wire that is mounted on a bending beam in a three-point bending configuration. A weak spot is introduced in the middle of the wire, which serves to initiate a break in the wire when the substrate is bent. The first break is only made once the wire is cold, at temperatures close to the boiling point of liquid helium, and under vacuum. This ensures that the fracture surfaces remain atomically clean, and the two wire ends can then be brought back into contact by relaxing the bending of the substrate. The MCBJ technique is a simple method for creating clean and stable single-atom contacts, and can in principle be applied to any metal.
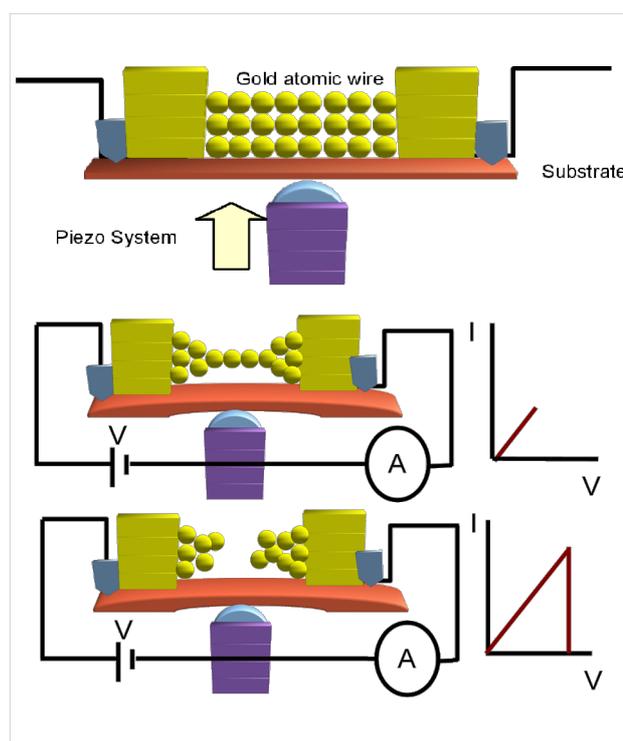
Figure 1: Schematic illustration of the MCBJ technique and the method of current-induced breaking. The top panel (not to scale) shows the initial configuration of a metal wire with a notch formed in the middle of the wire, and mounted in a three-point bending configuration. The middle panel illustrates the formation of an atomic chain after stretching the wire electrodes. The black lines represent the wires that connect the atomic sized structure to the bias voltage and to a current–voltage converter for recording the current. The small current–voltage diagram on the right emphasises that the currents and voltages remain low in this phase of the experiment. The bottom panel illustrates the current-induced breaking of the atomic chain.

The fine control of the bending and breaking is done by means of a piezo electric element (Figure 1). When gently breaking a small contact in this fashion at the last stages one observes a step-wise decrease in the conductance, which is due to the atom-by-atom break down of the contact. The conductance of the last atom bridging the gap depends on the type of metal used in the experiment [12,13]. This conductance is very close to the value of the quantum of conductance, $G_0 = 2e^2/h$, for simple monovalent metals, such as Au. When stretching the contact further, once a single atom bridge has been formed for most metals the contact breaks at this weakest spot that is formed by just one atom. Interestingly, for Au, Pt, and Ir it has been shown that one can continue stretching the contact while new atoms are folding in from the banks in order to self-assemble into an atomic chain, as illustrated in the middle panel of Figure 1 [14-16]. The sample wires used here were Pt and Au, have a diameter of 0.1 mm and a purity of 99.995%.

The goal of the experiment is to study the current-induced breaking of atomic chains of given length by a procedure that is schematically illustrated in the bottom panel of Figure 1. At the start of each experiment for a fresh sample wire the conductance properties of the atomic chain are characterized by recording a conductance histogram: While repeatedly moving the wire ends toward and away from each other a contact is repeatedly formed and broken. During these breaking cycles the conductance is recorded and the digitized values are collected into a histogram, see Figure 2. Clean metallic Au contacts are characterized by a high sharp peak at $1G_0$, while Pt has a much broader peak at $1.5G_0$. The difference in atomic-scale conductance between the two metals is due to the difference in numbers of conductance channels per atom and their associated transmission probabilities [12,13]. Au has just one conductance channel with nearly perfect transmission associated with the 6s
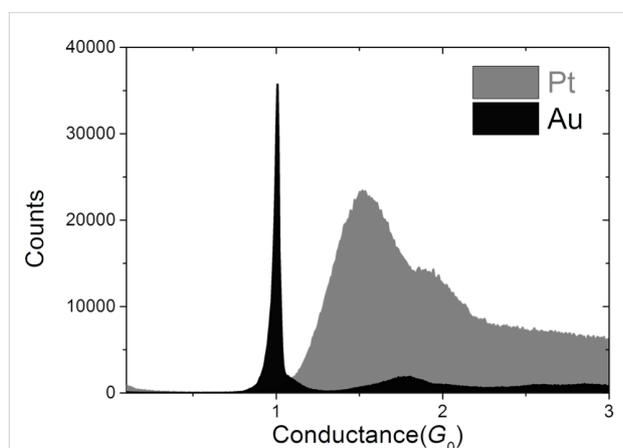
orbital, while for Pt the 5d orbitals give rise to additional conductance channels with transmissions smaller than 1, due to limited matching to the wave functions of the bulk electrodes [17,18]. In both cases, Pt and Au, the peak in the conductance histogram is exceptionally strong, which can be understood from the fact that both metals develop atomic chains in the process of breaking, and these chains have conductance values in the range given by the peaks in Figure 2.

An example of a long conductance plateau in a breaking phase of the cycle is shown for Au in Figure 3. The conductance is obtained as the ratio of the applied bias voltage (50 mV) to the current measured with the help of a current–voltage convertor. The conductance drops in steps as a result of atomic rearrangements taking place in the breaking process, and finally falls to a value below $1.2G_0$, which we take as the starting point of the building of an atomic chain. When continuing to increase the displacement of the wire ends with respect to each other the conductance remains at the same level of about $1G_0$, apart from small variations, as is expected for the buildup of an atomic chain. For the purpose of the present experiment we halt the displacement when a pre-set target length has been achieved, as measured from the starting point of the chain. In Figure 3 this is the distance between the arrow and the end of the graph at the right. In many cases, in particular when the target length is very long, a spontaneous break occurs before reaching the target. In those cases the curve is discarded and a new making-and-breaking cycle is started.
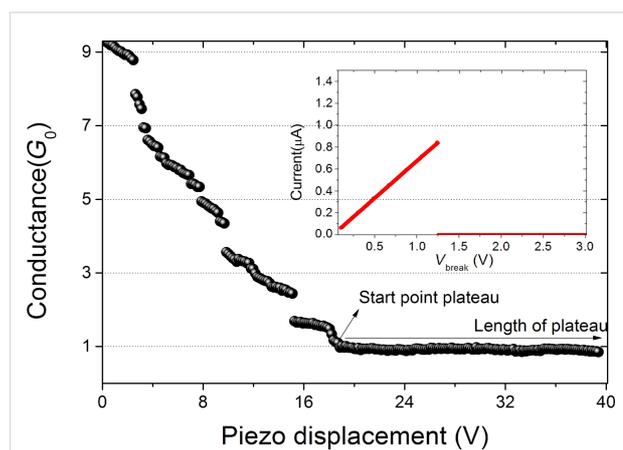
Figure 3: Example of a conductance breaking trace for Au. As soon as the conductance drops to the conductance of a single-atom junction, this point (arrow) is marked as the start of the formation of an atomic chain. Inset: Current vs bias voltage leading to breakup of the atomic chain at about 1.25 V.

Results and Discussion

Once we obtain a junction that reaches the target length without breaking, we halt the displacement of the wire ends and a

Figure 2: Histograms of conductance values for Au and Pt collected from 20000 individual breaking traces.

routine is started that ramps the bias voltage from 50 mV up with a speed of 3 V/s. Well before the maximum voltage of 3 V is reached the junction breaks under the influence of the high current (inset in Figure 3). The bias voltage at which the break occurs, V_b, is stored, together with other data characterizing the junction, including the atomic chain length (taken as the length of the last plateau), the break current, and the low-bias conductance. All these processes are controlled by software, and when a break voltage has been found, a new cycle is started automatically. In this way we have collected statistical information on the break voltage for atomic chains of Au and Pt, for a range of atomic chain lengths. The only difference in procedure between Au and Pt is the difference in conductance starting values for counting the length of the last plateau. We have used a start value of $2G_0$ for Pt and, although there is some ambiguity in the actual conductance at the start of chain formation for Pt, it has been shown that the choice does not influence the statistical data obtained [15].

The fraction of the total set of atomic chains, breaking at a given bias voltage is presented in Figure 4 in the form of histograms for each target length, for Au and Pt. The central observation for the purpose of this paper is the fact that the histogram for Au has two peaks: one at low break voltage, and a second broad peak that shifts from $V_b = 1.4$ V at a chain length of 0.38 nm down to $V_b = 1.1$ V at a length of 0.97 nm. Pt has only one broad peak shifting down from $V_b = 0.42$ V at a chain

length of 0.2 nm to $V_b = 0.15$ V at 0.8 nm. The position of the lower peak for Au remains fixed at the lowest voltage values, but grows in intensity and width with increasing length of the atomic chains.

The results reported above confirm the data reported earlier by Smit et al. [10]. The structure of the break-voltage distribution for Pt, and the two-peak distribution for Au agree with those reported by Smit et al. The broad peaks at finite bias for Au and Pt are found at slightly higher values, except for the lowest two lengths for Pt that lie about 30% higher than in the work by Smit et al. The difference is possibly related to the fact that the initial preparation of a chain of a given length is done here at a higher bias voltage (50 mV) compared to that used by Smit et al. (10 mV). By using a higher bias at preparation we effectively eliminate chain configurations that are unstable at low-bias voltages, which affects the shape of the distribution. The broad peaks at finite break voltage for Au and Pt have been attributed to a mechanism of thermal breakup of the atomic chains in [10], and it was demonstrated that a simple model involving Joule heating produces a reasonable description. The model assumes the ensemble of breaking events can be described by thermal activation over a distribution of barrier heights. Dissipation raises the effective temperature above the bath temperature T according to $T_{\text{eff}} = (T^2 + T_V^2)^{1/4}$ [19], with T_V being determined by the applied bias voltage as $T_V = \gamma\sqrt{L|V|}$ [20], where $\gamma = 60$ K·V$^{-1/2}$·nm$^{-1/2}$ and L is the
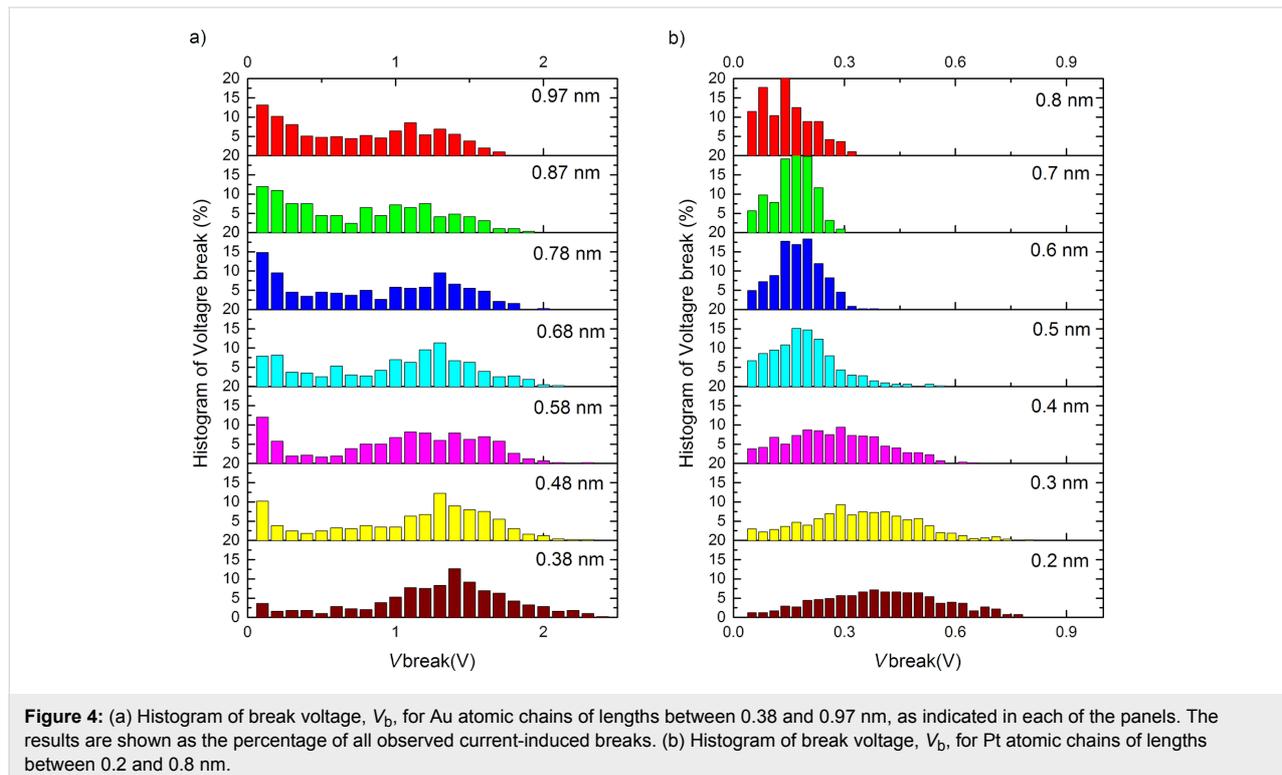
Figure 4: (a) Histogram of break voltage, V_b, for Au atomic chains of lengths between 0.38 and 0.97 nm, as indicated in each of the panels. The results are shown as the percentage of all observed current-induced breaks. (b) Histogram of break voltage, V_b, for Pt atomic chains of lengths between 0.2 and 0.8 nm.

length of the chain. The parameters influencing the barrier height were taken from experiments, but the tensile stress will vary depending on the atomic arrangements at the end points of the chain and is not easily obtained from the experimental data. Therefore, this was assumed to be the main factor giving rise to variations in the barrier. The tensile force was assumed to be given by a normal distribution centred at 0.95 nN, and a width of 0.3 nN. A simulation of breaking events based on these assumptions reproduces the main characteristics of the second peak in the experimental distribution, including its shape and its length dependence. As mentioned above, in the analysis of [10] the lower peak in the break-voltage distribution for Au was set aside, and has remained unexplained.

Figure 5 shows density plots and histograms for all the data collected for all chain lengths for Au, with the break voltage given along the abscissa and the low-bias conductance along the ordinate. The data collected here for a preparation voltage of 50 mV, given in Figure 5b, is compared to the data set from [10] given in Figure 5a. The data clearly show that there are two disjunct regions of maximum density in the plots, and the separation between the two regions is enhanced by the higher preparation voltage (panel b). For Pt, Figure 6 only displays a single region of high density. We will focus our discussion now on the nature of the region of high density at the left side in the plots for Au.

The breaking of the atomic chains at low bias is remarkable for at least two reasons. First, we verified that the atomic chains survive for very long times (hours) when the displacement of the electrodes is kept fixed and also the bias voltage is held at 50 mV, or 10 mV depending on the experiment. As soon as we ramp up the bias a large fraction of the chains break spontaneously, even below 100 mV. For higher bias voltages the fraction of chains breaking decreases. Second, after seeing the probability for breaking decrease, it rises again towards a second peak. These observations are difficult to explain assuming a homogeneous population of chain configurations. If every newly formed chain is subject to the same mechanisms of current-induced breaking once a process is activated, more current should lead to a smaller probability to survive to that level of current.

For a given mechanism of current-induced breaking there may be a threshold, or optimum, value for the mechanism. Indeed, this is what was considered by Smit et al. for the second region for Au at higher bias, where a certain level of Joule heating is needed for breaking to have a high probability. After this optimum breaking voltage the probability of breaking decreases, not because it is less likely for a chain to break at higher bias. On the contrary, a higher bias should always

Figure 5: (a) Density plot (top panel) and histogram (lower panel) collecting all breaking voltages for all chain lengths for Au at 10 mV preparation voltage, as obtained from the data in [10]. (b) Density plot (top panel) and histogram (lower panel) collecting all breaking voltages for all chain lengths for Au at 50 mV preparation voltage.
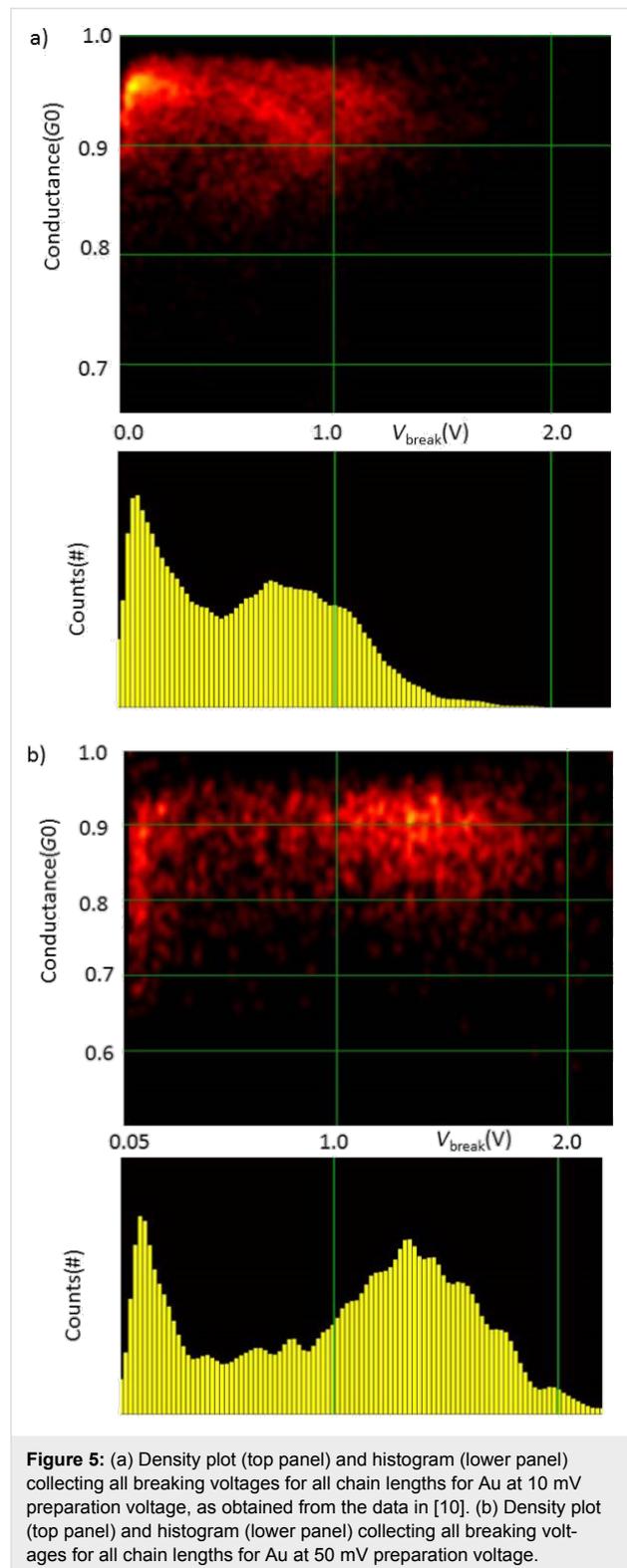
enhance the probability of breaking. However, because less of the chain population survives to such high bias there are fewer left to break at the higher voltage, explaining the decaying rate of breaking observed.

Figure 6: Density plot (top panel) and histogram (lower panel) collecting all breaking voltages for all chain lengths for Pt at 50 mV preparation voltage
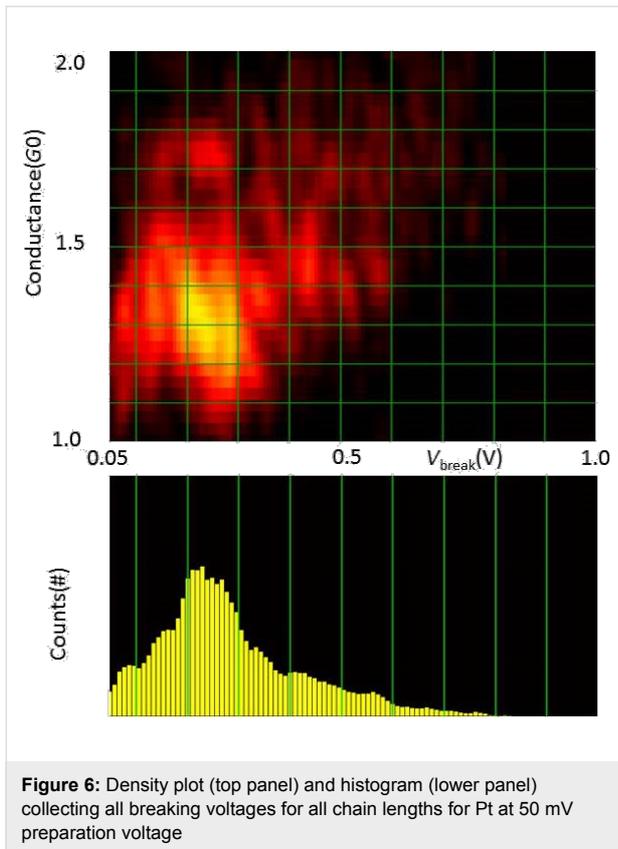
Through this reasoning we conclude that a decaying rate of breaking indicates a decaying survival of the population. This implies that the first region for Au must be associated with a subset of chain configurations that possess a property that sets it apart from the other subset that is characterized by regular breaking due to Joule heating. Each time the contact is stretched to form an atomic chain the atoms arrange themselves in different ways. Some of these arrangements make the chains susceptible to a mechanism that leads to breaking at low bias, while the other arrangements are insensitive to this mechanism.

In principle the two subsets of chain configurations can differ in many ways, e.g., by the way the atoms are arranged at the ends of the chain, or by the states of strain. The difficulty that we meet is that such variations are expected to give rise to a somewhat continuous range of possibilities, and this range has already been included in the model describing the second peak in the distribution for Au. One would need a property that sets a fraction of chain configurations apart, not just quantitatively, but qualitatively.

The non-conservative force mechanism discussed in [4-7] provides an appealing candidate for such a mechanism. The mechanism requires the presence of two nearly degenerate vibration modes with strong coupling to the current. When these

conditions are met the combined action of pumping of energy into the modes by the non-conservative force and the periodic motion in phase space imposed by the Berry force lead to a growing amplitude of the combined motion of the two modes. As the amplitude continues to grow at a given moment the chain will become unstable and break.

Thus, we propose the non-conservative forces as a tentative explanation for the anomalous region of low-bias chain breaking that is observed for Au. In the population of atomic chain configurations those that have a set of suitable nearly-degenerate vibration modes fall into the subset that belongs to the low-bias region of current breaking. The other atomic chain configurations, which may have a less symmetric arrangement of the atoms at the connections to the banks, will only break by regular thermal activation due to Joule heating. The threshold of about 0.2 V for a runaway mode for Au obtained in the model calculation of Lü et al. [6] agrees with the range of the low-bias breaking voltages observed in our experiments.

The absence of a disjunct low-bias voltage region for Pt may be explained by the fact that the runaway modes for Pt in the calculation appear at higher bias, 0.4 V, while at the same time the thermal breaking takes place at lower bias as compared to Au. This would indicate that the bias regions for both mechanisms for Pt overlap.

The current-induced breaking mechanism of Lü et al. [6] has a sharp threshold voltage, which we do not observe here. This can be understood by the fact that the experiment shows the result of a population of chain configurations with widely different atomic arrangements. For each of these chain configurations the threshold may be different. Since we cannot discern a low-bias maximum for Au at finite bias, we must assume that a fraction of the chain configurations has a threshold below the initial bias voltage used during the preparation of the chains. Since these chains will be lost during the chain preparation process they are not included in the statistics. The qualitative agreement between the distributions obtained for 10 and 50 mV preparation voltage indicates that breaking below 50 mV becomes less probable.

From the density plots for Au in Figure 5 we further note a trend in the region of low-bias breaking towards lower conductance the lower the break voltage of the chains. This suggests that the transmission for these anomalous chain configurations is lower, which gives another indication that the configurations are exceptional. The density plot for Pt, Figure 5, also shows a slight trend, on a much wider scale, of increasing conductance for higher break voltage. In this case this is likely due to lumping of the short and long chain data in one plot. Pt has several conductance channels with transmissions that depend on

the structure, where short Pt atomic chains have a higher conductance [21].

A full comparison of theory and experiment will require further work on both fronts. Experimentally, progress would require methods to determine the atomic arrangement of atomic chains, or the investigation of other atomic scale systems that permit a higher degree of control. On the side of theory the effects of phonon decay have not been included. Qualitative estimates of the effect of phonon decay suggest that they can have a profound influence on the final size of the non-conservative force and the runaway modes [6].

Acknowledgements

References

1. Paprotny, I.; Bergbreiter, S., Eds. *Small-Scale Robotics. From Nano-to-Millimeter-Sized Robotic Systems and Applications;* Lecture Notes in Artificial Intelligence, Vol. 8336; Springer: Berlin, Germany, 2014.
2. Kudernac, T.; Ruangsupapichat, N.; Parschau, M.; Maciá, B.; Katsonis, N.; Harutyunyan, S. R.; Ernst, K.-H.; Feringa, B. L. *Nature* **2011,** *479,* 208–211. doi:10.1038/nature10587
3. Chu, P.-L. E.; Wang, L.-Y.; Khatua, S.; Kolomeisky, A. B.; Link, S.; Tour, J. M. *ACS Nano* **2013,** *7,* 35–41. doi:10.1021/nn304584a
4. Dundas, D.; McEniry, E. J.; Todorov, T. N. *Nat. Nanotechnol.* **2009,** *4,* 99–102. doi:10.1038/nnano.2008.411
5. Lü, J.-T.; Brandbyge, M.; Hedegård, P.; Todorov, T.; Dundas, D. *Phys. Rev. B* **2012,** *85,* 245444. doi:10.1103/PhysRevB.85.245444
6. Lü, J.-T.; Brandbyge, M.; Hedegård, P. *Nano Lett.* **2010,** *10,* 1657–1663. doi:10.1021/nl904233u
7. Bode, N.; Kusminskiy, S. V.; Egger, R.; von Oppen, F. *Phys. Rev. Lett.* **2011,** *107,* 036804. doi:10.1103/PhysRevLett.107.036804
8. Sorbello, R. Theory of Electromigration. In *Solid State Physics;* Ehrenreich, F.; Spaepen, H., Eds.; Academic Press: San Diego, CA, U.S.A., 1998; pp 159–231.
9. Schirm, C.; Matt, M.; Pauly, F.; Cuevas, J. C.; Nielaba, P.; Scheer, E. *Nat. Nanotechnol.* **2013,** *8,* 645. doi:10.1038/nnano.2013.170
10. Smit, R. H. M.; Untiedt, C.; van Ruitenbeek, J. M. *Nanotechnology* **2004,** *15,* S472–S478. doi:10.1088/0957-4484/15/7/055
11. Muller, C. J.; van Ruitenbeek, J. M.; de Jongh, L. J. *Phys. Rev. Lett.* **1992,** *69,* 140–143. doi:10.1103/PhysRevLett.69.140
12. Agraït, N.; Levy Yeyati, A.; van Ruitenbeek, J. M. *Phys. Rep.* **2003,** *377,* 81–279. doi:10.1016/S0370-1573(02)00633-6
13. Scheer, E.; Agraït, N.; Cuevas, J. C.; Levy Yeyati, A.; Ludoph, B.; Martín-Rodero, A.; Rubio Bollinger, G.; van Ruitenbeek, J. M.; Urbina, C. *Nature* **1998,** *394,* 154–157. doi:10.1038/28112
14. Yanson, A. I.; Rubio Bollinger, G.; van den Brom, H. E.; Agraït, N.; van Ruitenbeek, J. M. *Nature* **1998,** *395,* 783–785. doi:10.1038/27405
15. Smit, R. H. M.; Untiedt, C.; Yanson, A. I.; van Ruitenbeek, J. M. *Phys. Rev. Lett.* **2001,** *87,* 266102. doi:10.1103/PhysRevLett.87.266102
16. Bahn, S. R.; Jacobsen, K. W. *Phys. Rev. Lett.* **2001,** *87,* 266101. doi:10.1103/PhysRevLett.87.266101
17. Cuevas, J. C.; Levy Yeyati, A.; Martín-Rodero, A. *Phys. Rev. Lett.* **1998,** *80,* 1066–1069. doi:10.1103/PhysRevLett.80.1066
18. de la Vega, L.; Martín-Rodero, A.; Yeyati, A. L.; Saúl, A. *Phys. Rev. B* **2004,** *70,* 113107. doi:10.1103/PhysRevB.70.113107
19. Todorov, T. N.; Hoekstra, J.; Sutton, A. P. *Phys. Rev. Lett.* **2001,** *86,* 3606–3609. doi:10.1103/PhysRevLett.86.3606
20. Todorov, T. N. *Philos. Mag. B* **1998,** *77,* 965–973. doi:10.1080/13642819808206398
21. Strigl, F.; Espy, C.; Bückle, M.; Scheer, E.; Pietsch, T. *Nat. Commun.* **2015,** *6,* 6172. doi:10.1038/ncomms7172

License and Terms

High electronic couplings of single mesitylene molecular junctions

Yuki Komoto, Shintaro Fujii[*], Tomoaki Nishino and Manabu Kiguchi

Abstract

We report on an experimental analysis of the charge transport properties of single mesitylene (1,3,5-trimethylbenzene) molecular junctions. The electronic conductance and the current–voltage characteristics of mesitylene molecules wired into Au electrodes were measured by a scanning tunnelling microscopy-based break-junction method at room temperature in a liquid environment. We found the molecular junctions exhibited two distinct conductance states with high conductance values of ca. $10^{-1}G_0$ and of more than $10^{-3}G_0$ ($G_0 = 2e^2/h$) in the electronic conductance measurements. We further performed a statistical analysis of the current–voltage characteristics of the molecular junctions in the two states. Within a single channel resonant tunnelling model, we obtained electronic couplings in the molecular junctions by fitting the current–voltage characteristics to the single channel model. The origin of the high conductance was attributed to experimentally obtained large electronic couplings of the direct π-bonded molecular junctions (ca. 0.15 eV). Based on analysis of the stretch length of the molecular junctions and the large electronic couplings obtained from the *I–V* analysis, we proposed two structural models, in which (i) mesitylene binds to the Au electrode perpendicular to the charge transport direction and (ii) mesitylene has tilted from the perpendicular orientation.

Introduction

Along with increasing interests in molecular electronics on the single molecular scale [1], much efforts have been devoted to understand charge transport in a single molecular junction, in which a single molecule is wired to two metal electrodes. In recent years single molecular junctions with electronic functionalities such as diodes [2-8] and transistors [9-13] have been demonstrated. Electronic conductances for most of the single molecular junctions were reported to be below $0.01G_0$ ($G_0 = 2e^2/h$, $G_0^{-1} \approx 12.9$ kΩ). The low electronic conductances prevent practical application of the molecular junctions for the molecular electronics. To bind a single molecule to metal electrodes, anchoring groups such as –SH [14] and –NH$_2$ or (R)$_3$–N

[15,16] have been used. Such anchoring groups form strong chemical bonds with metal electrodes and the anchoring regions act as resistive space, leading to low electronic conductances of the single molecular junctions. Recently several groups [17-20] including ours [17,21,22] developed a direct π-binding technique, where a π-conjugated molecule is directly bound to metal electrodes without anchoring groups. The direct π-binding technique has been applied for various systems such as benzene derivatives [17,19,20], C_{60} [23,24], ethylene [25], and pyrazine [22,26]. The conductance values of these molecular junctions were close to those of metal atomic contacts. The high electronic conductance is expected to be caused by effective metal–molecule couplings in the direct π-binding to the electrodes. However, there are little direct experimental results revealing strong metal–molecule couplings.

The electronic structure of molecular junctions including metal–molecule couplings can be characterized by current-voltage (*I–V*) characteristics of molecular junctions. Transition voltage spectroscopy [27,28] is one of the methods to characterize energy level of conduction orbitals in junctions by analysing *I–V* characteristics. Energy level alignment of conduction orbitals with respect to Fermi level of metal electrodes has been examined for the molecular junctions of alkanedithiol, 1,4-benzenedithiol (BDT) and other molecules [29-31]. Recently *I–V* curve analysis [32] based on the Breit–Wigner model [33-37] has been becoming a promising technique to characterize the metal–molecule couplings of the single molecular junctions. Within the Breit–Wigner model, electronic conductance of the single molecular junction can be described by two parameters of (i) the electronic coupling between electrodes and molecule and (ii) the relative energy level alignment of the conduction orbital of molecule with respect to the Fermi level of the metal electrodes. By fitting the experimentally obtained *I–V* characteristics to the Breit-Wigner model, the metal–molecule coupling Γ, and energy difference between Fermi level and conduction orbital ε_0 are obtained. This *I–V* analysis has been applied for molecular junctions with a variety of anchoring groups. For example Γ = 60 meV and ε_0 = 0.6 eV have been reported for BDT [37], and Γ = 6 meV and ε_0 = 0.5 eV for thiolated oligo(phenylene ethynylene) [36].

In this study, we report on the *I–V* analysis for the direct π-bonded molecular junction system without anchoring groups, i.e., mesitylene molecular junctions (Figure 1) to characterize Γ as well as ε_0. Very recently Afsari et al. have investigated the single mesitylene molecular junction with a scanning tunnelling microscopy (STM)-based break junction (BJ) technique [20]. The conductance of a single mesitylene molecular junction has been founded to be approximately $0.1G_0$, which is at least 10 times larger than di-substituted benzene such as BDT [38]
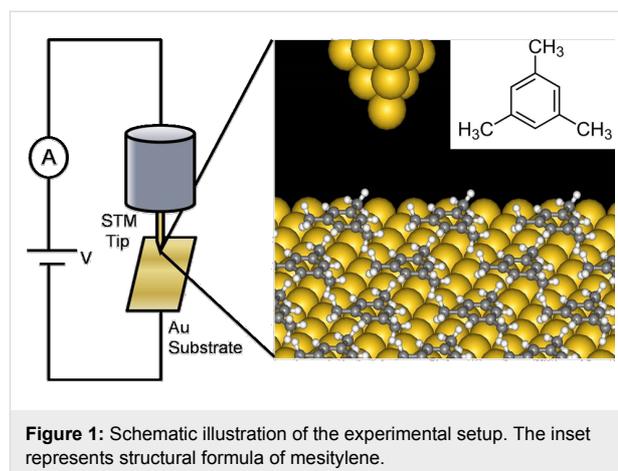
Figure 1: Schematic illustration of the experimental setup. The inset represents structural formula of mesitylene.

and 1,4-benzenediamine (BDA) [16]. The mesitylene molecule can bind to metal electrodes with its molecular plane perpendicular to the direction of charge transport [20]. Here, we investigate the possible origin of the high conductance of the direct π-bonded system. By analysing the *I–V* characteristics of the mesitylene junctions, we demonstrate that the direct π-bonded system features larger metal–molecule coupling.

Results and Discussion

Mesitylene molecular junctions sandwiched by Au electrodes were prepared by the BJ method [39]. We used the STM-BJ method [15] operating in a liquid environment where thousands of molecular junctions were repeatedly made for statistical analysis of the molecular conductance and *I–V* characteristics. Figure 2 shows the conductance traces and histograms during stretching processes of the junctions. In the presence of the molecule, the conductance traces display plateaus at $1G_0$, and the corresponding conductance histograms show a peak at $1G_0$ (Figure 2a,d). These results indicate that a single Au atomic contact of $1G_0$ is formed at the initial stage of the stretching process. This suggests that nano-sized (atomic scale) Au electrodes are repeatedly made just after the rupture of the Au contact to trap a single mesitylene. At the conductance range below $1G_0$, conductance steps preferentially appeared around $0.1G_0$ and $0.03G_0$ (Figure 2b,c), which are absent in blank measurements. Conductance histograms show molecular conductance-peaks around $0.1G_0$ and $0.03G_0$. We observed two distinct high and low conductance states for a mesitylene junction. In a thousand of measured conductance traces, a small number of traces exhibit switch between the two states. The preferential conductance peaks around $0.1G_0$ agrees with the previously reported results by Afsari et al. According to [20], this conductance corresponds to single molecular junctions where mesitylene binds to Au electrodes with its molecular plane perpendicular to the charge transport direction. It should be noted that a side-peak at $0.2G_0$ is noticeable in Figure 2e,

Figure 2: Conductance traces (a–c) and semi-logarithmic conductance histograms (d,e) during STM-BJ rupture process with (black) and without (red) adding mesitylene solution. The bias voltage was set to 20 mV. Conductance windows are $0–3G_0$ for (a) and $0–0.3G_0$ for (b,c). In (b) traces display high and low conductance steps around $0.1G_0$ and $0.03G_0$, which are marked by dotted circles. In (c) the two types of steps are magnified. Dotted guide lines are drawn at $0.1G_0$ and $0.03G_0$ in (c–e). Histograms in (d) and (e) are constructed from a choice of 200 conductance traces. A bin size of $\Delta\log(G/G_0) = 0.02$ is used.

which is possibly due to formation of multi-molecular junctions. In our conductance measurement, plateaus are also present around $0.03G_0$. In STM-BJ experiments, molecular conductance appears as integer multiple plateaus of a fundamental molecular conductance [15] and the fundamental conductance corresponds to the single molecular conductance. Hence, this peak also represents the single molecular conductance of mesitylene junction. In our previous report [40], we have performed STM-BJ experiments on BDA in the mesitylene solution. It has been demonstrated that anime-derivatives form self-assembled adlayer on Au surface [41,42]. In the presence of BDA, both surfaces of the Au tip and Au substrate were covered by BDA in the mesitylene solution. Therefore BDA

junctions can preferentially form in the 10 mM BDA mesitylene solution in our previous study. In [20], conductance analysis has been performed using linear-binned histograms and the low conductance state ($0.03G_0$) found in the present study can be hidden in background tunnelling currents.

To estimate the effective separation of electrodes for the high-conductance and the low-conductance state, we analysed the electrodes separation length in the conductance traces. Figure 3 shows length histograms of the two types of conductance steps. The step length (i.e., the stretch length after the breakage of Au atomic contact) is defined as length of conductance plateau within the conductance range from $0.07G_0$ to $0.7G_0$ for the

high-conductance state and from $0.02G_0$ to $0.7G_0$ for the low-conductance state. Gaussian fits of the length distribution reveal average step lengths of 0.044 and 0.079 nm for high- and low-conductance states, respectively. The stretch length of the low-conductance state is larger than that of the high-conductance state. It should be noted here that the length does not directly correspond with the actual gap size. The breakage of the Au atomic contact leads to the immediate formation of a nanogap of finite size as a result of the elastic response of the electrode banks. In case of Au atomic contact, the width of the gap thus created is typically 0.4 nm [43]. Considering that mesitylene binds to the Au electrodes with its molecular plane perpendicular to the charge transport direction [20] for the high conductance state of $0.1G_0$, the larger stretch length for the low state of $0.03G_0$ can be interpreted as a result of tilted orientation of the mesitylene junction upon stretching. We will discuss this matter in a later section.

We examined *I–V* characteristic to obtain the electronic couplings of single molecular junction. In previous research [20], the current-versus-bias relationship of mesitylene junctions has been investigated by repeating current measurement at fixed bias voltages under 0.3 V. It has been reported that the current increases quasi-linearly with the bias voltage at the low bias regime. In this study we measured *I–V* characteristics of the mesitylene junctions by sweeping a wide bias range of ±1 V at fixed electrode separations. Figure 4 shows a 2D histogram and typical *I–V* curves of mesitylene molecular junctions. In addition to the almost linear increase of the current at low bias

Figure 3: Stretch length histograms on a semi-log scale constructed from 2000 of all conductance traces taken at the bias voltage of 20 mV for (a) high and (b) low conductance states (For a detail see main text). The bin size is log (stretch length/nm) = 0.1. Solid curves are results of Gaussian fits. Peak center positions are indicated by dotted lines ((a) 0.044 nm and (b) 0.079 nm).
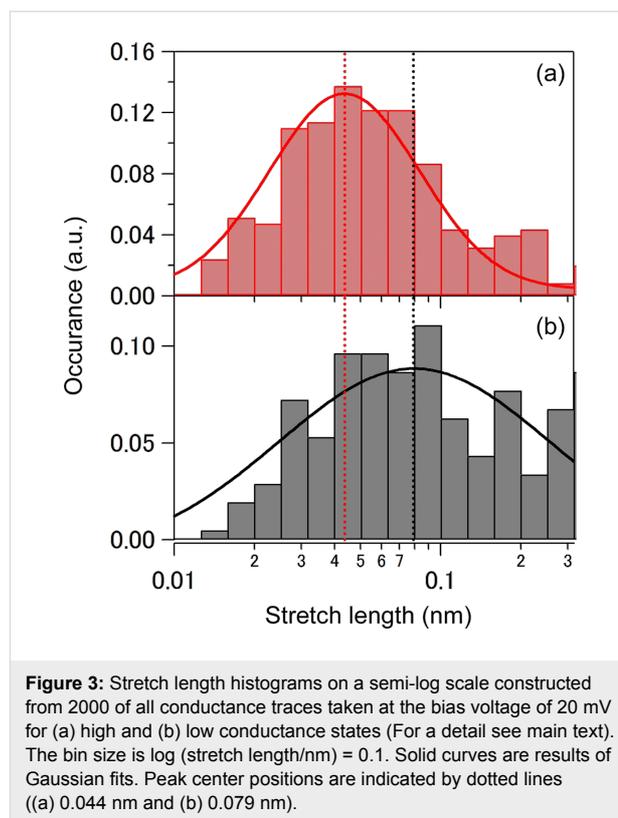
voltages, a non-linear increase of the current is apparent at high bias voltages. In the high-bias range, the Fermi level of the Au electrode moves close to the energy levels of the mesitylene conduction orbitals. Thus, the charge transport changes from

Figure 4: (a) 2D histogram of *I–V* curves of the mesitylene molecular junctions. The histogram is built from 1000 *I–V* curves. The bin size is 16 mV × 100 nA. Two current windows at 0.3 V are indicated by arrows of (i) and (ii). The current ranges of (i) and (ii) are 700–1500 nA (0.03–$0.065G_0$) and above 2400 nA (above $0.1G_0$), respectively. The conductance windows are chosen to separate *I–V* curves into two states with the conductance values of $0.1G_0$ and $0.03G_0$ observed in Figure 2. The mean current values at 0.3 V are 1100 and 4600 nA in the current windows (i) and (ii), respectively. Deviations are 200 and 1500 nA for (i) and (ii), respectively. (b,c) Typical *I–V* curves of the mesitylene molecular junctions in the current windows of (ii) and (i).

non-resonant to resonant transport. Two clear distributions are present in the 2D histogram (Figure 4a). This result is in agreement with the two states (high and low sates) in the STM-BJ conductance measurement (Figure 2). To obtain statically averaged *I–V* curves for the two states, the current windows of 700–1500 nA ($0.03–0.065G_0$) and above 2400 nA (above $0.1G_0$) at +0.3 V are selected for low and high states, respectively. The conductance windows are chosen to separate the *I–V* curves into two states with the conductance values of $0.1G_0$ and $0.03G_0$ observed in Figure 2.

The transmission of single molecular junction in a single channel resonant tunnelling model is represented by Equation 1 [44].

$$\tau(E) = \frac{4\Gamma_L \Gamma_R}{\left(\Gamma_L + \Gamma_R\right)^2 + \left(E - \varepsilon_0\right)^2}, \quad (1)$$

where ε_0, Γ_L, and Γ_R are the energy alignment of the conduction orbital, and the strength of the coupling between molecule and left and right electrodes, respectively. The current in the molecular junction is represented by

$$I(V) = n \int_{-eV/2}^{eV/2} dE \tau(E) \left\{ f\left(E - \frac{eV}{2}\right) - f\left(E + \frac{eV}{2}\right) \right\}, \quad (2)$$

where *n* is the number of bridging molecules. The formula for the current in molecular junctions (Equation 3) is obtained from Equation 1 and Equation 2:

$$I(V) = n \frac{8e}{h} \alpha (1-\alpha)$$
$$\times \Gamma \left\{ \arctan\left(\frac{\alpha \cdot eV - \varepsilon 0}{\Gamma}\right) + \arctan\left(\frac{(1-\alpha) \cdot eV + \varepsilon 0}{\Gamma}\right) \right\}. \quad (3)$$

Here, $\Gamma = \Gamma_L + \Gamma_R$, and $\alpha = \Gamma_L/\Gamma$. The parameters of electronic structure, Γ and ε_0, of each states of the mesitylene junction are determined by fitting of the statistically averaged *I–V* curves with Equation 3. The fitting results are $\Gamma_{\_H}$ = 0.15 eV, ε_{0_H} = 0.31 eV for the high conductance state using bias window ±0.4 V and $\Gamma_{\_L}$ = 0.16 eV, ε_{0_L} = 0.72 eV for the low conductance state using bias window ±1.0 V ($\Gamma_{\_L}$ = 0.10 eV, ε_{0_L} = 0.49 eV for the bias window ±0.4 V). For both of the high and low conductance states the couplings were found to be symmetric ($\alpha = \Gamma_L/\Gamma \approx 0.5$). If the high conductance state is due to formation of multi-molecular junctions, we should also observe a fundamental conductance state that comes from the formation of a single molecular junction. Then we checked whether the *I–V* curve of the high state can be fitted by multiple

formation of the observed low conductance state. The conductance of the high state is 3–4 times higher than that of the low state. The fitting results are $\Gamma_{\_H,n=3}$ = 0.098 eV, ε_{0_H-n3} = 0.32 eV for *n* = 3, $\Gamma_{\_H-n4}$ = 0.076 eV, ε_{0_H-n4} = 0.37 eV for *n* = 4. The ε_{0_H-n3} and ε_{0_H-n4} are roughly half of ε_{0_L}. This mismatch indicates that the high state cannot be explained by multiple formation of molecular junctions. In other words, the high state is not due to the formation of multiple molecular junctions because there is no fundamental conductance state in lower conductance regions for the high state. The *I–V* analysis of the statistically averaged data revealed the high and low states have different electronic structures. In contrast to BDT junctions with the anchoring group [37], the coupling of mesitylene junction (Γ = 0.15 eV) is substantially larger than BDT (Γ = 0.06 eV). This result supports the assumption that the molecule binds to the metal via direct π-binding with a strong metal–molecule coupling.

Finally, we comment on structural models for the experimentally observed two states of the mesitylene-molecular junctions. In conductance traces, plateaus corresponding to the low conductance state appear after the plateau corresponding to the high conductance state (Figure 2c). The stretch length analysis of the molecular junctions suggests that the distance between two Au electrodes is larger for the low conductance state than that of the high conductance state. Based on these experimental results, we proposed two structural models for to the high and low conductance states as shown in Figure 5. In the high conductance state, the molecule binds to metal electrode with its

Figure 5: Proposed structural models of the mesitylene molecular junctions for (a) high-conductance and (b) low-conductance states. Mesitylene is oriented perpendicular to the charge transport direction in (a). In (b) stretching of the junction leads to a tilted orientation of the mesitylene molecule. White, grey and yellow balls represent H, C and Au atoms, respectively.

molecular plane parallel to the metal electrode (parallel configuration) as proposed previously [20]. Further stretching of the junction in the high state causes tilting of mesitylene and reduction of the conductance in the low state in analogy with benzene molecular junctions [17,19].

Conclusion

We fabricated single molecular junctions of mesitylene with the STM-BJ method and performed conductance and *I–V* measurements. In the conductance measurement and *I–V* measurement, two conductance states (a high-conductance and a low-conductance state) were identified. The energy level alignment and the electronic couplings of mesitylene to Au electrodes were determined by fitting of statistically averaged *I–V* curves. The origin of the high conductance for the direct π-bonded molecular junctions was ascribed to the experimentally obtained large electronic couplings of ca. 0.15 eV for the two states. Based on the stretch length of the conductance trace and the large electronic coupling obtained from the *I–V* analysis, we proposed two structural models.

Experimental

Conductance measurements were performed using an electrochemical scanning tunnelling microscope (Nanoscope V, Bruker, Santa Barbara, CA). Au(111) substrate was prepared by thermal deposition of Au on cleaved mica surface at 625–675 K. The Au substrate was cleaned by flame annealing before use. Then the Au substrate was fixed in a Teflon liquid cell with the Viton O-ring. Pure mesitylene solvent was poured into the cell. STM-BJ experiments were performed as reported previously. The STM tip was prepared by mechanically cutting Au wire (diameter = 0.3 mm, purity >99%) [45]. In the *I–V* experiments, the STM tip was approached to the substrate until a metal junction with conductance of $6.5G_0$ was formed in air at room temperature. Subsequently, the tip was withdrawn for 10 nm at a tip speed of 38 nm/s to break the Au junction and to prepare the molecular junction. The tip was held and the bias voltage was simultaneously swept at 100 kHz frequency to record one *I–V* curve. The bias voltage range was ±1 V. Then, the junction was broken by pulling away of the tip from the substrate. We repeated this process and obtained more than 1000 *I–V* curves. The *I–V* characteristics of molecular junction were obtained by removing *I–V* curves of Au junctions or vacuum gaps. The *I–V* curves for the vacuum tunnelling are defined as *I–V* curves with less than 100 nA current at a bias of 1 V (ca. $0.0013G_0$) while *I–V* curves with less than 10000 nA current at a bias of 0.2 V (ca. $0.65G_0$) were assigned to charge transport through metal contacts. More than 95% of the *I–V* curves recorded in blank experiments fall into either the vacuum tunnelling or the charge transport through metal contacts.

Acknowledgements

References

1. Ratner, M. *Nat. Nanotechnol.* **2013,** *8,* 378–381. doi:10.1038/nnano.2013.110
2. Elbing, M.; Ochs, R.; Koentopp, M.; Fischer, M.; von Hänisch, C.; Weigend, F.; Evers, F.; Weber, H. B.; Mayor, M. *Proc. Natl. Acad. Sci. U. S. A.* **2005,** *102,* 8815–8820. doi:10.1073/pnas.0408888102
3. Morales, G. M.; Jiang, P.; Yuan, S.; Lee, Y.; Sanchez, A.; You, W.; Yu, L. *J. Am. Chem. Soc.* **2005,** *127,* 10456–10457. doi:10.1021/ja051332c
4. Díez-Pérez, I.; Hihath, J.; Lee, Y.; Yu, L.; Adamska, L.; Kozhushner, M. A.; Oleynik, I. I.; Tao, N. *Nat. Chem.* **2009,** *1,* 635–641. doi:10.1038/nchem.392
5. Lörtscher, E.; Gotsmann, B.; Lee, Y.; Yu, L.; Rettner, C.; Riel, H. *ACS Nano* **2012,** *6,* 4931–4939. doi:10.1021/nn300438h
6. Fu, X.-X.; Zhang, R.-Q.; Zhang, G.-P.; Li, Z.-L. *Sci. Rep.* **2014,** *4,* 6357. doi:10.1038/srep06357
7. Fujii, S.; Tada, T.; Komoto, Y.; Osuga, T.; Murase, T.; Fujita, M.; Kiguchi, M. *J. Am. Chem. Soc.* **2015,** *137,* 5939–5947. doi:10.1021/jacs.5b00086
8. Capozzi, B.; Xia, J.; Adak, O.; Dell, E. J.; Liu, Z.-F.; Taylor, J. C.; Neaton, J. B.; Campos, L. M.; Venkataraman, L. *Nat. Nanotechnol.* **2015,** *10,* 522–527. doi:10.1038/nnano.2015.97
9. Chen, F.; He, J.; Nuckolls, C.; Roberts, T.; Klare, J. E.; Lindsay, S. *Nano Lett.* **2005,** *5,* 503–506. doi:10.1021/nl0478474
10. Xu, B.; Xiao, X.; Yang, X.; Zang, L.; Tao, N. *J. Am. Chem. Soc.* **2005,** *127,* 2386–2387. doi:10.1021/ja042385h
11. Pobelov, I. V.; Li, Z.; Wandlowski, T. *J. Am. Chem. Soc.* **2008,** *130,* 16045–16054. doi:10.1021/ja8054194
12. Song, H.; Kim, Y.; Jang, Y. H.; Jeong, H.; Reed, M. A.; Lee, T. *Nature* **2009,** *462,* 1039–1043. doi:10.1038/nature08639
13. Capozzi, B.; Chen, Q.; Darancet, P.; Kotiuga, M.; Buzzeo, M.; Neaton, J. B.; Nuckolls, C.; Venkataraman, L. *Nano Lett.* **2014,** *14,* 1400–1404. doi:10.1021/nl404459q
14. Reed, M. A.; Zhou, C.; Muller, C. J.; Burgin, T. P.; Tour, J. M. *Science* **1997,** *278,* 252–254. doi:10.1126/science.278.5336.252
15. Xu, B.; Tao, N. J. *Science* **2003,** *301,* 1221–1223. doi:10.1126/science.1087481
16. Venkataraman, L.; Klare, J. E.; Tam, I. W.; Nuckolls, C.; Hybertsen, M. S.; Steigerwald, M. L. *Nano Lett.* **2006,** *6,* 458–462. doi:10.1021/nl052373+
17. Kiguchi, M.; Tal, O.; Wohlthat, S.; Pauly, F.; Krieger, M.; Djukic, D.; Cuevas, J. C.; van Ruitenbeek, J. M. *Phys. Rev. Lett.* **2008,** *101,* 046801. doi:10.1103/PhysRevLett.101.046801
18. Schneebeli, S. T.; Kamenetska, M.; Cheng, Z.; Skouta, R.; Friesner, R. A.; Venkataraman, L.; Breslow, R. *J. Am. Chem. Soc.* **2011,** *133,* 2136–2139. doi:10.1021/ja111320n
19. Yelin, T.; Vardimon, R.; Kuritz, N.; Korytár, R.; Bagrets, A.; Evers, F.; Kronik, L.; Tal, O. *Nano Lett.* **2013,** *13,* 1956–1961. doi:10.1021/nl304702z
20. Afsari, S.; Li, Z.; Borguet, E. *Angew. Chem., Int. Ed.* **2014,** *53,* 9771–9774. doi:10.1002/anie.201402343
21. Kaneko, S.; Nakazumi, T.; Kiguchi, M. *J. Phys. Chem. Lett.* **2010,** *1,* 3520–3523. doi:10.1021/jz101506u

22. Kaneko, S.; Kiguchi, M. *Fullerenes, Nanotubes, Carbon Nanostruct.* **2014,** *22,* 166–172. doi:10.1080/1536383X.2013.798723
23. Kiguchi, M.; Murakoshi, K. *J. Phys. Chem. C* **2008,** *112,* 8140–8143. doi:10.1021/jp802475k
24. Martin, C. A.; Ding, D.; Sørensen, J. K.; Bjørnholm, T.; van Ruitenbeek, J. M.; van der Zant, H. S. J. *J. Am. Chem. Soc.* **2008,** *130,* 13198–13199. doi:10.1021/ja804699a
25. Nakazumi, T.; Kaneko, S.; Matsushita, R.; Kiguchi, M. *J. Phys. Chem. C* **2012,** *116,* 18250–18255. doi:10.1021/jp304733u
26. Kaneko, S.; Motta, C.; Brivio, G. P.; Kiguchi, M. *Nanotechnology* **2013,** *24,* 315201. doi:10.1088/0957-4484/24/31/315201
27. Huisman, E. H.; Guédon, C. M.; van Wees, B. J.; van der Molen, S. J. *Nano Lett.* **2009,** *9,* 3909–3913. doi:10.1021/nl9021094
28. Beebe, J. M.; Kim, B.; Gadzuk, J. W.; Frisbie, C. D.; Kushmerick, J. G. *Phys. Rev. Lett.* **2006,** *97,* 026801. doi:10.1103/PhysRevLett.97.026801
29. Widawsky, J. R.; Kamenetska, M.; Klare, J.; Nuckolls, C.; Steigerwald, M. L.; Hybertsen, M. S.; Venkataraman, L. *Nanotechnology* **2009,** *20,* 434009. doi:10.1088/0957-4484/20/43/434009
30. Guo, S.; Hihath, J.; Díez-Pérez, I.; Tao, N. *J. Am. Chem. Soc.* **2011,** *133,* 19189–19197. doi:10.1021/ja2076857
31. Bruot, C.; Hihath, J.; Tao, N. *Nat. Nanotechnol.* **2012,** *7,* 35–40. doi:10.1038/nnano.2011.212
32. Lörtscher, E.; Weber, H. B.; Riel, H. *Phys. Rev. Lett.* **2007,** *98,* 176807. doi:10.1103/PhysRevLett.98.176807
33. Zotti, L. A.; Kirchner, T.; Cuevas, J.-C.; Pauly, F.; Huhn, T.; Scheer, E.; Erbe, A. *Small* **2010,** *6,* 1529–1535. doi:10.1002/smll.200902227
34. Kim, Y.; Pietsch, T.; Erbe, A.; Belzig, W.; Scheer, E. *Nano Lett.* **2011,** *11,* 3734–3738. doi:10.1021/nl201777m
35. Briechle, B. M.; Kim, Y.; Ehrenreich, P.; Erbe, A.; Sysoiev, D.; Huhn, T.; Groth, U.; Scheer, E. *Beilstein J. Nanotechnol.* **2012,** *3,* 798–808. doi:10.3762/bjnano.3.89
36. Frisenda, R.; Perrin, M. L.; Valkenier, H.; Hummelen, J. C.; van der Zant, H. S. J. *Phys. Status Solidi B* **2013,** *250,* 2431–2436. doi:10.1002/pssb.201349236
37. Matsuhita, R.; Horikawa, M.; Naitoh, Y.; Nakamura, H.; Kiguchi, M. *J. Phys. Chem. C* **2013,** *117,* 1791–1795. doi:10.1021/jp3112638
38. Xiao, X.; Xu, B.; Tao, N. J. *Nano Lett.* **2004,** *4,* 267–271. doi:10.1021/nl035000m
39. van Ruitenbeek, J. M.; Alvarez, A.; Piñeyro, I.; Grahmann, C.; Joyez, P.; Devoret, M. H.; Esteve, D.; Urbina, C. *Rev. Sci. Instrum.* **1996,** *67,* 108. doi:10.1063/1.1146558
40. Nakashima, S.; Takahashi, Y.; Kiguchi, M. *Beilstein J. Nanotechnol.* **2011,** *2,* 755–759. doi:10.3762/bjnano.2.83
41. Xiang, D.; Lee, T.; Kim, Y.; Mei, T.; Wang, Q. *Nanoscale* **2014,** *6,* 13396–13401. doi:10.1039/C4NR03480E
42. Balandina, T.; van der Meijden, M. W.; Ivasenko, O.; Cornil, D.; Cornil, J.; Lazzaroni, R.; Kellogg, R. M.; De Feyter, S. *Chem. Commun.* **2013,** *49,* 2207–2209. doi:10.1039/c3cc37159j
43. Zhao, J.; Murakoshi, K.; Yin, X.; Kiguchi, M.; Guo, Y.; Wang, N.; Liang, S.; Liu, H. *J. Phys. Chem. C* **2008,** *112,* 20088–20094. doi:10.1021/jp8055448
44. Paulsson, M.; Datta, S. *Phys. Rev. B* **2003,** *67,* 241403(R). doi:10.1103/PhysRevB.67.241403
45. Komoto, Y.; Fujii, S.; Hara, K.; Kiguchi, M. *J. Phys. Chem. C* **2013,** *117,* 24277–24282. doi:10.1021/jp404858x

BEILSTEIN JOURNAL OF NANOTECHNOLOGY

Effects of spin–orbit coupling and many-body correlations in STM transport through copper phthalocyanine

Benjamin Siegert[*], Andrea Donarini and Milena Grifoni

Full Research Paper

`Open Access`

Abstract

The interplay of exchange correlations and spin–orbit interaction (SOI) on the many-body spectrum of a copper phtalocyanine (CuPc) molecule and their signatures in transport are investigated. We first derive a minimal model Hamiltonian in a basis of frontier orbitals that is able to reproduce experimentally observed singlet–triplet splittings. In a second step SOI effects are included perturbatively. Major consequences of the SOI are the splitting of former degenerate levels and a magnetic anisotropy, which can be captured by an effective low-energy spin Hamiltonian. We show that scanning tunneling microscopy-based magnetoconductance measurements can yield clear signatures of both these SOI-induced effects.

Introduction

Spin–orbit interaction (SOI) can play a major role in molecular spintronics. For example, in combination with the configuration of the non-magnetic component (organic ligand), it is known to be essential in establishing magnetic anisotropy in high-spin molecular magnets [1], and it is quite generally expected in metalorganic compounds. Effective spin-Hamiltonians are commonly used to describe this anisotropy, and usually capture well the low energy properties of these systems [1-3]. Such effective Hamiltonians have been derived microscopically for widely studied molecular magnets such as Fe_8,

Fe_4 and Mn_{12} [4]. Recently, magnetic anisotropy effects could be directly probed by magnetotransport spectroscopy for Fe_4 in quantum-dot setups [5,6]. An interesting question is hence if other classes of metallorganic compounds, such as the widely studied metal phthalocyanines [7,8], exhibit sizeable magnetic anisotropy induced by the interplay of electronic correlations and SOI. Indeed, in an X-ray magnetic circular dichroism (XMCD) analysis copper phthalocyanine (CuPc) was found to exhibit enormous anisotropies in both spin and orbital dipole moments [9]. Furthermore, recent experimental findings for

cobalt pththalocyanine in a scanning tunneling microscopy (STM) setup [10] suggest that many-body correlations play an important role in the interpretation of the transport measurements. In a recent work [11], we have explicitly investigated long-range and short-range electron–electron correlation effects in CuPc and found a singlet–triplet splitting of the former anionic groundstate of about 18 meV, and thus a triplet as anionic ground state.

In this work we add the SOI to our analysis. We find that it further removes the triplet degeneracy by inducing splittings of few tenths of millielectronvolts. Moreover, in combination with exchange correlations, it produces a magnetic anisotropy which can in turn be captured by an effective spin Hamiltonian.

In general, the accurate calculation of the many-body properties of metallorganic molecules, such as molecular magnets or our CuPc, is a highly nontrivial task. In fact, the number of their atomic constituents is large enough that exact diagonalization is not possible and standard density-functional schemes have difficulties in capturing short ranged electron–electron correlations [4]. In order to reduce the size of the many-body Fock space, we use a basis of frontier molecular orbitals as the starting point to include electronic correlations [11,12] and construct a generalized Hubbard Hamiltonian. Furthermore, the symmetry of the molecule greatly helps to reduce the number of matrix elements one has to calculate in this basis.

To probe both SOI-induced splittings and magnetic anisotropy, we further investigated the current characteristics of a CuPc molecule in an STM configuration similar to the experiments in [13,14]: The molecule is put on a thin insulating layer grown on top of a conducting substrate. The layer functions as a tunneling barrier and decouples the molecule from the substrate. Hence the CuPc molecule acts as a molecular quantum dot weakly coupled by tunneling barriers to metallic leads (here the STM tip and the substrate). This quantum dot configuration should be favourable to experimentally probe SOI splittings and magnetic anisotropies when an external magnetic field is applied to the system, in analogy to the experiments in [6]. Indeed, we demonstrate that experimentally resolvable SOI splitting should be observed at magnetic fields of a few teslas.

The paper is organized as follows: We first derive a microscopic Hamiltonian for CuPc in the frontier orbital basis which includes exchange correlations and the SOI. This Hamiltonian is diagonalized exactly and used in further spectral analysis and transport calculations. Its spectrum is also used to benchmark the prediction of an effective spin Hamiltonian that captures well the low-energy properties of CuPc both in its neutral and anionic configurations. Finally, transport calculations with and without magnetic fields are presented and SOI-induced signatures are analyzed.

Results and Discussion
Microscopic model Hamiltonian for CuPc
The focus of this section is the establishment of a minimal model Hamiltonian for an isolated CuPc molecule capable to account for both electron–electron interaction and spin–orbit coupling effects. As discussed below, parameters are fixed such that experimental observations for the singlet–triplet splitting [8] as well as positions of anionic and cationic resonances [14] are satisfactorily reproduced. In its most general form and for a generic molecule such Hamiltonian reads

$$\widehat{H}_{mol} = \widehat{H}_0 + \widehat{V}_{ee} + \widehat{V}_{SO}, \qquad (1)$$

where the single-particle Hamiltonian of the molecule is given by $\widehat{H}_0$, $\widehat{V}_{ee}$ describes electronic interactions and $\widehat{V}_{SO}$ accounts for the spin–orbit interaction (SOI).

Single-particle Hamiltonian for CuPc
The one-body Hamiltonian $\widehat{H}_0$, written in the atomic basis $|\alpha\rangle$, reads

$$\widehat{H}_0 = \sum_{\alpha\beta\sigma} \left(\varepsilon_\alpha \delta_{\alpha\beta} + b_{\alpha\beta} \right) \hat{d}^\dagger_{\alpha\sigma} \hat{d}_{\beta\sigma}, \qquad (2)$$

where α is a multi-index combining atomic species and orbital quantum number at position $\mathbf{r}_\alpha$, see Figure 1a. For the ligand we consider the set of all 2s (1s for hydrogen), $2p_x$ and $2p_y$ orbitals as the σ-system, and consequently the set of $2p_z$ orbitals as the π-system. On the metal, the $3d_{xy}$, $3d_{x^2-y^2}$, $3d_{z^2}$ and 4s orbitals contribute to the σ-system, while the $3d_{zx}$ and $3d_{yz}$ belong to the π-system. This basis yields a total of 195 valence electrons for neutral CuPc. Atomic on-site energies ε_α and geometrical parameters were taken from [7,15]. The hopping matrix elements $b_{\alpha\beta}$ in Equation 2 are obtained by using the Slater–Koster [16] and Harrison [17] LCAO schemes, similar to [18]. Numerical diagonalization of $\widehat{H}_0$ finally yields single particle energies ε_i, see Figure 1b, and molecular orbitals $|i\sigma\rangle = \sum_\alpha c_{i\alpha} |\alpha\sigma\rangle$, cf. Supporting Information File 1.

Stemming from Hartree–Fock calculations for isolated atoms [15], the atomic on-site energies ε_α do not take into account the ionic background of the molecule and crystal field contributions. Therefore, molecular orbital energies ε_i have to be renormalized with parameters δ_i to counteract this shortage, yielding (cf. Supporting Information File 2)
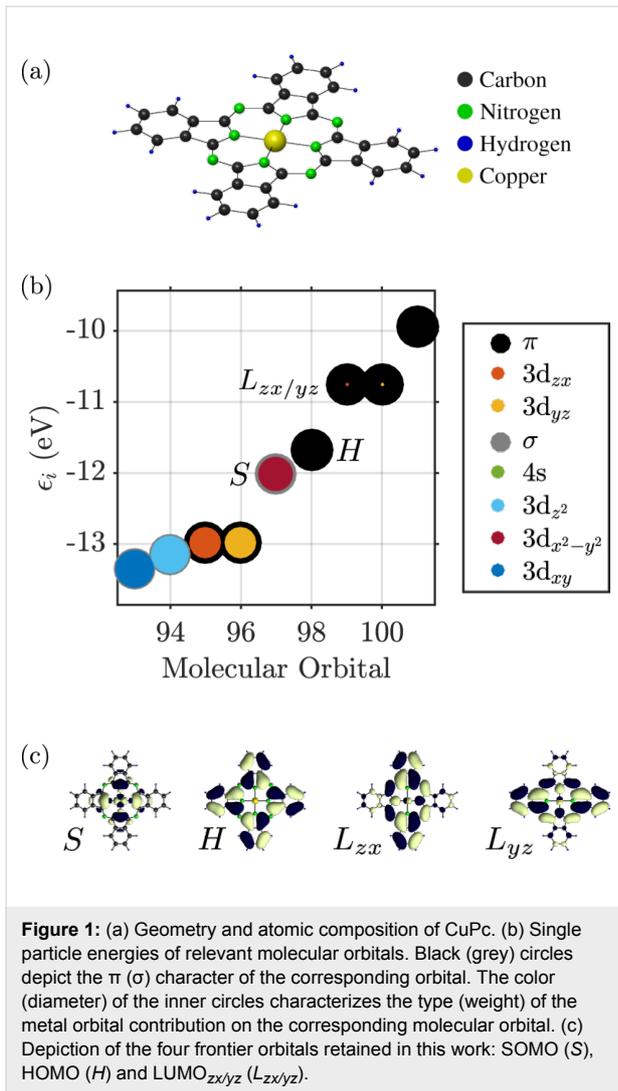
Figure 1: (a) Geometry and atomic composition of CuPc. (b) Single particle energies of relevant molecular orbitals. Black (grey) circles depict the π (σ) character of the corresponding orbital. The color (diameter) of the inner circles characterizes the type (weight) of the metal orbital contribution on the corresponding molecular orbital. (c) Depiction of the four frontier orbitals retained in this work: SOMO (S), HOMO (H) and LUMO$_{zx/yz}$ ($L_{zx/yz}$).

$$\widehat{H}_0 = \sum_{i\sigma} \left(\varepsilon_i + \delta_i \right) \hat{n}_{i\sigma}. \tag{3}$$

In this work we use a constant shift $\delta_i = \delta = 1.83$ eV.

Due to the odd number of valence electrons, in its neutral configuration CuPc has a singly occupied molecular orbital (SOMO). When the molecule is in its anionic groundstate, this orbital does not become doubly occupied [7]. Hence, the orbitals most relevant for transport (frontier orbitals) are the SOMO (S), the HOMO (H) and the two degenerate LUMOs ($L_{zx/yz}$), which transform according to the b_{1g}, a_{1u} and e_g irreducible representations of the point group of CuPc (D_{4h}), respectively. They are depicted in Figure 1c. The LUMO orbitals in their real-valued representations, $\left| L_{zx} \right\rangle$ and $\left| L_{yz} \right\rangle$, have equal contributions $c_L \approx 0.097$ on both $3d_{zx}$ and $3d_{yz}$ orbitals of the metal. Due to their degeneracy, they can be transformed into their complex, rotational invariant representations:

$$\begin{aligned}\left| L \pm \right\rangle &= \mp 2^{-1/2} \left(\left| L_{zx} \right\rangle \pm i \left| L_{yz} \right\rangle \right) \\ &= \mp 2^{-1/2} \sqrt{1 - c_L^2} \left(\left| L_{zx} \right\rangle_{\mathrm{Pc}} \pm i \left| L_{yz} \right\rangle_{\mathrm{Pc}} \right) \\ &\quad \mp 2^{-1/2} c_L \left(\left| 3d_{zx} \right\rangle_{\mathrm{Cu}} \pm i \left| 3d_{yz} \right\rangle_{\mathrm{Cu}} \right) \\ &= \sqrt{1 - c_L^2} \left| L \pm \right\rangle_{\mathrm{Pc}} + c_L \left| 3, 2, \pm 1 \right\rangle_{\mathrm{Cu}}, \end{aligned} \tag{4}$$

where $\left| 3, 2, \pm 1 \right\rangle_{\mathrm{Cu}}$ is the $n = 3$ metal orbital with angular momentum $\ell = 2$ and magnetic quantum number $m = \pm 1$. To distinguish contributions from the pure phthalocyanine (Pc) ligand and the copper (Cu) center, we introduced $\left| \cdot \right\rangle_{\mathrm{Pc}}$ and $\left| \cdot \right\rangle_{\mathrm{Cu}}$, respectively. Likewise, with $c_S \approx 0.90$, we can write for the SOMO:

$$\begin{aligned}\left| S \right\rangle &= \sqrt{1 - c_S^2} \left| S \right\rangle_{\mathrm{Pc}} + c_S \left| 3d_{x^2 - y^2} \right\rangle_{\mathrm{Cu}} \\ &= \sqrt{1 - c_S^2} \left| S \right\rangle_{\mathrm{Pc}} + 2^{-1/2} c_S \left(\left| 3, 2, -2 \right\rangle_{\mathrm{Cu}} + \left| 3, 2, 2 \right\rangle_{\mathrm{Cu}} \right), \end{aligned} \tag{5}$$

where $\left| 3, 2, \pm 2 \right\rangle_{\mathrm{Cu}}$ is the $n = 3$ metal orbital with angular momentum $\ell = 2$ and projection $m = \pm 2$ onto the z-axis. Finally, the HOMO has no metal contributions and thus we have trivially $\left| H \right\rangle = \left| H \right\rangle_{\mathrm{Pc}}$. The representations introduced in Equation 4 have the advantage that the four frontier orbitals can then be characterized by the phases φ_i acquired under rotations of $\pi/2$ around the main molecular symmetry axis. For the SOMO $\varphi_S = \pi$, for the HOMO $\varphi_H = 0$ and for the two LUMOs $\varphi_{L\pm} = \pm \pi/2$.

Many-body Hamiltonian in the frontier orbitals basis

In order to set up a minimal many-body Hamiltonian, we restrict the full Fock space to many-body states spanned by the SOMO (S), the HOMO (H) and the two LUMO ($L\pm$) orbitals and write Equation 1 in this basis. Hence, for neutral CuPc the number of electrons populating the frontier orbitals is $N_0 = 3$.

We exploit the distinct phases acquired by the frontier orbitals under 90° rotations to determine selection rules for the matrix elements V_{ijkl} in $\widehat{V}_{\mathrm{ee}}$,

$$\widehat{V}_{\mathrm{ee}} = \sum_{ijkl} \sum_{\sigma\sigma'} V_{ijkl} \, \hat{d}_{i\sigma}^\dagger \hat{d}_{k\sigma'}^\dagger \hat{d}_{l\sigma'} \hat{d}_{j\sigma}, \tag{6}$$

namely $V_{ijkl} \neq 0$ if $\phi_i - \phi_j + \phi_k - \phi_l = 2\pi \cdot n$, $n \in \mathbb{Z}$, cf. Supporting Information File 2. Equation 6 in this basis then reads

$$\widehat{V}_{ee} = \sum_i U_i \hat{n}_{i\uparrow}\hat{n}_{i\downarrow} + \frac{1}{2}\sum_{[ij]} U_{ij}\hat{n}_i\hat{n}_j$$
$$-\frac{1}{2}\sum_{[ij]}\sum_\sigma J_{ij}^{ex}\left(\hat{n}_{i\sigma}\hat{n}_{j\sigma} - \hat{d}_{i\sigma}^\dagger\hat{d}_{j\overline{\sigma}}^\dagger\hat{1}_{i\overline{\sigma}}\hat{d}_{j\sigma}\right)$$
$$+\frac{1}{2}\sum_{[ij]}\sum_\sigma J_{ij}^p \hat{d}_{i\sigma}^\dagger\hat{d}_{i\overline{\sigma}}^\dagger\hat{d}_{j\overline{\sigma}}\hat{d}_{j\sigma}$$
$$+\frac{1}{2}\sum_{[ijk]}\sum_\sigma\left(\tilde{J}_{ijk}^p \hat{d}_{i\sigma}^\dagger\hat{d}_{i\overline{\sigma}}^\dagger\hat{d}_{k\overline{\sigma}}\hat{d}_{j\sigma} + h.c.\right) \qquad (7)$$

where the indices *i, j, k* now run over the set of frontier orbitals, and the notation [*ijk*] means that the sum runs only over unlike indices, i.e., *i, j* and *k* are different from each other in the corresponding sum. The abbreviations we introduced in Equation 7 are the orbital Coulomb interaction $U_i = V_{iiii}$, the inter-orbital Coulomb interaction $U_{ij} = V_{iijj}$, the exchange integral $J_{ij}^{ex} = V_{ijji}$, the ordinary pair hopping term $J_{ij}^p = V_{ijjj}$ and the split pair hopping term $\tilde{J}_{ijk}^p = V_{ijik}$. Contributions with four different indices are found to be very small (of the order of microelectronvolts) and thus omitted in this work. The matrix elements V_{ijkl} are calculated numerically using Monte Carlo integration [19] and renormalized with a dielectric constant $\varepsilon_r = 2.2$ in order to account for screening by frozen orbitals [12]. A table with the numerically evaluated interaction constants is found in Supporting Information File 2.

Spin–orbit interaction (SOI) in the frontier orbitals basis

A perturbative contribution to the bare one-body Hamiltonian $\widehat{H}_0$ relevant in molecular systems is provided by the SOI. In the following we derive an effective spin–orbit coupling operator acting on the subset of frontier orbitals. The atomic SOI operator reads

$$\widehat{V}_{SO} = \sum_{\alpha,\ell_\alpha} \xi_{\ell_\alpha}\hat{\boldsymbol{\ell}}_\alpha\cdot\hat{\mathbf{s}}_\alpha, \qquad (8)$$

where α and ℓ_α run over all atoms and shells, respectively. By evaluating Equation 8 only on the central copper atom, i.e., $\ell = 2$ and $\alpha = Cu$, $\widehat{V}_{SO}$ in second quantization is given by

$$\widehat{V}_{SO} = \xi_{Cu}\left(\sum_{m=-2}^2 \frac{m}{2}\left(\hat{d}_{m\uparrow}^\dagger\hat{d}_{m\uparrow} - \hat{d}_{m\downarrow}^\dagger\hat{d}_{m\downarrow}\right)\right.$$
$$+\sqrt{\frac{3}{2}}\left(\hat{d}_{0\downarrow}^\dagger\hat{d}_{-1\uparrow} + \hat{d}_{1\downarrow}^\dagger\hat{d}_{0\uparrow} + h.c.\right) \qquad (9)$$
$$\left.+\left(\hat{d}_{2\downarrow}^\dagger\hat{d}_{1\uparrow} + \hat{d}_{-1\downarrow}^\dagger\hat{d}_{-2\uparrow} + h.c.\right)\right),$$

where $\hat{d}_{m\sigma}^\dagger$ creates an electron with spin σ on the copper atom in the orbital specified by $(\ell = 2, m)$. For an electron in the 3d shell of Cu we use $\xi_{Cu} \approx 100$ meV [20]. Projecting Equation 9 onto the minimal set of frontier orbitals then yields:

$$\widehat{V}_{SO} = \lambda_1\sum_{\tau=\pm}\tau\left(\hat{d}_{L\tau\uparrow}^\dagger\hat{d}_{L\tau\uparrow} - \hat{d}_{L\tau\downarrow}^\dagger\hat{d}_{L\tau\downarrow}\right)$$
$$+\lambda_2\left(\hat{d}_{S\uparrow}^\dagger\hat{d}_{L-\downarrow} + \hat{d}_{L+\uparrow}^\dagger\hat{d}_{S\downarrow} + h.c.\right), \qquad (10)$$

where $\lambda_1 = 1/2\xi_{Cu}|c_L|^2 = 0.47$ meV and $\lambda_2 = \xi_{Cu}(c_S c_L)/\sqrt{2} = 6.16$ meV are now effective spin–orbit coupling constants. A similar analysis of SOI in CuPc, laying more focus on the central Cu atom, can be found in [21].

Finally, many-body eigenenergies E_{Nk} and eigenstates $|Nk\rangle$, labeled after particle number *N* and state index *k*, are obtained by exact numerical diagonalization of $\widehat{H}_{mol}$ in the frontier orbitals basis. Despite numerically tractable, the problem described by $\widehat{H}_{mol}$ is still highly intricate, as the Fock space has dimension $4^4 = 256$. In reality, though, only few low-lying many-body states are relevant at low energies. This enables further simplification and even an analytical treatment, as discussed in the next subsection.

Low-energy spectrum of CuPc and effective spin Hamiltonian

In the following we will analyze the neutral and anionic low-energy part of the many-body spectrum of CuPc and establish an effective Hamiltonian which enables us to analyze the low-energy behaviour in a more lucid way. To this extent, we start by observing that $\widehat{H}_{mol}$ (in the considered particle number subblocks) contains different energy scales, in particular, $U > J > \lambda$, which suggests a hierarchy of steps. We use *U, J* and λ to denote the set of all Hubbard-like parameters (U_i, U_{ij}), all exchange parameters ($J_{ij}^{ex}, J_{ij}^p, \tilde{J}_{ijk}^p$) and all SOI parameters (λ_i), respectively. As a first step we set both the exchange (*J*) and SOI (λ) contributions to $\widehat{H}_{mol}$ to zero and determine the neutral and anionic groundstates. In a second and third step exchange and SOI are added, respectively.

Neutral low-energy spectrum

In the neutral low-energy part of the spectrum, we retain the two spin-degenerate groundstates of $\widehat{H}_{mol}(J=0, \lambda=0)$,

$$|N_0, \sigma\rangle := \hat{d}_{S\sigma}^\dagger |\Omega\rangle, \qquad (11)$$

with corresponding energy $E_{N_0}^g$. We defined $|\Omega\rangle = \hat{d}_{H\uparrow}^\dagger\hat{d}_{H\downarrow}^\dagger|0\rangle$. The groundstates in Equation 11 are neither affected by $\widehat{V}_{SO}$

nor by the exchange terms in Equation 7. Trivially, the effective Hamiltonian in the basis of $\left| N_0, g\sigma \right\rangle$ reads:

$$\mathrm{H}_0^{N_0} = E_{N_0}^{\mathrm{g}}. \tag{12}$$

In principle Equation 7 also contains terms that act on the neutral groundstate, such as for example pair hopping terms proportional to $\tilde{J}_{HL+L-}^{\mathrm{p}}$, and cause admixtures with other many-body states. However, according to our full numerical calculations, these admixtures are rather small and do not affect transitions between neutral and anionic states.

Anionic low-energy spectrum

Continuing with the anionic low-energy part of the spectrum of $\widehat{\mathrm{H}}_{\mathrm{mol}}(J=0, \lambda=0)$, we find an eightfold degenerate ground-state:

$$\left| N_0 + 1, \tau\sigma\sigma' \right\rangle := \hat{\mathrm{d}}_{S\sigma}^{\dagger} \hat{\mathrm{d}}_{L\tau\sigma'}^{\dagger} \left| \Omega \right\rangle, \tag{13}$$

with corresponding energy $E_{N_0+1}^{\mathrm{g}}$. The eightfold degeneracy comes from the two unpaired spins in either SOMO or LUMO and the orbital degeneracy of the LUMO orbitals. In order to make the anionic eigenstates also eigenstates of the spin operators $\hat{\mathbf{S}}^2$ and $\hat{S}_z$, they can be rewritten as

$$\begin{aligned}
\left| \mathbf{S}_\tau \right\rangle &= \frac{1}{\sqrt{2}} \left(\hat{\mathrm{d}}_{S\uparrow}^{\dagger} \hat{\mathrm{d}}_{L\tau\downarrow}^{\dagger} - \hat{\mathrm{d}}_{S\downarrow}^{\dagger} \hat{\mathrm{d}}_{L\tau\uparrow}^{\dagger} \right) \left| \Omega \right\rangle, \\
\left| \mathbf{T}_\tau^+ \right\rangle &= \hat{\mathrm{d}}_{S\uparrow}^{\dagger} \hat{\mathrm{d}}_{L\tau\uparrow}^{\dagger} \left| \Omega \right\rangle, \\
\left| \mathbf{T}_\tau^0 \right\rangle &= \frac{1}{\sqrt{2}} \left(\hat{\mathrm{d}}_{S\uparrow}^{\dagger} \hat{\mathrm{d}}_{L\tau\downarrow}^{\dagger} + \hat{\mathrm{d}}_{S\downarrow}^{\dagger} \hat{\mathrm{d}}_{L\tau\uparrow}^{\dagger} \right) \left| \Omega \right\rangle, \\
\left| \mathbf{T}_\tau^- \right\rangle &= \hat{\mathrm{d}}_{S\downarrow}^{\dagger} \hat{\mathrm{d}}_{L\tau\downarrow}^{\dagger} \left| \Omega \right\rangle.
\end{aligned} \tag{14}$$

The orbital degeneracy of the LUMOs, expressed by the index τ, is responsible for the two sets of singlets (total spin $S=0$) and triplets (total spin $S=1$). Considering exchange interaction in a second step, we find that only the J_{SL}^{ex} term in Equation 7,

$$-\sum_{\tau\sigma} J_{SL}^{\mathrm{ex}} \left(\hat{n}_{S\sigma} \hat{n}_{L\tau\sigma} - \hat{\mathrm{d}}_{S\sigma}^{\dagger} \hat{\mathrm{d}}_{L\tau\bar{\sigma}}^{\dagger} \hat{\mathrm{d}}_{S\bar{\sigma}} \hat{\mathrm{d}}_{L\tau\sigma} \right), \tag{15}$$

directly determines the low-energy structure of the anionic low-energy part because of the singly occupied SOMO and LUMOs: The degeneracy between singlets and triplets is lifted, see Figure 2, and we obtain

$$\begin{aligned}
E_{\mathbf{S}} &= E_{N_0}^{\mathrm{g}} + J_{SL}^{\mathrm{ex}}, \\
E_{\mathbf{T}} &= E_{N_0}^{\mathrm{g}} - J_{SL}^{\mathrm{ex}}
\end{aligned} \tag{16}$$

for the singlets and triplets, respectively.
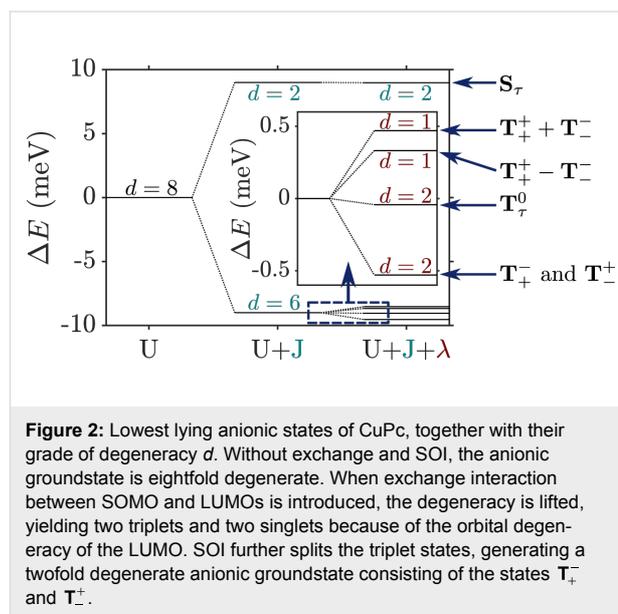
Figure 2: Lowest lying anionic states of CuPc, together with their grade of degeneracy *d*. Without exchange and SOI, the anionic groundstate is eightfold degenerate. When exchange interaction between SOMO and LUMOs is introduced, the degeneracy is lifted, yielding two triplets and two singlets because of the orbital degeneracy of the LUMO. SOI further splits the triplet states, generating a twofold degenerate anionic groundstate consisting of the states $\mathbf{T}_+^-$ and $\mathbf{T}_-^+$.

Finally, to analyze in a third step how $\widehat{\mathrm{V}}_{\mathrm{SO}}$ affects the low-energy part of the anionic part of the spectrum, in particular which degeneracies are lifted, we treat it as a perturbation and apply second-order perturbation theory to obtain the energy shifts. To this end, some additional states have to be considered. They are listed in Supporting Information File 3.

The states $\mathbf{T}_-^+$ and $\mathbf{T}_+^-$ experience a downshift due to $\widehat{\mathrm{V}}_{\mathrm{SO}}$ and become the groundstates. Measuring energies with respect to $E_{\mathbf{T}}$, we get

$$\Delta E_{\mathbf{T}_+^-} = \Delta E_{\mathbf{T}_-^+} = -\lambda_1 - \frac{2\lambda_2^2}{\Delta_1 + J_{SL}^{\mathrm{ex}}}, \tag{17}$$

see Figure 2. Note that in our numerical calculations $\mathbf{T}_+^-$ and $\mathbf{T}_-^+$ are mixed and the degeneracy of the resulting states is lifted by a small shift in the range of some µeV. A more detailed discussion concerning the mixing of $\mathbf{T}_+^-$ and $\mathbf{T}_-^+$ can be found in Supporting Information File 3. The next states are $\mathbf{T}_+^0$ and $\mathbf{T}_-^0$ with

$$\Delta E_{\mathbf{T}_+^0} = \Delta E_{\mathbf{T}_-^0} = -\frac{\lambda_1^2}{2 J_{SL}^{\mathrm{ex}}} - \frac{\lambda_2^2}{\Delta_1 - J_{SL}^{\mathrm{ex}}}. \tag{18}$$

Due to their quadratic dependence on λ_1 and λ_2, these states change very little with $\widehat{V}_{SO}$. The degeneracy of the states $\mathbf{T}_+^+$ and $\mathbf{T}_-^-$ is lifted by the mixing of these states through $\widehat{V}_{SO}$. We find

$$|\alpha\rangle = \frac{1}{\sqrt{2}} \left(\left| T_+^+ \right\rangle + \left| T_-^- \right\rangle \right), \tag{19}$$

$$|\beta\rangle = \frac{1}{\sqrt{2}} \left(\left| T_+^+ \right\rangle - \left| T_-^- \right\rangle \right), \tag{20}$$

where for $|\beta\rangle$ we omitted smaller additional contributions from other states. The energies change according to

$$\Delta E(\alpha) = \lambda_1, \tag{21}$$

$$\Delta E(\beta) = \lambda_1 - 4\lambda_2^2 \left(\frac{1}{\Delta_1 + J_{SL}^{ex}} + \frac{1}{\Delta_2 + J_{SL}^{ex}} \right). \tag{22}$$

For further details we refer to Supporting Information File 3. Finally, the singlets $\mathbf{S}_+$ and $\mathbf{S}_-$, similar to $\mathbf{T}_+^0$ and $\mathbf{T}_-^0$, change very little (with respect to $E_{\mathbf{S}}$):

$$\Delta E_{\mathbf{S}_\tau} = \frac{\lambda_1^2}{2J_{SL}^{ex}} - \frac{\lambda_2^2}{\Delta_1 - J_{SL}^{ex}}. \tag{23}$$

By introducing $\hat{\tau}_z := \hat{n}_{L+} - \hat{n}_{L-}$, an approximate Hamiltonian up to first order in $\widehat{V}_{SO}$ can be given for the $N_0 + 1$ particle subblock:

$$H_0^{N_0+1} = E_{N_0+1}^g - J_{SL}^{ex} \left(\hat{S}^2 - 1 \right) + \lambda_1 \hat{\tau}_z \hat{S}_z. \tag{24}$$

Equation 24 is one major result of this work. It shows that, similar to the well-studied molecular magnets [3-6], the interplay of spin–orbit coupling and exchange interactions yield magnetic anisotropies that can be captured by effective spin Hamiltonians. Noticeably, because Equation 24 was derived from the microscopic molecular Hamiltonian $\widehat{H}_{mol}$, it was possible to check that deviations are in range of microelectronvolts and only of quantitative nature by comparison of the spectrum to the numerically evaluated one. Another source of magnetic anisotropy is the Dzyaloshinskii–Moriya interaction [22,23]. Although the latter is also linear with respect to the SOI, it does not appear in our model. The fundamental reason for neglecting it is the large ratio between the hopping integrals (of the order of electronvolts) and the SOI ($\xi_{Cu} \approx 100$ meV), which also justifies our perturbative analysis in terms of molecular orbitals. However, for molecular quantum

dots with comparable SOI and hopping integrals the Dzyaloshinskii–Moriya interaction is sizeable and produces interesting effects on magnetization [24] and transport characteristics [25].

Interaction with magnetic fields

An experimentally accessible way to probe magnetic anisotropies is to apply external magnetic fields. In order to account for interactions of orbitals with magnetic fields, the atomic hopping matrix elements $b_{\alpha\beta}$ in Equation 2 have to be corrected with Peierls phase factors,

$$b_{\alpha\beta} \rightarrow b_{\alpha\beta} \, e^{i\phi_{\alpha\beta}}, \tag{25}$$

where, using the gauge $\mathbf{A} = -B_z \, y\hat{x}$, the phase is given by

$$\phi_{\alpha\beta} = \frac{eB_z}{2\hbar} \left(y_\alpha + y_\beta \right)\left(x_\alpha - x_\beta \right). \tag{26}$$

Here (x_α, y_α) are the in-plane atomic coordinates. Owing to the planar geometry of CuPc, $\phi_{\alpha\beta}$ depends only on the z-component B_z of the magnetic field $\mathbf{B}$. In Figure 3 we show the dependence of the energies of the frontier molecular orbitals on the strength of the magnetic field in z-direction, B_z. For the two LUMOs we observe a linear dependence on the magnetic field, yielding an effective orbital moment of $\mu_{orb} = 33.7 \ \mu eVT^{-1}$, while the LUMO−(+) goes down (up) in energy with B_z (Figure 3a). The energies of the HOMO and the SOMO, however, scale quadratically with the magnetic field at a much lower scale (Figure 3b). This behaviour is expected, since the a_{1u} and b_{1g} representations have characters +1 under C_2' rotations, which transform B_z to $-B_z$. Thus the energies of HOMO and SOMO can not depend on the sign of B_z and must move at least quadratically with B_z. The two-dimensional e_g representa-
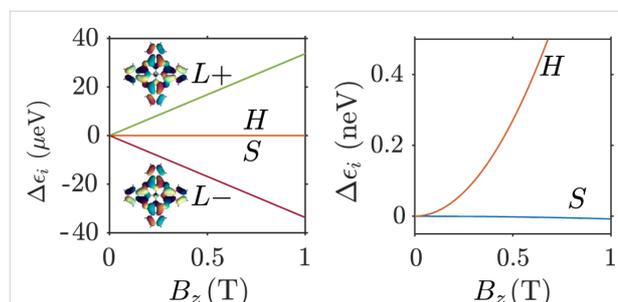
Figure 3: (a) Dependence of the single particle orbital energies on the magnetic field strength. From this, the effective orbital moment of the LUMOs, here depicted in their complex representation, can be extracted as $\mu_{orb} = 33.7 \ \mu eVT^{-1}$. The energies of the SOMO and HOMO orbitals depend quadratically on the magnetic field and involve a much lower scale than the LUMOs, as seen in the close-up in panel (b).

tion on the other hand has zero character under C_2' rotations, which implies that the constituents of e_g transform under such rotations either with different signs or into each other; indeed under a C_2' rotation LUMO+ is mapped onto LUMO− and vice versa.

Finally, the interaction of electronic spins with magnetic fields is represented by adding a Zeeman term $\widehat{V}_Z$ to Equation 1,

$$\widehat{H}_{mol} \rightarrow \widehat{H}_{mol} + \widehat{V}_Z = \widehat{H}_{mol} + g_S \mu_B \hat{\mathbf{S}} \cdot \mathbf{B}, \qquad (27)$$

where $g_S = 2$ and $\mathbf{S}$ is the total spin operator on the molecule written in the frontier orbital basis.

Effective low-energy Hamiltonian
Putting everything together, an effective low-energy Hamiltonian including magnetic interaction terms for both orbital and spin degrees of freedom can thus be given. It reads

$$H_{eff}^N = H_0^N + \mu_{orb} \hat{\tau} B_z + g_S \mu_B \hat{\mathbf{S}} \cdot \mathbf{B}, \qquad (28)$$

where H_0^N is the Hamiltonian for the corresponding low-energy N-particle subblock as given by Equation 12 and Equation 24.

Dynamics and transport
Reduced density operator and current
The transport calculations for the molecule in an STM setup are done by using the formalism introduced in earlier works [18,26,27]. For the sake of clarity, in the following we briefly discuss the main steps to obtain the current through the molecule. The full system is described by the Hamiltonian

$$\widehat{H} = \widehat{H}_{mol} + \widehat{H}_{ic} + \widehat{H}_S + \widehat{H}_T + \widehat{H}_{tun}, \qquad (29)$$

where $\widehat{H}_{mol}$ describes the isolated molecule, see Equation 1. To incorporate image charge effects in our model, leading to renormalizations of the energies of the system's charged states [28], we included a term $\widehat{H}_{ic}$[11],

$$\widehat{H}_{ic} = -\delta_{ic} \left(\hat{N} - N_0 \right)^2, \qquad (30)$$

where $\hat{N}$ is the particle number operator on the molecule. Electrostatic considerations regarding the geometry of the STM setup yielded $\delta_{ic} \approx 0.32$ eV [11]. The Hamiltonians $\widehat{H}_S$ and $\widehat{H}_T$ corresponding to substrate (S) and tip (T), respectively, are describing noninteracting electronic leads. They read

$$\widehat{H}_{\eta=S,T} = \sum_{\mathbf{k}\sigma} \varepsilon_{\eta\mathbf{k}} \hat{c}^\dagger_{\eta\mathbf{k}\sigma} \hat{c}_{\eta\mathbf{k}\sigma}, \qquad (31)$$

where $\hat{c}^\dagger_{\eta\mathbf{k}\sigma}$ creates an electron in lead η with spin σ and momentum $\mathbf{k}$. The tunneling Hamiltonian $\widehat{H}_{tun}$ finally is given by

$$\widehat{H}_{tun} = \sum_{\eta\mathbf{k}i\sigma} t^\eta_{\mathbf{k}i} \hat{c}^\dagger_{\eta\mathbf{k}\sigma} \hat{d}_{i\sigma} + \text{h.c.} \qquad (32)$$

It contains the tunneling matrix elements $t^\eta_{\mathbf{k}i}$, which are obtained by calculating the overlap between the lead wavefunctions $|\eta\mathbf{k}\rangle$ and the molecular orbitals $|i\rangle$[26]. They yield the tunneling rates

$$\Gamma^\eta_{ij}(E) = \frac{2\pi}{\hbar} \sum_{\mathbf{k}} t^\eta_{i\mathbf{k}} \left(t^\eta_{j\mathbf{k}} \right)^* \delta\left(\varepsilon_{\eta\mathbf{k}} - E \right), \qquad$$

which are of the order of 10^{-6} eV and 10^{-9} eV for the substrate and the tip, respectively. Finally, the dynamics of the transport itself is calculated by evaluating the generalized master equation,

$$\dot{\rho}_{red} = \mathcal{L}\left[\rho_{red} \right], \qquad (33)$$

for the reduced density operator [26,29] $\rho_{red} = \text{Tr}_{S,T}(\rho)$. The Liouvillian superoperator

$$\mathcal{L} = \mathcal{L}_S + \mathcal{L}_T + \mathcal{L}_{rel} \qquad (34)$$

contains the terms $\mathcal{L}_S$ and $\mathcal{L}_T$ describing tunneling from and to the substrate and the tip, respectively. To account for relaxation processes leading to de-excitation of molecular excited states, we included a relaxation term $\mathcal{L}_{rel}$, analogously to [30]:

$$\mathcal{L}_{rel}\left[\rho \right] = -\frac{1}{\tau}\left(\rho - \sum_N \rho^{th,N} \sum_l \rho^N_{ll} \right). \qquad (35)$$

It depends on the deviation of ρ from the thermal distribution $\rho^{th,N}$ of the N-particle subblock, which is given by a Boltzmann distribution:

$$\rho^{th,N} = \sum_k \frac{e^{-\beta E_{Nk}}}{\sum_l e^{-\beta E_{Nl}}} |Nk\rangle\langle Nk|, \qquad (36)$$

with $\beta = (k_B T)^{-1}$. Since $\mathcal{L}_{rel}$ acts separately on each N-particle subblock, it conserves the particle number on the molecule and thus does not contribute to transport directly. In this work, the relaxation factor $1/\tau$ is around the same order of magnitude as the mean tip tunneling rate onto the molecule. In particular, we are interested in the stationary solution ρ_{red}^{∞} for which $\dot{\rho}_{red}^{\infty} = \mathcal{L}[\rho_{red}^{\infty}] = 0$. Finally, the current through the system in the stationary limit can be evaluated as

$$\left\langle \hat{I}_S + \hat{I}_T \right\rangle = \frac{d}{dt} \langle \hat{N} \rangle = \mathrm{Tr}_{mol}\left(\hat{N}\mathcal{L}\left[\rho_{red}^{\infty} \right] \right) = 0, \qquad (37)$$

yielding the current operator for lead η as $\hat{I}_{\eta} = \hat{N}\mathcal{L}_{\eta}$.

Transport characteristics

In this work, a tip–molecule distance of 5 Å was used and simulations were done at the temperature $T = 1$ K. We assumed a renormalization of the single particle energies $\delta_i = \delta = 1.83$ eV (cf. Equation 3), an image-charge renormalization $\delta_{ic} = 0.32$ eV and a dielectric constant $\varepsilon_r = 2.2$ in order to fit our spectrum to the experiment of Swart et al. [14], which was carried out with CuPc on a NaCl(3 ML)/Cu(100) substrate with a workfunction of $\phi_0 = 4.65$ eV. With this, we find a triplet–singlet separation of the anionic ground state of 18 meV, which is in good agreement with experimental measurements of 21 meV [8]. Numerical results for the current and the differential conductance, according to Equation 37 and using the full Hamiltonian $\hat{H}_{mol}$ in Equation 29, are shown in Figure 4. Anionic (cationic) resonances at positive (negative) bias voltages are clearly seen.
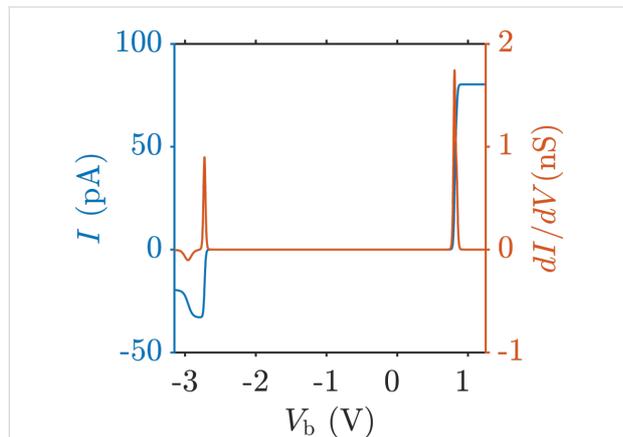
Figure 4: Current and differential conductance curves exhibiting the anionic (cationic) resonance at positive (negative) bias voltage. Note that in contrast to all other results in this work, this curve is taken at a temperature of 60 K to emphasize the resonances in the *dI/dV* curve.

Notice that, in our model, the bias voltage at which a tip-mediated transition from the *m*-th neutral state to the *n*-th anionic state of the molecule is happening is

$$V_{res,mn} = \frac{1}{\alpha_T |e|}\left(E_{N_0+1,n} - E_{N_0,m} - \delta_{ic} + \phi_0 \right), \qquad (38)$$

where e is the electron charge and α_T accounts for the fact that in STM setups the bias voltage drops asymmetrically across the junction. Electrostatic considerations yielded $\alpha_T = 0.59$ for the tip and $\alpha_S = -0.16$ for the substrate [11]. If given without indices, V_{res} denotes the bias voltage corresponding to the groundstate-to-groundstate resonance.

The negative differential conductance at large negative bias in Figure 4 is caused by blocking due to population of excited states of the molecule. This has already been discussed in a previous work [27] and will not be of further interest here.

Transport simulations at finite magnetic fields

In Figure 5 we show the splitting of the anionic resonance with applied magnetic field in a *dI/dV* map. In the upper panel SOI is switched off, whereas in the lower panel it is switched on. One striking difference at first glance is the zero-field splitting for non-vanishing SOI, which is proportional to λ_1 but enhanced by the bias drop, cf. Equation 38. For vanishing SOI, when S_z is a good quantum number, we can readily identify the corresponding transitions by using the effective spin Hamiltonian introduced in Equation 28. In the following, transitions from the neutral groundstate will be denoted by arabic numbers:

$$(1): \quad \left| N_0, \downarrow \right\rangle \rightarrow \left| T_-^- \right\rangle,$$

$$(2): \quad \left| N_0, \downarrow \right\rangle \rightarrow \left| T_+^- \right\rangle,$$

$$(3): \quad \left| N_0, \downarrow \right\rangle \rightarrow \left| T_-^0 \right\rangle,$$

$$(4): \quad \left| N_0, \downarrow \right\rangle \rightarrow \left| T_+^0 \right\rangle,$$

while transitions from the neutral excited state will be denoted by Roman numerals:

$$(i): \quad \left| N_0, \uparrow \right\rangle \rightarrow \left| T_-^0 \right\rangle,$$

$$(ii): \quad \left| N_0, \uparrow \right\rangle \rightarrow \left| T_+^0 \right\rangle,$$

$$(iii): \quad \left| N_0, \uparrow \right\rangle \rightarrow \left| T_-^+ \right\rangle,$$

$$(iv): \quad \left| N_0, \uparrow \right\rangle \rightarrow \left| T_+^+ \right\rangle.$$

Other transitions are forbidden due to the selection rule for S_z, $\Delta S_z = \pm(1/2)$. The reason for the splitting into four lines observed in the upper panel of Figure 5 is that the orbital moment of the LUMO is not of the same size as the Bohr magneton.
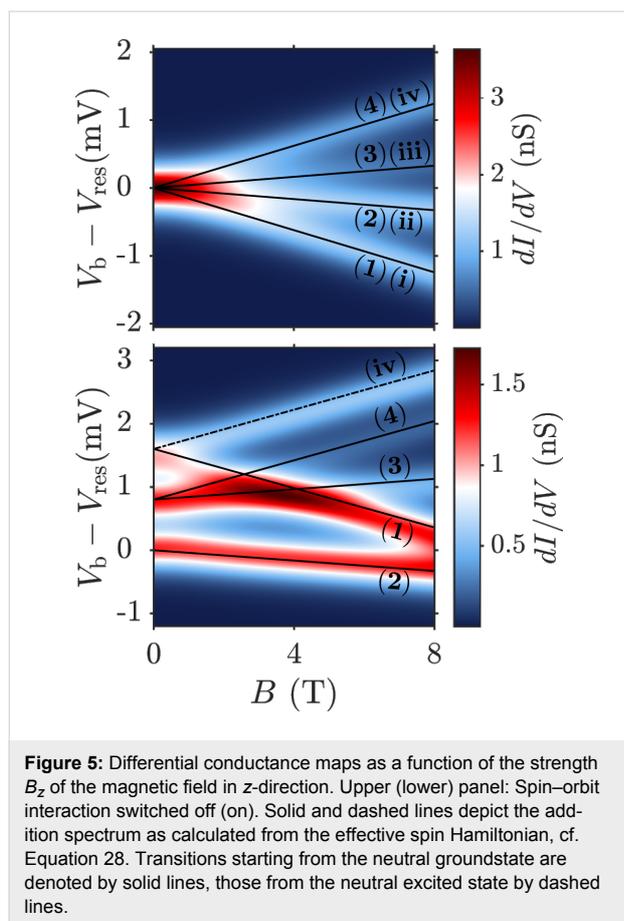
Figure 5: Differential conductance maps as a function of the strength B_z of the magnetic field in z-direction. Upper (lower) panel: Spin–orbit interaction switched off (on). Solid and dashed lines depict the addition spectrum as calculated from the effective spin Hamiltonian, cf. Equation 28. Transitions starting from the neutral groundstate are denoted by solid lines, those from the neutral excited state by dashed lines.

For non-vanishing SOI, see lower panel of Figure 5, the definite assignment of transitions is not straightforward, at least for small magnetic fields. Since $\mathbf{T}_+^-$ and $\mathbf{T}_-^+$ are shifted downward by SOI, transition (2) now is the lowest lying transition, whereas transition (1) is shifted upward due to the positive contribution $+\lambda_1$ to $\mathbf{T}_-^-$. Furthermore, transition (iv) is the only excited-state transition which can be definitely assigned to a line in the lower panel in Figure 5.

Figure 6 finally shows dI/dV maps as a function of the angle θ between the magnetic field and the z-axis. Panels (a), (b) and (c) show results obtained with vanishing SOI and panels (d), (e) and (f) are for finite SOI. Again, the results were fitted using the effective spin Hamiltonian introduced in Equation 28 with good agreement. The respective transitions can be identified by checking the assigned transitions in Figure 5 at the corresponding field strength.

Already at $|\mathbf{B}| = B = 1$ T, cf. panels (a) and (d), the influence of SOI can be clearly seen. While for vanishing SOI any anisotropy of the dI/dV map is hidden beneath the temperature broadening, for finite SOI a slight θ-dependence can be observed. For $B = 3$ T, now also in the vanishing SOI case, Figure 6b, a slight

anisotropy due to the orbital moment of the LUMOs can be observed, although still blurred by temperature. Again, at finite SOI in Figure 6e there is a much more pronounced dependence on θ. The high conductance areas at θ = 0° and θ = 180° for $V_b - V_{res} \approx 0.8$ meV correspond to the high conductance area in the middle of Figure 5 bottom, where many transitions are taking place at the same time. At $B = 8$ T, the magnetic field is dominating and a characteristic double cosine-like behaviour of the resonances can be observed, for both the case with no SOI, Figure 6c, and finite SOI, Figure 6f. For vanishing SOI, this behaviour is caused by the orbital moment of the LUMOs, since they interchange their positions when going from B_z to $-B_z$. The overall splitting between the double cosines, most evident at θ = 90°, is caused by the Zeeman term. The results for $B = 8$ T in Figure 6f at finite SOI are similar to those in Figure 6c, with the only difference that the cosine at large biases is more stretched, the one at low bias more compressed.

Conclusion

We established a model Hamiltonian for CuPc which accounts for electron–electron, spin–orbit and magnetic interactions in a minimal single particle basis represented by four frontier orbitals; the SOMO, the HOMO and two degenerate LUMOs. The distinct properties of these orbitals under rotations allowed us to deduce selection rules for matrix elements of the Coulomb interaction, which drastically reduce the number of nonvanishing terms and simplify the numerical diagonalization of the full many-body Hamiltonian. For the low-energy parts of the neutral and anionic blocks of the many-body spectrum we could further derive an effective spin Hamiltonian, capturing both SOI-induced splittings and magnetic anisotropy. Analogous Hamiltonians accounting for the effect of atomic SOI in molecular systems with orbital degeneracies have been derived for example in carbon nanotubes [31].

In order to study fingerprints of the SOI under realistic experimental conditions, we have studied the magnetotransport characteristics of a CuPc based junction in an STM setup. To this extent, a generalized master equation for the reduced density matrix associated to the full many-body Hamiltonian had to be solved in order to numerically obtain both the current and the differential conductance. Noticeably, by using the effective spin Hamiltonian, it was possible to reconstruct the nature of the many-body resonances observed in the numerical calculations.

In summary, we believe that our work significantly advances the present understanding of spin properties of CuPc. Moreover, the flexibility of our model Hamiltonian approach opens new perspectives for the investigation of other configurationally similar metallorganic compounds.

Figure 6: Differential conductance maps vs the angle θ, formed by the applied magnetic field with the *z*-axis. Left (right) panels are without (with) SOI. Upper, middle and lower panels are calculated for a magnetic field strength of 1, 3 and 8 T, respectively. Solid and dashed lines depict the addition spectrum as calculated from the effective spin Hamiltonian, cf. Equation 28. Transitions starting from the neutral groundstate are denoted by solid lines, those from the neutral excited state by dashed lines.

Supporting Information

Supporting Information File 1

Transformation from the atomic to the molecular orbital basis.
[http://www.beilstein-journals.org/bjnano/content/supplementary/2190-4286-6-254-S1.pdf]

Supporting Information File 2

Symmetries in the frontier orbitals basis.
[http://www.beilstein-journals.org/bjnano/content/supplementary/2190-4286-6-254-S2.pdf]

Supporting Information File 3

Details on the perturbative treatment of the SOI.
[http://www.beilstein-journals.org/bjnano/content/supplementary/2190-4286-6-254-S3.pdf]

Acknowledgements

References

1. Gatteschi, D.; Sessoli, R.; Villain, J. *Molecular Nanomagnets;* Oxford University Press, 2006.
2. Abragam, A.; Bleaney, B. *Electron Paramagnetic Resonance of Transition Ions;* Oxford University Press, 1970.
3. Mannini, M.; Pineider, F.; Danieli, C.; Totti, F.; Sorace, L.; Sainctavit, P.; Arrio, M.-A.; Otero, E.; Joly, L.; Cezar, J. C.; Cornia, A.; Sessoli, R. *Nature* **2010,** *468,* 417. doi:10.1038/nature09478
4. Chiesa, A.; Carretta, S.; Santini, P.; Amoretti, G.; Pavarini, E. *Phys. Rev. Lett.* **2013,** *110,* 157204. doi:10.1103/PhysRevLett.110.157204

5. Misiorny, M.; Burzurí, E.; Gaudenzi, R.; Park, K.; Leijnse, M.; Wegewijs, M. R.; Paaske, J.; Cornia, A.; van der Zant, H. S. J. *Phys. Rev. B* **2015,** *91,* 035442. doi:10.1103/PhysRevB.91.035442

6. Burzurí, E.; Gaudenzi, R.; van der Zant, H. S. J. *J. Phys.: Condens. Matter* **2015,** *27,* 113202. doi:10.1088/0953-8984/27/11/113202

7. Liao, M.-S.; Scheiner, S. *J. Chem. Phys.* **2001,** *114,* 9780. doi:10.1063/1.1367374

8. Mugarza, A.; Robles, R.; Krull, C.; Korytár, R.; Lorente, N.; Gambardella, P. *Phys. Rev. B* **2012,** *85,* 155437. doi:10.1103/PhysRevB.85.155437

9. Stepanow, S.; Mugarza, A.; Ceballos, G.; Moras, P.; Cezar, J. C.; Carbone, C.; Gambardella, P. *Phys. Rev. B* **2010,** *82,* 014405. doi:10.1103/PhysRevB.82.014405

10. Schulz, F.; Ijäs, M.; Drost, R.; Hämäläinen, S. K.; Harju, A.; Seitsonen, A. P.; Liljeroth, P. *Nat. Phys.* **2015,** *11,* 229. doi:10.1038/nphys3212

11. Siegert, B.; Donarini, A.; Grifoni, M. *arXiv* **2015,** No. 1507.05504.

12. Ryndyk, D. A.; Donarini, A.; Grifoni, M.; Richter, K. *Phys. Rev. B* **2013,** *88,* 085404. doi:10.1103/PhysRevB.88.085404

13. Repp, J.; Meyer, G.; Stojković, S. M.; Gourdon, A.; Joachim, C. *Phys. Rev. Lett.* **2005,** *94,* 026803. doi:10.1103/PhysRevLett.94.026803

14. Swart, I.; Sonnleitner, T.; Repp, J. *Nano Lett.* **2011,** *11,* 1580. doi:10.1021/nl104452x

15. Mann, J. B. *Atomic Structure Calculations I. Hartree-Fock Energy Results for the Elements Hydrogen to Lawrencium;* Los Alamos Scientific Laboratory of the University of California, 1967.

16. Slater, J. C.; Koster, G. F. *Phys. Rev.* **1954,** *94,* 1498. doi:10.1103/PhysRev.94.1498

17. Froyen, S.; Harrison, W. A. *Phys. Rev. B* **1979,** *20,* 2420–2422. doi:10.1103/PhysRevB.20.2420

18. Siegert, B.; Donarini, A.; Grifoni, M. *Phys. Status Solidi B* **2013,** *250,* 2444. doi:10.1002/pssb.201350002

19. Galassi, M.; Davies, J.; Theiler, J.; Gough, B.; Jungman, G.; Alken, P.; Booth, M.; Rossi, F. *GNU Scientific Library Reference Manual,* 3rd ed.; Network Theory Limited, 2009.

20. Bendix, J.; Brorson, M.; Schaffer, C. E. *Inorg. Chem.* **1993,** *32,* 2838–2849. doi:10.1021/ic00065a010

21. Yu, Z. G. *Phys. Rev. B* **2012,** *85,* 115201. doi:10.1103/PhysRevB.85.115201

22. Dzyaloshinsky, I. *J. Phys. Chem. Solids* **1958,** *4,* 241. doi:10.1016/0022-3697(58)90076-3

23. Moriya, T. *Phys. Rev. Lett.* **1960,** *4,* 228. doi:10.1103/PhysRevLett.4.228

24. Miyahara, S.; Fouet, J.-B.; Manmana, S. R.; Noack, R. M.; Mayaffre, H.; Sheikin, I.; Berthier, C.; Mila, F. *Phys. Rev. B* **2007,** *75,* 184402. doi:10.1103/PhysRevB.75.184402

25. Herzog, S.; Wegewijs, M. R. *Nanotechnology* **2010,** *21,* 274010. doi:10.1088/0957-4484/21/27/274010

26. Sobczyk, S.; Donarini, A.; Grifoni, M. *Phys. Rev. B* **2012,** *85,* 205408. doi:10.1103/PhysRevB.85.205408

27. Donarini, A.; Siegert, B.; Sobczyk, S.; Grifoni, M. *Phys. Rev. B* **2012,** *86,* 155451. doi:10.1103/PhysRevB.86.155451

28. Kaasbjerg, K.; Flensberg, K. *Phys. Rev. B* **2011,** *84,* 115457. doi:10.1103/PhysRevB.84.115457

29. Darau, D.; Begemann, G.; Donarini, A.; Grifoni, M. *Phys. Rev. B* **2009,** *79,* 235404. doi:10.1103/PhysRevB.79.235404

30. Koch, J.; von Oppen, F. *Phys. Rev. Lett.* **2005,** *94,* 206804. doi:10.1103/PhysRevLett.94.206804

31. Laird, E. A.; Kuemmeth, F.; Steele, G. A.; Grove-Rasmussen, K.; Nygård, J.; Flensberg, K.; Kouwenhoven, L. P. *Rev. Mod. Phys.* **2015,** *87,* 703. doi:10.1103/RevModPhys.87.703

Probing the local environment of a single OPE3 molecule using inelastic tunneling electron spectroscopy

Riccardo Frisenda[‡], Mickael L. Perrin[‡] and Herre S. J. van der Zant[*]

Abstract

We study single-molecule oligo(phenylene ethynylene)dithiol junctions by means of inelastic electron tunneling spectroscopy (IETS). The molecule is contacted with gold nano-electrodes formed with the mechanically controllable break junction technique. We record the IETS spectrum of the molecule from direct current measurements, both as a function of time and electrode separation. We find that for fixed electrode separation the molecule switches between various configurations, which are characterized by different IETS spectra. Similar variations in the IETS signal are observed during atomic rearrangements upon stretching of the molecular junction. Using quantum chemistry calculations, we identity some of the vibrational modes which constitute a chemical fingerprint of the molecule. In addition, changes can be attributed to rearrangements of the local molecular environment, in particular at the molecule–electrode interface. This study shows the importance of taking into account the interaction with the electrodes when describing inelastic contributions to transport through single-molecule junctions.

Introduction

Vibrational degrees of freedom in molecules are of crucial importance in many physical, chemical and biological processes [1,2]. In recent years, their involvement in biological processes has attracted much attention, for instance in the olfactory system [3-5] and in photosynthetic activity of chromophores [6,7]. In these systems the processes occurring at the single-molecule level are dramatically influenced by the environment. Therefore, to understand the role of vibrations, experiments that

can study the properties at the single-molecule level are very suited [8], as they do not suffer from collective effects and ensemble averaging. Different approaches have been proposed to extract the vibrational spectrum of an individual molecule, either employing optical [9-11] or electrical [12-15] measurements. Among the electrical methods, many different approaches have been employed such as current fluctuations [14], resonant transport [16,17], and inelastic electron tunneling

spectroscopy (IETS) [12,13,18-21], of which the latter is the most popular.

Figure 1a schematically depicts the IETS process, where the metallic electrodes are represented as Fermi distributions. In between these electrodes a molecule resides which is described as a Lorentzian broadened single level coupled to a vibrational mode. The molecular level is located outside the bias window, and at low bias voltage, transport via this level is elastic and off-resonant. The elastic contribution results in an approximately linear dependence of the current on the voltage, as can be seen in the upper panel of Figure 1b. When the bias voltage is larger than the vibrational mode energy $\hbar\omega/e$, an electron from the left lead can tunnel inelastically to the right lead by exciting a vibration of the molecule. In this process, the electron loses an energy $\hbar\omega$, and a phonon with the same energy is created. In the case of a small inelastic current, the vibrationally excited molecule then returns to its ground state typically before the excitation of a new vibration by a subsequent electron. The excess energy is converted to phonons in the electrodes and/or the formation of an electron–hole pair [22]. This inelastic contribution of the current leads to a kink in the

current–voltage characteristic (*IV*) at the vibrational energy, as shown in Figure 1b. However, as the ratio between the elastic and inelastic currents is large, the vibrational excitations become more evident when looking at the differential conductance (d*I*/d*V*) or the d^2I/dV^2, where they show up as steps, or peaks (dips), respectively. In this manuscript, when dealing with experimental data, we call IETS spectra the d^2I/dV^2/(d*I*/d*V*) signals calculated from the *IV* characteristics.

Here, we investigate the IETS signal of an oligo(phenylene ethynylene)dithiol molecule (OPE3) single-molecule junction at liquid helium temperature (4.2 K). Exploiting the high stability of the mechanically controlled break junction technique in cryogenic vacuum, we investigate the evolution of the junction in time. Multiple junction configurations are observed with distinct IETS spectra. In a second experiment, we monitor the IETS spectrum of a molecular junction as a function of the electrode displacement. The IETS spectra recorded at different locations display large variations among each other. A comparison with quantum chemistry calculations for different junction geometries allows for identifying some of the vibrational modes contributing to transport. Our findings suggest that the different

Figure 1: (a) Schematic of the inelastic electron tunneling spectroscopy (IETS) in a single-molecule junction. Charge transport happens through the tail of the Lorentzian broadened occupied molecular level depicted. The wiggly red line represents a molecular vibration excited after an inelastic scattering event (shown also in the right panel). (b) IETS shows up as a kink in the *IV* (upper panel), a step in the d*I*/d*V* (middle panel), and a peak in d^2I/dV^2 (lower panel). (c) Schematic illustration of the MCBJ technique. The large green arrow indicate the force to bend the sample. The small arrows illustrate the attenuated electrode displacement. The inset shows an idealized illustration of a single-molecule junction, with OPE3 trapped between the electrodes.

junction configurations are characterized by differences in the molecule–electrode interface.

Results

In our implementation of the MCBJ technique, a lithographically defined gold constriction is broken by bending the substrate in a three-point bending mechanism. Upon rupture of the gold contact, two atomically sharp electrodes are formed, of which the separation can be tuned with picometer resolution. When breaking the gold wire in the presence of OPE3, a molecule can bridge the freshly broken electrodes, as is schematically illustrated in Figure 1c. When measuring the conductance as a function of electrode displacement (a so-called breaking trace), one can distinguish two types of behavior. The left breaking trace in Figure 2a shows the typical signal of an empty junction, in which the conductance after the rupture of the last gold contact decreases exponentially with distance. This is a signature of vacuum tunneling between two metallic electrodes. Once a molecular junction is formed (junction 1, right breaking trace in Figure 2a, a plateau in the conductance is observed, in this particular case around $5 \cdot 10^{-4} G_0$ a value that matches well previous studies on OPE3 dithiol molecular junctions [23]. By increasing the distance between the electrodes, one can eventually break the molecular junction, characterized by an abrupt

drop in conductance. The high mechanical stability of the electrodes at low-temperature allows to interrupt the stretching while being on a plateau, and perform *IV* measurements.

Figure 2b shows an *IV* recorded at the position indicated by the red dot in Figure 2a. The current is linear at low bias due to the dominating elastic contribution, which is indicated by the dashed line. Above a certain voltage threshold, the current deviates as a result of an additional inelastic contribution. When numerically calculating the second derivative, peaks and dips are visible. We recorded 1200 consecutive *IV*s for the same fixed electrode position. For all these *IV*s, the low-bias conductance is calculated using a linear fit, and shown in Figure 2c as a function of time. The conductance fluctuates between $3.5 \cdot 10^{-4}$ and $6.5 \cdot 10^{-4} G_0$. Remarkably, the conductance clusters around specific values, suggesting the presence of multiple junction configurations at the same electrode separation, between which the molecule switches. About seven to eight configurations can be distinguished. To identify these, we build a conductance histogram (see right panel), in which peaks represent the most probable conductance values.

To gain more insight in the inelastic contributions to transport, we extracted the IETS spectra for the different junction configu-
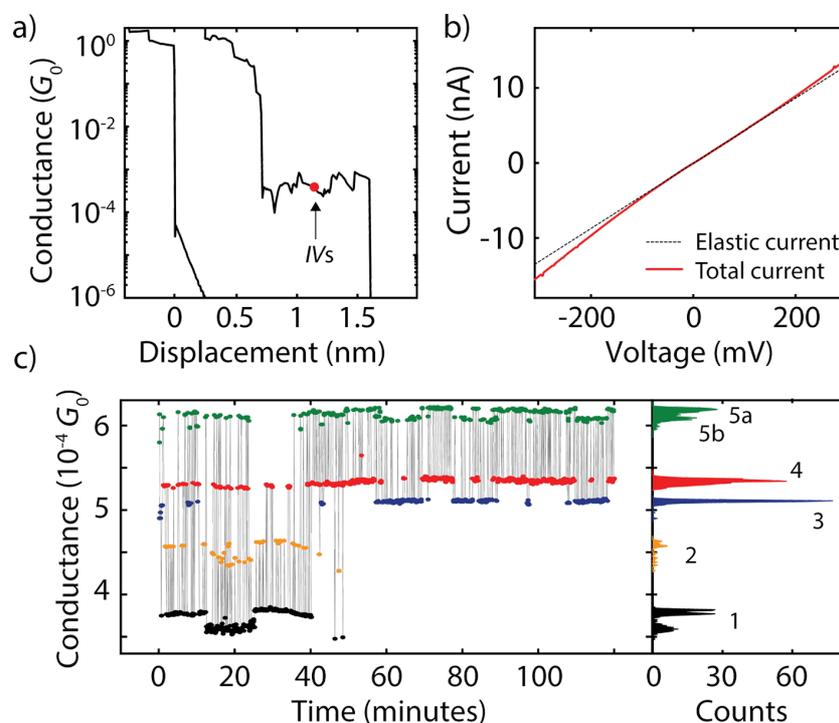
Figure 2: (a) Typical breaking traces recorded on a junction without molecule (left) and with OPE3 (right). (b) IV recorded at the location indicated by a red dot along the OPE3 plateau in (a). The dashed line represents the elastic contribution obtained from a linear fit at low-bias. (c) Low-bias conductance for the 1200 consecutive *IV*s recorded at the location indicated by a red dot along the OPE3 plateau in (a). The colors used in (c) correspond to the different junction configurations 1–5.

rations. Since the ratio between the inelastic and elastic contributions is small and bias-induced fluctuations are present [24], we employ a novel method to extract a reliable IETS signal. In our approach, we record a large number of *IV*s, from which we calculate the first and the second derivative. We then divide point by point the second derivative by the first derivative to obtain the IETS signal. To increase the signal-to-noise ratio and reduce the effect of fluctuations, we build two-dimensional histogram from all the individual IETS curves of which two examples are shown in Figure 3a. An IETS 'master-curve' signal is constructed by extracting the most probable IETS value at each bias point using a Gaussian fit. For more details about our approach, see Supporting Information File 1.

Our extracted IETS spectra exhibit both peaks and dips and a summary of the observed (antisymmetric) peak energies is presented in Table 1; the table only contains energies of peaks for which a dip at the corresponding negative bias has been observed (see Figure S3 of Supporting Information File 1). As discussed in the introduction, from theoretical considerations, vibrations show up in the IETS spectra as peak/dip pairs which should be anti-symmetric in the applied bias voltage. In the experiment however, not all peaks are anti-symmetric and for some the line shape appears to be asymmetric in bias. In literature, the lack of anti-symmetry in a IETS spectrum can be explained by an asymmetry in the contacts [25,26], leading to a shift in the peaks energy or a change in the amplitude for

Table 1: Experimental IETS peaks energies (junction 1) and theoretical vibrational modes.

exp. (mV)	DFT (meV)	description	notes
24–27	26	Au–S	
58–59	59	entire molecule	
80–85	80	in-plane ring	I
105	102	in-plane ring	II
119–122	126	in-plane ring	III
—	130	C–S	IV
180–183	183	in-plane ring	
215–220	—		
275–280	270	C≡C	

different bias polarities. Another possibility is that some of the experimental peaks/dips do not have a vibrational origin. This issue deserves further studies, both experimentally and theoretically.

In the remainder of the paper. we will discuss only peaks that can both be found at the negative and positive biases within 5 mV. In Figure 3b we show the IETS spectrum for the junction configuration 1–5 at positive bias voltages. In all five configurations peaks around 25 and 60 mV are present. For bias voltages between 60 and 140 mV, four peaks are visible (numbered I–IV in Figure 3b), of which the position and ampli-

Figure 3: (a) Two-dimensional histograms of two configurations built from the individual spectra measured on OPE3. The histograms are built from all the individual second derivative traces by binning the x-axis with 600 bins/V and the y-axis with 12 bins/(1/V). (b) Master-curves of the spectra for the five junction configurations extracted from the two-dimensional histograms. The colors used in (b) correspond to the different junction configurations 1–5.

tude depend on the junction configuration. In addition, a few dips are present. In the bias range of 140 to 300 mV, all junctions show a peak around 180 mV. Junction 1–2 then show a strong noise for biases larger than 200 mV. For junction 3–5, this noise is not as pronounced and peaks can be distinguished at 220 and 275 mV.

In the measurements presented previously, different IETS spectra were recorded due to switches between different configurations, while the electrode separation was being kept constant. In the following, we investigate the influence of the displacement on the IETS spectra on a different single-molecule junction (junction 2). We started from the metallic regime (conductance > 20G_0) and after having broken the gold quantum point contact we formed a molecular junction. During the stretching of this junction, for each electrode position, 250 *IV*s were recorded and the IETS master-curve was extracted. In between two IETS spectra, the electrode separation was increased by 6 pm. The top panel of Figure 4a shows the conductance breaking trace extracted from a linear fit of the *IV*s at low bias. The plateau in conductance indicates the formation of the single-molecule junction. Continuous regions are observed and separated by steps, which are attributed to stress-releasing rearrangements of the molecular junction.

In the lower panel of Figure 4a we present the IETS spectra as a function of stretching as a color map. Peaks and dips are present in the IETS spectra, as observed previously. Along the continuous conductance regions, the features evolve smoothly with small changes in position and amplitude. In contrast, large differences are present between different regions, with

pronounced rearrangements of the peaks and the dips. This becomes evident from Figure 4b, in which one spectrum is presented for each continuous conductance region. We note that for the second and fourth region, the low-bias conductance is similar, but the IETS spectra are different. This shows that junctions with similar low-bias conductance can have different IETS spectra and overall, the measurement point to a large dependence of the IETS features on the local environment. A similar conclusion has been drawn by Ward et al. for the Raman response of single-molecule junctions [27], in which spectral diffusion and blinking were reported.

To relate the peaks in the IETS spectra to the vibrational modes, we used the Amsterdam Density Functional (ADF) package and performed density function theory (DFT) calculations of the OPE3 molecular junction. All calculations were optimized using a TZP Slater-type orbital local basis-set and the PBE GGA functional. We stretch the molecular junction starting from the configuration shown in the left panel of Figure 5a (for more details see Supporting Information File 1). During the stretching of the junction, we observe continuous regions where the stress accumulates (see Figure S4 of Supporting Information File 1), separated by events in which the molecule typically switches between binding sites on the electrodes. This can explain the switches in the conductance plateau of Figure 4a and, as we have seen, the IETS spectrum show large variation before and after the jump.

The middle and right panel of Figure 5a show two typical geometries obtained during the stretching. In the first geometry (19.40 Å), in addition to the usual Au–S covalent bond, the
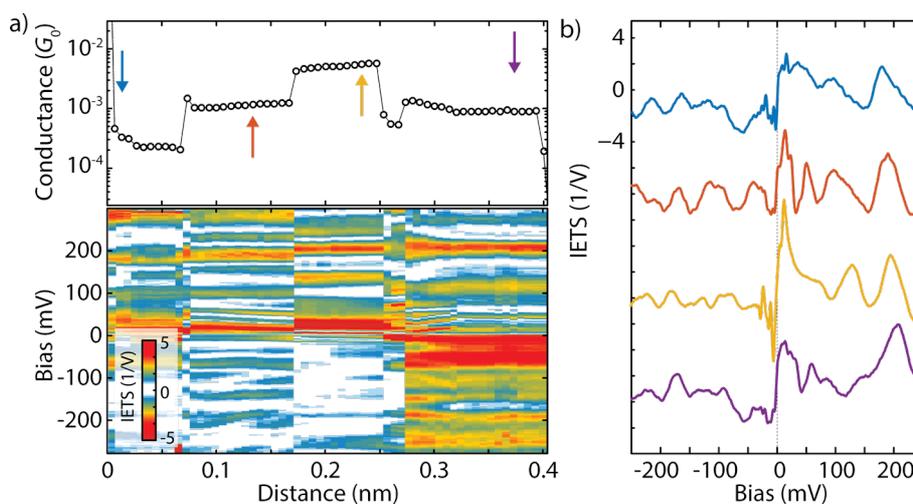
Figure 4: (a) Low-bias conductance trace recorded during the stretching of an OPE3 single-molecule junction (top) and color-map representing the IETS signal upon stretching (bottom). (b) Extracted IETS master-curves at the positions indicated by the arrows in (a). Note that not all peaks/steps are visible in the color-map for this choice of contrast.
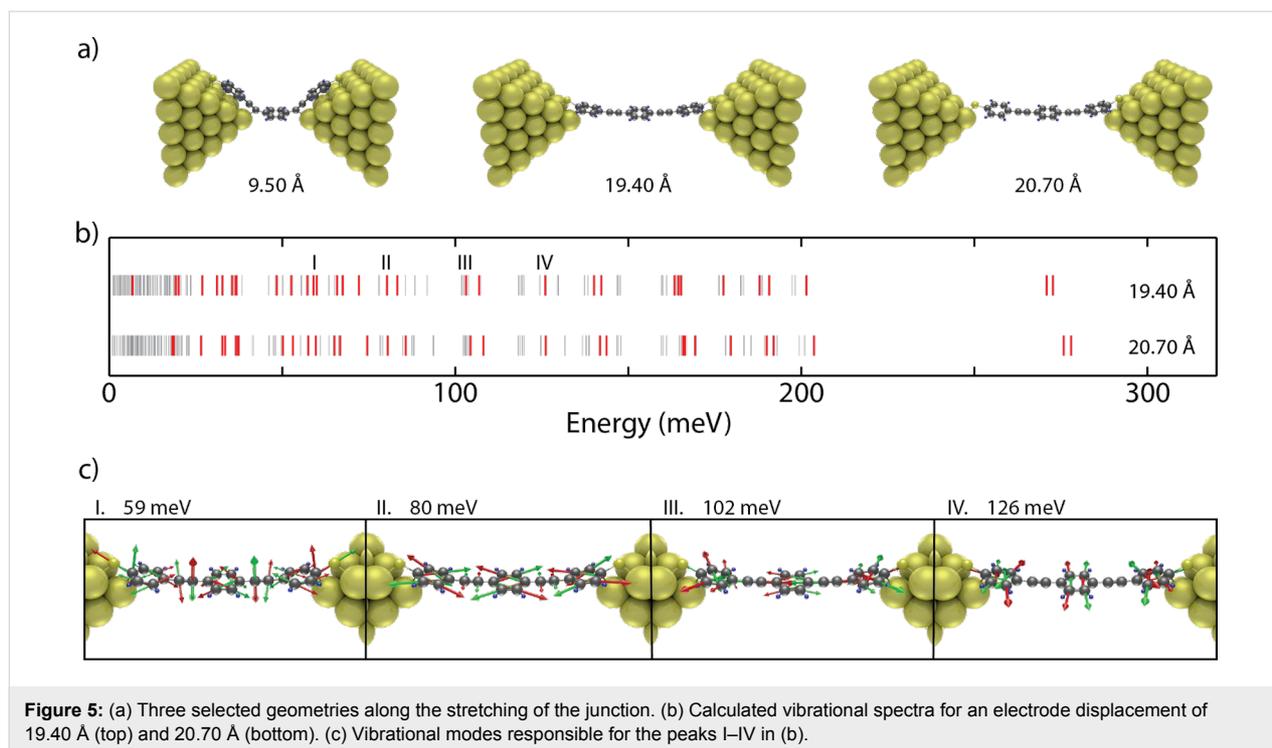
Figure 5: (a) Three selected geometries along the stretching of the junction. (b) Calculated vibrational spectra for an electrode displacement of 19.40 Å (top) and 20.70 Å (bottom). (c) Vibrational modes responsible for the peaks I–IV in (b).

molecule interacts on both sides with the outer phenyl rings. In the second geometry (20.70 Å), the molecule is more extended and interacts only on one side with the outer ring, while on the other side the binding occurs through the sulphur atoms. For the two geometries we calculated the frequency spectrum, as shown with lines in Figure 5b. Some of those modes are expected to couple to transport. Due to the lack of selection rules (in contrast to infrared and Raman scattering processes), we highlight in red the modes that are expected to contribute to transport, based on the propensity rules proposed by Troisi and Ratner [28]. In the OPE3 spectrum, many modes are expected to couple to transport due to their symmetry and their modulation of the π-system. Comparing the two geometries, we notice that for the largest separation, some modes shift towards higher energies, an indication of the stretching of the molecule.

Comparing the experimental modes with the calculated energies, the following observations can be made: some of the vibrational modes (183 and 270 meV) correspond to modes reported in literature [28,29] and are known to couple to transport. These originate from the phenyl rings and the ethynyl (C≡C) triple bonds, respectively. In the experiments, we observe peaks in the spectra around the energies of those modes. The peak around 180 mV is observed in all configurations, and attributed to vibrational modes involving the center and outer phenyl rings. In configuration 1–2, noise appears for bias voltage larger that 220 mV and seems to correspond with the onset of an additional contribution to the noise. In configur-

ation 3–5, this noise contribution is less pronounced and a peak around 275 mV is observed, which matches the calculated mode of the stretching of the ethynyl bond (C≡C). We also note the presence in all configurations of a peak around 25 meV, which corresponds to vibrations involving the Au–S bonds. The modes discussed above constitute a chemical fingerprint of the molecule in the junction, and are consistent with previous experiments on large-area OPE3 junctions [29] and theoretical predictions [30,31]. We would like to stress that, although we attributed each peak to a single vibrational mode, in the experiments, the peaks may originate from multiple modes that are located closely together, as can be seen in the DFT spectrum. The peak at 215–220 mV is not identified in the calculations. This may be due to contaminants close to the molecular junction, and/or overtones of lower energy modes.

In contrast to the modes mentioned above, the experimental modes labeled with Roman numbers in Table 1 and Figure 2 are present with different intensities and/or different energies. These modes are located between 80 and 120 meV and interestingly, they are mostly related to in-plane ring modes. This could indicate that one or more phenyl rings interact differently with the metallic electrode and that the molecule–metal interface plays a large role in determining the IETS spectra. Thus, next to constituting the chemical fingerprint of the molecule, the IETS spectra contain additional information about the molecular geometry in the junction. Altogether, the changes in the spectra may be related to small changes in the molecular geometry at

the interface between the molecule and the metallic electrodes or in the electronic configuration.

Finally, to investigate the switching dynamics of OPE3 between the different configurations (1–5) we recorded the conductance of junction 1 as a function of time (see Figure 6a). The traces have been acquired at a rate of 400 Hz for bias voltages ranging from 0.14 to 0.24 V. For clarity, the consecutive traces have been offset by 7 nA. For bias voltages below 0.14 V, the current does not change over time, for example at 0.14 V the average current is 2.4 nA. At 0.16 V, a switch is observed around 4 s to a higher value and then it switches back to the original values shortly thereafter. For increasing voltage, the switching behavior becomes more frequent, resembling telegraph noise. This points to a two-level system characterized by two different conductance values [32]. By comparing the conductance values with the different configurations obtained in Figure 2c, we identify the low-conductance state as configuration 3 and the high-conductance state as 5a. Following the reasoning obtained from the IETS spectra, the two-level fluctuations may be caused by the different configurations. Finally, we notice that for bias voltages higher than 0.20 V, some of the two-level fluctuations involve configurations 4 and 5b, and four levels of current are present. In conclusion we observed fluctuations induced by the bias voltage, two-level switching between 3 and 5a, above 0.16 V, and four-level switching between 3, 4, 5a and 5b, above 0.22 V.

Conclusion

In conclusion, we studied the IETS spectra of OPE3 single-molecule junctions, both as a function of time and electrode separation. We find that the IETS spectra depend heavily on the junction geometry and are sensitive to the local molecular envi-ronment. We compared our results to quantum chemistry calculations for the molecule sandwiched between gold electrodes and identified some of the peaks in the experimental spectra. Finally, current versus time traces for different bias voltages reveal an interesting interplay between bias voltage and current fluctuations caused by different molecular configurations. Our findings provide a way to gain additional information regarding the molecule–electrode interaction, in particular, the interesting interplay between molecular conformation, vibrations and charge transport.

Supporting Information

Supporting Information File 1

Additional experimental data.
[http://www.beilstein-journals.org/bjnano/content/
supplementary/2190-4286-6-257-S1.pdf]

Acknowledgements

References

1. Lambert, N.; Chen, Y.-N.; Cheng, Y.-C.; Li, C.-M.; Chen, G.-Y.; Nori, F. *Nat. Phys.* **2013,** *9,* 10–18. doi:10.1038/nphys2474
2. Zimbovskaya, N. A.; Pederson, M. R. *Phys. Rep.* **2011,** *509,* 1–87. doi:10.1016/j.physrep.2011.08.002
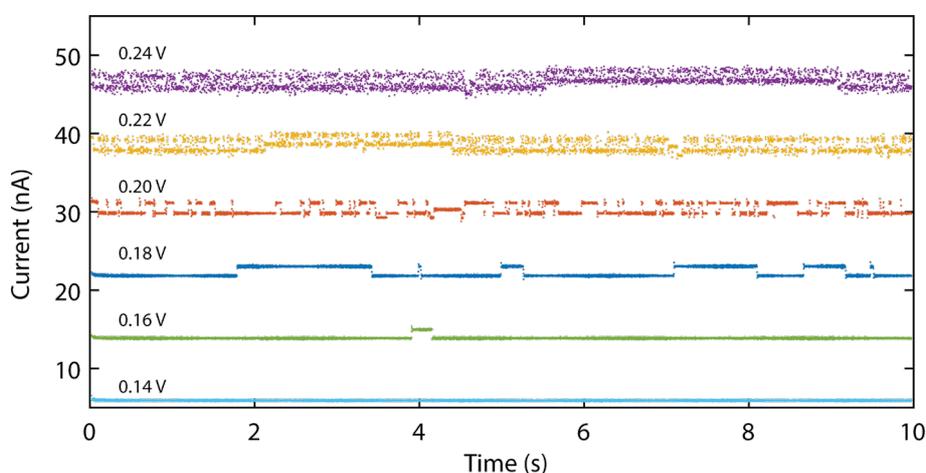
Figure 6: Current versus time traces acquired at bias voltages varying between 0.14 and 0.24 V. The traces have been offset vertically by 7 nA for clarity. Notice the increase in switching rate for higher bias voltages.

3. Turin, L. *Chem. Senses* **1996,** *21,* 773–791.
doi:10.1093/chemse/21.6.773

4. Franco, M. I.; Turin, L.; Mershin, A.; Skoulakis, E. M. C.
Proc. Natl. Acad. Sci. U. S. A. **2011,** *108,* 3797–3802.
doi:10.1073/pnas.1012293108

5. Gane, S.; Georganakis, D.; Maniati, K.; Vamvakias, M.; Ragoussis, N.;
Skoulakis, E. M. C.; Turin, L. *PLoS One* **2013,** *8,* e55780.
doi:10.1371/journal.pone.0055780

6. Chin, A. W.; Prior, J.; Rosenbach, R.; Caycedo-Soler, F.; Huelga, S. F.;
Plenio, M. B. *Nat. Phys.* **2012,** *9,* 113–118. doi:10.1038/nphys2515

7. Fuller, F. D.; Pan, J.; Gelzinis, A.; Butkus, V.; Senlik, S. S.;
Wilcox, D. E.; Yocum, C. F.; Valkunas, L.; Abramavicius, D.;
Ogilvie, J. P. *Nat. Chem.* **2014,** *6,* 706–711. doi:10.1038/nchem.2005

8. Aradhya, S. V.; Venkataraman, L. *Nat. Nanotechnol.* **2013,** *8,* 399–410.
doi:10.1038/nnano.2013.91

9. Ward, D. R.; Corley, D. A.; Tour, J. M.; Natelson, D. *Nat. Nanotechnol.*
2011, *6,* 33–38. doi:10.1038/nnano.2010.240

10. Liu, Z.; Ding, S.-Y.; Chen, Z.-B.; Wang, X.; Tian, J.-H.; Anema, J. R.;
Zhou, X.-S.; Wu, D.-Y.; Mao, B.-W.; Xu, X.; Ren, B.; Tian, Z.-Q.
Nat. Commun. **2011,** *2,* 305. doi:10.1038/ncomms1310

11. Yampolsky, S.; Fishman, D. A.; Dey, S.; Hulkko, E.; Banik, M.;
Potma, E. O.; Apkarian, V. A. *Nat. Photonics* **2014,** *8,* 650–656.
doi:10.1038/nphoton.2014.143

12. Stipe, B. C.; Rezaei, M. A.; Ho, W. *Science* **1998,** *280,* 1732–1735.
doi:10.1126/science.280.5370.1732

13. Smit, R. H. M.; Noat, Y.; Untiedt, C.; Lang, N. D.; van Hemert, M. C.;
van Ruitenbeek, J. M. *Science* **2002,** *419,* 906–909.
doi:10.1038/nature01103

14. Tsutsui, M.; Taniguchi, M.; Kawai, T. *Nat. Commun.* **2010,** *1,* No. 138.
doi:10.1038/ncomms1141

15. Kim, Y.; Song, H.; Strigl, F.; Pernau, H.-F.; Lee, T.; Scheer, E.
Phys. Rev. Lett. **2011,** *106,* 196804.
doi:10.1103/PhysRevLett.106.196804

16. Frederiksen, T.; Franke, K. J.; Arnau, A.; Schulze, G.; Pascual, J. I.;
Lorente, N. *Phys. Rev. B* **2008,** *78,* 233401.
doi:10.1103/PhysRevB.78.233401

17. Franke, K. J.; Pascual, J. I. *J. Phys.: Condens. Matter* **2012,** *24,*
394002. doi:10.1088/0953-8984/24/39/394002.

18. Persson, B. N. J.; Baratoff, A. *Phys. Rev. Lett.* **1987,** *59,* 339.
doi:10.1103/PhysRevLett.59.339

19. Hihath, J.; Arroyo, C. R.; Rubio-Bollinger, G.; Tao, N.; Agraït*, N.
Nano Lett. **2008,** *8,* 1673–1678. doi:10.1021/nl080580e

20. Song, H.; Kim, Y.; Jang, Y. H.; Jeong, H.; Reed, M. A.; Lee, T. *Nature*
2009, *462,* 1039. doi:10.1038/nature08639

21. Arroyo, C. R.; Frederiksen, T.; Rubio-Bollinger, G.; Vélez, M.;
Arnau, A.; Sánchez-Portal, D.; Agraït, N. *Phys. Rev. B* **2010,** *81,*
075405. doi:10.1103/PhysRevB.81.075405

22. Persson, B. N. J.; Ueba, H. *Surf. Sci.* **2002,** *502,* 18–25.
doi:10.1016/S0039-6028(01)01893-3

23. Frisenda, R.; Perrin, M. L.; Valkenier, H.; Hummelen, J. C.;
van der Zant, H. S. J. *Phys. Status Solidi B* **2013,** *250,* 2431–2436.
doi:10.1002/pssb.201349236

24. Gaudioso, J.; Lauhon, L. J.; Ho, W. *Phys. Rev. Lett.* **2000,** *85,*
1918–1921. doi:10.1103/PhysRevLett.85.1918

25. Galperin, M.; Nitzan, A.; Ratner, M. A.; Stewart, D. R. *J. Phys. Chem. B*
2005, *109,* 8519–8522. doi:10.1021/jp0457500

26. Härtle, R.; Volkovich, R.; Thoss, M.; Peskin, U. *J. Chem. Phys.* **2010,**
133, 081102. doi:10.1063/1.3474464

27. Ward, D. R.; Halas, N. J.; Ciszek, J. W.; Tour, J. M.; Wu, Y.;
Nordlander, P.; Natelson, D. *Nano Lett.* **2008,** *8,* 919–924.
doi:10.1021/nl073346h

28. Troisi, A.; Ratner, M. A. *J. Chem. Phys.* **2006,** *125,* 214709.
doi:10.1063/1.2390698

29. Kushmerick, J. G.; Lazorcik, J.; Patterson, C. H.; Shashidhar, R.;
Seferos, D. S.; Bazan, G. C. *Nano Lett.* **2004,** *4,* 639–642.
doi:10.1021/nl049871n

30. Troisi, A.; Ratner, M. A. *Phys. Rev. B* **2005,** *72,* 033408.
doi:10.1103/PhysRevB.72.033408

31. Paulsson, M.; Frederiksen, T.; Brandbyge, M. *Nano Lett.* **2006,** *6,*
258–262. doi:10.1021/nl052224r

32. Thijssen, W. H. A.; Djukic, D.; Otte, A. F.; Bremmer, R. H.;
van Ruitenbeek, J. M. *Phys. Rev. Lett.* **2006,** *97,* 226806.
doi:10.1103/PhysRevLett.97.226806

License and Terms

Effects of electronic coupling and electrostatic potential on charge transport in carbon-based molecular electronic junctions

Richard L. McCreery

Abstract

Molecular junctions consisting of 2–20 nm thick layers of organic oligomers oriented between a conducting carbon substrate and a carbon/gold top contact have proven to be reproducible and reliable, and will soon enter commercial production in audio processing circuits. The covalent, conjugated bond between one or both sp^2-hybridized carbon contacts and an aromatic molecular layer is distinct from the more common metal/molecule or silicon/molecule structures in many reported molecular junctions. Theoretical observations based on density functional theory are presented here, which model carbon-based molecular junctions as single molecules and oligomers between fragments of graphene. Electronic coupling between the molecules and the contacts is demonstrated by the formation of hybrid orbitals in the model structure, which have significant electron density on both the graphene and the molecule. The energies of such hybrid orbitals correlate with tunneling barriers determined experimentally, and electronic coupling between the two graphene fragments in the model correlates with experimentally observed attenuation of transport with molecular layer thickness. Electronic coupling is affected significantly by the dihedral angle between the planes of the graphene and the molecular π-systems, but is absent only when the two planes are orthogonal. Coupling also results in partial charge transfer between the graphene contacts and the molecular layer, which results in a shift in electrostatic potential which affects the observed tunneling barrier. Although the degree of partial charge transfer is difficult to calculate accurately, it does provide a basis for the "vacuum level shift" observed in many experiments, including transport and ultraviolet photoelectron spectroscopy of molecular layers on conductors.

Introduction

The field of Molecular Electronics investigates the behavior of molecules as elements in electronic circuits, with the intent of exploiting variations of molecular structure to realize unusual electronic functions [1-4]. Charge transport through single molecules and through ensembles of molecules in nanoscale (1–20 nm) films has been studied experimentally since the late

1990s, with particular interest in how structure affects transport. The experimental paradigms are numerous [1,5], but they all share a common phenomenon of electrical communication between molecules and "contacts" made from conventional conductors or semiconductors. An extensive theoretical effort has accompanied the experiments [6-12], with one objective being a rational design of particular molecular structures to realize desirable electronic responses. The driving force for the field is the possibility of electronic components that are smaller than existing transistors or diodes, have unusual properties not possible with conventional semiconductors, use less power, or are cheaper than existing microelectronics. A basic element of Molecular Electronics is the "molecular junction (MJ)" consisting of molecules oriented between two conductors, with charge transport through the molecular layer. The vast majority of existing junction structures are based on metal/molecule bonding such as the Au/thiol self-assembled monolayers [13-21], Langmuir–Blodgett films on metals [22,23], or molecules bonded to silicon [24-27].

Our research group has developed a distinct approach based on conducting carbon substrates with covalently bonded molecular layers applied by reduction of diazonium reagents [2,28-33]. The strong carbon–carbon bonds result in thermally stable MJs (−260 to +350 °C), which operate for billions of continuous current–voltage cycles over a period of several months, and have a shelf life of at least seven years in air. The sp^2 carbon substrate and aromatic molecular layer introduce a special property into carbon-based MJs, in that they contain a covalent, conjugated "contact" between two aromatic π-systems. The reproducibility, reliability, and operating life of carbon-based MJs resulted in an application in audio processing of electronic music, available commercially in 2015 as an accessory for electric guitars. The fundamental structural difference between metal/molecule and carbon/molecule MJs is expected to result in possibly significant differences in electronic behavior. In particular, the electronic interactions between the molecules and the contacts might be quite different, leading to changes in transport barriers and junction conductance [2,34,35]. A consequence of electrode/molecule interactions is that "vacuum level shifts" can change the transport barriers significantly from those based on the free molecule energy levels [14,31,36-40]. An unexpected result likely due to this effect is the "compression" of tunneling barriers predicted to range over 2.4 eV based on the free molecule energy levels to an observed range of 1.3 ± 0.2 eV in carbon-based MJs [31,34]. The current report describes the application of density functional theory (DFT) to carbon-based MJs, in order to investigate which aspects of junction behavior are attributable to the unique carbon–carbon bonding at one or both contacts of the molecular junction.

A simple model based on single molecules and oligomers bonded to small graphene fragments representing the sp^2 carbon contacts provides insights into how electronic interactions between the molecules and the contacts affect tunneling barriers and local electrostatic potential. The approach is an extension of a detailed theoretical analysis of graphene/molecule interfaces [34], with the addition of a second sp^2 carbon conducting contact. Although real carbon-based MJs are structurally complex, the simple model yields significant correlations between theoretical predictions and experimental observations. In particular, four general questions are considered to evaluate the model: First, how does bonding between the carbon contact and the molecular layer alter the orbital energies and electron distributions? Second, does the calculated electronic coupling across the carbon MJ correlate with the observed junction conductance? Third, how does charge transfer between the graphene contacts and molecular layers affect the transport barriers? Fourth, can the model predict the behavior of carbon MJs to provide guidance for molecule synthesis and junction fabrication? Throughout the discussion, the main purpose is identification of the major factors affecting the electronic behavior of the completed carbon/molecule/carbon MJ, in addition to quantitative correlations with experimental results where possible.

Experimental

Common DFT procedures were used, in part to maximize availability to potential users. Gaussian09 version 9.5 (revision D.01 Windows 64 bit) and Gaussview 5.0.9 software packages were used for all calculations and visualization of molecular structures and orbitals, using the B3LYP functionals and 6-31G(d) basis set unless stated otherwise. Although we have reported more sophisticated treatments with significant computational demands [34], the calculations reported here were carried out with a Pentium 4-processor desktop computer. The B3LYP functionals were used in the current report rather than the BLYP functionals used previously, partly because B3LYP is generally more accurate, but also because it was not available for the more complex models in the previous work. In most cases the maximum computing time was a few hours using the multiprocessor version of Gaussian09 for Windows. Orbital visualization with Gaussview used the default isovalue of 0.02, which is commonly used to represent the majority of the electron density. Predictions of charge transfer within model molecules used the Mulliken charges calculated during the DFT analysis. There is some uncertainty about the most accurate calculations of local charges [41], but the trends are consistent with electronegativity and Hammet parameters, and are useful for estimating electrostatic effects on barriers, as described below.

The model

The molecules subjected to DFT analysis are shown in Figure 1, for the case of an azobenzene (AB) molecule covalently bonded to an edge site in a 9-ring graphene fragment, denoted "G9". We described the rationale for investigating edge-bonding previously [2,34,42,43], and it is the most likely site in real devices. Since the carbon surface is disordered and the molecular layers are often multilayers, the real system will have a range of dihedral angles between the molecular aromatic rings and those of the graphene. The important effect of this dihedral angle will be discussed below. The choice of a "corner" site rather than the more common "armchair" and "zig-zag" sites reduces steric hindrance at the molecule–G9 bonding site. In a detailed discussion of the bonding site with higher level theory, we showed that the site type had a much smaller effect on tunneling barriers than the dihedral angle [34]. The corner site shown in Figure 1c and Figure 1d will be used in all calculations and figures unless noted otherwise.

Also shown in Figure 1 are the highest occupied molecular orbitals (HOMO) and lowest unoccupied molecular orbitals (LUMO) for G9 and AB. In all cases, the orbital energies are stated relative to a vacuum reference, consistent with commonly used conventions, including that of Gaussian09 software.

Whenever the parameters for a planar molecular configuration are calculated, the molecule was first optimized, then the dihedral angles between the π-system of the molecule and the G9 plane were set to zero and the orbital energies recalculated. The discussion starts with consideration of the effects of covalent bonding between the graphene "contact" and the aromatic molecule in the molecular layer.

Results and Discussion
1 Orbital energies and electron distribution

Given that both the molecular layer and the graphitic contact are aromatic π-systems, there likely are significant electronic interactions between the two, which should alter the electron distribution and energies compared to the separated molecule and contact. Figure 2 shows the energies of orbitals near the HOMO and LUMO for G9, AB, and the G9–AB combination.

The electron density distributions for selected orbitals are also shown, all for the case of the optimized geometry, which has a dihedral angle between the G9 plane and the AB phenyl ring of 37°. The G9 orbitals are not shown, but they all have the general appearance of the HOMO and LUMO shown in Figure 1, with extensive delocalization over the nine benzene rings. The orbitals of the G9–AB combination in the right side
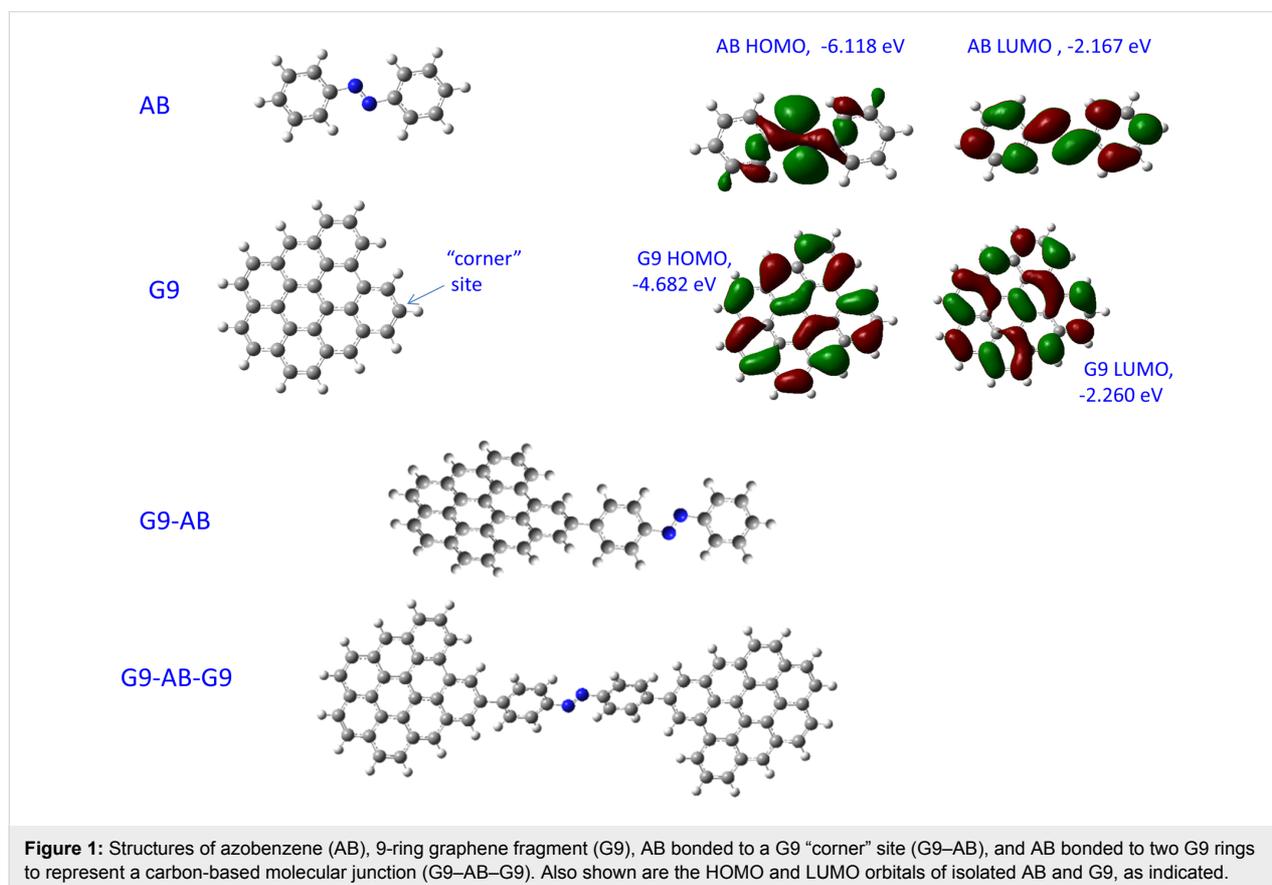
Figure 1: Structures of azobenzene (AB), 9-ring graphene fragment (G9), AB bonded to a G9 "corner" site (G9–AB), and AB bonded to two G9 rings to represent a carbon-based molecular junction (G9–AB–G9). Also shown are the HOMO and LUMO orbitals of isolated AB and G9, as indicated.
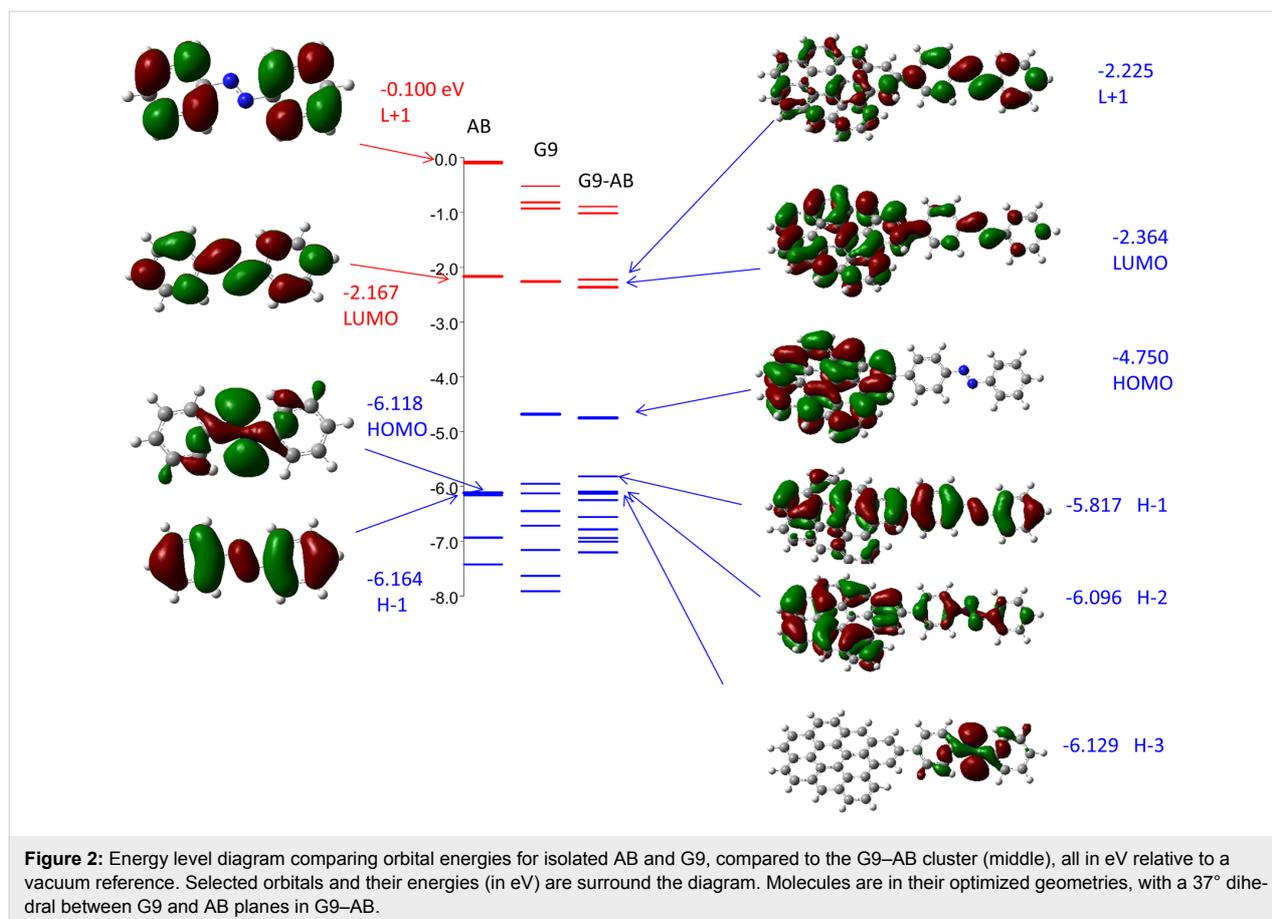
Figure 2: Energy level diagram comparing orbital energies for isolated AB and G9, compared to the G9–AB cluster (middle), all in eV relative to a vacuum reference. Selected orbitals and their energies (in eV) are surround the diagram. Molecules are in their optimized geometries, with a 37° dihedral between G9 and AB planes in G9–AB.

of Figure 2 provide clear indications that there are significant interactions between the orbitals of G9 and AB molecules upon covalent bond formation. We will refer to orbitals of G9–AB (and later G9–AB–G9) as "system orbitals", since they often differ significantly from the orbitals of the free AB and G9 molecules. The system L+1, LUMO, H−1 and H−2 orbitals all show shared electron density across both G9 and AB, while the system HOMO at −4.75 eV is localized on G9 and has an energy close to that of the free G9 HOMO (−4.75 eV). The system H−3 orbital resembles the original AB HOMO, and is localized on the AB molecule in the G9−AB system. It is important to note here that the system H−1 and H−2 orbitals are "hybrid" orbitals formed when the AB is bonded to the G9 cluster. G9–AB is a different molecule from the individual components, and permits delocalization not possible in the free molecules. The system HOMO and H−3 could be considered remnants of the corresponding orbitals in the free molecules, but H−1 and H−2 are characteristic only of the G9–AB system. The importance of these orbitals to transport in an AB molecular junction will be considered below.

Since the G9 aromatic systems and the AB phenyl rings are conjugated and covalently bonded, we expect that the degree of

interaction between the two π-systems should depend on the dihedral angle between the G9 plane and the AB rings. Figure 3 shows the HOMO and H−1 orbitals for G9–AB with five dihedral angles, along with their energies. Additional orbital energies are listed in Table 1. As expected, the degree of delocalization varies significantly with dihedral angle, becoming larger as the dihedral angle approaches zero. Two additional observations are important to subsequent discussions about transport and energy barriers. First, the HOMO is localized nearly completely on the G9 fragment, and is largely unaffected by the dihedral angle, with its energy varying by 33 meV between 0 and 90° dihedrals. In contrast, the H−1 orbital is delocalized over both G9 and AB fragments, and has a much larger dependence on dihedral, with a range of 256 meV. Second, the sum of the Mulliken charges on the AB moiety of G9–AB is negative, indicating partial charge transfer between the G9 and AB portions of the G9–AB system. The extent of charge transfer varies with angle, from 0.8% of an electron to 2.2% as the dihedral angle is decreased from 90 to 0°.

This small degree of charge transfer should not be considered "reduction" in the electrochemical sense, but rather a redistribution of charge due to the different electronegativity of portions

Figure 3: HOMO and H−1 orbitals for G9–AB for a range of dihedral angles between the G9 plane and AB aromatic rings, indicated at left. Orbital energies for all orbitals are indicated in blue, while the sum of the Mulliken charges on the AB moiety is indicated in red. A negative Mulliken charge indicates partial electron transfer from G9 to AB upon forming the covalent G9–AB cluster.

Table 1: Orbital energies for G9, azobenzene (AB) and G9–AB.

molecule	dihedral angle[a], °	stability, eV[b]	LUMO, eV	HOMO, eV	H−1, eV	H−2, eV	charge on AB[c]
free AB			−2.167	−6.118	−6.164	−6.935	
free G9			−2.260	−4.682	−5.950	−6.126	
G9–AB	0	0.124	−2.401	−4.761	−5.729	−6.102	−0.022
	20	0.050	−2.390	−4.758	−5.757	−6.100	−0.020
	37.3	0.000	−2.364	−4.750	−5.818	−6.096	−0.016
	45	0.010	−2.351	−4.745	−5.849	−6.095	−0.014
	65	0.073	−2.321	−4.735	−5.934	−6.103	−0.010
	75	0.108	−2.317	−4.731	−5.967	−6.117	−0.0088
	90	0.128	−2.309	−4.728	−5.984	−6.146	−0.0084

[a]Between G9 and AB planes; [b]relative to optimized structure (37.3° dihedral angle); [c]total Mulliken charge on AB moiety.

of the entire molecule. For example, similar calculations for G9 attached to different molecules show charge transfer ranging from 0.0005 e− for G9–biphenyl to 0.049 e− for G9–nitrophenyl. Although the predicted charge transfer is small, it has significant consequences, as discussed below in section 3.

We have reported various top contacts for MJs with carbon substrates, including Cu [31,33,35], TiO$_2$ [44-46], Si [47], and e-beam deposited carbon (eC) [30,43]. The "all-carbon molecular junction" is of particular interest, since it is more stable than Cu toward voltage and temperature extremes and is less

prone to electromigration and oxidation than most metals [43]. The covalent bond between an sp²-hybridized carbon substrate and the aromatic molecular layer represented by the G9–AB model structure is well characterized, but the nature of the "contact" between the top eC layer and the molecular layer in all carbon MJs is currently unknown. We showed that the Raman spectrum of the molecular layer is not significantly altered by eC/Au deposition [43], but a covalent bond is likely to form given the reactivity of carbon atoms and clusters generated in an e-beam source. With these caveats in mind, consider the G9–AB–G9 model structure shown in Figure 1, which represents an idealized structure of a single AB molecule covalently bonded to two graphene fragments. The orbital energies for an optimized G9–AB–G9 molecule having 37° dihedral angles between the AB plane and the G9 rings are shown in Figure 4, along with the electron distributions of several orbitals.

Note that the HOMO and H−1 orbitals of G9–AB–G9 have energies close to that of free G9, and that the electron density is localized on the graphene fragments. The H−2 orbital of G9–AB–G9 is analogous to H−1 for G9–AB, and has electron density that extends across the AB molecule and onto both G9 fragments. Figure 5 shows the effect of dihedral angles in the G9–AB–G9 system, with the HOMO, H−1 and H−2 orbitals shown when both dihedral angles are 0° to make a fully planar geometry, and both are 90°, for comparison to the 36°and 39° angles in the optimized case of Figure 4. Note that the G9 rings are coplanar in all cases, and the AB molecule rotates relative to this common plane as the dihedral angle is increased. Not surprisingly, the delocalization across the entire molecule for H−2 is absent when the AB and G9 rings are orthogonal. Note also that the H−2 energy varies by 400 meV as the dihedral angle increases from 0 to 90°.

2 Electronic coupling across the molecular layer

A primary motive for considering the G9–AB and G9–AB–G9 model structures is the ability to predict electronic coupling between the contacts and the molecules. Electronic coupling is a factor in most treatments of electron transfer, including Marcus theory, tunneling between two sites, and transport through numerous sites in the "tight binding" models of conducting solids. In all three cases, stronger electronic coupling increases

Figure 4: Orbitals for G9–AB–G9 added to the orbital energy diagram of Figure 2. All structures are presented in their optimized geometry, with dihedral angles between AB and G9 of 36 and 39°.

Figure 5: Effect of dihedral angle on orbital electron distributions in G9–AB–G9. In the 0° case, the G9s and AB are coplanar, while in the 90° case the G9s are coplanar but the AB plane is perpendicular to both G9s. Orbital energies are shown below each structure, in eV.

the electron transfer and/or the conductance relevant to the chemical system considered. These theories will not be reviewed here, but all contain a factor for electronic coupling, often denoted "*t*", or "H_{ab}". For example, the "tight binding" model for off-resonance transport in molecular tunnel junctions predicts that the transport is proportional to $t^{2(N-1)}$, where *N* is the number of "sites" between the contacts [48]. For transport in conducting polymers, H_{ab} is related to charge propagation between polarons both along the chain and between different chains [49,50]. These theories include a barrier height as well as a coupling term, both of which affect the overall electron transfer rate. A case relevant to the current discussion is coupling between two orbitals in separate but identical molecules, for example the HOMO orbitals of G9. By definition, these orbitals have identical energies when the two G9 fragments are widely separated. When they are brought into close proximity, electrons in both HOMO orbitals interact to generate "splitting", creating two hybrid orbitals with energies above and below the HOMO of the free molecules. For example, the free G9 HOMO energy is −4.682 eV, while the HOMO and H−1 orbitals of two parallel G9 planes separated by 1.2 nm have equal energies of −4.682 eV, with no indication of electronic coupling. The parameter "*t*" is given by Equation 1, and is zero in this case.

$$t = \left(E_{\mathrm{H}} - E_{\mathrm{H}-1} \right) / 2 \qquad (1)$$

Values of *t* were calculated for two G9 clusters in a vacuum, oriented in parallel or edge to edge, with the latter representing an idealized vacuum gap consisting of a G9–molecule–G9 system with the molecule absent. Several orientations are listed in Table 2, and Figure S1 (Supporting Information File 1) illustrates the different orientations. For the case of parallel, face-to-face G9 planes, the original HOMO levels (H and H−1 in Table 2) change from a common value of −4.650 eV for 1.2 nm separation to −3.740 and −4.982 eV for 0.3 nm separation, clearly indicating an electronic perturbation in the absence of covalent bonding. The value of $t_{\mathrm{H/H}-1}$ determined from Equation 1 increases from 0 to 621 meV, with significant electronic interactions occurring below 0.6 nm between planes. Also listed in Table 2 are the same energies for the case of edge-to-edge spacing with the G9 rings in the same plane. Electronic coupling is much weaker in this case, and also depends on the dihedral angle between the G9 planes. Note that $t_{\mathrm{H/H}-1}$ for orthogonal edge-oriented G9s is an order of magnitude lower than for parallel edge oriented planes, and both of these are approximately two orders of magnitude lower than that observed for basal-basal orientation.

Table 2: Orbital energies and electronic coupling between G9 molecules.

	gap[a] between C–C, nm	dihedral angle between G9 planes, °	stability, eV	LUMO, eV	HOMO, eV	H−1, eV	$t_{H/H-1}$, meV	$t_{H-2/H-3}$, meV	$t_{L/L+1}$, meV
free G9				−2.260	−4.682	−5.950			
G9–G9 edge orientation	1.208	0	−0.006	−2.266	−4.688	−4.688	0.0	0.0	0.0
	0.600	0	−0.003	−2.278	−4.700	−4.700	0.0	0.0	0.0
	0.400	0	0.053	−2.290	−4.712	−4.713	0.1	1.1	0.0
	0.350	0	0.333	−2.293	−4.715	−4.715	0.3	3.3	0.0
	0.316	0	1.086	−2.294	−4.716	−4.717	0.5	6.7	0.0
	0.252	0	4.276	−2.297	−4.718	−4.727	4.5	5.7	0.0
G9–G9 edge separated by 0.4 nm	0.400	0	0.053	−2.290	−4.712	−4.713	0.1	1.1	0.0
	0.400	37	0.050	−2.288	−4.709	−4.710	0.1	1.0	0.1
	0.400	60	0.044	−2.285	−4.707	−4.707	0.3	0.5	0.3
	0.400	90	0.042	−2.284	−4.705	−4.706	0.3	0.1	0.3
G9–G9 parallel basal orientation	1.200	0	0.005	−2.228	−4.650	−4.650	0.0	0.0	0.0
	0.600	0	0.038	−2.159	−4.577	−4.581	2.3	43.1	2.4
	0.500	0	0.070	−2.158	−4.528	−4.577	24	25	27
	0.400	0	0.168	−2.251	−4.366	−4.665	150	90	157
	0.300	0	3.910	−2.779	−3.740	−4.982	621	14	679

[a]Distance between nearest C atoms in separate G9 molecules.

Venkataraman, et al. considered the relevance of electronic coupling in Au/molecule/Au single molecule junctions by calculating $4t^2$ for the frontier Au orbitals in the contacts, as modulated by the intervening molecular "bridge" [8]. Changing the substituents on the diamine "bridge" varied the junction conductance, and the theoretical $4t^2$ approximately tracked the observed conductance. We use here a conceptually similar approach for carbon-based molecular junctions by considering the electronic coupling between the G9 "contacts" of the G9–molecule–G9 system depicted in Figure 1. We consider the unmodified G9 clusters of Table 2 as models of a vacuum gap between two graphene "contacts", with either edge-to-edge or basal–basal orientations of the two G9 planes. These will be compared to covalently bonded model structures as G9–AB–G9 to determine the electronic coupling between contacts, since such coupling is at least one factor controlling charge transport through the junction.

Consider first the G9–AB–G9 model of Figure 1, in which the distance between the nearest carbon atoms in the two G9 rings in the optimized structure is 1.21 nm. Table 3 lists the H, H−1, and H−2 orbital energies and *t* values for the indicated pairs of orbitals. With the AB molecule absent, $t_{H/H-1}$ for two G9s with the same spacing in edge orientation from Table 2 is negligible (below 0.1 meV), while with the AB present $t_{H/H-1}$ is 3 meV. Recall that the H and H−1 orbitals of G9–AB–G9 are derived from the original HOMO orbitals of G9, and the low $t_{H/H-1}$

indicates weak interactions between the two G9 "contacts". However, as is apparent in Figure 5, the H−2 orbital spans both G9s and the AB molecule, so the coupling between H−2 and H−3 might be more relevant to transport. $t_{H-2/H-3}$ is 111 meV, implying significantly stronger coupling compared to the same parameter for unbonded G9s ($t_{H-2/H-3}$ < 0.1 meV). Note also that H−2 and H−3 in the G9–AB–G9 system have electron density on both G9 contacts as well as the molecule, which may indicate their likely involvement in transport. Also shown in Table 3 is the effect of rotation of the plane of the AB molecule while the G9 planes are kept parallel. Not surprisingly, $t_{H/H-1}$ remains small (below 5 meV) for the full range of planar to orthogonal planes, while $t_{H-2/H-3}$ decreases from 187 meV for the planar case to less than 1 meV for dihedral angles of 90°. In our previous theoretical analysis of electronic interactions between the larger G54 graphene fragment and AB, we proposed that the tunneling barrier is related to the offset between the G9–AB HOMO and the G9–AB orbital having significant electron density on the AB molecule [34]. This postulate is consistent both with transport measurements and with independent evaluations by ultraviolet photoelectron spectroscopy and photocurrent measurements [31,51,52]. For the G9–AB–G9 model, this offset would be approximated by the difference between the HOMO and H−2 orbitals, or 0.96 eV for the optimized case. The offset varies with dihedral angle, from 0.83 to 1.25 eV for the planar to the orthogonal structures. Our previous postulate that the orbital determining the tunneling

Table 3: Orbital energies for G9–AB–G9.

molecule	gap between C–C, nm	dihedral angle between G9s, °	LUMO, eV	HOMO, eV	H−1, eV	H−2, eV	$t_{H/H-1}$, meV	$t_{H-2/H-3}$, meV	$t_{L/L+1}$, meV
G9–AB–G9 37° dihedral angle (opt)	1.208	15	−2.410	−4.747	−4.753	−5.708	3.0	110.9	38.9
G9–AB–G9 90° dihedral angle	1.208	0	−2.316	−4.733	−4.733	−5.987	0.1	0.8	1.5
G9–AB–G9 75°	1.208	0	−2.321	−4.734	−4.736	−5.948	1.1	20.1	3.1
G9–AB–G9 60°	1.208	0	−2.351	−4.738	−4.742	−5.854	1.9	66.3	15.6
G9–AB–G9 45°	1.208	0	−2.391	−4.744	−4.748	−5.760	2.0	111.2	31.8
G9–AB–G9 37° (opt)	1.208	15	−2.410	−4.747	−4.753	−5.708	3.0	110.9	38.9
G9–AB–G9 20°	1.208	0	−2.451	−4.752	−4.760	−5.627	4.1	170.9	54.7
G9–AB–G9 0° (planar)	1.208	0	−2.468	−4.753	−4.763	−5.586	4.9	187.1	62.0
G9–(AB)₂–G9 opt	2.268	46	−2.567	−4.759	−4.761	−5.659	0.7	119.0	105.0
G9–(AB)₃–G9 opt	3.324	12.4	−2.665	−4.764	−4.765	−5.634	0.4	91.6	128.0
G9–(AB)₄–G9 opt	4.386	13	−2.716	−4.765	−4.766	−5.622	0.3	68.0	103.0
G9–(AB)₅–G9 opt	5.008	8.6	−2.748	−4.767	−4.767	−5.616	0.1	51.0	78.9
G9–AB–G9 planar	1.208	0	−2.468	−4.753	−4.763	−5.586	4.9	187.1	62.0
G9–(AB)₂–G9 planar	2.268	0.3	−2.644	−4.769	−4.771	−5.525	1.4	151.2	131.8
G9–(AB)₃–G9 planar	3.382	0.5	−2.746	−4.774	−4.775	−5.500	0.5	109.9	146.3
G9–(AB)₄–G9 planar	4.389	1.2	−2.805	−4.776	−4.776	−5.487	0.3	79.6	117.3
G9–(AB)₅–G9 planar	5.011	0.4	−2.840	−4.779	−4.779	−5.480	<0.1	59.6	90.6

barrier is the closest G9–AB orbital with electron density on the AB moiety can now be enhanced by the further postulate that the tunneling orbital span both the entire G9–AB–G9 system, as shown in Figure 4 for the H−2 orbital. While the LUMO orbitals can also show electronic coupling across the entire junction (apparent in Figure 4), they are energetically less favorable, with an offset from the electrode Fermi level of ca. 2.3 eV in G9–AB–G9 compared to approx. 1 eV for the H−2 orbital.

The model was extended to oligomers of AB between the G9 contacts, in order to assess the effect of molecular layer thickness. Oligomers were assumed to be bonded at the ends of the AB molecules (i.e., para to the azo group) and the optimized structures of G9–(AB)$_n$–G9 were determined for $n = 1$–5. Selected orbital energies and t values appear in Table 3, and more details are included in Table S1 (Supporting Information File 1). The electronic coupling between the G9 molecules decreases as the molecule becomes longer, and the H/H−1 coupling is always much less than the H−2/H−3 coupling. Electronic coupling for the AB oligomers is compared to that for a vacuum gap in Figure 6, with the log axis of Figure 6B showing the very weak coupling for the vacuum gap. Note that the changes in $t_{H-2/H-3}$ between the optimized and planar geometries are small compared to the difference between the presence and absence of the AB molecule.

In order to assess the effects of molecular structure on electronic coupling, several series of oligomers between G9 fragments were calculated, which differ in the degree of conjugation, including alkanes, alkene, and alkynes, with the results summarized in Table 4 and Figure 7. The optimized geometries for G9–molecule–G9 models with variations in molecular structure often have significant dihedral angles between the G9 planes, which complicates interpretation of molecular structural effects on electronic coupling. For this reason, further comparisons considered below were made for the planar configurations of G9–molecule–G9 structures. The real system has a range of dihedral angles, of course, but the effect of dihedral angle on coupling is generally minor compared to changes in conjugation and length. The large Table S2 (Supporting Information File 1) lists orbital energies and coupling calculated for both the optimized and planar configurations for a wide range of model structures. The G9 rings were close to coplanar for both the optimized and planar structures, and some of the alkanes were chosen to be rigid, such as cyclohexane and decalin. For the conjugated systems, the G9–molecule–G9 system was first optimized, then the dihedral angles forced to zero to form a planar structure and the energies recalculated.

As was the case with AB, similar trends were observed for both the planar and optimized structures, as shown in Table S2 (Supporting Information File 1). Figure 7 compares $t_{H-2/H-3}$ for

Figure 6: Comparisons of calculated electronic coupling *t* values in meV for G9–(AB)$_n$–G9 and edge-oriented G9–gap–G9 structures. A) *t* for the indicated orbital combinations for G9–G9 gaps of varying width and for G9–(AB)$_n$–G9 with varying numbers of AB subunits. *t* was determined between the HOMO and H−1 orbitals for the system containing two G9 units (labeled H/H−1) and for H−2/H−3 orbitals, as indicated. "opt" indicates optimized structures and "planar" structures were forced planar after optimization. B) same data as in panel A, but plotted on a logarithmic Y-axis. X axis is distance between the closest carbon atoms in the G9 fragments.

the molecules listed in Table 4 to that for AB and the vacuum gap. In all cases, coupling is stronger with the molecule present, although $t_{H-2/H-3}$ covers a wide range from below 1 meV to above 700 meV. With the exceptions of alkenes and alkynes, $t_{H-2/H-3}$ decreases as the separation of the G9 "contacts" increases, and logically must reach zero at infinite molecular layer thickness. The increase in coupling with distance calculated for alkenes and alkynes is unexpected, although it is small compared to the differences between alkanes, vacuum, and aromatics. The alkene and alkyne cases are not readily accessible with carbon contacts, hence this unexpected result is difficult to test experimentally. As suggested by a reviewer, it may be an indication that the electronic coupling represented by $t_{H-2/H-3}$ is not due simply to coupling between the G9 contacts (which should certainly decrease with distance), but might instead indicate coupling between molecule and G9 orbitals. This possibility is testable by further experiments with variations in molecular structure. For the readily fabricated aromatic molecular junctions, it is likely that the particular orbitals most involved in transport will be revealed by further correlations of calculated orbital energy splitting with experimental results.

The conjugated systems show similar electronic coupling, with a weaker decrease with thickness than the alkanes. The trends in electronic coupling evident in Figure 7B have a striking similarity to experimental results from a variety of laboratories and paradigms [1,5,31,53]. Electron transport across thin organic layers often decays exponentially with layer thickness, with an "attenuation length (β)" equal to the slope of a plot of the natural log of transport rate vs layer thickness. Real alkane

junctions exhibit a significantly higher β (8–9 nm^{-1}) than conjugated systems (β = 2–4 nm^{-1}), and many of the latter have similar β values despite structural differences. AQ is an interesting case, because is it "cross conjugated" with a much smaller $t_{H-2/H-3}$ than that for the structurally related anthracene case [54]. Several experimental reports have shown a quite distinct behavior of AQ compared to AN "bridges", attributed to cross conjugation and quantum interference [54-58]. Since the relationship between $t_{H-2/H-3}$ and the attenuation coefficient β depends on the transport mechanism, the similarity between Figure 7B and various experimental β plots should be considered qualitative. Although the model structure is significantly simplified compared to the real carbon/oligomer/carbon MJ, $t_{H-2/H-3}$ determined for G9–molecule–G9 structures is at least a guide toward predicting transport in proposed junction structures, or for systems which are difficult to realize experimentally.

3 Energy barriers and partial charge transfer

As noted in the introduction, we have examined the postulate that the energy barrier for tunneling across carbon-based molecular junctions correlates with the difference in energy between the system HOMO and the orbital closest in energy that has significant electron density on the molecule [34]. The arguments of the previous section indicate that electronic coupling is strongest for orbitals that bridge across the entire G9–molecule–G9 structure, often H−2 and H−3 in the structures considered here. It is tempting to conclude that $E_{HOMO} - E_{H-2}$ represents the magnitude of the tunneling barrier, in which case prediction of the barrier is straightfor-

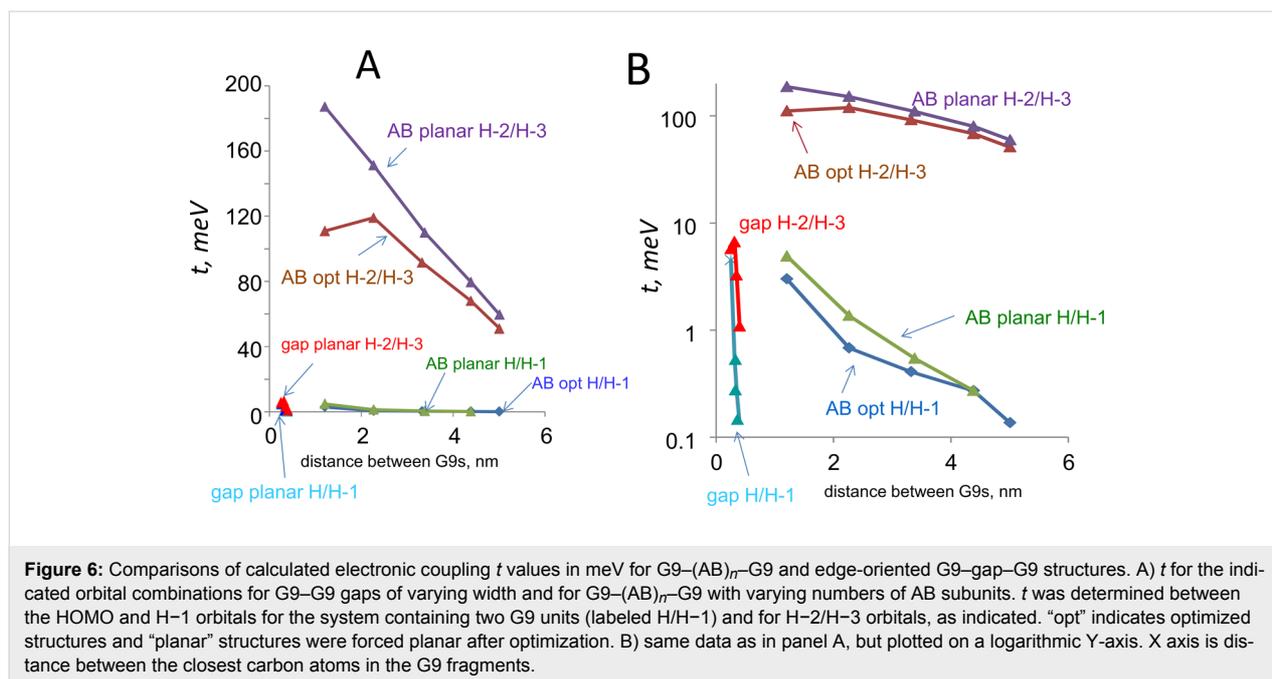**Table 4:** Orbital energies and coupling for planar G9–molecule–G9 systems.

molecule	distance between G9s, nm	dihedral angle between G9s, degrees	HOMO, eV	H−1, eV	H−2, eV	$t_{H/H-1}$, meV	$t_{H-2/H-3}$, meV	$t_{L/L+1}$, meV
alkanes								
G9–CH$_2$–G9 planar[a]	0.256	17.5	−4.693	−4.710	−5.901	8.6	17.7	7.9
G9–ethane–G9 planar	0.41	1	−4.673	−4.702	−5.871	14.4	45.6	38.2
G9–cyclohexane–G9 planar[b]	0.59	2	−4.675	−4.678	−5.903	1.9	9.9	5.4
G9–decalin–G9 planar[b]	0.821	1	−4.653	−4.654	−5.889	0.4	1.8	1.2
G9–tri-decalin–G9 planar[b]	1.063	1	−4.648	−4.654	−5.889	3.0	3.8	4.2
(oligo)ethenylenes[c]								
G9–ethene–G9 planar	0.389	0	−4.710	−4.748	−5.520	18.9	248.0	14.7
G9–butadiene–G9 planar	0.635	0	−4.702	−4.739	−5.312	18.5	339.5	13.9
G9–hexatriene–G9 planar	0.882	0	−4.693	−4.735	−5.143	21.1	406.0	17.1
G9–octatetraene–G9 planar	1.13	0	−4.682	−4.731	−5.012	24.8	440.4	22.3
(oligo)ethynylenes								
G9–ethyne–G9 planar	0.407	0	−4.742	−4.773	−5.631	15.6	211.3	19.2
G9–butadiyne–G9 planar	0.664	0	−4.781	−4.807	−5.581	12.9	245.9	19.6
G9–hexatriyne–G9 planar	0.922	0	−4.817	−4.839	−5.551	10.7	268.4	23.8
anthracene[d]								
G9–AN–G9 (corners) planar	1.036	0.2	−4.695	−4.725	−5.199	14.8	358.2	25.7
G9–(AN)$_2$–G9 (corners) planar	1.923	0	−4.702	−4.714	−5.071	6.0	185.0	11.0
G9–(AN)$_3$–G9 (corners) planar	2.821	0.5	−4.707	−4.727	−5.000	9.7	125.7	16.1
G9–(AN)$_4$–G9 (corners) planar	3.713	5.8	−4.706	−4.709	−4.965	1.5	98.8	3.8
anthraquinone[d]								
G9–AQ–G9 planar	1.042	0.46	−4.805	−4.810	−5.955	2.6	22.0	210.2
G9–(AQ)$_2$–G9 planar	1.938	2.1	−4.838	−4.839	−6.013	0.1	2.2	99.0
G9–(AQ)$_3$–G9 planar	2.836	1.46	−4.851	−4.851	−6.028	0.1	0.5	74.6
bis(thienyl)benzene								
G9–BTB–G9 planar	1.358	1.5	−4.716	−4.741	−5.089	12.5	371.3	10.9
G9–(BTB)$_2$–G9 planar	2.565	2.9	−4.718	−4.736	−4.909	8.7	208.2	9.4

[a]Planarity prevented by steric interactions; [b]G9s parallel, but offset below 0.2 nm; [c]all in trans-configuration; [d]AN–AN and AQ–AQ linked at 2-position.

ward for the model system. However, several authors have pointed out that electronic coupling between the contacts and molecules at organic/conductor interfaces can significantly perturb the simple picture, due to local electrostatic effects [36-38,40,59,60]. "Vacuum level alignment" effects on interfacial barriers are often attributed to surface dipoles which cause charge transfer across an interface, resulting in changes in local electrostatic potential [14,38,40]. For the case of G9–AB, if electrons are transferred from G9 to AB when the G9–AB bond is formed, the electrostatic potential of AB increases, thus raising its HOMO level compared to that of the free molecule. Figure 8 shows the effect schematically, starting with two sep- arated G9 planes and an AB molecule with its HOMO at −6.16 eV for the free molecule. The −4.7 eV work function observed experimentally is close to the −4.68 eV HOMO calcu-

lated for G9, and both G9s have identical HOMO levels. When the G9–AB–G9 system is formed, DFT predicts that 0.032 e$^-$ are transferred to the AB molecules, as shown in Figure 8B.

The local electrostatic potential associated with these electrons shifts all of the orbitals in AB to higher energy, and decreases the transport barrier predicted from the work function and HOMO energy of the separated contact and molecule. Although there is some concern about the accuracy of DFT for predicting Mulliken charges [41], trends are generally reliable, such as the dependence on dihedral angle shown in Figure 3. At least in principle, the DFT-determined energies for G9–molecule–G9 model structures should include such electrostatic effects, including local dipoles and Mulliken charges. As an indication of the magnitude of the effect, Guerrero et al. have provided an
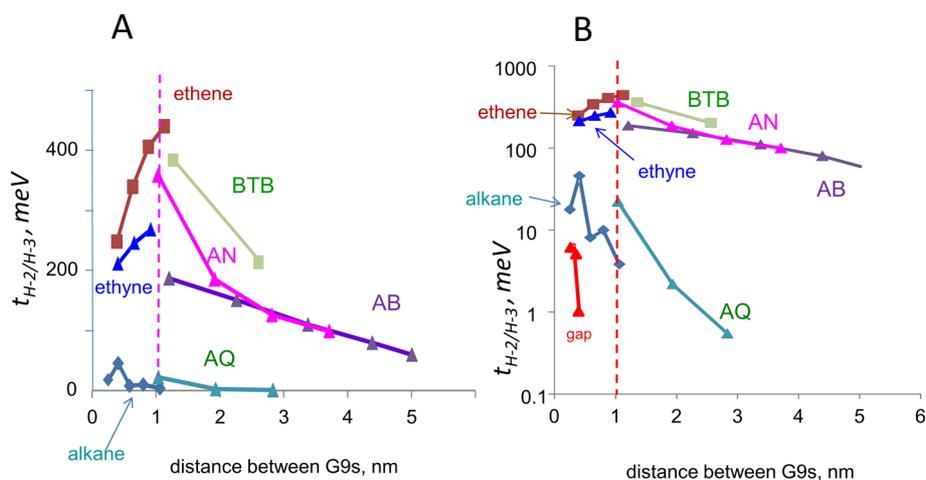
Figure 7: A) $t_{H-2/H-3}$ calculated for the planar geometries of the indicated G9–molecule–G9 clusters with various molecular oligomers with lengths from 0.2 to 5 nm. B) same data as panel A on a log scale. BTB = bis(thienyl)benzene, AN = 2-anthracene, AB = azobenzene, ethene = *trans*-oligoethenylenes, ethyne = oligoethynylenes, AQ = anthraquinone.
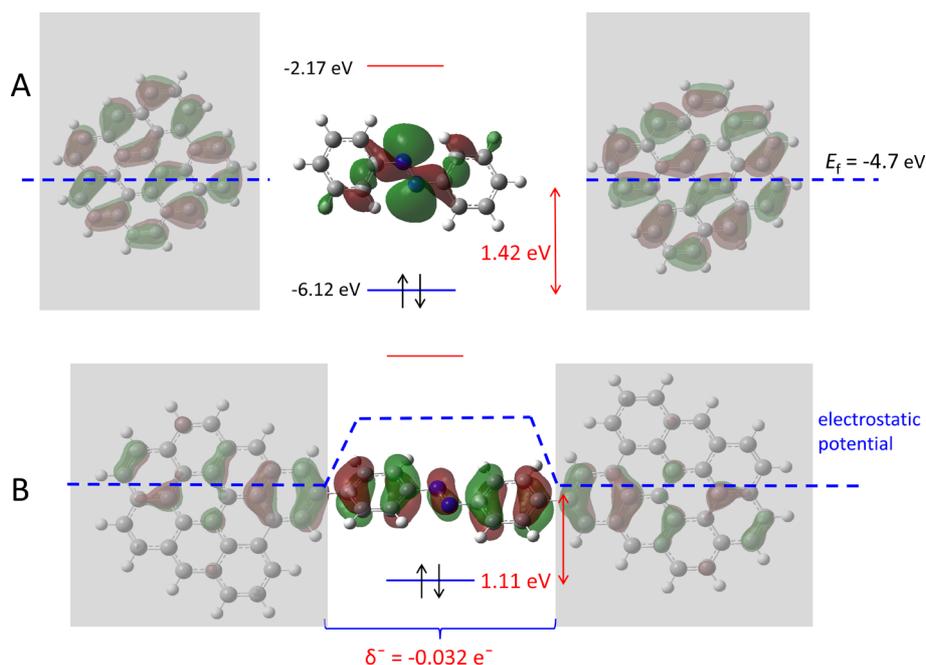
Figure 8: A) Isolated AB and G9 molecules showing the calculated HOMO and LUMO energies relative to the experimentally observed carbon Fermi level of −4.7 eV. Also shown is the 1.42 eV tunneling barrier predicted from the free molecules. B. Schematic of electrostatic potential resulting from charge transfer of 0.032 e⁻ to the AB molecule from the G9s accompanying covalent bond formation. The expected tunneling barrier is reduced to 1.11 eV, as shown.

expression for predicting the vacuum level shift, Δ, from the charge transferred, Q, the dielectric constant, ε, and an estimated interface thickness, δ: $\Delta = \delta Q / \varepsilon$ [61]. Using this approach, we predict a vacuum level shift of 0.35 V for ε = 4 and δ = 1 nm, implying that $E_f - E_{HOMO}$ would decrease from the value predicted for the free molecule by 0.35 V. The assump-

tions required for this calculation do not permit a rigorous quantitative analysis of the effect, but it does indicate that transport barriers can be significantly perturbed by partial charge transfer. We showed previously that the effect is sufficiently large in carbon MJs with aromatic molecular layers that differences in free molecule HOMO levels caused a small effect on junction

conductance. Since low HOMO levels cause larger charge transfer than higher HOMO levels, the effect "levels" a range of barriers of 0.7 to 3.0 eV based on the free molecule HOMOs to 1.3 ± 0.2 eV determined experimentally [31].

Conclusion

The author agrees with the often-quoted words attributed to I. M. Koltoff: "theory guides, experiment decides". The purpose of the current paper is to identify some of the "guides" that apply to how molecular structure affects electron transport in carbon-based molecular electronic devices. With that objective in mind, several observations are available from the DFT results. First, electronic coupling is an important factor in understanding transport, both coupling between the molecule and the contacts, and between subunits within the molecular layer. Strong coupling indicated by a large *t* value should promote electron transfer for both tunneling and activated "hopping" mechanisms, and decreases with increasing distance between the coupled sites. All molecules examined increase electronic coupling between graphene "contacts" compared to a vacuum gap, but the increase is strongly structure-dependent, as shown in Figure 7B. Although electronic coupling depends on the dihedral angles between aromatic subunits, real experimental systems in use currently have a range of dihedral angles, and device behavior represents an average over this range. Second, the electronic coupling across G9–molecule–G9 is weak for the HOMO and H−1 orbitals, which were the original HOMOs of the isolated G9 fragments. Coupling is much stronger for hybrid orbitals H−2 and H−3, which exhibit electron density on both the G9 and molecule moieties, implying they are more likely involved in transport. For many cases, these orbitals are approximately 1 eV below the system HOMO, and likely represent the orbitals responsible for the experimentally observed barriers of 1.3 ± 0.2 eV [31]. Third, electronic coupling can also result in partial charge transfer between contacts and the molecular layer, which leads to the electrostatic perturbation of the tunneling barrier illustrated in Figure 8. Unfortunately, this effect decreases the influence of electron donating and withdrawing groups on the observed barrier, thus frustrating some attempts to modulate transport with structure. Although the magnitude of the effect is difficult to predict theoretically, it can be measured with various probes such as UPS and inverse photoemission for molecular layers on surfaces [14,31,40,62,63], and photocurrents for intact molecular junctions [51,52]. Finally, the conjugated covalent bond between the aromatic π-systems of the carbon substrate and aromatic molecular layer is responsible for both the strong electronic coupling and the excellent stability of carbon-based molecular junctions. The guidance provided by DFT illustrated here should prove useful for designing new MJ structures which exploit these properties.

Supporting Information

Supporting Information features the orientations of G9 fragments used to calculate the energies of Table 2 as well as a complete table of orbital energies for the molecules shown in Figure 6 and Figure 7 for both the optimized and planar geometries.

Supporting Information File 1
Additional computational data.
[http://www.beilstein-journals.org/bjnano/content/supplementary/2190-4286-7-4-S1.pdf]

References

1. Metzger, R. M. *Chem. Rev.* **2015,** *115,* 5056–5115. doi:10.1021/cr500459d
2. McCreery, R. L.; Yan, H.; Bergren, A. J. *Phys. Chem. Chem. Phys.* **2013,** *15,* 1065–1081. doi:10.1039/C2CP43516K
3. McCreery, R. L.; Bergren, A. J. *Adv. Mater.* **2009,** *21,* 4303–4322. doi:10.1002/adma.200802850
4. Heath, J. R. *Annu. Rev. Mater. Res.* **2009,** *39,* 1–23. doi:10.1146/annurev-matsci-082908-145401
5. Amdursky, N.; Marchak, D.; Sepunaru, L.; Pecht, I.; Sheves, M.; Cahen, D. *Adv. Mater.* **2014,** *26,* 7142–7161. doi:10.1002/adma.201402304
6. Aradhya, S. V.; Meisner, J. S.; Krikorian, M.; Ahn, S.; Parameswaran, R.; Steigerwald, M. L.; Nuckolls, C.; Venkataraman, L. *Nano Lett.* **2012,** *12,* 1643–1647. doi:10.1021/nl2045815
7. Chen, W.; Widawsky, J. R.; Vázquez, H.; Schneebeli, S. T.; Hybertsen, M. S.; Breslow, R.; Venkataraman, L. *J. Am. Chem. Soc.* **2011,** *133,* 17160–17163. doi:10.1021/ja208020j
8. Venkataraman, L.; Park, Y. S.; Whalley, A. C.; Nuckolls, C.; Hybertsen, M. S.; Steigerwald, M. L. *Nano Lett.* **2007,** *7,* 502–506. doi:10.1021/nl062923j
9. Li, Z.; Smeu, M.; Ratner, M. A.; Borguet, E. *J. Phys. Chem. C* **2013,** *117,* 14890–14898. doi:10.1021/jp309871d
10. DiBenedetto, S. A.; Facchetti, A.; Ratner, M. A.; Marks, T. J. *J. Am. Chem. Soc.* **2009,** *131,* 7158–7168. doi:10.1021/ja9013166
11. Solomon, G. C.; Andrews, D. Q.; Van Duyne, R. P.; Ratner, M. A. *J. Am. Chem. Soc.* **2008,** *130,* 7788–7789. doi:10.1021/ja801379b
12. Lindsay, S. M.; Ratner, M. A. *Adv. Mater.* **2007,** *19,* 23–31. doi:10.1002/adma.200601140
13. Luo, L.; Choi, S. H.; Frisbie, C. D. *Chem. Mater.* **2011,** *23,* 631–645. doi:10.1021/cm102402t

14. Kim, B.; Choi, S. H.; Zhu, X.-Y.; Frisbie, C. D. *J. Am. Chem. Soc.* **2011,** *133,* 19864–19877. doi:10.1021/ja207751w

15. Choi, S. H.; Kim, B.; Frisbie, C. D. *Science* **2008,** *320,* 1482–1486. doi:10.1126/science.1156538

16. Yoon, H. J.; Shapiro, N. D.; Park, K. M.; Thuo, M. M.; Soh, S.; Whitesides, G. M. *Angew. Chem., Int. Ed.* **2012,** *51,* 4658–4661. doi:10.1002/anie.201201448

17. Cademartiri, L.; Thuo, M. M.; Nijhuis, C. A.; Reus, W. F.; Tricard, S.; Barber, J. R.; Sodhi, R. N. S.; Brodersen, P.; Kim, C.; Chiechi, R. C.; Whitesides, G. M. *J. Phys. Chem. C* **2012,** *116,* 10848–10860. doi:10.1021/jp212501s

18. Nijhuis, C. A.; Reus, W. F.; Whitesides, G. M. *J. Am. Chem. Soc.* **2010,** *132,* 18386–18401. doi:10.1021/ja108311j

19. Akkerman, H. B.; Kronemeijer, A. J.; Harkema, J.; van Hal, P. A.; Smits, E. C. P.; de Leeuw, D. M.; Blom, P. W. M. *Org. Electron.* **2010,** *11,* 146–149. doi:10.1016/j.orgel.2009.09.013

20. Van Hal, P. A.; Smits, E. C. P.; Geuns, T. C. T.; Akkerman, H. B.; De Brito, B. C.; Perissinotto, S.; Lanzani, G.; Kronemeijer, A. J.; Geskin, V.; Cornil, J.; Blom, P. W. M.; De Boer, B.; De Leeuw, D. M. *Nat. Nanotechnol.* **2008,** *3,* 749–754. doi:10.1038/nnano.2008.305

21. Akkerman, H. B.; Blom, P. W. M.; de Leeuw, D. M.; de Boer, B. *Nature* **2006,** *441,* 69. doi:10.1038/nature04699

22. Green, J. E.; Wook Choi, J.; Boukai, A.; Bunimovich, Y.; Johnston-Halperin, E.; DeIonno, E.; Luo, Y.; Sheriff, B. A.; Xu, K.; Shik Shin, Y.; Tseng, H.-R.; Stoddart, J. F.; Heath, J. R. *Nature* **2007,** *445,* 414. doi:10.1038/nature05462

23. DeIonno, E.; Tseng, H.-R.; Harvey, D. D.; Stoddart, J. F.; Heath, J. R. *J. Phys. Chem. B* **2006,** *110,* 7609–7612. doi:10.1021/jp0607723

24. Vilan, A.; Yaffe, O.; Biller, A.; Salomon, A.; Kahn, A.; Cahen, D. *Adv. Mater.* **2010,** *22,* 140–159. doi:10.1002/adma.200901834

25. Yu, X.; Lovrinčić, R.; Kraynis, O.; Man, G.; Ely, T.; Zohar, A.; Toledano, T.; Cahen, D.; Vilan, A. *Small* **2014,** *10,* 5151–5160. doi:10.1002/smll.201400484

26. Li, Y.; Calder, S.; Yaffe, O.; Cahen, D.; Haick, H.; Kronik, L.; Zuilhof, H. *Langmuir* **2012,** *28,* 9920–9929. doi:10.1021/la3010568

27. Seitz, O.; Vilan, A.; Cohen, H.; Hwang, J.; Haeming, M.; Schoell, A.; Umbach, E.; Kahn, A.; Cahen, D. *Adv. Funct. Mater.* **2008,** *18,* 2102–2113. doi:10.1002/adfm.200800208

28. McCreery, R. Electron Transport and Redox Reactions in Solid-State Molecular Electronic Devices. In *Nanoelectrochemistry;* Mirkin, M. V.; Amemiya, S., Eds.; CRC Press: Boca Raton, FL, U.S.A., 2015; pp 205–240. doi:10.1201/b18066-10

29. McCreery, R.; Bergren, A.; Morteza-Najarian, A.; Sayed, S. Y.; Yan, H. *Faraday Discuss.* **2014,** *172,* 9–25. doi:10.1039/C4FD00172A

30. Yan, H.; Bergren, A. J.; McCreery, R.; Della Rocca, M. L.; Martin, P.; Lafarge, P.; Lacroix, J. C. *Proc. Natl. Acad. Sci. U. S. A.* **2013,** *110,* 5326–5330. doi:10.1073/pnas.1221643110

31. Sayed, S. Y.; Fereiro, J. A.; Yan, H.; McCreery, R. L.; Bergren, A. J. *Proc. Natl. Acad. Sci. U. S. A.* **2012,** *109,* 11498–11503. doi:10.1073/pnas.1201557109

32. Bergren, A. J.; McCreery, R. L. *Annu. Rev. Anal. Chem.* **2011,** *4,* 173–195. doi:10.1146/annurev-anchem-061010-113847

33. Anariba, F.; Steach, J. K.; McCreery, R. L. *J. Phys. Chem. B* **2005,** *109,* 11163–11172. doi:10.1021/jp051093f

34. Kondratenko, M.; Stoyanov, S. R.; Gusarov, S.; Kovalenko, A.; McCreery, R. L. *J. Phys. Chem. C* **2015,** *119,* 11286–11295. doi:10.1021/jp5128332

35. Bergren, A. J.; McCreery, R. L.; Stoyanov, S. R.; Gusarov, S.; Kovalenko, A. *J. Phys. Chem. C* **2010,** *114,* 15806–15815. doi:10.1021/jp106362q

36. Salomon, A.; Boecking, T.; Seitz, O.; Markus, T.; Amy, F.; Chan, C.; Zhao, W.; Cahen, D.; Kahn, A. *Adv. Mater.* **2007,** *19,* 445–450. doi:10.1002/adma.200601729

37. Cahen, D.; Kahn, A. *Adv. Mater.* **2003,** *15,* 271–277. doi:10.1002/adma.200390065

38. Braun, S.; Salaneck, W. R.; Fahlman, M. *Adv. Mater.* **2009,** *21,* 1450–1472. doi:10.1002/adma.200802893

39. Ishii, H.; Sugiyama, K.; Ito, E.; Seki, K. *Adv. Mater.* **1999,** *11,* 605–625. doi:10.1002/(SICI)1521-4095(199906)11:8<605::AID-ADMA605>3.0.CO;2-Q

40. Hwang, J.; Wan, A.; Kahn, A. *Mater. Sci. Eng., R* **2009,** *64,* 1–31. doi:10.1016/j.mser.2008.12.001

41. Saha, S.; Roy, R. K.; Ayers, P. W. *Int. J. Quantum Chem.* **2009,** *109,* 1790–1806. doi:10.1002/qua.21901

42. McCreery, R. L.; Bergren, A. J. Diazonium reagents in molecular electronics. In *Aryl Diazonium Salts: New Coupling Agents in Polymer and Surface Science;* Chehimi, M. M., Ed.; Wiley-VCH: Weinheim, Germany, 2012. doi:10.1002/9783527650446.ch10

43. Yan, H.; Bergren, A. J.; McCreery, R. L. *J. Am. Chem. Soc.* **2011,** *133,* 19168–19177. doi:10.1021/ja206619a

44. Wu, J.; McCreery, R. L. *J. Electrochem. Soc.* **2009,** *156,* P29–P37. doi:10.1149/1.3021033

45. Wu, J.; Mobley, K.; McCreery, R. L. *J. Chem. Phys.* **2007,** *126,* 24704. doi:10.1063/1.2423011

46. McCreery, R. L.; Wu, J.; Kalakodimi, R. P. *Phys. Chem. Chem. Phys.* **2006,** *8,* 2572–2590. doi:10.1039/b601163m

47. Kumar, R.; Yan, H.; McCreery, R. L.; Bergren, A. J. *Phys. Chem. Chem. Phys.* **2011,** *13,* 14318–14324. doi:10.1039/c1cp20755e

48. Mujica, V.; Ratner, M. A. *Chem. Phys.* **2001,** *264,* 365–370. doi:10.1016/S0301-0104(00)00394-3

49. Lacroix, J. C.; Chane-Ching, K. I.; Maquère, F.; Maurel, F. *J. Am. Chem. Soc.* **2006,** *128,* 7264–7276. doi:10.1021/ja060390a

50. Sancho-García, J. C.; Pérez-Jiménez, A. J. *J. Chem. Phys.* **2008,** *129,* 024103–024114. doi:10.1063/1.2951991

51. Fereiro, J. A.; Kondratenko, M.; Bergren, A. J.; McCreery, R. L. *J. Am. Chem. Soc.* **2015,** *137,* 1296–1304. doi:10.1021/ja511592s

52. Fereiro, J. A.; McCreery, R. L.; Bergren, A. J. *J. Am. Chem. Soc.* **2013,** *135,* 9584–9587. doi:10.1021/ja403123a

53. Bonifas, A. P.; McCreery, R. L. *Nat. Nanotechnol.* **2010,** *5,* 612–617. doi:10.1038/nnano.2010.115

54. Fracasso, D.; Valkenier, H.; Hummelen, J. C.; Solomon, G. C.; Chiechi, R. C. *J. Am. Chem. Soc.* **2011,** *133,* 9556–9563. doi:10.1021/ja202471m

55. Guédon, C. M.; Valkenier, H.; Markussen, T.; Thygesen, K. S.; Hummelen, J. C.; van der Molen, S. J. *Nat. Nanotechnol.* **2012,** *7,* 305–309. doi:10.1038/nnano.2012.37

56. Rabache, V.; Chaste, J.; Petit, P.; Della Rocca, M. L.; Martin, P.; Lacroix, J.-C.; McCreery, R. L.; Lafarge, P. *J. Am. Chem. Soc.* **2013,** *135,* 10218–10221. doi:10.1021/ja403577u

57. Valkenier, H.; Guédon, C. M.; Markussen, T.; Thygesen, K. S.; van der Molen, S. J.; Hummelen, J. C. *Phys. Chem. Chem. Phys.* **2014,** *16,* 653–662. doi:10.1039/C3CP53866D

58. Darwish, N.; Díez-Pérez, I.; Da Silva, P.; Tao, N.; Gooding, J. J.; Paddon-Row, M. N. *Angew. Chem., Int. Ed.* **2012,** *51,* 3203–3206. doi:10.1002/anie.201107765

59. Van Dyck, C.; Ratner, M. A. *Nano Lett.* **2015,** *15,* 1577–1584. doi:10.1021/nl504091v

60. Van Dyck, C.; Geskin, V.; Cornil, J. *Adv. Funct. Mater.* **2014,** *24,* 6154–6165. doi:10.1002/adfm.201400809

61. Guerrero, A.; Marchesi, L. F.; Boix, P. P.; Ruiz-Raga, S.;
    Ripolles-Sanchis, T.; Garcia-Belmonte, G.; Bisquert, J. *ACS Nano*
    2012, *6,* 3453–3460. doi:10.1021/nn300486a
62. Shpaisman, H.; Seitz, O.; Yaffe, O.; Roodenko, K.; Scheres, L.;
    Zuilhof, H.; Chabal, Y. J.; Sueyoshi, T.; Kera, S.; Ueno, N.; Vilan, A.;
    Cahen, D. *Chem. Sci.* **2012,** *3,* 851–862. doi:10.1039/C1SC00639H
63. Segev, L.; Salomon, A.; Natan, A.; Cahen, D.; Kronik, L.; Amy, F.;
    Chan, C. K.; Kahn, A. *Phys. Rev. B: Condens. Matter Mater. Phys.*
    2006, *74,* 165323–165326. doi:10.1103/PhysRevB.74.165323

Current-induced runaway vibrations in dehydrogenated graphene nanoribbons

Rasmus Bjerregaard Christensen[1], Jing-Tao Lü[2], Per Hedegård[3] and Mads Brandbyge[*1]

Address:
[1]Center for Nanostructured Graphene (CNG), Department of Micro- and Nanotechnology, Technical University of Denmark, Ørsteds Plads, Bldg. 345E, DK-2800 Kongens Lyngby, Denmark, [2]School of Physics, Huazhong University of Science and Technology, 430074 Wuhan, P. R. China and [3]Niels-Bohr Institute and Nano-Science Center, University of Copenhagen, Universitetsparken 5, 2100 Copenhagen Ø, Denmark

Email:
Mads Brandbyge[*] - mads.brandbyge@nanotech.dtu.dk

* Corresponding author

Abstract

We employ a semi-classical Langevin approach to study current-induced atomic dynamics in a partially dehydrogenated armchair graphene nanoribbon. All parameters are obtained from density functional theory. The dehydrogenated carbon dimers behave as effective impurities, whose motion decouples from the rest of carbon atoms. The electrical current can couple the dimer motion in a coherent fashion. The coupling, which is mediated by nonconservative and pseudo-magnetic current-induced forces, change the atomic dynamics, and thereby show their signature in this simple system. We study the atomic dynamics and current-induced vibrational instabilities using a simplified eigen-mode analysis. Our study illustrates how armchair nanoribbons can serve as a possible testbed for probing the current-induced forces.

Introduction

The electronic and transport properties of graphene has been the focus of intense study since its discovery in 2004 [1]. Due to the strong σ-bonding between carbon atoms, graphene has a very high thermal conductivity, and can potentially sustain much higher current intensities than other materials. Graphene nanoribbons (GNR) exhibit a bandgap opening due to quantum confinement in the transverse ribbon direction. This opens the possibilities of realizing various electronic devices, especially field-effect transistors, using graphene nanoribbons. Atomically precise ribbons [2], as well as more advanced ribbon-

based structures [3,4], have been fabricated "bottom-up" on metal surfaces. The conductance through the ribbons has been investigated using STM [5], and the signals of electron vibrations in the current have been addressed by theory [6].

When cutting graphene into one-dimensional ribbons, dangling bonds emerge at the boundary carbon atoms. If there is an electrical current passing through the ribbon, we expect that these boundary atoms with dangling bonds are mechanically weak compared to the central atoms. Actually, it has been observed experimentally that these atoms can be removed by the passing electrical current due to current-induced local heating [7,8]. One theoretical study suggests that the carbon dimers at the armchair edge vibrate locally and interact strongly with the electrical current [8]. They can be thought as atomic scale defects at the boundary. How the current-induced forces affect the dynamics of these dimers is an interesting question to ask since it could be addressed by experiments. Employing a semi-classical Langevin approach, we have previously studied the current-induced atomic dynamics of a graphene nano-constriction [9]. However, the number of atoms involved even in such a small system makes a simple analysis difficult.

On the other hand, since the first prediction that current-induced forces are nonconservative with respect to energy [10], there has been a substantial theoretical effort aimed at exploring its consequences for the stability of current-carrying nano-systems [11-15], or the possibility of driving atomic motors [10,16]. Moreover, it has been shown that, in addition to the nonconservative force, the current-induced forces also include an effective Lorentz force or pseudo-magnetic force, originated from the Berry phase of electrons [11]. Performing similar analysis using a scattering theory approach shows that the predictions apply equally well to much larger mesoscopic coherent conductors [16,17]. A requirement of impact of the nonconservative force is that two or more vibrational modes close in frequency couple to each other via the current carrying electronic states. This can establish a generalized circular "water-wheel" motion, either in real space [10] or in mode space. Another requirement is that these modes have little damping due to the coupling to the phonon reservoir. Unfortunately, there has not been a clear experimental setup where these new theoretical findings can be put to a test proving their effect in an unambiguous way. Thus, it is of interest to be able to propose such a setup based on first principles calculations with realistic unadjustable parameters.

In this paper, we study the current-induced dynamics in a partially dehydrogenated armchair graphene ribbon. We show that, atomic motion of the dehydrogenated carbon dimer at the nanoribbon boundaries are relatively decoupled from other

dimers and also from the rest carbon atoms. This results in several nearly degenerate atomic vibrations, where each of these involves mainly one dimer. However, a coupling of the dimer vibrations takes place via the flowing electrical current. All these features are favorable to observe the effect of current-induced forces, thus making armchair nanoribbon an ideal candidate to study.

In the rest of the paper, we summarize our theoretical (section "Theory") and numerical (section "Numerical Calculation") methods, and present our analysis of the armchair graphene ribbon (section "Results and Discussion"). We end this paper with our concluding remarks (section "Conclusion").

Theory

We consider a standard Landauer-type transport setup described in Figure 1a. The system/device is in contact with the left and right leads. Each lead serves as both electronic and phononic bath. The bath degrees of freedom are non-interacting. We are interested in the atomic dynamics in the device region (displacements U), which can be described by the semi-classical generalized Langevin equation (SGLE) [12,18-20],

$$\ddot{U}(t) - F\big(U(t)\big) = -\int^{t}\Pi^{r}(t-t')U(t')dt' + f(t). \quad (1)$$

Here $F(U)$ is the force between atoms in the device region and $f(t)$ is a random force due to thermal and voltage-bias-induced fluctuations. The Π^{r} (self-energy) describes the time-delayed back action of the bath on the system due to the motion of the system. It has three contributions,

$$\Pi^{r} = \Pi^{r}_{L} + \Pi^{r}_{R} + \Pi^{r}_{e} , \quad (2)$$

where Π^{r}_{L} and Π^{r}_{R} describe the coupling to the phonon reservoirs outside device, while the self-energy Π^{r}_{e} describes the coupling to the electrons. In equilibrium, this result has been obtained by, i.e., Head-Gordon and Tully [21]. In principle we may apply the SGLE including the non-linear part of F [22], but here we will restrict ourselves to the harmonic approximation, $F(U) = -\mathbf{K}U$.

Non-equilibrium

The semi-classical Langevin equation can be extended to include the non-equilibrium effects in the electronic system due to the current [11,12,23]. In accordance with intuition the

Figure 1: (a) Structure of the transport setup defining device and symmetric electrode(left shown) regions. The motion of atoms is considered in the dynamical region. (b) Electron transmission in a perfect, infinite ribbon (dotted), and with broadened states in the electrodes to mimic metallic contacts with/without dehydrogenation (dashed/full). (Red and green vertical dashed lines indicate the shifts in Fermi energy used below in Figure 2). (c) Solid line is phonon transmission for the structure in (a), dotted line is phonon transmission for a pristine hydrogenated ribbon.

$$\Pi_{\mathrm{e}}^{r}\left(t-t'\right)=\theta\left(t-t'\right)\int\frac{d\omega}{2\pi}e^{-i\omega(t-t')}\Lambda\left(\omega\right),\qquad(3)$$

with Λ (including spin), given by,

$$\Lambda\left(\omega\right)=\sum_{\alpha,\beta}\Lambda^{\alpha\beta}\left(\omega\right),\qquad(4)$$

$$
\begin{aligned}
\Lambda_{kl}^{\alpha\beta}\left(\omega\right)=2\int\frac{d\varepsilon_{1}}{2\pi}\int\frac{d\varepsilon_{2}}{2\pi}\delta\left(\varepsilon_{1}-\varepsilon_{2}-\hbar\omega\right)\\
\times\mathrm{Tr}\left[M^{k}A_{\alpha}\left(\varepsilon_{1}\right)M^{l}A_{\beta}\left(\varepsilon_{2}\right)\right]\\
\times\left(n_{F}\left(\varepsilon_{1}-\mu_{\alpha}\right)-n_{F}\left(\varepsilon_{2}-\mu_{\beta}\right)\right).
\end{aligned}
\qquad(5)
$$

Here, $A_{\alpha/\beta}$ is the density of scattering states incoming from left and right electrodes (indices α and β), while M describes the electron–phonon couplings (k and l phonon indices). One can loosely think of the motion of phonon k excites an electron–hole pair of energy $\hbar\omega$ which is absorbed by phonon l.

The SGLE, in Equation 1, is given in the time domain. However, since we are considering steady state, it is convenient to work in the frequency domain. Thus, by Fourier transformation we obtain,

$$\Pi_{\mathrm{e}}^{r}\left(\omega\right)=\int_{-\infty}^{\infty}d\omega'\frac{\Lambda\left(\omega'\right)}{\omega'-\omega-i\eta}.\qquad(6)$$

By applying the Sokhatsky–Weierstrass theorem $\Pi^{r}(\omega)$ can be split into four contributions giving rise to the four forces

$$
\Pi_{\mathrm{e}}^{r}\left(\omega\right)=\underbrace{i\pi\,\mathrm{Re}\,\Lambda\left(\omega\right)}_{\mathrm{FR}}-\underbrace{\pi\,\mathrm{Im}\,\Lambda\left(\omega\right)}_{\mathrm{NC}}\\
+\underbrace{\pi\mathcal{H}\left[\mathrm{Re}\,\Lambda\left(\omega'\right)\right]\left(\omega\right)}_{\mathrm{RN}}+\underbrace{i\pi\mathcal{H}\left[\mathrm{Im}\,\Lambda\left(\omega'\right)\right]\left(\omega\right)}_{\mathrm{BP}}.
\qquad(7)
$$

"traditional" Joule-heating is present in the fluctuating force, f, while the current-induced forces show up in Π_{e}^{r}. Here we focus on the latter. The contribution from the electron degrees of freedom including the non-equilibrium effects can be expressed in terms of the coupling-weighted electron–hole pair density of states, Λ,

Here, FR, NC, RN, BP represent the electronic friction, nonconservative force, renormalization of the atomic potential, and Berry-phase-induced pseudo-magnetic force, respectively [12].

Run-away modes

In order to analyze the influence of the current we define the nonequilibrium phonon density of states (DOS) as,

$$ \mathrm{DOS}(\omega) = -\frac{\omega}{2\pi} \mathrm{Im}\,\mathrm{Tr}\left[\mathbf{D}^r(\omega) \right], \qquad (8) $$

where $\mathbf{D}^r(\omega)$ is the nonequilibrium phonon Greens function obtained from the SCLE,

$$ \mathbf{D}^r(\omega) = \frac{1}{(\omega + i\eta)^2 - \mathbf{K} - \mathbf{\Pi}^r(\omega)}. \qquad (9) $$

Note that we introduced boldface to underline that these are matrices with mode-index (k,l). Contrary to the equilibrium situation, the DOS given in Equation 8 can take negative values at certain peak values, due to the electronic current. We can interpret a negative peak in the DOS at a frequency ω_0 as modes at ω_0 with a negative lifetime, i.e., with growing in amplitude as a function of time and denote these by "run-away" modes.

Mode analysis

In order to identify the modes that can show run-away behavior, we need to find the solutions to Equation 1 by setting the driving noise force, $f(\omega)$, to zero. This is done by treating the velocity and displacement as independent variables and use the relation $-i\omega U(\omega) = \dot{U}(\omega)$ to obtain the double-sized eigenvalue problem. However, the self-energy $\mathbf{\Pi}^r$ is frequency-dependent. Thus, to analyze a specific runaway mode giving rise to a negative peak in Figure 2a (see below), we evaluate the self-energy at the negative peak frequency ω_0 as given below in Equation 10,

Thus, the dynamical matrix is renormalized by $\mathrm{Re}[\mathbf{\Pi}_{\mathrm{ph}}^r(\omega_0) + \mathbf{\Pi}_{\mathrm{e}}^r(\omega_0)]$ and the friction originates from $\mathrm{Im}[\mathbf{\Pi}_{\mathrm{ph}}^r(\omega_0) + \mathbf{\Pi}_{\mathrm{e}}^r(\omega_0)]/\omega_0$. Solving Equation 10 gives a set of eigenmodes and complex eigenfrequencies, but only the "self-consistent" mode, which fulfills $\mathrm{Re}(\omega) = \omega_0$, is relevant.

For a given eigenmode a corresponding positive imaginary part of the eigenfrequency designates that the mode is a run-away mode, while if the imaginary part is negative the mode is damped. The damping can be quantified by the inverse Q-factor giving the change in energy per period

$$ Q_i^{-1} = \left(2\pi \frac{\Delta E_i}{E_{i,\mathrm{tot}}} \right)^{-1} = -\frac{2\,\mathrm{Re}\,\omega_i}{\mathrm{Im}\,\omega_i}. \qquad (11) $$

Thus, the run-away modes can be identified as the modes where $\mathrm{Im}(\omega) > 0$. The run-away modes are a linear combination of the non-perturbed normal modes. Normally, the runaway makes closed loops in real or in abstract mode space. Thus, the NC force allows the mode to pick up energy every time a loop is completed, eventually leading to break down of the harmonic approximation, ending with, e.g., rupture or damping by anharmonic effects leading to a limit cycle motion [24].

Numerical Calculation

We have calculated the electronic and phononic structure of the graphene nanoribbon from density function theory (DFT) using the SIESTA/TranSIESTA codes [25,26]. The generalized gradient approximation is used for the exchange–correlation functional, and a single-ζ polarized basis set is used for the carbon and hydrogen atoms. A cut-off energy of 400 Ry is used for the real-space grid. The electron-vibrational coupling is calculated using the INELASTICA package, which uses a finite difference scheme [27].

Results and Discussion

The partially dehydrogenated graphene nanoribbon we considered is shown in Figure 1a, where four hydrogen atoms have been removed on each side of the ribbon. In principle, dehydrogenation could be performed at chosen positions with an STM [28]. The same structure has been considered in our recent work, focusing on the asymmetry in phonon emission and heat

$$ \begin{bmatrix} \mathbf{0} & -\mathbf{1} \\ \mathbf{K} + \mathrm{Re}\left[\mathbf{\Pi}_{\mathrm{ph}}^r(\omega_0) + \mathbf{\Pi}_{\mathrm{e}}^r(\omega_0) \right] & -\mathrm{Im}\left[\mathbf{\Pi}_{\mathrm{ph}}^r(\omega_0) + \mathbf{\Pi}_{\mathrm{e}}^r(\omega_0) \right]/\omega_0 \end{bmatrix} \begin{bmatrix} U(\omega) \\ \dot{U}(\omega) \end{bmatrix} = i\omega \begin{bmatrix} U(\omega) \\ \dot{U}(\omega) \end{bmatrix}. \qquad (10) $$

distribution due to the nonequilibrium for lower voltage than where run-away instability occurs [29]. This asymmetry is intrinsically linked to momentum transfer from electrons to phonons and thus to the nonconservative current-induced forces ("electron wind") [30]. As we mentioned before, the reason we choose this structure is that the dehydrogenated carbon dimers can be considered as "defects" in the armchair ribbon. In general defects give rise to modes localized around the defect. They originate from the local change in force constants shifting the mode out of its unperturbed subband [31].

The relative motion of the two carbon atoms in each dimer only couples weakly to the motion of neighbouring dimers and to the phonons in the leads. This high-energy mode is shifted out of the entire phonon bandstructure. Meanwhile, the flowing electrical current passing through these dimers introduce a small bias-dependent coupling via the self-energy ($\mathbf{\Pi}_e$) in Equation 10. In principle, one can tune the relative distance between different dimers by changing the ribbon width or the position of the dehydrogenation. It is an ideal and clean system to study the current-induced atomic dynamics, with some tunability since one may imagine doping or gating to shift the Fermi level, E_F, as well as changes in geometry such as varying the distance between dimers.

In this study, the nanoribbon has a width of 7 dimers corresponding to a C–C edge distance of 7.5 Å. The lateral confinement introduces a direct semi-conducting band gap, giving rise to the gap in the electronic transmission for the perfect ribbon as shown in Figure 1b. We have introduced a broadening of the electronic states as in Christensen et al. [6] to mimic coupling to metallic electrodes. This in effect smoothens the transmission curves Figure 1b (dotted lines) akin to the experimental conductance [5]. The introduction of the defects results mainly in a potential shift, but besides this does not impact the transmission dramatically, as seen in Figure 1b (solid lines).

In order to characterize the phonons we show the phononic transmission in Figure 1c. The phonon transmission shows a significant reduction of approx. 50% for $\hbar\omega$ above 25 meV. The fact that we see little difference between a perfect and a defect system at low phonon energy is expected when the wavelength is much larger than the defect. We note that, ideally, the translation (T) in the three spatial directions and rotation around the longitudinal direction of the GNR should lead to perfect $T = 4$ at $\hbar\omega$, equal exactly to zero for both pristine and defected structure. The deviation is due to our numerical neglect of long-range elastic forces. However, while the low energy/long wavelength modes are important for heat transport, we are here concerned with modes with a higher frequency above 25 meV, where the calculation is expected to be accurate.

The influence of the current-induced forces on the phonon self-energy depend on the underlying electronic properties. Thus, besides the unperturbed phonon DOS exclusive the current-induced forces (black solid line in Figure 2a), we also calculate the non-equilibrium DOS using Equation 8 shifting the Fermi energy away from the gap to $E_F = -1.4$ eV (green dotted line) and $E_F = 1.4$ eV (red dashed line), and applying a bias of $V_b = 0.5$ V. Comparing these results, we see that there are several run-away modes (negative peaks) for $E_F = 1.4$ eV, but not for $E_F = -1.4$ eV. In Figure 2b and Figure 2e we show two typical run-away modes marked as 1 and 2 in Figure 2a. In

Figure 2: (a) The black solid line shows the phonon density of states excluding the self-energy due to the electronic degrees of freedom. The green dotted and the red dashed lines show the phonon DOS including the current-induced forces for an applied bias of 0.5 V, shifting the Fermi energy to $E_F = -1.4$ eV and $E_F = 1.4$ eV, respectively, corresponding to the vertical lines in Figure 1b; (b) the run-away mode giving rise to the dip in (a) indicted by arrow 1 ($Q \approx 10^{-3}$); (c,d) the most important normal modes taking part in (b); (e) the run-away mode giving rise to the dip in (a) indicted by arrow 2 ($Q \approx 0.5 \cdot 10^{-3}$); (f–h) the normal modes taking part in (b).

Figure 2c,d and Figure 2f–h, we also plot the "bare" normal modes (without coupling to electron and phonon baths), which give the largest contribution to the two selected run-away modes. These run-away modes have in common that they are spatially localized, meaning a vanishing damping due to the coupling to the phonon reservoirs, which is a prerequisite for the run-away instability here. The driving of the motion by the current has to exceed this damping. Both run-away modes involve mainly the dehydrogenated carbon dimers, but while mode 2 lies outside the bulk phonon bands and is thus localized, the frequency of mode 1 is well within the entire phonon band, illustrating that this is not a necessary requirement. In the case of 1 the localization is due to a shift out of a ribbon phonon sub-band. Most of the "bare" normal modes (Figure 2c,d and Figure 2f–h contributing to run-away motion can be considered as a in or out of phase combination of different dimer vibrations.

The two selected modes illustrate how the run-away modes can display circular motion in real-space or in abstract mode space. For the modes showing circular motion it is intuitively clear why these have been dubbed "water-wheel" modes [10], and that the direction of rotation is linked to the direction of current via (angular) momentum transfer [30]. Mode 1 is made up by two principal bare modes, while mode 2 does so in abstract mode space, and consists of mainly three bare modes. In both cases the nonconservative force pump energy into these modes when they oscillate around closed loops. We note that anharmonic coupling will lead to additional damping, which is not included in the harmonic approximation applied here, but we expect a lower anharmonic coupling to the mode well outside the bulk band (mode 2) due to the frequency mismatch. The structure we consider has mirror symmetry in the lateral direction perpendicular to the transport. The resulting motion of the run-away mode respects this symmetry. But, the motion along the current direction is asymmetric since the current breaks the symmetry. This is more obvious for mode 1 (Figure 2c). Mode 2 is strictly localized in the center, but mode 1 has weak coupling to the leads. Consequently, mode 1 shows larger asymmetry. We should mention that this asymmetry in the local heating already shows up before the run-away modes emerge [29].

Conclusion

In conclusion, we have studied the effect of current-induced forces on the dynamics of dehydrogenated carbon dimers at the edges of graphene armchair ribbon. These carbon dimers are weakly coupled to each other and the rest of the carbon atoms, but they interact with the electrical current. This induces effective coupling between them, and the nonconservative and effective magnetic force become important in describing their

dynamics. Using a simplified eigenmode analysis, we analyze how the carbon dimer motion is modified by these forces at different Fermi level positions. The possibility of observing the atomic structure of the two-dimensional structures in microscopy, gating or doping, and atomic scale modification of graphene ribbon boundaries makes it an ideal candidate to study current-induced forces in nanoconductors, where interesting theoretical predictions are awaiting for experimental confirmation.

So far current-induced motion and desorption have been observed around edges in graphene sheets [7,8]. One signature of the nonconservative forces is, besides the asymmetry build into the momentum transfer, the highly non-linear heating of modes with bias [11], which in principle could be observed around edges [32].

References

1. Castro Neto, A. H.; Guinea, F.; Peres, N. M. R.; Novoselov, K. S.; Geim, A. K. *Rev. Mod. Phys.* **2009,** *81,* 109. doi:10.1103/RevModPhys.81.109
2. Cai, J.; Ruffieux, P.; Jaafar, R.; Bieri, M.; Braun, T.; Blankenburg, S.; Muoth, M.; Seitsonen, A. P.; Saleh, M.; Feng, X.; Müllen, K.; Fasel, R. *Nature* **2010,** *466,* 470–473. doi:10.1038/nature09211
3. Cai, J.; Pignedoli, C. A.; Talirz, L.; Ruffieux, P.; Söde, H.; Liang, L.; Meunier, V.; Berger, R.; Li, R.; Feng, X.; Müllen, K.; Fasel, R. *Nat. Nanotechnol.* **2014,** *9,* 896–900. doi:10.1038/nnano.2014.184
4. Liu, J.; Li, B.-W.; Tan, Y.-Z.; Giannakopoulos, A.; Sanchez-Sanchez, C.; Beljonne, D.; Ruffieux, P.; Fasel, R.; Feng, X.; Müllen, K. *J. Am. Chem. Soc.* **2015,** *137,* 6097–6103. doi:10.1021/jacs.5b03017
5. Koch, M.; Ample, F.; Joachim, C.; Grill, L. *Nat. Nanotechnol.* **2012,** *7,* 713–717. doi:10.1038/nnano.2012.169
6. Christensen, R. B.; Frederiksen, T.; Brandbyge, M. *Phys. Rev. B* **2015,** *91,* 075434. doi:10.1103/PhysRevB.91.075434
7. Jia, X.; Hofmann, M.; Meunier, V.; Sumpter, B. G.; Campos-Delgado, J.; Romo-Herrera, J. M.; Son, H.; Hsieh, Y.-P.; Reina, A.; Kong, J.; Terrones, M.; Dresselhaus, M. S. *Science* **2009,** *323,* 1701–1705. doi:10.1126/science.1166862
8. Engelund, M.; Fürst, J. A.; Jauho, A. P.; Brandbyge, M. *Phys. Rev. Lett.* **2010,** *104,* 036807. doi:10.1103/PhysRevLett.104.036807
9. Gunst, T.; Lü, J.-T.; Hedegård, P.; Brandbyge, M. *Phys. Rev. B* **2013,** *88,* 161401. doi:10.1103/PhysRevB.88.161401
10. Dundas, D.; McEniry, E. J.; Todorov, T. N. *Nat. Nanotechnol.* **2009,** *4,* 99–102. doi:10.1038/NNANO.2008.411
11. Lü, J.-T.; Brandbyge, M.; Hedegård, P. *Nano Lett.* **2010,** *10,* 1657–1663. doi:10.1021/nl904233u

12. Lü, J.-T.; Brandbyge, M.; Hedegård, P.; Todorov, T. N.; Dundas, D.
    Phys. Rev. B **2012,** *85,* 245444. doi:10.1103/PhysRevB.85.245444
13. Dundas, D.; Cunningham, B.; Buchanan, C.; Terasawa, A.;
    Paxton, A. T.; Todorov, T. N. *J. Phys.: Condens. Matter* **2012,** *24,*
    402203. doi:10.1088/0953-8984/24/40/402203
14. Cunningham, B.; Todorov, T. N.; Dundas, D. *Phys. Rev. B* **2014,** *90,*
    115430. doi:10.1103/PhysRevB.90.115430
15. Todorov, T. N.; Dundas, D.; Lü, J.-T.; Brandbyge, M.; Hedegård, P.
    Eur. J. Phys. **2014,** *35,* 065004. doi:10.1088/0143-0807/35/6/065004
16. Bustos-Marún, R.; Refael, G.; von Oppen, F. *Phys. Rev. Lett.* **2013,**
    111, 060802. doi:10.1103/PhysRevLett.111.060802
17. Bode, N.; Kusminskiy, S. V.; Egger, R.; von Oppen, F. *Phys. Rev. Lett.*
    2011, *107,* 036804. doi:10.1103/PhysRevLett.107.036804
18. Feynman, R. P.; Vernon, F. L., Jr. *Ann. Phys.* **1963,** *24,* 118–173.
    doi:10.1016/0003-4916(63)90068-X
19. Caldeira, A. O.; Leggett, A. J. *Physica A* **1983,** *121,* 587–616.
    doi:10.1016/0378-4371(83)90013-4
20. Schmid, A. *J. Low Temp. Phys.* **1982,** *49,* 609–626.
    doi:10.1007/BF00681904
21. Head-Gordon, M.; Tully, J. C. *J. Chem. Phys.* **1995,** *103,*
    10137–10145. doi:10.1063/1.469915
22. Lü, J.-T.; Gunst, T.; Hedegård, P.; Brandbyge, M.
    Beilstein J. Nanotechnol. **2011,** *2,* 814–823. doi:10.3762/bjnano.2.90
23. Brandbyge, M.; Hedegård, P. *Phys. Rev. Lett.* **1994,** *72,* 2919–2922.
    doi:10.1103/PhysRevLett.72.2919
24. Bode, N.; Kusminskiy, S. V.; Egger, R.; von Oppen, F.
    Beilstein J. Nanotechnol. **2012,** *3,* 144–162. doi:10.3762/bjnano.3.15
25. Soler, J. M.; Artacho, E.; Gale, J. D.; García, A.; Junquera, J.;
    Ordejón, P.; Sánchez-Portal, D. *J. Phys.: Condens. Matter* **2002,** *14,*
    2745–2779. doi:10.1088/0953-8984/14/11/302
26. Brandbyge, M.; Mozos, J.-L.; Ordejón, P.; Taylor, J.; Stokbro, K.
    Phys. Rev. B **2002,** *65,* 165401. doi:10.1103/PhysRevB.65.165401
27. Frederiksen, T.; Paulsson, M.; Brandbyge, M.; Jauho, A.-P.
    Phys. Rev. B **2007,** *75,* 205413. doi:10.1103/PhysRevB.75.205413
28. Wang, Y. F.; Kröger, J.; Berndt, R.; Vázquez, H.; Brandbyge, M.;
    Paulsson, M. *Phys. Rev. Lett.* **2010,** *104,* 176802.
    doi:10.1103/PhysRevLett.104.176802
29. Lü, J.-T.; Christensen, R. B.; Wang, J.-S.; Hedegård, P.;
    Brandbyge, M. *Phys. Rev. Lett.* **2015,** *114,* 096801.
    doi:10.1103/PhysRevLett.114.096801
30. Todorov, T. N.; Dundas, D.; Paxton, A. T.; Horsfield, A. P.
    Beilstein J. Nanotechnol. **2011,** *2,* 727–733. doi:10.3762/bjnano.2.79
31. Savin, A. V.; Kivshar, Y. S. *Phys. Rev. B* **2013,** *88,* 125417.
    doi:10.1103/PhysRevB.88.125417
32. Islam, M. S.; Tamakawa, D.; Tanaka, S.; Makino, T.; Hashimoto, A.
    Carbon **2014,** *77,* 1073–1081. doi:10.1016/j.carbon.2014.06.023

Single-molecule mechanics of protein-labelled DNA handles

Vivek S. Jadhav[‡1,2], Dorothea Brüggemann[‡1,3], Florian Wruck[1] and Martin Hegner[*1]

Abstract

DNA handles are often used as spacers and linkers in single-molecule experiments to isolate and tether RNAs, proteins, enzymes and ribozymes, amongst other biomolecules, between surface-modified beads for nanomechanical investigations. Custom DNA handles with varying lengths and chemical end-modifications are readily and reliably synthesized en masse, enabling force spectroscopic measurements with well-defined and long-lasting mechanical characteristics under physiological conditions over a large range of applied forces. Although these chemically tagged DNA handles are widely used, their further individual modification with protein receptors is less common and would allow for additional flexibility in grabbing biomolecules for mechanical measurements. In-depth information on reliable protocols for the synthesis of these DNA–protein hybrids and on their mechanical characteristics under varying physiological conditions are lacking in literature. Here, optical tweezers are used to investigate different protein-labelled DNA handles in a microfluidic environment under different physiological conditions. Digoxigenin (DIG)-dsDNA-biotin handles of varying sizes (1000, 3034 and 4056 bp) were conjugated with streptavidin or neutravidin proteins. The DIG-modified ends of these hybrids were bound to surface-modified polystyrene (anti-DIG) beads. Using different physiological buffers, optical force measurements showed consistent mechanical characteristics with long dissociation times. These protein-modified DNA hybrids were also interconnected in situ with other tethered biotinylated DNA molecules. Electron-multiplying CCD (EMCCD) imaging control experiments revealed that quantum dot–streptavidin conjugates at the end of DNA handles remain freely accessible. The experiments presented here demonstrate that handles produced with our protein–DNA labelling procedure are excellent candidates for grasping single molecules exposing tags suitable for molecular recognition in time-critical molecular motor studies.

Introduction

Most mechano-enzyme and protein–DNA interaction studies using optical tweezers (OT) are performed in a dumbbell configuration, where a single or double-stranded DNA molecule or protein is tethered between two optically trapped beads. Alternatively, one of the two beads can be held by a micropipette via suction in a single optical trap arrangement [1]. The DNA

strand either interacts with a protein or mechano-enzyme directly or it serves as a spacer and a handle to isolate and tether a single mechano-enzyme of interest at a distance from the second bead. We here focus on the latter case and present a novel assay for reliably producing protein-labelled DNA hybrids (PDHs) to be used as molecular spacers and handles, exhibiting the necessary stability for time-critical displacement and force measurements. Streptavidin and neutravidin were used for protein labelling, acting as a molecular connection between the DNA spacer and the experimental target.

When a certain protein or enzyme of interest is tethered to surface-modified beads it is desirable to avoid unspecific surface interactions between the optically trapped spheres. This can be achieved by using single molecular handles. The use of DNA handles as molecular spacers is well documented in literature [2-8]. It may also be necessary to keep the two beads at a certain distance from each other during measurements involving large displacements, especially in dual-trap optical tweezers prone to polarization scrambling induced crosstalk [9]. In a stable and well-aligned instrument, the magnitude of the parasitic signal due to optical crosstalk is greatest when both traps overlap and reduces rapidly with increasing trap separation, oscillating about some mean value. By designing DIG-dsDNA-biotin handles (DHs) of specific lengths, one can choose a certain trap separation during experiments that minimizes contributions due to crosstalk.

DH lengths of 1000, 3034 and 4056 bp were chosen for the PDHs in this study. Short handles with greater stiffness could be produced quite easily and increase the signal-to-noise ratio (SNR) in high-resolution measurements [10]. We previously presented optical force rupture measurements of the nascent polypeptide chain from biotinylated ribosomes, which were specifically bound to surface-modified polystyrene beads [11]. While the ribosome was translating, the biotinylated lysine residue at the beginning of the nascent polypeptide chain was labelled in situ with streptavidin. This arrangement enabled us to grasp the protein chain with a DIG-DNA-Bio handle of 4056 bp length. Although we were able to study the rupture forces using this approach, the labelling of the nascent proteins during translation was not very efficient. To overcome these problems the development of mechanically stable DHs with pre-labelled protein ends were required. The constructs should enable efficient single hook-ups with the biotinylated tag of the probed biomolecule (e.g., nascent protein chain). Here, we present a labelling technique of DIG-DNA-Bio with two different proteins, streptavidin and neutravidin. Using optical tweezers the mechanical characteristics and the dissociation times of the novel DNA–protein hybrids were studied in various physiological buffers.

Experimental
Protein labelling of dsDNA and coupling to polystyrene beads

PCR amplification of plasmid pTYB1 (7477 bp, New England Biolabs, Ireland (NEB)) with 5'-biotin (5'-AAT TCT TGA AGA CGA AAG GGC GGC-3' for 4056 bp DNA and 5'-GGA TAC GAC GAT ACC GAA GAC AGC-3' for 3034 bp DNA) and 5'-thiol or 5'-DIG end-modified primers (both have the sequence 5'-TGT AAC TCG CCT TGA TCG TTG GGA-3') were used to prepare DNA molecules (4056 and 3034 bp). BSAI linearized pNEB193 plasmids (2713 bp, NEB) were used to produce the 1000 bp long dsDNA handles. Here the primers 5'-biotin CAA CTG TTG GGA AGG GCG ATC-3' and 5'-DIG-CTG TTA CCA GTG GCT GCT GCC-3' were used. The Q5-DNA polymerase (NEB) was used throughout the experiments with appropriate annealing temperatures and elongation times to produce the dsDNA fragments in a high purity and quantity. The DIG-DNA-Bio (ca. 100 nM) strands were incubated with either streptavidin (Sigma-Aldrich, Arklow, Ireland) or neutravidin (Pierce, Fisher Scientific, Dublin, Ireland) (both with approx. 60 kDa = 9.96×10^{-20} g each) at different ratios ranging from 100 to 500 proteins per DNA molecule. During incubation (30 min up to 48 h) the reactions were gently shaken to ensure efficient protein binding at the biotin end groups of the DHs at room temperature. Unbound proteins were removed using a ChargeSwitch® cleaning kit (Invitrogen, Bio-Sciences, Dun Laoghaire, Ireland). For an enhanced yield we modified the cleaning kit protocol and increased the incubation time at the binding and elution step to 15 min. The successful labelling of the DHs with proteins, compared with unlabelled DHs, was confirmed via electrophoresis in a 1% (SeaKem® Gold, Lonza Rockland, USA) and 1.8% agarose gel (NuSieve™ GTG™ Agarose, Lonza Rockland, USA) with 1× Tris-acetate-EDTA buffer (Eppendorf AG, Hamburg, Germany) using a 1 kb DNA ladder (NEB & Promega). We utilized UV–vis spectroscopy (Nanodrop spectrophotometer ND-1000, Fisher Scientific, Dublin, Ireland) to measure the concentration of the DHs and PDH constructs. These measurements were also indicative for the presence of protein after 90 min of incubation and the quality of the subsequent cleaning using the ChargeSwitch® kit.

To anchor the DIG end of the DHs we have surface-modified polystyrene beads with the antibody anti-DIG. Protein G beads of 2.9 µm or 840 nm diameter (Spherotech, Lake Forest, IL, USA) were washed by pelleting three times in PBS buffer. Anti-digoxigenin antibodies (200 µg/mL in PBS; Roche Diagnostics, Rotkreuz, Switzerland) were incubated for 1 h at room temperature and washed once by pelleting in 0.05 M sodium tetraborate, pH 8.2. The anti-DIG antibodies were then cross-linked to the protein G beads using 10 mg/mL DMP crosslinker (Pierce/Fisher Scientific, Dublin, Ireland) in 0.2 M

triethanolamine (Sigma, Arklow, Ireland). The DMP cross-linking reaction was then quenched in 0.1 M ethanolamine at pH 8.2 for 5 min pelleted and resupended in 0.05 M sodium tetraborate, pH 8.2. Non-crosslinked anti-DIG antibodies were removed by pelleting twice in 0.1 M glycine, pH 2.8. Finally the anti-DIG can be stored at 4 °C in PBS containing 0.05% sodium azide and 0.1% tween 20. Alternatively, aldehyde/sulfate latex beads with 2 µm diameter (Invitrogen, Dublin, Ireland) were used, which had been covered with anti-DIG via passive adsorption. The coupling of PDHs to anti-DIG spheres was carried out at room temperature for 90 min with different coupling ratios as discussed in the result section. We used this standardised protocol in the entire study and were able to reproduce the result multiple times (more than about 250 times) with specific interactions using the OT setup. For DNA with DIG at the 5' end and thiol at the 3' end a PCR using the 7477 bp long plasmid pTYB1 was carried out with 5'-DIG end-modified and 5'-thiol end-modified primers. Subsequently, the thiol-end was covalently coupled to amino-beads with 2.1 µm diameter (Spherotech, Lake Forest, IL, USA) using a sulfo-SMCC cross linker (Fisher Scientific, Dublin, Ireland). DIG-DNA-Thiol was activated for 1 h at room temperature with a ratio of approx. 1000 SMCC molecules per DNA as previously described [8].

Excess of SMCC was removed using a ChargeSwitch® cleaning kit, and the activated DNA was coupled to amino beads with an average of 50 DNA molecules per bead (Figure 1b).

A dsDNA linker of 24 bp length with biotinylated 3'- and 5'-ends was formed from two complementary single DNA strands (sequence: biotin-5'-AAT TCT TGA AGA CGA AAG GGC GGC-3'-biotin and its complementary sequence 5'-GCC GCC CTT TCG TCT TCA AGA ATT-3', Microsynth, Balgach, Switzerland) via thermal annealing. This linker was added to streptavidin beads of 3.1 µm diameter at a concentration of 1 µM to cover the bead surface with biotinylated linkers. In subsequent optical force measurements these bio-linker-streptavidin beads were used to enable specific interactions with the protein end of our PDHs (Figure 1c).

Lambda-dsDNA 48502 bp (Roche, Lifescience, Switzerland) was modified on either end at its cos-sites by ligating two oligonucleotides (5'-GGG CGG CGA CCT-3'-Bio and DIG-3'-CCC GCC GCT GGA-5') in an overnight reaction at 4 °C with T4 DNA ligase (Roche, Lifescience, Switzerland). Excess oligonucleotides were cleaned off by ethanol precipitation using sodium acetate as counter ions. Modified λ-DNA was resus-
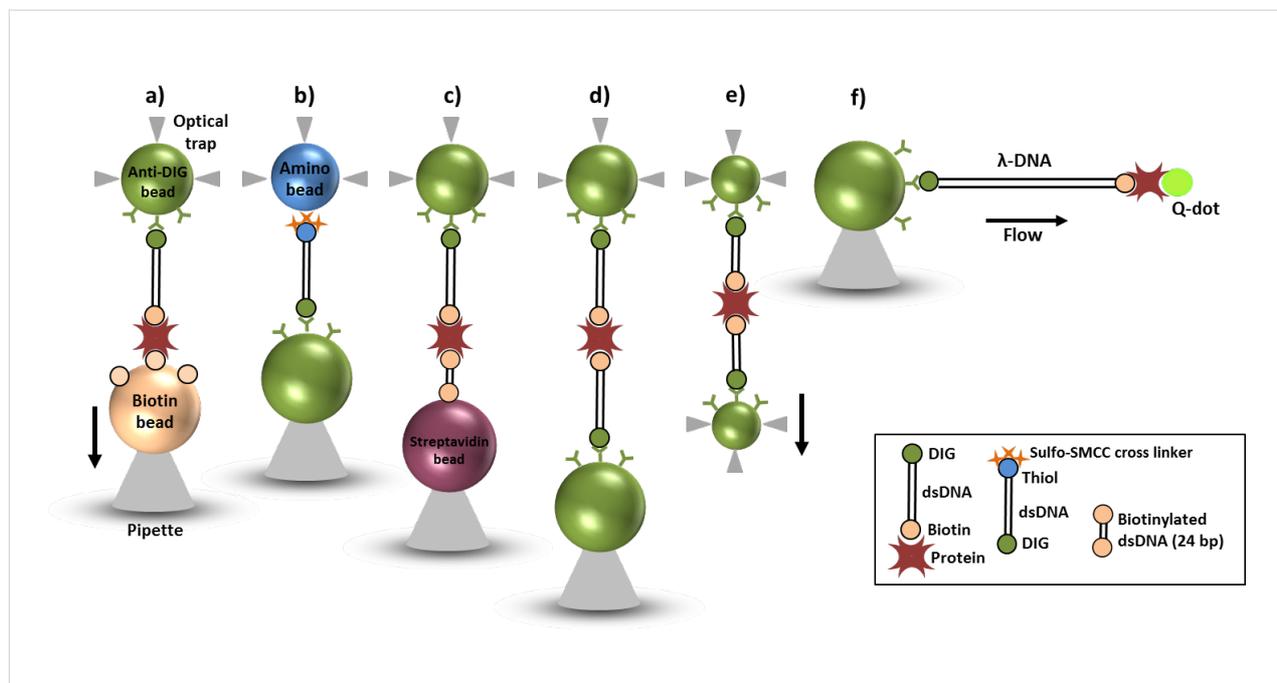
Figure 1: Bead arrangements in different optical force measurements. a) PDHs tethered to an anti-DIG bead (2.9 µm diameter) in the optical trap pulled versus a biotinylated polystyrene bead (3.2 µm). b) DIG-DNA-Thiol covalently bound to an amino bead (2.1 µm) in the trap pulled versus an anti-DIG bead (3.4 µm) in the pipette. c) Handle experiment with long DNA (3034 bp or 4056 bp) molecules: The pipette holds a streptavidin bead (3.1 µm) modified with short dsDNA linkers (24 bp) and is probed with PDHs. d) Double handle experiment with 4056 bp or 3034 bp DHs coupled to anti-DIG bead (3.4 µm) in the pipette and an anti-DIG bead (2.9 µm) of different diameter with PDHs tethered to it is optically trapped. The biotin end and the protein label are interconnected in situ to form a double-length DNA handle. e) Double-handle experiment using sub-micron beads (0.84 µm each) and short DNA molecules (1000 bp) utilizing a high-resolution dual trap OT. f) End-labelled DIG-λ-DNA-biotin bound to an anti-DIG bead (3.4 µm) held by a micropipette. Flow forces elongate the λ-DNA molecule that is tethered at one end to the microsphere. The streptavidin-modified end (labelled with quantum dots) is freely floating in the microfluidic chamber.

pended in 10 mM HEPES, 1 mM EDTA buffer, pH 7.2. The biotinylated end was modified with a 100× concentration of Qdot 525 streptavidin conjugate (Life technologies, Dublin, Ireland) (Figure 1f). Excess Qdots were washed out during the OT experiment.

Physiological buffers

Force measurements were performed in various protein translation buffers [2,11,12] in a microfluidic cell. All chemicals used in the buffer preparation were of a high purity grade and were used as received without further purification. Sodium chloride (≥98%), HEPES (BioUltra ≥99.5%), magnesium acetate tetrahydrate (99%), ammonium acetate (98%), 2-mercaptoethanol (BioUltra ≥99.0%) and DL-dithiothreitol (BioUltra ≥99.5%) were provided from Sigma-Aldrich (Dublin, Ireland). All aqueous solutions were prepared using nanopure water from a Millipore Milli-Q system, additionally filtered with 0.22 μm pore size filters. We used TICO buffer (20 mM HEPES-KOH, pH 7.5, 6 mM magnesium acetate, 30 mM ammonium acetate, 4 mM 2-mercaptoethanol) to examine various coupling ratios of PDHs to anti-DIG beads for the subsequent biotin-streptavidin binding in OT experiments. All experiments were also performed in TICO buffer with an increased Mg content of 12 mM (high Mg TICO). Control experiments were carried out in standard buffer (150 mM NaCl, 10 mM HEPES, pH 7.5) and in DTT buffer (40 mM HEPES-KOH, pH 7.5, 60 mM NH_4Cl, 10 mM magnesium acetate, 1 mM DTT and 3.6 mM 2-mercaptoethanol) (adapted from [12]).

Optical force measurements

Measurements of the DNA mechanics were performed with a previously described counter-propagating dual-beam OT setup [13] (Figure 1a–d, f) and a high resolution dual trap OT device [14] (Figure 1e). The PDHs coupled to anti-DIG spheres were injected into a microfluidic cell chamber placed in-between two identical water immersion microscope objectives and the beads were optically trapped. For experiments with PDHs (to confirm protein modification (streptavidin or neutravidin) at the biotin end of the DNA handle) a biotin coated bead of 3.2 μm diameter (Spherotech, Lake Forest, USA) was held in a micropipette by suction (Figure 1a).

An anti-DIG bead covered with the PDH constructs was injected and optically trapped. The protein label at the 3' end of the bead-coupled DNA strand was tethered to a biotin-coated bead, by bringing both beads within close proximity of each other (a few hundred nanometres). The position of this pipette was controlled with a closed-loop piezoelectric element, during force–displacement measurements the bead in the pipette was moved away from the trapped bead at a constant velocity of 100 nm/s and force signals were low-pass filtered at 159 Hz.

The setup directly measured the change in light momentum flux when the trapped bead experienced a lateral force [13]. Control experiments were carried out to check for specific interactions between the PDH constructs (bound to anti-DIG beads) and streptavidin surface-modified beads (3.1 μm diameter, Spherotech, Lake Forest, USA), no interactions were observed. Protein labelling at the biotinylated ends of the DNA constructs was essential, as ends that are not protein-labelled could lead to false positive interactions between the bare biotinylated DNA ends and streptavidin or neutravidin surface-modified beads or molecules.

To characterize the binding strength of the DIG::anti-DIG bond (the weakest link in the molecular construct) we trapped amino beads covalently coupled to DIG-DNA-Thiol handles and tethered those in situ to anti-DIG beads (2.9 μm diameter) held in place through suction by a pipette (Figure 1b). In the configuration shown in Figure 1c we could test the protein-modified end of the PDHs when no short dsDNA linker molecules were implemented (not shown) and test configurations in which a prospective biomolecular construct was directly grafted to the sphere surfaces. To simulate in situ tethering to complex biomolecules, we used PDHs to grasp single DNA molecules in situ (Figure 1d,e). For experimental configurations illustrated in Figure 1d, we held DHs tethered to anti-DIG beads (3.4 μm diameter) in the pipette. Then, smaller anti-DIG beads (2.9 μm diameter) with PDHs were optically trapped to obtain hook-ups between the protein label and the biotin end of the molecule at the pipette-held bead. In Figure 1e the same configuration was tested using the 1000 base pair PDHs in a dual-trap configuration. Because the in situ tethering took place between individual molecules suspended within the inter-bead liquid (Figure 1d,e) compared to the configurations shown in Figure 1a–c the hook-up times were generally longer, on the order of approx. 2 min.

For proof-of-concept that the PDH end remains freely accessible in liquids, the biotin end of the DH was labelled with streptavidin–Qdot conjugates. Then, they were anchored to anti-DIG beads (Figure 1f), and the position of individual Qdots under varying fluid flow velocities was monitored using an EMCCD camera (Andor Technology, Belfast, NI). Laminar fluid flow inside the microfluidic chamber constrained the free Qdot-modified end of the DNA within the image plane of the EMCCD camera (Figure 8). The distance between the bead surface and the position of the Qdot represented the fluid-flow dependent DNA extension, corresponding to the hydrodynamic drag experienced by the DNA molecule. The flow force induced stretching as presented here is consistent with the original experimental findings by Perkins et al. [15] and follows the theoretical description of Stigter et al. [16].

Results and Discussion
Protein labelling of dsDNA

Labelling of protein to DIG-DNA-Bio (4056, 3034 and 1000 bp) was carried out as discussed in the Experimental section. The labelled and unlabelled PDHs were analysed using electrophoresis in a 1.8% (for 1000 bp) and 1% (for 4056 bp) agarose gel and UV–vis absorption spectra. The mobility of the PDHs was expected to be less than that of the unlabelled DIG-biotin strands and was confirmed with band shifts in agarose gel electrophoresis tests (Figure 2). 1.8% (a) and 1% gel (b) images are shown next to each other, these shifts are more prominent in gel lanes 2 and 3 where the bare 1000 bp dsDNA population is compared with streptavidin protein conjugated 1000 bp dsDNA. The proportional band shifts in the DNA–protein hybrid constructs with 4056 bp DHs are also seen in lane 5 and 6, where bare DIG-DNA-Bio is compared with protein-labelled DIG-DNA-Bio. This is within the limitation of the size/charge discrimination of the agarose gel technology. The PDHs analysed in lane 3 showed that a small portion of the modified dsDNA molecules formed double handles linked by streptavidin when an incubation ratio of 100:1 proteins per dsDNA was used. Densitometry analysis of the 1.8% gel image using ImageJ revealed that less than 5% of the molecules resulted in double length molecules. The integrated values of the analysed individual bands are: lane 2 – 12500 a.u., lane 3a – 11100 a.u. and 3b – 1100 a.u. Here, 1100 a.u. in lane 3b correspond to the double-length molecule of 2000 bp, consequently resulting in twice the fluorescence intensity. The densitometry analysis also confirmed that the purified PDH constructs were representing over 99% PDHs, and no observable 'naked' modified dsDNA remained in the sample.

The yield of PDHs after 90 min of incubation was approx. 10 nM when 100 nM of DHs were used, no significant increase in the yield of protein labelled DNA molecules was observed, when the reaction time was extended from 90 min to 48 h. Shorter incubations resulted in lower yields of PDHs. Reactions with nominal ratios of 300 and 500 protein molecules per DNA showed higher purification losses and yielded lower concentrations of PDHs than incubations where 100 proteins per DNA were used. Low coupling ratios such as 10, 20 and 50 proteins per DNA, resulted in very low specific hook-up rates to biotin beads/handles, probably due to the greater number of DNA molecules (>1) per protein. Also, the number of unlabelled DNAs could be too high, resulting in too many unwanted interactions with streptavidin-coated beads. We assume that the cleaning procedure with the ChargeSwitch® kit becomes less efficient when coupling ratios greater than 100:1 are used in the reaction volume, since they lead to a higher total loss of PDHs during cleaning. These observations were independent of the respective protein (streptavidin or neutravidin) used.
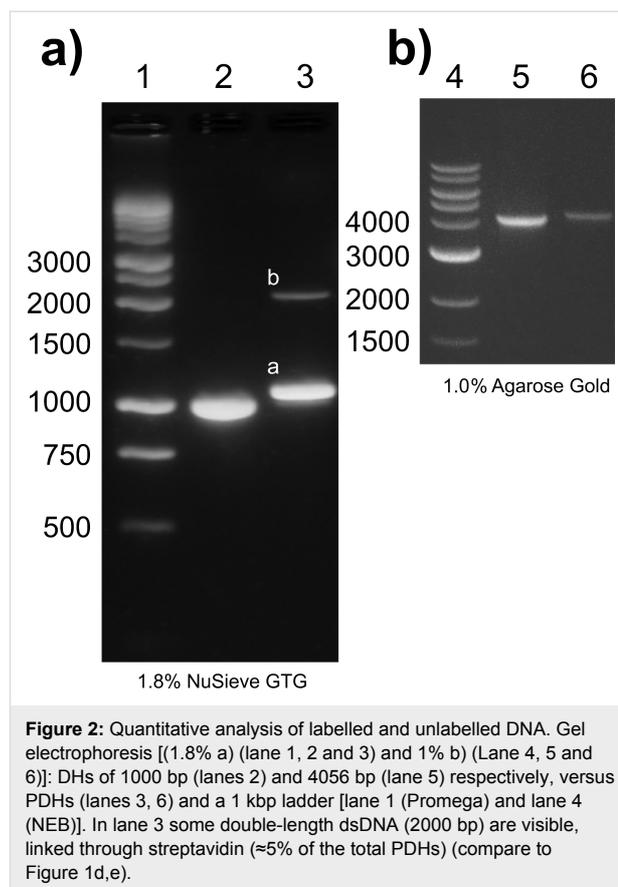
Figure 2: Quantitative analysis of labelled and unlabelled DNA. Gel electrophoresis [(1.8% a) (lane 1, 2 and 3) and 1% b) (Lane 4, 5 and 6)]: DHs of 1000 bp (lanes 2) and 4056 bp (lane 5) respectively, versus PDHs (lanes 3, 6) and a 1 kbp ladder [lane 1 (Promega) and lane 4 (NEB)]. In lane 3 some double-length dsDNA (2000 bp) are visible, linked through streptavidin (≈5% of the total PDHs) (compare to Figure 1d,e).

Optical force measurements with protein-labelled DNA

The overall rate of specific interactions was examined by modifying the coupling ratio of PDH to anti-DIG beads. During 90 min of incubation the various PDH constructs were tethered to anti-DIG beads (2.9 μm diam.) with nominal ratios of 20, 40 and 80 molecules per bead. Optical force measurements of these constructs were carried out in different buffers (Table 1) versus biotin microspheres (Figure 1a), and interaction rates as well as rupture and plateau forces were compared. The interaction rate was calculated by dividing the number of specific interactions (i.e., DNA hookup and elongation) and the number of approaches.

The force measurements repeatedly yielded evidence of specific protein–biotin interactions, often with typical force–extension curves (Figure 3). The PDHs were overstretched at around 60–65 pN, a force range in good accordance with previous studies [17,18]. In many experiments rupture forces below 60 pN were observed due to the increasing loading-rate before the dsDNA strands were overstretched. The weakest linkage of the molecular construct is between DIG and the anti-DIG antibody [19]. In TICO buffer we found a stretch modulus of ca. 800 pN while measurements in high Mg TICO yielded approx.

1000 pN an increase consistent with previous studies [17,20]. The persistence lengths of force curves measured in TICO and high Mg TICO are 50 ± 3.5 nm (SD) [18,21].

Figure 3: Characteristic force–extension curve. The biotin bead interacting with the protein moiety by molecular recognition is moved away from the DNA-labelled bead in the trap at a constant velocity of 100 nm/s until rupturing occurs. Lower pulling speeds, e.g., 10 nm/s and 50 nm/s were tested and resulted in similar force versus extension plots.
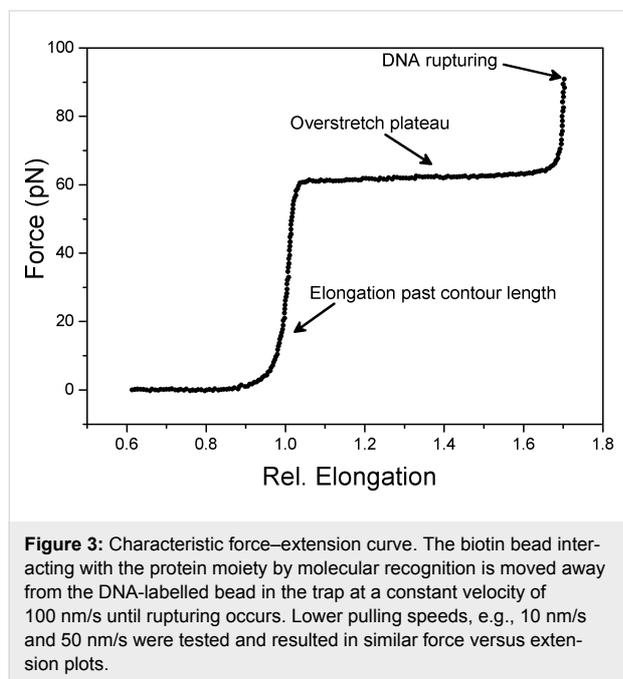
With the lowest coupling ratio of 20 DNA molecules tethered to one anti-DIG sphere (20:1) the successful hook-up rate was between 18% for neutravidin-DNA and 25% for streptavidin-DNA in TICO buffer. With high Mg TICO buffer both PDHs yielded 35% of specific DNA interaction. These interaction ratios were rather low for studying the force characteristics of PDHs. Subsequently, with a 80:1 coupling ratio, the number of specific force interactions increased from 25 to 50% for streptavidin and 18 to 64% for neutravidin in TICO buffer and 35 to 87% and 35 to 60% in high Mg TICO for streptavidin and neutravidin-DNA, respectively.

However, multiple rupture events were observed with this coupling ratio (80:1) because several DNA strands were tethered between the two beads. These multiple interactions impeded the study of single molecule mechanics. Ideal experimental conditions with protein–DNA handles allowing for single hook-up experiments were then found with 40:1 handle-to-bead cou-

pling ratio (bead diameter 2.9 μm). For smaller beads (0.84 μm diam.) the optimal ratio of PDHs coupling to beads was determined to be around 100:1.

In TICO streptavidin–DNA yielded specific interactions in 52% of the measurements while neutravidin-DNA showed 49% interactions with the ratio 40:1. The interaction rates were greater in high Mg TICO (streptavidin-DNA 66%, neutravidin-DNA 63%) as compared to 6 mM TICO buffer. However, a strong tendency of unfavourable bead clustering was witnessed in the microfluidic channel of our flow cell when DNA tethering and optical trapping were performed in high Mg TICO buffer. For future experiments involving the ribosomal machinery we therefore recommend the use of TICO buffer.

For the optimum DNA tethering ratio of 40:1, we also performed optical force measurements in standard buffer and in DTT buffer (Table 1). In standard buffer very high interaction ratios were obtained (streptavidin-DNA 79%, neutravidin-DNA 81%), and clustering only occurred in 16–17% of the experiments for both protein labels. With DTT buffer the interaction rate was only 53% for neutravidin-DNA and 61% for streptavidin-DNA, and bead clusters were observed in 20–35% of the experiments. A nominal ratio of 40:1 enabled efficient single molecule force measurements (90%) with the complete protein-labelled DNA construct against biotinylated beads (Figure 1a).

Rupture forces were analysed in all buffers for DHs with streptavidin or neutravidin labels, respectively. Rupture force distributions for both protein labels are shown in Figure 4. The rupture force distributions for both protein–DNA constructs were very wide with average rupture forces of around 60–65 pN in all buffers. Data representing the four individual buffer experiments could be merged since the individual histograms exhibited comparable appearance. It can be seen from the distribution peaks in Figure 4 that the rupture forces of streptavidin constructs were comparable to neutravidin hybrids. The pulling speed for all these measurements was constant at 100 nm/s but the loading rate varied depending on the relative elongation of the dsDNA at the rupturing point. The loading rate is the most relevant factor. Therefore in the molecular unbinding experiments shown here (Figure 4b1–b4) the rupture force distribu-

Table 1: Interaction rate of streptavidin- and neutravidin-DNA coupled to anti-DIG beads with the ratio 40:1 in various buffers.

interaction ratio 40:1	TICO percentage % (absolute #)	high Mg TICO	standard buffer	DTT buffer
streptavidin	52% (48)	66% (52)	79% (97)	61% (89)
neutravidin	49% (70)	63% (67)	81% (68)	53% (72)

Figure 4: Selected force distributions for protein–DNA coupled to anti-DIG beads with the ratio 40:1. a) Combined rupture forces of streptavidin-DNA (b1 and b2) and neutravidin-DNA (b3 and b4) (*N* = 176; 88 measurements per PDH, bin size 5). b1) Rupture forces of streptavidin-DNA in high Mg TICO (34 force measurements, bin size 5). b2) Distribution of rupture forces for streptavidin–DNA in DTT buffer (54 measurements, bin size 5). b3) Rupture forces of neutravidin–DNA in TICO (34 measurements, bin size 5). b4) Rupture forces of neutravidin–DNA in standard buffer (54 measurements, bin size 5).

tions exhibited a maximum shortly at the highest loading rate before the force induced overstretch transition of the dsDNA at about 62 pN [17,22]. Maximum rupture forces of up to 120 pN occurred when the protein-labelled molecules could be stretched past the overstretch plateau. Considering the weaker nature of the non-covalent DIG::anti-DIG bond compared to covalent coupling where up to 200 pN can be reached [23,24], rupture forces of 120 pN underlines the mechanical strength of the protein-labelled molecules designed in this study.

To characterise the strength of the non-covalent DIG::anti-DIG coupling we studied the force characteristics of DIG-DNA-Thiol handles that were covalently coupled to amino beads with an average ratio of 50 DNA molecules per amino bead [8]. The construct was expected to rupture at the DIG::anti-DIG bond because the covalent thiol-amino bond is the more durable link in this configuration [23,25]. We pulled the DIG-Thiol handles versus anti-DIG beads (Figure 1b) in TICO and in standard buffer. The distribution of rupture forces for the DIG-Thiol constructs is shown in Figure 5. Most ruptures occurred at around 60 pN with maximum rupture forces of up to 115 pN. This force distribution accords with the results obtained using our PDHs, thus indicating that the DIG::anti-DIG bond is the weakest link in these constructs and the place where the molecules rupture [24]. When the anti-DIG antibody was not covalently linked to the protein G spheres, the average rupture forces were also observed to be around 60 pN. This observation indicates that the protein G interacting with the Fc part of the antibody ruptures earlier when no DMP crosslinking step was performed. Therefore, covalent crosslinking of the antibody to beads that are modified with protein G is advised.

Figure 5: Optical force measurements of DIG-DNA-Thiol. Distribution of rupture forces for DIG-DNA-Thiol pulled versus anti-DIG beads (72 measurements, bin size 5). The average rupture force is around 60 pN with maximum forces reaching up to 115 pN. Pulling speed 100 nm/s.
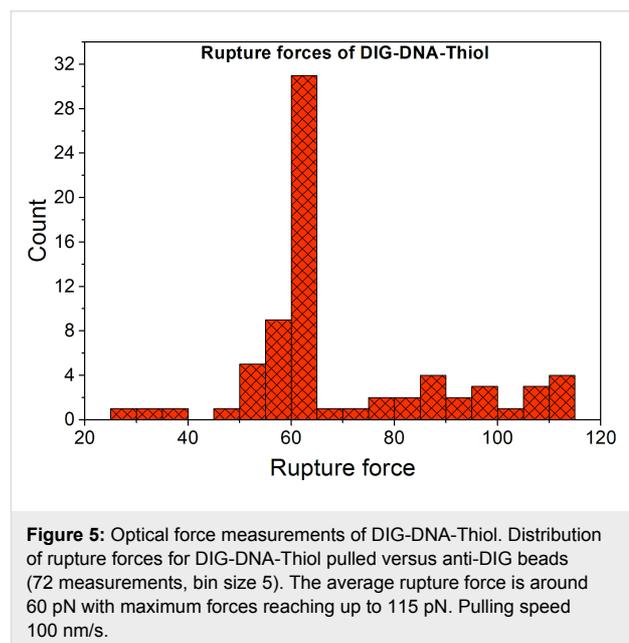
We examined the dissociation time of PDH constructs with different lengths in TICO buffer with a constant bead-bead displacement by measuring the force as a function of time until the molecule ruptured (Figure 6a). With initial forces of 20 pN applied to 4056 bp streptavidin-labelled DHs we have checked the mean stability of DIG::anti-DIG bond in TICO buffer against biotinylated beads (Figure 1a). It can be clearly seen that at lower forces (20 pN) the mean stability and dissociation time of DIG::anti-DIG averaged around 50 min. Exposing the constructs to constant forces below 20 pN resulted in much longer stable connections. Increasing the constant applied forces
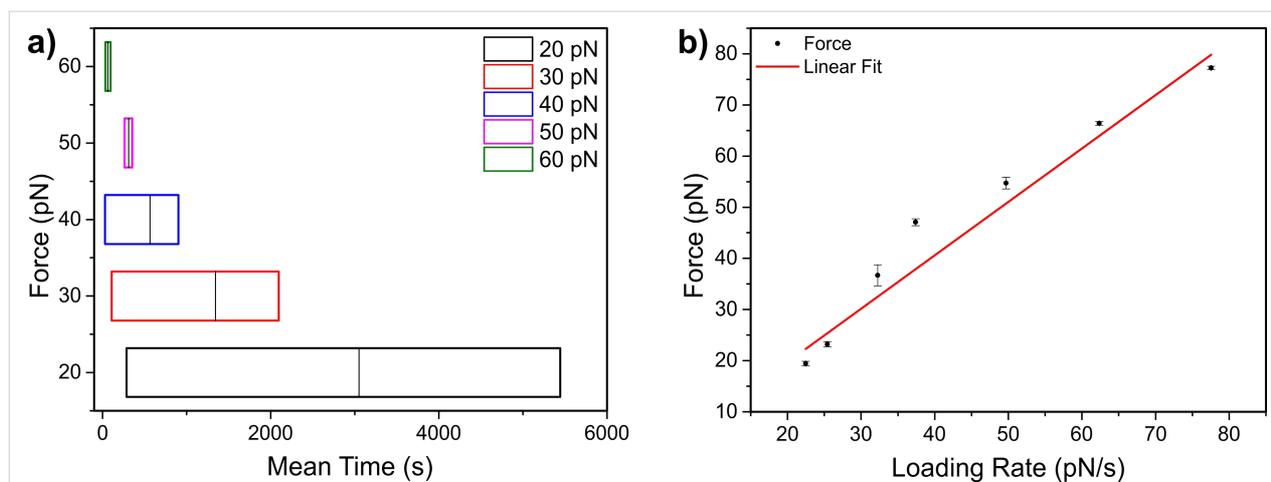
Figure 6: Studying the stability and force-induced disruption of streptavidin-labelled DNA handles in TICO buffer. a) Constant-force measurements were conducted to check the stability of the DIG::anti-DIG bond for a range of different applied tensions over time. The mean dissociation times to rupture individual PDHs are shown as vertical lines, the coloured boxes highlight the range of 25–75% of the fitted Gaussian distribution. b) Measured rupture forces plotted against loading rates. Laser tweezers analyses of streptavidin-labelled DNA handles identified rupture forces ranging from 25–110 pN during a constant elongation velocity of 100 nm/s, with correspondingly varying loading rates. The loading rate (pN/s) was highest shortly before the dsDNA underwent the overstretching transition. The individually measured rupture forces at a specific loading rate were averaged. Error bars represent the SD of the individual means.

on these particular constructs resulted in earlier rupturing of the tethers. Such long dissociation times will enable the use of these PDHs in constant force experiments in time critical motor protein studies. In Figure 6b, we show the rupture forces dependency of the streptavidin modified dsDNA handles on the loading rate [26-28] the results are comparable to a recent study of Sitters et al. [29].

Protein–DNA handles for grasping single molecules

As an application of our PDHs, we employed these constructs to grasp the biotin end of a DH as shown in Figure 1d,e. When connecting the two DHs the contour length of the newly formed double handle was expected to be doubled. This change in molecular length should also become apparent in the measured overstretch plateau length, which corresponds to approx. 70% of the contour length of a DNA molecule as previously reported [17,30,31]. Figure 7a shows a force–extension curve of a double handle formed by DHs and PDHs, each 4056 bp long (1379 nm each, Figure 1d). With more than 1800 nm the plateau length of this double DNA construct was twice the length of the characteristic value of 965 nm for one single handle. This double-plateau length indicates that the connection between the two molecules had successfully taken place in situ. Furthermore, we used PDHs with 4056 bp length to interconnect with short biotinylated dsDNA handles of 24 bp length, which were tethered to streptavidin spheres (Figure 1c). This experimental setup also yielded specific interactions with force–extension curves displaying characteristic force plateaus (Figure 7b). The successful tethering of short biotinylated DNA

handles to streptavidin beads was confirmed in control experiments versus streptavidin spheres, which yielded up to 100% interactions. With the high resolution dual-trap OT (Figure 1e), using small beads (0.84 µm), optical crosstalk is observed between the two orthogonal polarized beams due to polarization scrambling within the objectives. The resulting parasitic signal, caused by interference between the scrambled portions of the two overlapping beams, can be seen in Figure 7c. Approximately 2% polarization scrambling was observed on both detectors [14] and the resulting differential crosstalk signal was obtained by increasing the distance between the two optically trapped beads. For nanomechanical experiments short molecular handles are preferred due to their increased mechanical stiffness, resulting in a favourable signal-to-noise ratio [14]. In order to achieve optimal positional and force resolution a balance had to be found between minimising the parasitic optical crosstalk signal in the dual-trap instrument and maximising the stiffness of the tethers. Double handle experiments with DNA handles of 1000 bp (contour lengths of more than 340 nm each), were the shortest possible constructs that still featured the least amount of parasitic cross-talk in measurements at forces above 10 pN using this particular dual-trap OT instrument. Measurements with the dual-trap tweezers using double handles (1000 bp each) yielded stable specific interactions and a representative force curve of such a double-handle construct is shown in Figure 7d. Thus, PDH constructs could be employed in such a dual-handle configuration to grasp doubly biotinylated molecules (or ensembles of molecules) in situ, for instance to tether a biotinylated ribosome exposing a stalled biotinylated nascent polypeptide chain. Using 0.84 µm beads

Figure 7: Characteristic force–extension curves of double-handle experiments. a) DIG-DNA-Bio and streptavidin-DNA, both tethered to anti-DIG beads (Figure 1d). With more than 1800 nm the plateau length was greater than 70% of the contour length of one DH, thus indicating a specific and stable connection between the two DNA molecules. b) Bio-linker modified streptavidin beads and streptavidin-DNA at anti-DIG bead with a plateau length of about 900 nm (Figure 1c). A stable tether was achieved, yielding a force–extension curve with a characteristic force plateau. c) Using dual-trap OT (Figure 1e) crosstalk is observed between two orthogonally polarized beams below a certain trap–trap distance (less than 700 nm separation betwenn the surfaces of the beads) due to polarization scrambling of the objectives resulting a parasitic signal. The red line indicates the optimum double DNA contour length of 680 nm (1000 bp each). d) Double-handle experiment using the dual-trap OT, where DHs and PDHs (1000 bp each) were tethered to small (0.84 μm) beads and tethered in situ. The assembly was stable over time and featured the characteristic double-handle contour length of 680 nm at a tension of approx. 10 pN.

and 1 kbp double handles, sub-nanometre position noise (FWHM) measurements were possible with the dual-trap tweezers for applied forces greater than 30 pN. Between 10 and 30 pN the measured position noise varied between 1 and 2 nm.

To study the efficiency of our protein-labelling procedure in more detail and to facilitate further single-molecule spectroscopy applications we have coupled streptavidin-modified quantum dots (Q-dot 525, Hayward CA) to the 3' end of DIG-λ-DNA-Bio constructs with 48502 bp length, which were tethered to anti-DIG beads held by suction with a pipette (Figure 1f). This experiment with λ-dsDNA was carried out as previously shown [13]. The Images in Figure 8 show that a streptavidin

conjugate Q-dot is located at the free end of the biotin-labelled λ-dsDNA in the chamber and was excited using a 488 nm argon laser. Qdot emission at 525 nm was captured with an EMCCD camera and was recorded using IXON software (Andor, Belfast, NI). Multiple stretching and shortening cycles of the DNA strand due to variations in the fluid flow speeds were observed (10 cycles), as well as a variation in the emitted light intensity, which can be attributed either to moving of the Q-dot in and out of focus or the known blinking of fluorescing quantum dots [32] (Figure 8). This single molecule fluorescence experiment clearly visualizes the specific binding of a protein to the biotinylated end of the dsDNA. Since the dsDNA was not labelled with intercalating dyes in this fluorescence measurement only
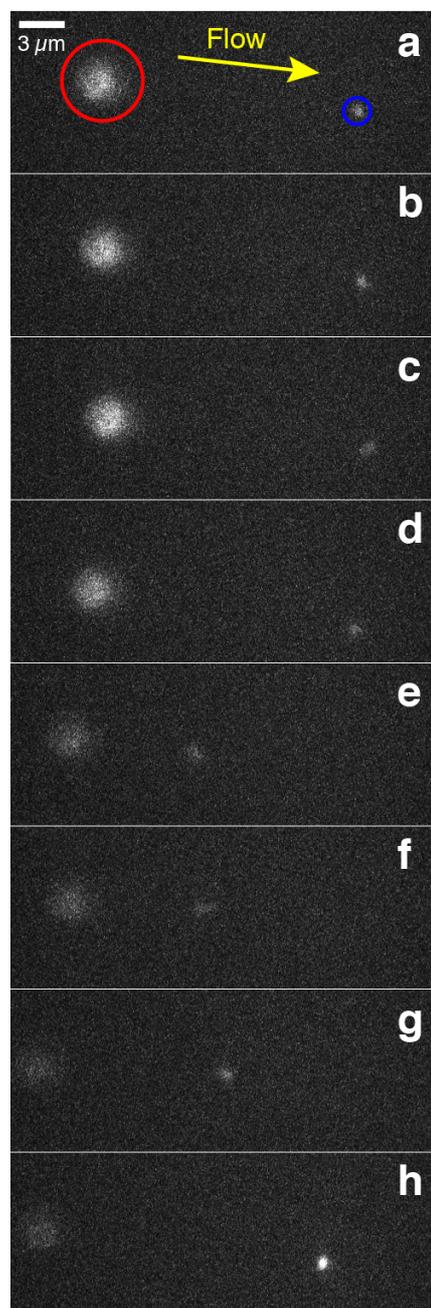
Figure 8: Fluorescence measurements of Qdot–streptavidin conjugates that were attached to freely accessible DIG -λ-dsDNA-Bio strands. a) The blue circle highlights the fluorescent emission of a quantum dot at 525 nm, and the red circle shows the auto-fluorescent bead on the pipette, the yellow arrow represents the direction of the flow. b–h) are the consecutive images obtained via EMCCD video recording. These images show one cycle of the relative position change of the tethered quantum dot, whilst bound to the biotinylated end of a single DIG-λ-DNA-Bio strand within the microfluidic chamber. It can be seen that the freely accessible Qdot changes its position according to the flow. a–c depict a constant fast fluid velocity. d–e show a sudden decrease and f–h a gradual increase in the flow rate within the microfluidic cell. Variations in the fluid flow speed change the hydrodynamic drag experienced by the long dsDNA molecule, altering its extension.

the Qdot streptavidin conjugate indicates the end of the modified DNA–protein hybrid.

Conclusion

We present a simple and very reliable method to produce novel PDHs suitable as molecular handles for single molecule experiments. Gel electrophoresis confirmed the labelling procedure with either streptavidin or neutravidin. EMCCD imaging successfully shows that these protein-modified DNA ends are freely moving in solution by imaging the streptavidin conjugate Qdot linked to a long λ-dsDNA tethered to a streptavidin sphere in a liquid flow configuration. An optimal DNA-modification and purification yield was achieved with 100 proteins per handle. In optical force measurements with PDHs tethered to anti-DIG beads the highest number of single interactions without any clustering of the beads was obtained with a nominal ratio of 40 PDHs per anti-DIG bead. The protein-labelled DNA molecules repeatedly exhibited reliable mechanical characteristics in varying buffer conditions with rupture forces reaching maximum values of 120 pN. Furthermore, high dissociation times (longer than 50 min) were obtained when a constant force of 20 pN was applied to single protein–DNA molecule constructs. The length ranges of PDHs produced for single molecule experiments are defined by the optical tweezers set-up. Using dual-trap OT some optical (see Figure 1e) crosstalk is observed below a certain trap–trap distance. Here PDHs of a total length of approx. 700 nm are advised to minimize parasitic signals whilst maximizing the signal-to-noise ratio. The upper PDHs length limit is defined by the range of the steerable piezo-mirror (ca. 8 μm in the device used here). For tweezers systems utilizing a pipette and an optical trap (see Figure 1a–d) PDH molecules as short as 30 nm up to 30 μm can be investigated. Using these stable protein–DNA constructs of various lengths will greatly facilitate kinetic polypeptide elongation and unfolding/refolding experiments in future single molecular-motor studies involving the ribosome and will also be useful in the study of other biotinylated molecules and mechano-enzymes.

Acknowledgements

References

1. Heller, I.; Hoekstra, T. P.; King, G. A.; Peterman, E. J. G.; Wuite, G. J. L. *Chem. Rev.* **2014,** *114,* 3087–3119. doi:10.1021/cr4003006
2. Kaiser, C. M.; Goldman, D. H.; Chodera, J. D.; Tinoco, I., Jr.; Bustamante, C. *Science* **2011,** *334,* 1723–1727. doi:10.1126/science.1209740

3. Cecconi, C.; Shank, E.; Marqusee, S.; Bustamante, C. DNA Molecular Handles for Single-Molecule Protein-Folding Studies by Optical Tweezers. In *DNA Nanotechnology;* Zuccheri, G.; Samorì, B., Eds.; Springer, 2011; Vol. 749, pp 255–271. doi:10.1007/978-1-61779-142-0_18

4. Cecconi, C.; Shank, E. A.; Dahlquist, F. W.; Marqusee, S.; Bustamante, C. *Eur. Biophys. J.* **2008,** *37,* 729–738. doi:10.1007/s00249-007-0247-y

5. Liphardt, J.; Onoa, B.; Smith, S. B.; Tinoco, I., Jr.; Bustamante, C. *Science* **2001,** *292,* 733–737. doi:10.1126/science.1058498

6. Caldarini, M.; Sonar, P.; Valpapuram, I.; Tavella, D.; Volonté, C.; Pandini, V.; Vanoni, M. A.; Aliverti, A.; Broglia, R. A.; Tiana, G.; Cecconi, C. *Biophys. Chem.* **2014,** *195,* 32–42. doi:10.1016/j.bpc.2014.08.001

7. Moayed, F.; Mashaghi, A.; Tans, S. J. *PLoS One* **2013,** *8,* e54440. doi:10.1371/journal.pone.0054440

8. Hegner, M. *Single Mol.* **2000,** *1,* 139–144. doi:10.1002/1438-5171(200006)1:2<139::AID-SIMO139>3.0.CO;2-C

9. Mangeol, P.; Bockelmann, U. *Rev. Sci. Instrum.* **2008,** *79,* 083103. doi:10.1063/1.2957652

10. Forns, N.; de Lorenzo, S.; Manosas, M.; Hayashi, K.; Huguet, J. M.; Ritort, F. *Biophys. J.* **2011,** *100,* 1765–1774. doi:10.1016/j.bpj.2011.01.071

11. Katranidis, A.; Grange, W.; Schlesinger, R.; Choli-Papadopoulou, T.; Brüggemann, D.; Hegner, M.; Büldt, G. *FEBS Lett.* **2011,** *585,* 1859–1863. doi:10.1016/j.febslet.2011.04.045

12. Wen, J.-D.; Lancaster, L.; Hodges, C.; Zeri, A.-C.; Yoshimura, S. H.; Noller, H. F.; Bustamante, C.; Tinoco, I. *Nature* **2008,** *452,* 598–603. doi:10.1038/nature06716

13. Grange, W.; Husale, S.; Güntherodt, H. J.; Hegner, M. *Rev. Sci. Instrum.* **2002,** *73,* 2308–2316. doi:10.1063/1.1477608

14. Bustamante, C.; Chemla, Y. R.; Moffitt, J. R. *Cold Spring Harb. Protoc.* **2009,** pdb.ip73. doi:10.1101/pdb.ip73

15. Perkins, T. T.; Smith, D. E.; Larson, R. G.; Chu, S. *Science* **1995,** *268,* 83–87. doi:10.1126/science.7701345

16. Stigter, D.; Bustamante, C. *Biophys. J.* **1998,** *75,* 1197–1210. doi:10.1016/S0006-3495(98)74039-1

17. Smith, S. B.; Cui, Y.; Bustamante, C. *Science* **1996,** *271,* 795–799. doi:10.1126/science.271.5250.795

18. Gross, P.; Laurens, N.; Oddershede, L. B.; Bockelmann, U.; Peterman, E. J. G.; Wuite, G. J. L. *Nat. Phys.* **2011,** *7,* 731–736. doi:10.1038/Nphys2002

19. Husale, S.; Grange, W.; Hegner, M. *Single Mol.* **2002,** *3,* 91–96. doi:10.1002/1438-5171(200206)3:2/3<91::AID-SIMO91>3.0.CO;2-R

20. Baumann, C. G.; Smith, S. B.; Bloomfield, V. A.; Bustamante, C. *Proc. Natl. Acad. Sci. U. S. A.* **1997,** *94,* 6185–6190. doi:10.1073/pnas.94.12.6185

21. Wang, M. D.; Yin, H.; Landick, R.; Gelles, J.; Block, S. M. *Biophys. J.* **1997,** *72,* 1335–1346. doi:10.1016/S0006-3495(97)78780-0

22. Hegner, M.; Smith, S. B.; Bustamante, C. *Proc. Natl. Acad. Sci. U. S. A.* **1999,** *96,* 10109–10114. doi:10.1073/pnas.96.18.10109

23. Hegner, M.; Grange, W. *J. Muscle Res. Cell Motil.* **2002,** *23,* 367–375. doi:10.1023/A:1023446103620

24. Neuert, G.; Albrecht, C.; Pamir, E.; Gaub, H. E. *FEBS Lett.* **2006,** *580,* 505–509. doi:10.1016/j.febslet.2005.12.052

25. Grandbois, M.; Beyer, M.; Rief, M.; Clausen-Schaumann, H.; Gaub, H. E. *Science* **1999,** *283,* 1727–1730. doi:10.1126/science.283.5408.1727

26. Evans, E.; Ritchie, K. *Biophys. J.* **1999,** *76,* 2439–2447. doi:10.1016/S0006-3495(99)77399-6

27. Merkel, R.; Nassoy, P.; Leung, A.; Ritchie, K.; Evans, E. *Nature* **1999,** *397,* 50–53. doi:10.1038/16219

28. De Paris, R.; Strunz, T.; Oroszlan, K.; Güntherodt, H.-J.; Hegner, M. *Single Mol.* **2000,** *1,* 285–290. doi:10.1002/1438-5171(200012)1:4<285::AID-SIMO285>3.0.CO;2-3

29. Sitters, G.; Kamsma, D.; Thalhammer, G.; Ritsch-Marte, M.; Peterman, E. J. G.; Wuite, G. J. L. *Nat. Methods* **2015,** *12,* 47–50. doi:10.1038/nmeth.3183

30. Cluzel, P.; Lebrun, A.; Heller, C.; Lavery, R.; Viovy, J.-L.; Chatenay, D.; Caron, F. *Science* **1996,** *271,* 792–794. doi:10.1126/science.271.5250.792

31. Danilowicz, C.; Limouse, C.; Hatch, K.; Conover, A.; Coljee, V. W.; Kleckner, N.; Prentiss, M. *Proc. Natl. Acad. Sci. U. S. A.* **2009,** *106,* 13196–13201. doi:10.1073/pnas.0904729106

32. Galland, C.; Ghosh, Y.; Steinbrück, A.; Sykora, M.; Hollingsworth, J. A.; Klimov, V. I.; Htoon, H. *Nature* **2011,** *479,* 203–207. doi:10.1038/nature10569

Molecular machines operating on the nanoscale:
from classical to quantum

Igor Goychuk

Abstract

The main physical features and operating principles of isothermal nanomachines in the microworld, common to both classical and quantum machines, are reviewed. Special attention is paid to the dual, constructive role of dissipation and thermal fluctuations, the fluctuation–dissipation theorem, heat losses and free energy transduction, thermodynamic efficiency, and thermodynamic efficiency at maximum power. Several basic models are considered and discussed to highlight generic physical features. This work examines some common fallacies that continue to plague the literature. In particular, the erroneous beliefs that one should minimize friction and lower the temperature for high performance of Brownian machines, and that the thermodynamic efficiency at maximum power cannot exceed one-half are discussed. The emerging topic of anomalous molecular motors operating subdiffusively but very efficiently in the viscoelastic environment of living cells is also discussed.

Introduction

A myriad of minuscule molecular nanomotors (not visible in standard, classical, optical microscopes) operate in living cells and perform various tasks. These utilize metabolic energy, for example, the energy stored in ATP molecules maintained at out-of-equilibrium concentrations, or in nonequilibrium ion concentrations across biological membranes. Conversely, they may replenish the reserves of metabolic energy using other sources of energy, for example, light by plants, or energy of covalent bonds of various food molecules by animals [1]. The main

physical principles of their operation are more or less understood by now [2,3], although the statistico-mechanical details of any single particular molecular motor (e.g., a representative of a large family of kinesin motors) are not well understood.

The advances and perspectives of nanotechnology have inspired us to devise our own nanomotors [4-6]. Learning from nature can help to make the artificial nanomotors more efficient, and possibly even better than those found in nature. Along this way,

understanding the main physical operating principles within the simplest, minimalist physical models can indeed be of help.

First of all, any periodically operating motor or engine requires a working body undergoing cyclic changes and a source of energy to drive such cyclic changes. Furthermore, it should be capable of doing work on external bodies. In the case of thermal heat engines, the source of energy is provided by heat exchange with two heat reservoirs or baths at different temperatures, T_1, and $T_2 > T_1$, with the maximum possible Carnot efficiency of $\eta_C = 1 - T_1/T_2$ [7]. This very famous textbook result of classical thermodynamics (or rather thermostatics) is modified when the heat flow is considered as a function of time. Thus, for an infinitesimally slow heat flow occurring over a finite time, one obtains the Curzon and Ahlborn result, $\eta_{CA} = 1 - \sqrt{T_1/T_2} \leq \eta_C$ [7,8]. The analogy with heat engines is, however, rather misleading for isothermal engines operating at the same temperature, $T_1 = T_2$. Here, the analogy with electrical motors is much more relevant. The analogy becomes almost literal in the case of rotary ATP-synthase [9] or flagellar bacterial motors (the electrical nanomotors of living cells). Here, the energy of a proton electrochemical gradient (an electrochemical rechargeable battery) is used to synthesize ATP molecules out of ADP and the orthophosphate P_i (the useful work done), in the case of ATP-synthase, or to produce mechanical motion by flagellar motors [1,3]. An ATP-synthase nanomotor can also operate in reverse [9], and the energy of ATP hydrolysis can be used to pump protons against their electrochemical gradient to recharge the "battery". These and similar nanomotors can operate at ambient temperature in a highly dissipative environment with nearly 100% thermodynamic efficiency defined as the ratio of useful work done to the input energy spent. This is the first counter-intuitive remarkable feature, which needs to be explained. It is easy to derive this result within the simplest model (see below) for an infinitesimally slow operating motor at zero power. At maximum power at a finite speed, the maximum thermodynamic efficiency within such a model is one-half. This is still believed by many to be the maximum, theoretically possible, thermodynamic efficiency of isothermal motors at maximum power. However, this belief is born from underestimating the role played by thermal fluctuations in nonlinear stochastic dynamics and the role of the fluctuation–dissipation theorem (FDT) on the nano- and microscale. It is generally wrong. It is valid only for some particular dynamics, as clarified below by giving three counter-examples. The presence of strong thermal fluctuations at ambient temperature, playing a constructive and useful role, is a profound physical feature of nanomotors as compared with the macroscopic motors of our everyday experience. It is necessary to understand and to develop an intuition for this fundamental feature. Nanomotors are necessarily

Brownian engines, very different from their macroscopic counterparts.

Review
Fluctuation–dissipation theorem, the role of thermal fluctuations

Motion in any dissipative environment is necessarily related to the dissipation of energy. Particles experience a frictional force, which in the simplest case of Stokes friction is linearly proportional to the particle velocity with a viscous friction coefficient denoted as η. When the corresponding frictional energy losses are no longer compensated for by an energy supply, the motion will eventually stop. However, this does not happen in microworld for micro- or nanosized particles. Their stochastic Brownian motion can persist forever even at thermal equilibrium. The energy necessary for this is supplied by thermal fluctuations. Therefore, friction and thermal noise are intimately related, which is the physical context of the fluctuation–dissipation theorem [10]. Statistical mechanics allows the development of a coherent picture to rationalize this fundamental feature of Brownian motion.

We start with some generalities that can be easily understood within a standard dynamical approach to Brownian motion that can be traced back to pioneering contributions by Bogolyubov [11], Ford, Kac and Mazur [12,13], and others. Consider a motor particle with mass M, coordinate x, and momentum p. It is subjected to a regular, dynamical force $f(x,t)$, as well as the frictional and stochastically fluctuating forces of the environment. The latter are modeled by an elastic coupling of this particle to a set of N harmonic oscillators with masses m_i, coordinates q_i, and momenta p_i. This coupling is of the form $V_{int} = \sum_{i=1}^{N} \kappa_i (x - q_i)^2 / 2$, with spring constants κ_i. This is a standard mechanistic model of nonlinear, classical Brownian motion known within quantum dynamics as the Caldeira–Leggett model [14] upon modification of the coupling term or making a canonical transformation [13]. Both classically and quantum mechanically [13] (in the Heisenberg picture) the equations of motion are

$$\dot{x} = p/M,$$
$$\dot{p} = f(x,t) - \sum_{i=1}^{N} \kappa_i (x - q_i), \qquad (1)$$
$$\dot{q}_i = p_i/m_i,$$

$$\dot{p}_i = \kappa_i (x - q_i). \qquad (2)$$

In the quantum case, x, q_i, p, p_i are operators obeying the commutation relations $[x,p] = i\hbar$, $[q_k, p_j] = i\delta_{kj}\hbar$, $[x,q_i] = 0$,

$[p,p_i] = 0$. Force, $f(x,t)$, is also operator. Using Green's function of harmonic oscillators, the dynamics of bath oscillators can be excluded (projection of hyper-dimensional dynamics on the (x,p) plane) and further represented simply by the initial values $q_i(0)$ and $p_i(0)$. This results in a generalized Langevin equation (GLE) for the motor variables

$$M\ddot{x} + \int_0^t \eta(t-t')\dot{x}(t')dt' = f(x,t) + \xi(t), \qquad (3)$$

where

$$\eta(t) = \sum_i \kappa_i \cos(\omega_i t), \qquad (4)$$

is a memory kernel and

$$\xi(t) = \sum_i \kappa_i \left([q_i(0) - x(0)]\cos(\omega_i t) + \frac{p_i(0)}{m_i \omega_i}\sin(\omega_i t) \right) \quad (5)$$

is a bath force, where $\omega_i = \sqrt{\kappa_i/m_i}$ are the frequencies of the bath oscillators. Equation 3 is still a purely dynamical equation of motion that is exact. The dynamics of $[x(t),p(t)]$ is completely time-reversible for any given $q_i(0)$ and $p_i(0)$ by derivation, unless the time-reversibility is dynamically broken by $f(x,t)$ or by boundary conditions. Hence, time-irreversibility within dissipative Langevin dynamics is a statistical effect due to averaging over many trajectories. Such an averaging cannot be undone, i.e., there is no way to restore a single trajectory from their ensemble average. Considering a classical dynamics approach first, we choose initial $q_i(0)$ and $p_i(0)$ from a canonical, hyper-dimensional, Gaussian distribution, $\rho(q_i(0),p_i(0))$, zero-centered in $p_i(0)$ subspace and centered around $x(0)$ in $q_i(0)$ subspace, and characterized by the thermal bath temperature T, like in a typical molecular dynamics setup. Then, each $\xi(t)$ presents a realization of a stationary, zero-mean, Gaussian stochastic process, which can be completely characterized by its autocorrelation function, $\langle \xi(t)\xi(0)\rangle$. Here, $\langle...\rangle$ denotes statistical averaging done with $\rho(q_i(0),p_i(0))$. An elementary calculation yields the fluctuation–dissipation relation (FDR), also named the second FDT by Kubo [10]:

$$\langle \xi(t')\xi(t)\rangle = k_B T\eta(|t-t'|). \qquad (6)$$

Notice that it is valid even for a thermal bath consisting of a single oscillator. However, a quasi-continuum of oscillators is required for the random force correlations to decay to zero in time. This is necessary for $\xi(t)$ to be ergodic in correlations.

Kubo obtained this FDT in a very different way, namely by considering the processes of dissipation caused by phenomenological memory friction characterized by the memory kernel $\eta(t)$ (i.e., heat given by the particle to the thermal bath) and absorption of energy from the random force $\xi(t)$ (i.e., heat absorbed from the thermal bath). Here, both processes are balanced at thermal equilibrium, and the averaged kinetic energy of the Brownian particle is $k_B T/2$. This is in accordance with the equipartition theorem in classical equilibrium statistical mechanics. This is a very important point. At thermal equilibrium, the net heat exchange between the motor and its environment is zero for arbitrarily strong dissipation. This is a primary, fundamental reason why the thermodynamic efficiency of isothermal nanomotors can in principle achieve unity in spite of strong dissipation. For example, the thermodynamic efficiency of an F1-ATPase rotary motor can be close to 100% as recent experimental work has demonstrated [15]. For this to happen, the motor must operate most closely to thermal equilibrium in order to avoid net heat losses. One profound lesson from this is that there is no need to minimize friction on the nanoscale. This is a very misleading misconception that continues to plague research on Brownian motors. For example, the so-called dissipationless ratchets are worthless (more on this below). Very efficient motors can work at ambient temperature and arbitrarily strong friction. There is no need to go to deep, quantum cold temperatures, which require a huge energy expenditure to create in a laboratory.

Every thermal bath and its coupling to the particle can be characterized by the bath spectral density

$$J(\omega) = \frac{\pi}{2}\sum_i \frac{\kappa_i^2}{m_i\omega_i}\delta(\omega-\omega_i) = \frac{\pi}{2}\sum_i m_i\omega_i^3\delta(\omega-\omega_i)$$

[13,14,16]. It allows $\eta(t)$ to be expressed as

$$\eta(t) = (2/\pi)\int_0^\infty d\omega\, J(\omega)\cos(\omega t)/\omega$$

and the noise spectral density via the Wiener–Khinchin theorem, $S(\omega) = \int_{-\infty}^\infty \langle \xi(t)\xi(0)\rangle e^{i\omega t}dt$, as $S(\omega) = 2k_B TJ(\omega)/\omega$. The strict ohmic model, $J(\omega) = \eta\omega$, without a frequency cutoff, corresponds to the standard Langevin equation:

$$M\ddot{x} + \eta\dot{x} = f(x,t) + \xi(t), \qquad (7)$$

with uncorrelated white Gaussian thermal noise, $\langle \xi(t')\xi(t)\rangle = 2k_B T\eta\delta(|t-t'|)$. Such noise is singular, and its mean-square amplitude is infinite. This is, of course, a very strong idealization. A frequency cutoff must be physically

present, which results in a thermal GLE description with correlated Gaussian noise.

The above derivation can also be straightforwardly repeated for quantum dynamics. This leads to a quantum GLE, which formally looks the same as Equation 3 in the Heisenberg picture with only one difference: The corresponding random force becomes operator-valued with a complex-valued autocorrelation function as shown in Equation 8 [13,16,17].

$$\left\langle \hat{\xi}(t)\hat{\xi}(t')\right\rangle_{qm} = \frac{\hbar}{\pi}\int_0^\infty d\omega J(\omega)\left\{\coth\left(\hbar\omega/2k_\mathrm{B}T\right)\right.$$
$$\left.\times\cos\left[\omega(t-t')\right] - i\sin\left[\omega(t-t')\right]\right\}. \tag{8}$$

Here, the averaging is done with the equilibrium density operator of the bath oscillators. The classical Kubo result (Equation 6) is restored in the formal limit $\hbar \to 0$. To obtain a quantum generalization of Equation 7, one can introduce a frequency cutoff, $J(\omega) = \eta\omega\exp(-\omega/\omega_c)$ and split $\hat{\xi}(t)$ into a sum of zero-point quantum noise, $\hat{\xi}_{T=0}(t)$, and thermal quantum noise contributions, $\hat{\xi}_{T>0}(t)$, so that $\hat{\xi}(t) = \hat{\xi}_{T=0}(t) + \hat{\xi}_{T>0}(t)$. This yields

$$\left\langle \hat{\xi}(t)\hat{\xi}(0)\right\rangle_{qm} = \frac{1}{\pi}\frac{\hbar\eta\omega_c^2\left(1 - i\omega_c t\right)^2}{\left[1 + \left(\omega_c t\right)^2\right]^2} + 2k_\mathrm{B}T\eta\delta_T(t) \tag{9}$$

with

$$\delta_T(t) = \frac{1}{2\tau_T}\left[\frac{\tau_T^2}{t^2} - \frac{1}{\sinh^2\left(t/\tau_T\right)}\right], \tag{10}$$

where $\tau_T = \hbar/\left(\pi k_\mathrm{B}T\right)$ is the characteristic time of thermal quantum fluctuations. Notice the dramatic change of quantum thermal correlations, from a delta function at $\hbar \to 0$, to an algebraic decay $\delta_T(t) \propto t^{-2}$ for finite τ_T and $t \gg \tau_T$. The total integral of $\delta_T(t)$ is unity, and the total integral of the real part of the $T = 0$ contribution is zero. In the classical limit, $\hbar \to 0$, $\delta_T(t)$ becomes a delta function. Notice also that the real part of the first complex-valued term in Equation 9, which corresponds to zero-point quantum fluctuations, starts from a positive singularity at the origin $t = 0$ in the classical, white noise limit, $\omega_c \to \infty$, and becomes negative $-\hbar\eta/\left(\pi t^2\right)$ for $t > 0$. Hence, it lacks a characteristic time scale. However, it cancels precisely the same contribution, but with the opposite sign stemming formally from the thermal part in the limit $t \gg \tau_T$ at $T \neq 0$. Thus,

quantum correlations, which correspond to the Stokes or ohmic friction, decay nearly exponentially for $\omega_c \gg 1/\tau_T$, except for the physically unachievable condition of $T = 0$. Here, we see two profound quantum mechanical features in the quantum operator-valued version of the classical Langevin equation (Equation 7) with memoryless Stokes friction: First, thermal quantum noise is correlated. Second, zero-point quantum noise is present. This is the reason why quantum Brownian motion would not stop even at absolute zero of temperature $T = 0$. A proper treatment of these quantum mechanical features produced a controversial discussion in the literature in the case of nonlinear quantum dynamics when $f(x)$ is not constant or has a nonlinear dependence on x (see [16,17] for further references and details). Indeed, dissipative quantum dynamics cannot be fundamentally Markovian, as already revealed by this short explanation. This is contrary to a popular approach based on the idea of quantum semi-groups, which guarantees a complete positivity of such a dynamics [18]. The main postulate of the corresponding theory (the semi-group property of the evolution operator expressing the Markovian character of evolution) simply cannot be justified on a fundamental level, thinking in terms of interacting particles and fields (a quantum field theory approach). Nevertheless, Lindblad theory and its allies, for example, the stochastic Schroedinger equation [16], are extremely useful in quantum optics where the dissipation strength is very small. The application to condensed matter with appreciably strong dissipation should, however, be done with a great care. This could lead to clearly incorrect results, which contradict exactly solvable models [16]. Nonlinear quantum Langevin dynamics is very tricky, even within a semi-classical treatment, where the dynamics is treated as classical but with colored classical noise corresponding to the real part of $\hat{\xi}(t)$ treated as a c-number. As a matter of fact, quantum dissipative dynamics is fundamentally non-Markovian, which is a primary source of all the difficulties and confusion. Exact analytical results are practically absent (except for linear dynamics), and various Markovian approximations to nonlinear non-Markovian dynamics are controversial, being restricted to some parameter domains (e.g., weak system–bath coupling or a weak tunnel coupling/strong system–bath coupling). Moreover, they are susceptible of producing unphysical results (such as violation of the second law of thermodynamics) beyond their validity domains.

Furthermore, a profoundly quantum dynamics has often just a few relevant discrete quantum energy levels, rather than a continuum of quantum states. A two-state quantum system serves as a prominent example. Here, one may prefer a different approach to dissipative quantum dynamics (e.g., the reduced density operator method), leading to quantum kinetic equations for level populations and system coherence [19-22]. This provides

a description on the ensemble level and relates to the quantum Langevin equation in a similar manner as the classical Fokker–Planck equation (ensemble description) relates to the classical Langevin equation (description on the level of single trajectories).

Minimalist model of a Brownian motor

A minimalist model of a motor can be given by 1D cycling of the motor particle in a periodic potential, $V(\phi + 2\pi) = V(\phi)$, as shown in Figure 1. This models the periodic turnover of the motor within a continuum of intrinsic, conformational states [3], where ϕ is a chemical cyclic reaction coordinate. The motor cycles can be driven by an energy supplied by a constant driving force or torque, F, with free energy $\Delta\mu = 2\pi F$ spent per one motor turn. The motor can perform useful work against an opposing torque or load, f_L, so that the total potential energy is $U(\phi) = V(\phi) - F\phi + f_L\phi$. Overdamped Langevin dynamics is described by

$$\eta\dot{\phi} = f(\phi) + F - f_L + \xi(t), \qquad (11)$$

where $f(\phi) = -\partial V(\phi)/\partial\phi$, with uncorrelated white Gaussian thermal noise $\xi(t)$, $\langle\xi(t')\xi(t)\rangle = 2k_BT\eta\delta(|t-t'|)$. By introducing the stochastic dissipative force $F_d(t) = \eta\dot{\phi} - \xi(t)$, it can be understood as a force balance equation. The net heat exchange with the environment is

$Q(t) = \int_0^t \langle F_d(t')\dot{\phi}(t')\rangle dt'$ [23], where $\langle...\rangle$ denotes an ensemble average over many trajectory realizations. Furthermore, $E_{in}(t) = F\int_0^t \langle\dot{\phi}(t')\rangle dt' = F\langle\phi(t) - \phi(0)\rangle$ is the energy pumped into the motor turnovers, and $W(t) = f_L\int_0^t \langle\dot{\phi}(t')\rangle dt' = f_L\langle\phi(t) - \phi(0)\rangle$ is the useful work done against external torque. The fluctuations of the motor energy $\int_0^t \langle f(\phi(t'))\dot{\phi}(t')\rangle dt' = \int_0^{\phi(t)} \langle f(\phi)d\phi\rangle$ are bounded and can be neglected in the balance of energy in the long run, since $Q(t)$, $E_{in}(t)$, and $W(t)$ typically grow linearly (or possibly sublinearly in the case of anomalously slow dynamics with memory, see below) in time. The energy balance yields the first law of thermodynamics: $Q(t) + W(t) = E_{in}(t)$. The thermodynamic efficiency is obviously

$$R = \lim_{t\to\infty} \frac{W(t)}{E_{in}(t)} = \frac{f_L}{F} \qquad (12)$$

and independent of the potential $V(\phi)$. It reaches unity at the stalling force $f_L^{(st)} = F$. Then, the motor operates infinitesimally slow, $\dot{\phi} = \omega \to 0$. Henceforth, a major interest present the efficiency R_{max} at the maximum of the motor power $P_W = \dot{W}(t)$. This one is easy to find in the absence of potential $V(\phi)$, i.e., for $f(x) = 0$. Indeed, $P_W = f_L\langle\dot{\phi}(t)\rangle = f_L(F - f_L)/\eta$. This shows a parabolic dependence on f_L and reaches the maximum at $f_L = F/2$. Therefore, $R_{max} = 1/2$. Given this simple result, many have believed until now that this is a theoretical

Figure 1: (a) Simplest model for a periodic ratchet potential $V(\phi)$ with depth ε. Bias $\Delta\mu < 0$ per one rotation turn introduces directional rotations. (b) Discrete state model that corresponds to (a) with forward, ω_f, and backward, ω_b, rates calculated, e.g., by solving the Smoluchowski equation, see the text. This picture also holds quantum mechanically with quantum mechanical effects entering the rates in some models, where diagonal and off-diagonal elements of the reduced density matrix are completely decoupled in the energy basis of localized states depicted. (c) The general modeling route is inspired by enzyme dynamics, where an enzyme molecule cycles periodically between a substrate-free state **E**, a state with bound substrate **ES** and a state with bound product **EP**, which correspond to the three metastable states of an enzyme within a continuum of conformational states. $\Delta\mu$ corresponds to the free energy released by transformation *S→P* which drives the cyclic rotations of a "catalytic wheel" [24-26], see in (d). This energy can be used to do work against a loading force f_L, which is not shown. For example, an enzyme is an ion pump utilizing the energy of ATP hydrolysis, where ATP is the substrate, and ADP+P$_i$ is the product. The useful work done is transfer of an ion across a membrane against the corresponding electrochemical transmembrane gradient.

bound for the efficiency of isothermal motors at maximum power.

Digression on the role of quantum fluctuations. Within the simplest model considered ($f(x) = 0$) the quantum noise effects do not asymptotically play any role for $T > 0$. This is not generally so, especially within the framework of nonlinear dynamics and at low temperatures where it can be dominant [27]. Most strikingly, the role of the zero-point fluctuations of vacuum (i.e., quantum noise at $T = 0$) is demonstrated in the Casimir effect: Two metallic plates will attract each other in an attempt to minimize the "dark energy" of electromagnetic standing waves (quantized) in the space between the two plates [28]. This effect can be used, in principle, to make a one-shot motor, which extracts energy from zero-point fluctuations of vacuum, or "dark energy" by doing work against an external force, f_L. No violation of the second law of thermodynamics and/or the law of energy conservation occurs because such a "motor" cannot work cyclically. In order to repeatedly extract energy from vacuum fluctuations, one must again separate two plates and invest at least the same amount of energy in this. This example shows, nevertheless, that the role of quantum noise effects can be highly nontrivial, very important, poorly understood, and possibly confusing. And a possibility to utilize "dark energy" to do useful work in a giant, cosmic "one-shot engine" is really intriguing!

Thermodynamic efficiency of isothermal engines at maximum power can be larger than one-half

Here it is demonstrated that the belief that $R_{max} = 1/2$ is a theoretical maximum is completely wrong, and in accord with some recent studies [29-32], R_{max} can also achieve unity within a nonlinear dynamics regime. For this, we first find stationary $\omega = \dot{\phi}$ in a biased periodic potential. This can be done by solving the Smoluchowski equation for the probability density $P(x,t)$, which can be written as a continuity equation, $\partial P(\phi,t)/\partial t = -\partial J(\phi,t)/\partial \phi$, with the probability flux $J(x,t)$ written in the transport form

$$J(\phi,t) = -De^{-\beta U(\phi)} \frac{\partial}{\partial \phi} e^{\beta U(\phi)} P(\phi,t). \qquad (13)$$

This Smoluchowski equation is an ensemble description and counter-part to the Langevin equation (Equation 11). Here, D is the diffusion coefficient related to temperature and viscous friction by the Einstein relation, $D = k_B T/\eta$, and $\beta = 1/k_B T$ is the inverse temperature. For any periodic biased potential, the constant flux, $J = \omega/(2\pi) = $ constant, driven by $\Delta\mu < 0$, as well as the corresponding nonequilibrium steady state distribution, $P_{st}(\phi)$, can be found by twice-integrating Equation 13, using $U(\phi + 2\pi) = U(\phi) - 2\pi(F - f_L)$ and periodicity of $P_{st}(\phi)$. This

yields the famous Stratonovich result [33-35] for a steady-state angular velocity of phase rotation

$$\omega(\Delta\mu, f_L) = \omega_f(\Delta\mu, f_L)\left[1 - \exp(\beta(\Delta\mu + 2\pi f_L))\right]$$
$$\equiv \omega_f(\Delta\mu, f_L) - \omega_b(\Delta\mu, f_L) \qquad (14)$$

with forward rotation rate

$$\omega_f(\Delta\mu, f_L) = \frac{2\pi D}{\int_0^{2\pi} d\phi \int_\phi^{\phi+2\pi} e^{-\beta[U(\phi)-U(\phi')]} d\phi'} \qquad (15)$$

and backward rate $\omega_b(\Delta\mu, f_L)$ defined by the second equality in Equation 14. This result is quite general. The motor power is $P_W(f_L) = f_L\omega_f(\Delta\mu, f_L)[1 - \exp(\beta(\Delta\mu + 2\pi f_L))]$ and in order to find R_{max} one must find $f_L^{(max)}$ by solving $dP_W(f_L)/df_L = 0$. Then, $R_{max} = f_L^{(max)}/F$. In fact, Equation 14 is very general. It holds beyond the model of washboard potential, leading to the result in Equation 15. For example, given well-defined potential minima, one can introduce a picture of discrete states with classical Kramers rates for the transitions between those, as described in Figure 1b. Accordingly, within the simplest enzyme model, one has three discrete states. **E** corresponds to an empty enzyme with energy E_1. **ES** corresponds to an enzyme with a substrate molecule bound to it and energy E_2 of the whole complex. **EP** corresponds to an enzyme with product molecule(s) bound to it and energy E_3. The forward cyclic transitions **E→ES→EP→E** are driven by the free energy per one molecule $\Delta\mu$ released in the **S→P** transformation facilitated by the enzyme, while the backward cycling, **E→EP→ES→E**, requires backward reaction, **P→S**. This is normally neglected in the standard Michaelis–Menthen-type approach to enzyme kinetics as it is very unlikely to occur. This generally cannot be neglected for molecular motors. The simplest possible Arrhenius model for the forward rate of the whole cycle is

$$\omega_f(\Delta\mu, f_L) = \omega_0 \exp\left[-\beta\delta(\Delta\mu + 2\pi f_L)\right] \qquad (16)$$

where $0 < \delta < 1$ describes the asymmetry of the potential drop. Accordingly, the backward rate is $\omega_b(\Delta\mu, f_L) = \omega_0\exp[\beta(1-\delta)(\Delta\mu + 2\pi f_L)]$. This model allows one to realize under which conditions R_{max} can exceed one-half. Here we rephrase a recent treatment in [29,30] and come to the same conclusions. R_{max} is a solution of $dP_W(f_L)/df_L = 0$, which leads to a transcendental equation for R_{max}

$$\exp\left[r(1 - R_{max})\right] = 1 + \frac{rR_{max}}{1 + rbR_{max}}, \qquad (17)$$

where $r = |\Delta\mu|/(k_B T)$, $b = (k_B T/2\pi)\partial \ln \omega_f(\Delta\mu, f_L)/\partial f_L$. For Equation 16, $b = -\delta$. The limiting case $b = 0$ of extreme asymmetry is especially insightful. In this special case, $R_{max} = [LW(e^{1+r}) - 1]/r$ exactly, where $LW(z)$ denotes the Lambert W-function. This analytical result shows that $R_{max} \to 1/2$ as $r \to 0$, while $R_{max} \to 1$ as $r \to \infty$. Therefore, a popular statement that R_{max} is generally bounded by 1/2 is simply wrong. While it is true that in some models this Jacobi bound exists, it is generally not so. Even the simplest model of molecular motors, as considered here by following [29], completely refutes the Jacobi bound as the theoretical limit. Further insight emerges in the perturbative regime, $r << 1$, which yields in the lowest order of r

$$R_{max} = \frac{1}{2} + \frac{1}{8}\left(\frac{b+1}{2}\right)r + o(r)$$
$$\approx \frac{1}{2} + \frac{1}{8}\left(\frac{1}{2} - \delta\right)\frac{|\Delta\mu|}{k_B T}. \tag{18}$$

This is essentially the same result as in [30]. Hence, for $0 \le \delta < 1/2$, $R_{max} > 1/2$ for a small r, the effect is small for $r << 1$, but it exists.

The discussed model might seem a bit too crude. However, the result that R_{max} can achieve a theoretical limit of unity survives also within a more advanced, yet very simple model. Indeed, let us consider the simplest kind of sawtooth potential (Figure 1) inspired by the above discrete-state model with $\delta = 0$. Then, Equation 15 explicitly yields Equation 19.

The dependence of $\omega(\Delta\mu, f_L)$ on $\widetilde{\Delta\mu} := |\Delta\mu| - 2\pi f_L$ is very asymmetric within this model, as shown in Figure 2a.

This is a typical diode-type or rectifier dependence, if the same model is applied to transport of charged particles in a spatially periodic potential, with $\omega(\Delta\mu, f_L)$ corresponding to a scaled current and $\widetilde{\Delta\mu}$ to voltage. Clearly, within the latter context, if an additional, sufficiently slow, periodic voltage signal, $A\cos(\omega t)$, is applied at the conditions $\widetilde{\Delta\mu} = 0$, it will be rectified because of asymmetric *I–V* characteristics. This gives rise to a directional, dissipative current in a potential unbiased on average (both spatial and time averages are zero). The effect resulted in a huge amount of literature on rocking Brownian ratchets, in particular, and on Brownian motors, in general as described in a review article [36]. Coming back to the efficiency of molecular motors at maximum power within our model, we see clearly in Figure 2c that it can be well above 1/2, and even close to one. A sharply asymmetric dependence of P_W on $R = f_L/F$ (Figure 2b) beyond the linear response regime, $P_W = 4P_{max}R(1-R)$, which is not shown therein because of a very small P_{max}, provides an additional clue on the origin of this remarkable effect. Interestingly, if the work of the motor is reversed, i.e., f_L provides the supply of energy and useful work is done against $F \le f_L$, then the motor rotates in the opposite direction on average. This occurs, for example, in such enzymes as F0F1-ATPase [1,3,9], which presents a complex of two rotary motors F0 and F1 connected by a common shaft. The F0 motor uses an electrochemical gradient of protons to rotate the shaft which transmits the torque on the F1 motor. The mechanical torque applied to the F1 motor is used to synthesize ATP out of ADP and the phosphate group, P_i. This enzyme complex primarily utilizes

$$\omega_f(\Delta\mu, f_L) = \frac{D}{8\pi}\frac{\beta^2\varepsilon(\varepsilon - \Delta\mu - 2\pi f_L)}{\sinh^2(\beta\varepsilon/2) - [\varepsilon/(\Delta\mu + 2\pi f_L)]\sinh^2(\beta(\Delta\mu + 2\pi f_L)/2)}. \tag{19}$$
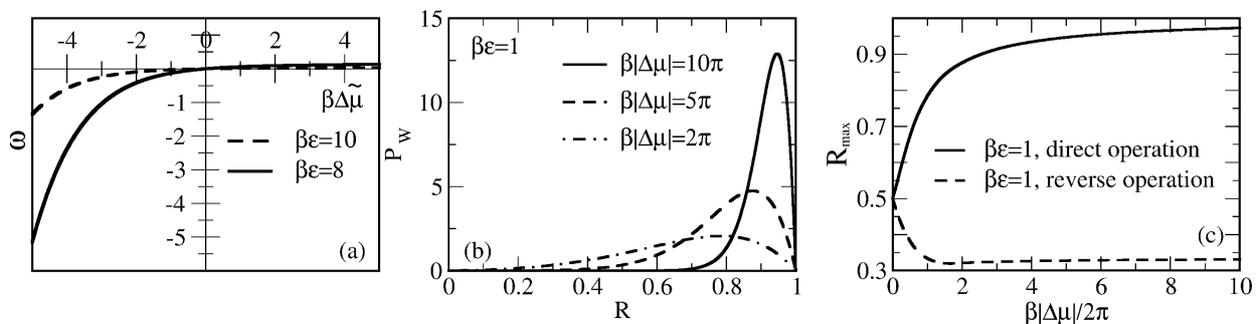
Figure 2: (a) Dependence of the net rotation rate, ω, on the net bias, $\widetilde{\Delta\mu}$, for the most asymmetric sawtooth model depicted in Figure 1a, for two values of the effective barrier height, $\beta\varepsilon$. (b) Dependence of the output power, P_W, on the thermodynamic efficiency, R, for $\beta\varepsilon = 1$ and several values of the scaled driving force, $\beta|\Delta\mu|$. (c) The maximum power efficiency as a function of driving force for the direct and inverse operation, when the roles of driving force and load are interchanged.

the electrochemical gradient of protons to synthesize ATP. It can, however, also work in reverse and pump protons using the energy of ATP hydrolysis [9]. Moreover, in a separate F1-ATPase motor, the energy of ATP hydrolysis can be used to create mechanical torque and do useful work against an external load, which is experimentally well studied [15]. For the reverse operation, our minimalist motor efficiency becomes $R' = P'_W / P'_{in}$, where $P'_W = F \left| \left\langle \dot{\phi}(t) \right\rangle \right|$ and $P'_{in} = f_L \left| \left\langle \dot{\phi}(t) \right\rangle \right|$. In this case, R'_{max} indeed cannot exceed 1/2, as shown in Figure 2c in the lower curve. Such a behavior is also expected from the above discrete-state model, because this corresponds to $\delta \rightarrow 1 = -b$ in Equation 18. This argumentation can be inverted: If a motor obeys the Jacobi bound, $R_{max} \leq 1/2$, then it can violate it when working in reverse. Hence, the concept of the Jacobi bound as a fundamental limitation is clearly a dangerous misconception that should be avoided.

Minimalist model of a quantum engine

In the quantum case, discrete state models naturally emerge. For example, energy levels depicted in Figure 1b can correspond to the states of a proton pump driven by a nonequilibrium electron flow. This is a minimalist toy model for pumps like the cytochrome c oxidase proton pump [1,37]. The driving force is provided by electron energy, $\Delta\mu$, released by dissipative tunneling of electrons between donor and acceptor electronic states of the pump. This process is complex. It requires, apart from intramolecular electron transfer, also uptake and release of electrons from two baths of electrons on different sides of a membrane, which can be provided, for example, by mobile electron carriers [1]. However, intramolecular electron transfer (ET) between two heme metalloclusters seems to be a rate limiting step. Such ET presents vibrationally assisted electron tunneling between two localized quantum states [38,39]. Given the weak electron tunneling coupling between the electronic states, the rate can be calculated using the quantum-mechanical Golden Rule. Within the classical approximation of nuclei dynamics (but not that of electrons!), and the simplest possible further approximations, one obtains the celebrated Marcus–Levich–Dogonadze rate,

$$\omega_f \left(\Delta\mu, \Delta\mu_p = 0 \right) = \omega_0 \exp \left[-\left(\Delta\mu + \lambda \right)^2 \middle/ \left(4\lambda k_B T \right) \right] \quad (20)$$

for forward transfer, and $\omega_b(\Delta\mu, \Delta\mu_p = 0) = \omega_f(\Delta\mu, \Delta\mu_p = 0)$ $\exp[\Delta\mu/(k_B T)]$. Here, $\omega_0 = \left(2\pi/\hbar \right) V_{tun}^2 \middle/ \sqrt{4\pi\lambda k_B T}$ is a quantum prefactor, where V_{tun} is the tunneling coupling, and λ is the reorganization energy of the medium. The energy released in the electron transport is used to pump protons against their electrochemical gradient, $\Delta\mu_p$, which corresponds to $2\pi f_L$ within the previous model. Hence, $R = \Delta\mu_p / |\Delta\mu|$. Of course, our model should not be considered as a realistic model for cytochrome c oxidase. However, it allows a possible role of quantum effects

to be highlighted that are contained in the dependence of the Marcus–Levich–Dogonadze rates on the energy bias $\Delta\mu$. Namely, the existence of an inverted ET regime when the rate becomes smaller with a further increase of $|\Delta\mu| > \lambda$, after reaching a maximum at $|\Delta\mu| = \lambda$ (activationless regime). The inverted regime is a purely quantum-mechanical feature. It cannot be realized within a classical adiabatic Marcus–Hush regime, for which the rate expression formally appears the same as Equation 20 but with a classical prefactor, ω_0. Classically, the inverted regime simply makes no physical sense. This fact can be easily realized upon plotting the lower adiabatic curve for the underlying curve crossing problem (within the Born–Oppenheimer approximation), and considering the pertinent activation barriers – the way the Marcus parabolic dependence of the activation energy on the energy bias is derived in textbooks [38]. The fact that the inverted ET regime can be used to pump electrons was first realized within a driven spin–boson model [22,40-42]. The model here is, however, very different, and pumping is not relied on in the inverted ET regime. However, the latter can be used to arrive at a high R_{max}, close to one. Indeed, within this model, the former (Arrhenius rates) parameter b becomes $b = -1/2 + (|\Delta\mu| - \Delta\mu_p)/(4\lambda)$, and Equation 17 is now replaced by

$$\exp \left[r \left(1 - R_{max} \right) \right] = \frac{1 + r \left[-1/2 + r \left(1 - R_{max} \right) \middle/ \left(4c \right) \right] R_{max}}{1 + r \left[1/2 + r \left(1 - R_{max} \right) \middle/ \left(4c \right) \right] R_{max}}. \quad (21)$$

A new control parameter $c = \lambda/(k_B T)$ enters this expression. The perturbative solution of Equation 21 for $r = |\Delta\mu|/k_B T \ll 1$ yields

$$R_{max} \approx \frac{1}{2} + \frac{1}{192} \frac{\left(\Delta\mu \right)^2}{\lambda k_B T} \left(3 - \frac{\lambda}{k_B T} \right) \quad (22)$$

to the lowest second order in $|\Delta\mu|/k_B T$ (compare with Equation 18). Hence, $R_{max} > 1/2$ for $\lambda < 3k_B T$ and $R_{max} < 1/2$ for $\lambda > 3k_B T$ in the perturbative regime. However, beyond this, R_{max} can essentially be larger than 1/2, as shown in Figure 3a.

These results are also expected for the pump working in reverse when $\Delta\mu \rightarrow -\Delta\mu$. Here, we also see a huge difference with the model based on Arrhenius rates. The dependence of the rotation rate, ω, on $\widetilde{\Delta\mu} = |\Delta\mu| - \Delta\mu_p$ is symmetric in this case. However, it exhibits a regime with a negative differential part, where $d\omega/d\widetilde{\Delta\mu} < 0$, for $\widetilde{\Delta\mu}$ exceeding some critical value that approaches λ for small T, as shown in Figure 3b. Here, the reason for the high performance is very different from the case of the asymmetric Arrhenius rates, or asymmetric $V(\phi)$. R_{max} can be close to one for $|\widetilde{\Delta\mu}| \gg \lambda$. For this to happen, the motor should be driven deeply into the inverted ET regime. Hence, the effect
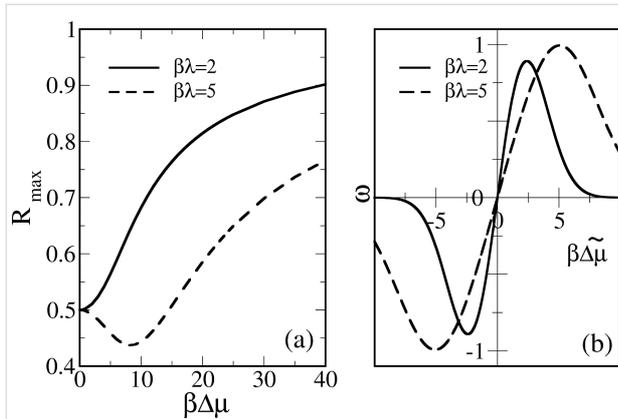
Figure 3: (a) Dependence of R_{max} on the absolute value of driving energy $\Delta\mu$ in units of $k_B T$ for two values of $\lambda/k_B T$. Within the perturbative regime, Equation 22 predicts the initial dependence well. (b) Dependence of enzyme velocity ω on $\beta\widetilde{\Delta\mu}$. Notice the existence of a maximum ω and negative differential regime.

is quantum-mechanical in nature, even if the considered setup looks purely classical. In this respect, the Pauli quantum master equation for the diagonal elements of the reduced density matrix decoupled from the off-diagonal elements has mathematical form of the classical master equation for population probabilities, and the corresponding classical probability description can be safely used. The rates entering this equation can, however, reflect such profound quantum effects as quantum-mechanical tunneling and yield non-Arrhenius dependencies of dissipative tunneling rates on temperature and external forces. The corresponding quantum generalizations of classical results become rather straightforward. The theory of quantum nanomachines with profound quantum coherence effects is, however, still in its infancy.

Can a rocking ratchet do useful work without dissipation?

As we just showed, strong dissipation is not an obstacle for either classical or quantum Brownian machines to achieve a theoretical limit of performance. This already indicates that to completely avoid dissipation is neither possible nor desirable to achieve to develop a good nanomachine on the nanoscale. Conversely, the so-called rocking ratchets without dissipation [43,44] are not capable of performing any useful work, despite that they can produce directional transport. However, this directional transport cannot continue against any non-zero force trying to stop it, as will now be demonstrated. The stalling force can become negligibly small, and the thermodynamical efficiency of such a device is zero, very different from genuine ratchets, which must be characterized by a non-zero stalling force [36]. Therefore, a ratchet current without dissipation clearly presents an interesting but futile artefact. The rocking ratchets without dissipation should be named pseudo-ratchets to

distinguish them from genuine ratchets characterized by a non-zero stalling force.

Let us consider the following setup. A particle in a periodic potential, $V(x)$, is driven by a time-periodic force, $g(t+\mathcal{T})=g(t)$, with period $\mathcal{T}$. Then, $U(x,t)=V(x)-xg(t)$, or $f(x,t)=f(x)+g(t)$ in Equation 7. For strong dissipation and overdamped Langevin dynamics, $M\to 0$, the rectification current can emerge in potentials with broken space-inversion symmetry, like one in Figure 1a, under a fully symmetric driving, $g(t)=A\cos(\Omega t)$, $\Omega=2\pi/\mathcal{T}$. A broken space-inversion symmetry means that there is no such x_0, so that $V(-x)=V(x+x_0)$. Likewise, a periodic driving is symmetric with respect to time reversal if such a t_0 exists (or equivalently, a phase shift $2\pi t_0/\mathcal{T}$), such that $g(-t)=g(t+t_0)$. Otherwise it breaks the time-reversal symmetry. Also, higher moments of driving,

$$\overline{g^n(t)}=\frac{1}{\mathcal{T}}\int_0^{\mathcal{T}}g^n(t)\,dt$$

where $n=2,3,\ldots$ are important with respect to a nonlinear response reasoning. The latter moments can also be defined for stochastic driving, using a corresponding time-averaging, with $\mathcal{T}\to\infty$. For overdamped dynamics, the rectification current already appears in the lowest second order of $\overline{g^2(t)}\neq 0$, for a potential with broken spatial-inversion symmetry, and in the lowest third order of $\overline{g^3(t)}\neq 0$ for potentials which are symmetric with respect to inversion $x\to -x$[36]. These results were easy to anticipate for memoryless dynamics, which displays asymmetric current–force characteristics in the case of an applied static force (broken spatial symmetry), or a symmetric one (unbroken symmetry), respectively. They hold also quantum mechanically in the limit of strong dissipation. The case of weak dissipation is, however, more intricate both classically and quantum mechanically. A symmetry analysis based on the Curie symmetry principle has been developed in order to clarify the issue [36,43]. The harmonic mixing driving [45],

$$g(t)=A_1\cos\left(\Omega t+\phi_0\right)+A_2\cos\left(2\Omega t+2\phi_0+\psi\right),\quad (23)$$

is especially interesting in this respect. Here, ψ is a relative phase of two harmonics, which plays a crucial role. ϕ_0 is an absolute initial phase, which physically cannot play any role because it corresponds to a time shift $t\to t+t_0$ with $t_0=\phi_0/\Omega$ and hence must be averaged out in the final results, if they are of any physical importance in real world. Harmonic mixing driving provides a nice testbed, because this is the simplest time-periodic driving which can violate the time-reversal symmetry. This occurs for any $\psi\neq 0,\pi$. On the other hand,

$\overline{g^3(t)} = (3/4)A_1^2 A_2 \cos(\psi)$. Hence, $\overline{g^3(t)} \neq 0$, for $\psi \neq \pi/2, 3\pi/2$. Interestingly, $\overline{g^3(t)} = (3/4)A_1^2 A_2$ is maximal for time-reversal symmetric driving. Conversely, $\overline{g^3(t)} = 0$, when the time reversal symmetry is maximally broken. Moreover, one can show that all odd moments $\overline{g^{2n+1}(t)} \propto \cos(\psi)$, $n = 1,2,3,\ldots$, vanish for $\psi = \pi/2$ or $3\pi/2$. The vanishing of odd moments for a periodic function means that it obeys a symmetry condition $g(t+T/2) = -g(t)$. Also, in application to potentials of the form $V(x) = V_1\cos(kx) + V_2\cos(2kx + \phi)$, these results mean that $\overline{V^3(x)} \propto \cos(\phi)$, and $\overline{f^3(x)} \propto \sin(\phi)$, for the corresponding spatial averages. Hence, for a space-inversion symmetric potential with $\phi = 0$, $\overline{f^3(x)} = 0$ (also all higher odd moments vanish). Moreover, $\overline{f^3(x)}$ is maximal, when the latter symmetry is maximally broken, $\phi = \pi/2$. This corresponds to the ratchet potentials. The origin of the rectification current can be understood as a memoryless nonlinear response in the overdamped systems: For $\overline{f^3(x)} \neq 0$, the current emerges already for standard harmonic driving as a second order response to driving. For $\overline{f^3(x)} = 0$ (e.g., standard cosine potential, $V_2 = 0$), one needs $\overline{g^3(t)} \neq 0$ for driving to produce the ratchet effect. For the above harmonic driving, the averaged current $\langle \dot{x}(t) \rangle \propto \cos(\psi)$. The same type of response behavior also features a quantum-mechanical, dissipative, single-band, tight-binding model for strong dissipation [46,47]. Very important is that any genuine fluctuating tilt or rocking ratchet is characterized by a non-zero stalling force, which means that the ratchet transport can sustain against a loading force and do useful work against it. It ceases at a critical stalling force. This has important implications. For example, in application to the photovoltaic effect in crystals with broken space-inversion symmetry [36] this means that two opposite surfaces of crystal (orthogonal to current flow) will be gradually charged until the produced photo-voltage stops the ratchet current flow. For a zero stalling force, no steady-state photo-voltage or electromotive force can in principle emerge!

In the case of weak dissipation, however, memory effects in the current response become essential. Generally, for classical dynamics, $\langle \dot{x}(t) \rangle \propto \cos(\psi - \psi_0)$, where ψ_0 is a phase shift which depends on the strength of dissipation with two limiting cases: (i) $\psi_0 = 0$ for for overdamped dynamics, and (ii) $\psi_0 \to \pi/2$ for vanishing dissipation $\eta \to 0$. In the later limit, the system becomes purely dynamical:

$$M\ddot{x} = f(x) + g(t) - f_L, \qquad (24)$$

where we added an opposing transport loading force f_L. For example, it corresponds to a counter-directed electrical field in the case of charged particles. Let us consider following [43,44], the two original papers on dissipationless ratchet current in the case

of $f_L = 0$, and the potential $V(x) = -V_1\sin(2\pi x) - V_2\sin(4\pi x)$, or $f(x) = f_1\cos(2\pi x) + f_2\cos(4\pi x)$, with $f_1 = 2\pi V_1, f_2 = 4\pi V_2$, and driven by $g(t)$ in Equation 23. The spatial period is set to one and $M = 1$ in dimensionless units. The emergence of a dissipationless current within the considered dynamics has been rationalized within a symmetry analysis in [43], and the subject of directed currents due to broken time–space symmetries has been born. In an immediate follow-up work [44], we have, however, observed that in the above case, the directed current is produced only by breaking the time-reversal symmetry by time-dependent driving, but not otherwise. The breaking of the spatial symmetry of the potential alone does not originate dissipationless current. The current is maximal at $\psi = \pi/2$. No current emerges, however, at $\psi = 0$ even in ratchet potential with broken space-inversion symmetry. Moreover, the presence of a second potential harmonic does not seem to affect the transport at $\psi = \pi/2$, as shown in Figure 4a. Here, there are two cases that differ by $V_2 = 0$, in one case, and $V_2 \neq 0$, in another one.

Moreover, when dissipation is present within the corresponding Langevin dynamics, each and every trajectory remains time-reversal symmetric for $\psi = 0$. However, for strongly overdamped dynamics, the rectification current in a symmetric cosine potential ceases at $\psi = \pi/2$, and not at $\psi = 0$. Moreover, for an intermediate dissipation, it stops at some ψ_0, $0 < \psi_0 < \pi/2$, as shown in [48]. Which symmetry forbids it then, given a particular non-zero dissipation strength? Dynamic symmetry considerations fail to answer such simple questions and are thus not infallible. The symmetry of individual trajectories within a Langevin description simply does not depend on the dissipation strength, which can be easily understood from a well-known dynamical derivation of this equation as presented above. Therefore, a symmetry argumentation based on the symmetry properties of single trajectories is clearly questionable, in general. The spontaneous breaking of symmetry is a well-known fundamental phenomenon both in quantum field theory and the theory of phase transitions. In this respect, any chaotic Hamiltonian dynamics possess the following symmetry: for any positive Lyapunov exponent, there is a negative Lyapunov exponent having the same absolute value of the real part. The time reversal changes the sign of the Lyapunov exponents. This symmetry is spontaneously broken in Hamiltonian dynamics by considering the forward evolution in time [49]. It becomes especially obvious upon coarse-graining, which is not possible to avoid neither in real life nor in numerical experiments. By the same token, the time irreversibility of the Langevin description given time-reversible trajectories is primarily a statistical and not a dynamical effect.

The emergence of such a current without dissipation has been interpreted as a reincarnation of the Maxwell–Loschmidt demon
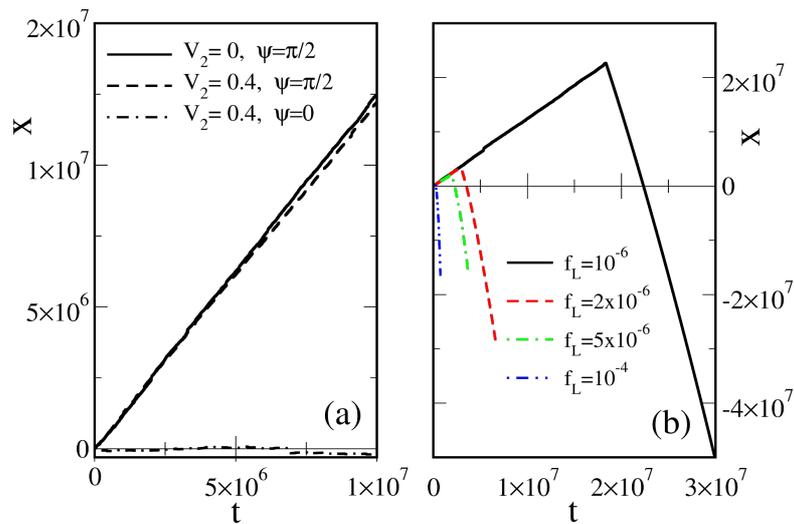
Figure 4: (a) Directed transport in standard cosine potential, $V_1 = 1$, $V_2 = 0$, and in a ratchet potential, $V_1 = 1$, $V_2 = 0.4$, in the case of harmonic mixing driving that breaks the time-reversal symmetry, $\psi = \pi/2$, with amplitudes $A_1 = 5$, $A_2 = 2$, and frequency $\Omega = 1$. Transport ceases at $\psi = 0$ even for ratchet potential with broken symmetry, when the time-reversal symmetry is restored (dash-dotted line). (b) Influence of a tiny (as compare with the periodic force modulation) constant loading force on transport for the case of a ratchet potential in part (a). The transport ceases after some random time, which depends on f_L and initial conditions, and the particle returns accelerating back. A very similar picture also emerges for a cosine potential with $V_2 = 0$ (not shown). The stalling force is obviously zero. Any genuine ratchet and motor must be characterized by a non-zero stalling force. A symplectic leapfrog/Verlet integration scheme (where no spurious dissipation is introduced by numerics) was used to obtain these results.

[44], and it has been argued that this demon is killed by a stochastically fluctuating absolute phase $\phi_0 \rightarrow \phi_0(t)$, with the relative phase ψ being fixed. In this respect, even in highly coherent light sources such as lasers, the absolute phase fluctuations cannot be avoided in principle. They yield a finite bandwidth of laser light. The phase shift ψ can be stabilized, but not the absolute phase. The typical dephasing time of semiconductor lasers used in laser pointers is in the range of nanoseconds, whereas in long tube lasers it is improved to milliseconds [50]. This is the reason why some averaging over such fluctuations must always be done (see [35], Chapter 12). The validity of this argumentation has been analytically proven in [44] with an exactly solvable example of a quantum-mechanical, tight binding model driven by harmonic mixing with a dichotomously fluctuating $\phi_0(t)$. Even more spectacularly, this is seen in dissipationless, tight-binding dynamics driven by an asymmetric, stochastic, two-state field. The current is completely absent even for $\overline{g^{2n+1}(t)} \neq 0$, as an exact solution shows [27]. Hence, dissipation is required to produce a ratchet current under stochastic driving $g(t)$. The validity of this result is far beyond the particular models in [27,44,46] because any coherent quantum current (one carried by Bloch electron with non-zero quasi-momentum) is killed by quantum decoherence produced by a stochastic field. Any dissipationless quantum current will proceed on a time scale smaller than the decoherence time.

Moreover, it is shown here that the directed transport without dissipation found in [43,44], and the follow-up research cannot

do any useful work against an opposing force, f_L. Indeed, the numerical results shown in Figure 4b reveal this clearly: After some random time (which depends, in particular, on the initial conditions and on the f_L load strength), the rectification current ceases. As a matter of fact, the particle then moves back much faster, with acceleration. The smaller the f_L, the longer the directional normal transport regime and smaller back acceleration, and nevertheless the forward transport is absent asymptotically. Therefore, this "Maxwell demon" cannot asymptotically do any useful work, unlike for example, highly efficient ionic pumps – the "Maxwell demons" of living cells working under the condition of strong friction. Plainly said, a dissipationless demon cannot charge a battery, it is futile. Therefore, the consideration of such a device as a "motor" cannot be scientifically justified. It is also clear that with vanishing friction, the thermodynamic efficiency of rocking Brownian motors also vanishes. Therefore, a naive feeling that smaller friction provides higher efficiency is completely wrong, in general.

The following is a brief summary of the major findings of this section. First, friction and noise are intimately related in the microworld, which is nicely seen from a mechanistic derivation of (generalized) Langevin dynamics. It results from hyper-dimensional Hamiltonian dynamics with random initial conditions like in a molecular dynamics approach. For this reason, the thermodynamic efficiency of isothermal nanomotors can reach 100% even under conditions of very strong dissipation, in the overdamped regime where the inertial effects become negli-

gible. Quite on the contrary, thermodynamical efficiency of low-dimensional dissipationless Hamiltonian ratchets is zero. Therefore, they cannot serve as a model for nanomotors in condensed media. Moreover, the geometrical size of some current realizations of Hamiltonian ratchets with optical lattices exceed that of F1-ATPase by several orders of magnitude. In this respect, the readers should be reminded that a typical wavelength of light is about 0.5 μm, which is the reason why motors such as F1-ATPase cannot be seen in a standard light microscope. Hence, the whole subject of Hamiltonian dissipationless ratchets is completely irrelevant for nanomachinery. Second, the thermodynamical efficiency at maximum power in nonlinear regimes can well exceed the upper bound of 50%, which is valid only for a linear dynamics. Therefore, nonlinear effects are generally very important to construct a highly efficient nanomachine. Third, important quantum effects can be already observed within the rate dynamics with quantum rates. For example, these rates can be obtained using a quantum-mechanical perturbation theory in tunnel coupling (within a Fermi's Golden Rule description) whose particularly simple limit results in Marcus–Levich–Dogonadze rates of nonadiabatic tunneling.

Adiabatic pumping and beyond

Having realized that thermodynamic efficiency at maximum power can exceed 50%, a natural question emerges: How to arrive at such an efficiency in practice? Intuitively, the highest thermodynamical efficiency of molecular and other nanomotors can be achieved for an adiabatic modulation of potential when the potential is gradually deformed so that its deep minimum gradually moves from one place to another and a particle trapped near this minimum follows adiabatic modulation of the potential in a peristaltic-like motion. The idea is that the relaxation processes are so fast (once again, a sufficiently strong dissipation is required!) that they occur almost instantly on the time scale of potential modulation. In such a way, the particle can be transferred in a highly dissipative environment from one place to another practically without heat losses, and can do useful work against a substantial load (see the discussion in [51]). If at any point in time the motor particle stays near the thermodynamic equilibrium, then in accordance with FDT, the total heat losses to the environment are close to zero. Therefore, thermodynamic efficiency of such an adiabatically operating motor can, in principle, be close to the theoretical maximum. One can imagine, given the three particular examples presented above, that it can be achieved, in principle, at the maximum of power for arbitrarily strong dissipation. The design of the motor thus becomes crucially important. Such an ideal motor can also be completely reversible. However, to arrive at the maximum thermodynamic efficiency at a finite speed is a highly nontrivial matter indeed.

Digression on the possibility of an (almost) heatless classical computation

Now, an important digression is considered. In application of these ideas to the physical principles of computation, the above physical considerations mean the following. Bitwise operation (bit "0" corresponds to one location of the potential minimum and bit "1" to another – let us assume that their energies are equal) does not require, in principle, any energy to finally dissipate. It can be stored and reused during adiabatically slow change of potential. Physical computation can, in principle, be heatless, and it can be also completely reversible at arbitrary dissipation. This is the reason why the original version of the Landauer minimum principle allegedly imposed on computation (i.e., there is a minimum of $k_B T \ln 2$ of energy dissipated per one bit of computation, 0→1, or 1→0 required) was completely wrong. This was recognized by the late Landauer himself [52] after Bennett [53], Fredkin and Toffoli [54] discovered how reversible computation can be done in principle [55]. Another currently popular version of the Landauer principle in formulations where one either needs to spend a minimum of $k_B T \ln 2$ energy to destroy or erase one bit of information, or a minimum of $k_B T \ln 2$ heat is released by "burning" one bit of information, is also completely wrong. These two formulations plainly and generally contradict the second law of thermodynamics, which in the differential form states that $dS \geq \delta Q/T$ (i.e., that the increase of entropy, or loss of information, $dI \equiv -dS/k_B \ln 2$ – a very fundamental equality, or rather tautology of the physical information theory), is equal to or exceeds the heat exchange with the environment in the units of T. For an adiabatically isolated system, $\delta Q = 0$; hence, $dI \leq 0$, i.e., entropy can increase and information can diminish spontaneously, without any heat being produced into the surroundings. This is just the second law of thermodynamics rephrased. As a matter of fact, $\delta Q = |dI| k_B T \ln 2$ is the maximal (not minimal!) amount of heat which can be produced by "burning" information in the amount of dI bits. To create and store one bit of information, one indeed needs to spend at least $k_B T \ln 2$ of free energy at T = constant, but not to destroy or erase it, in principle. Information can be destroyed spontaneously; however, this can take an infinite amount of time. The Landauer principle belongs to common scientific fallacies. However, at the same time, it has established a current hype in the literature. An "economical" reason for this is that the current clock rate of computer processors has not been increased beyond 10 GHz for over one decade because of immense heat production. Plainly said, it is not possible to further cool the processors down to increase their rate, and the energy consumption becomes unreasonable. We eagerly search for a solution to this severe problem. This problem is, however, a problem of the current design of these processors and our present technology, which indeed provides severe thermodynamical limitations [56]. However, it

has a little in common with the Landauer principle as heat is currently produced many orders of magnitude above the minimum of the Landauer principle, which should not be taken seriously as a rigorous, theoretical, universally valid bound anyway. Nevertheless, operation at a finite speed is inevitably related to heat loss. The question is, how to minimize this at a maximal speed? This question is clearly beyond a solution in equilibrium thermodynamics, but belongs rather to kinetic theory. The minimum energy requirements are inevitably related to the question of how fast to compute. This presents an open, unsolved problem.

Minimalist model of adiabatic pump

Coming back to the adiabatic operation of molecular motors or pumps, a minimalist model based on the time modulation of the energy levels is now analyzed. The physical background of the idea of adiabatic operation is sound. However, can it be realized in popular models characterized by discrete energy levels? The minimalist model contains just one time-dependent energy level, $E(t)$, and two constant energy levels corresponding to chemical potentials μ_1 and μ_2 of two baths of particles between which the transport occurs. They must be considered as electrochemical potentials for charged particles (e.g., Fermi levels of electrons in two leads) or electrochemical potentials of transferred ions in two bath solutions separated by a membrane. Pumping takes place when a time modulation of $E(t)$ can be used to pump against $\Delta\mu = \mu_2 - \mu_1 > 0$, as shown in Figure 5a. Here, both the energy level $E(t)$ and the corresponding rates $k_1(t)$ and $k_{-1}(t)$, $k_2(t)$ and $k_{-2}(t)$ are time dependent. Their proper description would be rate constants, if they were time independent. Given a sufficiently slow modulation and fast equilibration at any instant t, one can assume the local equilibrium conditions

$$
\frac{k_1(t)}{k_{-1}(t)} = \exp\{\beta[E(t) - \mu_1]\},
$$
$$
\frac{k_2(t)}{k_{-2}(t)} = \exp\{-\beta[E(t) - \mu_2]\}.
$$
(25)

Notice, that this condition is not universally valid. It can be violated by fast fluctuating fields (as shown in [22] and references cited therein) for a plenty of examples and using an approach beyond this restriction within a quantum-mechanical setting. The rates are generally retarded functionals of energy level fluctuations and not functions of instantaneous energy levels. However, a local equilibrium can be a very good approximation. Figure 5b rephrases the transport process in Figure 5a in terms of the states of the pump: empty (state ∅) and filled with one transferred particle (state 1). The former state is populated with probability $p_0(t)$, and the latter one with probability $p_1(t)$, $p_0(t) + p_1(t) = 1$. The empty level can be filled with rate $k_1(t)$ from the left bath level μ_1, and with rate $k_{-2}(t)$ from the right bath level μ_2. The filling flux is thus $j_f = (k_1 + k_{-2})p_0$. Moreover, it can be emptied with rate $k_2(t)$ to μ_2, and with rate $k_{-1}(t)$ to μ_1. The corresponding master equations reduce to a single relaxation equation because of probability conservation:

$$
\dot{p}_0(t) = -\left[k_1(t) + k_{-2}(t)\right]p_0(t) + \left[k_2(t) + k_{-1}(t)\right]p_1(t)
$$
$$
= -\Gamma(t)p_0(t) + R(t),
$$
(26)

where

$$
\Gamma(t) = k_1(t) + k_{-1}(t) + k_{-2}(t) + k_2(t),
$$
(27)

and

$$
R(t) = k_{-1}(t) + k_2(t).
$$
(28)

The instantaneous flux between the levels μ_1 and $E(t)$ is

$$
I_t(t) = k_1(t)p_0(t) - k_{-1}(t)p_1(t),
$$
(29)
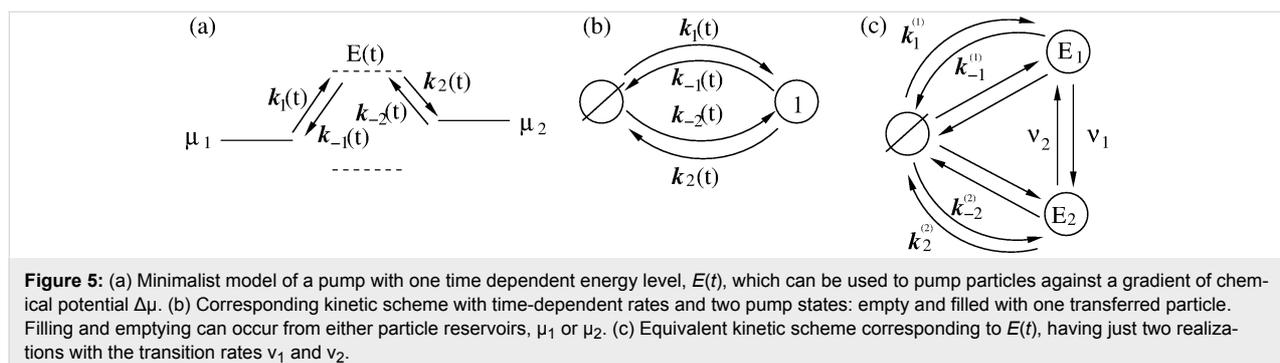
Figure 5: (a) Minimalist model of a pump with one time dependent energy level, $E(t)$, which can be used to pump particles against a gradient of chemical potential $\Delta\mu$. (b) Corresponding kinetic scheme with time-dependent rates and two pump states: empty and filled with one transferred particle. Filling and emptying can occur from either particle reservoirs, μ_1 or μ_2. (c) Equivalent kinetic scheme corresponding to $E(t)$, having just two realizations with the transition rates v_1 and v_2.

and

$$I_2(t) = k_2(t) p_1(t) - k_{-2}(t) p_0(t), \qquad (30)$$

between the levels $E(t)$ and μ_2. Clearly, the time averages

$$\overline{I}_1 = \lim_{t\to\infty} (1/t) \int_0^t I_1(t')\, dt'$$

and

$$\overline{I}_2 = \lim_{t\to\infty} (1/t) \int_0^t I_1(t')\, dt'$$

must coincide ($\overline{I}_1 = \overline{I}_2 = I$) because particles cannot accumulate on the level $E(t)$.

First, we show that pumping is impossible within the approximation of a quasi-static rate, that is, when the rates are considered to be constant at a frozen instant in time and one solves the problem within this approximation. Indeed, in this case for a steady-state flux that is an instantaneous function of time we obtain:

$$
\begin{aligned}
I(t) &= \frac{k_1(t) k_2(t) - k_{-1}(t) k_{-2}(t)}{\Gamma(t)} \\
&= \frac{k_1(t) k_2(t)}{\Gamma(t)} \left[1 - e^{\Delta\mu/(k_B T)} \right],
\end{aligned}
\qquad (31)
$$

where in the second line, Equation 25 was used. Clearly, for $\Delta\mu > 0$, $I(t) < 0$ at any t. Averaging over time yields,

$$\overline{I}_{qs} = \overline{I}_f \left[1 - e^{\Delta\mu/(k_B T)} \right], \qquad (32)$$

with

$$\overline{I}_f = \lim_{\mathcal{T}\to\infty} (1/\mathcal{T}) \int_0^{\mathcal{T}} k_1(t) k_2(t)\, dt / \Gamma(t).$$

The current always flows from higher μ_2 to lower μ_1. The same will happen for any number of intermediate levels $E_i(t)$ within such an approximation.

Origin of pumping

One can, however, easily solve Equation 26 for arbitrary $\Gamma(t)$ and $R(t)$:

$$p_0(t) = p_0(0) e^{-\int_0^t \Gamma(t')\,dt'} + \int_0^t dt'\, R(t') e^{-\int_{t'}^t \Gamma(t'')\,dt''}. \qquad (33)$$

The first term vanishes in the limit $t\to\infty$ and a formal expression for the steady-state averaged flux, $\overline{I}$, can be readily written as shown in Equation 34 where $\overline{k}_{-1}$ is time-averaged $k_{-1}(t)$.

However, to evaluate it for some particular conditions of energy and rate modulation is generally a rather cumbersome task. The fact that pumping is possible is easy to understand, with the following protocol of energy level and rate modulation: (step 1) energy level $E(t)$ decreases, $E(t) < \mu_1$, with an increasing prefactor in $k_{\pm 1}(t)$ (left gate opens), and a sharply decreasing prefactor in $k_{\pm 2}(t)$ (right gate is closed), a particle enters the pump from the left; (step 2) energy level $E(t)$ increases, $E(t) > \mu_2$, and the prefactor in $k_{\pm 1}(t)$ sharply drops, the left gate closes and the right one remains closed; (step 3) the right gate opens and the particle leaves to the right; (step 4) the right gate closes, the energy level $E(t)$ decreases and the left gate opens, so that the initial position in 3D parameter space (two prefactors and one energy level) is repeated, and one cycle is completed. The general idea of an ionic pump with two intermittently opening/closing gates has in fact been suggested a long time ago [57].

Some general results can be obtained within this model for adiabatic slow modulation and related to an adiabatic, geometric, Berry phase, $b(t)$. The origin of this can be understood per analogy with a similar approach used to solve the Schroedinger equation in quantum mechanics for adiabatically modulated, quasi-stationary energy levels [58], by making the following ansatz to solve Equation 26: $p_0(t) = e^{ib(t)} R(t)/\Gamma(t) + c.c.$ Making a loop in a 2D space of parameters adds or subtracts 2π to $b(t)$. Furthermore, an additional related contribution, the pumping current, appears in addition to one in Equation 32, with averaging done over one cycle period. This additional contribution is proportional to the cycling rate, ω (see [59] for details). However, it is small and cannot override one in Equation 32 consistently with the adiabatic modulation assumptions. Hence, adiabatic pumping against any substantial bias $\Delta\mu > 0$ is not possible within this model. This indeed can easily be understood by making a sort of adiabatic approximation in

$$\overline{I} = \lim_{\mathcal{T}\to\infty} \frac{1}{\mathcal{T}} \int_0^{\mathcal{T}} dt \left[k_1(t) + k_{-1}(t) \right] \int_0^t dt'\, R(t') e^{-\int_{t'}^t \Gamma(t'')\,dt''} - \overline{k}_{-1}, \qquad (34)$$

Equation 33, $\int_{t'}^{t}\Gamma(t'')dt'' \approx \Gamma(t)(t-t')$, and doing an integration by parts therein, so that in the long time limit $p_0(t) \approx R(t)/\Gamma(t) + \delta p_0(t)$, where $\delta p_0(t) \propto \dot{R}(t) \propto \omega$. The first term leads to Equation 32, and the second term corresponds to a small perturbative pump current, which vanishes as $\omega \rightarrow 0$. This pump current can be observed only for $\Delta\mu = 0$, where $\overline{I}_{qs} = 0$. Hence, the thermodynamic efficiency of this pump is close to zero in the adiabatic pumping regime.

Moreover, for realistic molecular pumps, e.g., driven by the energy of ATP hydrolysis, the adiabatic modulation is difficult (if even possible) to realize. A sudden modulation of the energy levels, (e.g., by a power stroke), when the energy levels jump to new discrete positions, is more relevant, especially on a single-molecule level.

Efficient nonadiabatic pumping

The cases where $E(t)$ takes on discrete values and is a time-continuous semi-Markovian process can be handled differently. Especially simple is a particular case with $E(t)$ taking just two values E_1 and $E_2 > E_1$ with transition rates ν_1, and ν_2 between those. Then, the transport scheme in Figure 5b can be rephrased as one in Figure 5c with rate constants $k_j^{(i)}$ for the transitions to and from the energy levels E_i, $i = 1,2, j = 1,2,-1,-2$, and

$$\frac{k_1^{(i)}}{k_{-1}^{(i)}} = \exp\left\{\beta\left[E_i - \mu_1\right]\right\},$$
$$\frac{k_2^{(i)}}{k_{-2}^{(i)}} = \exp\left\{-\beta\left[E_i - \mu_2\right]\right\}. \tag{35}$$

Now we have three populations, p_0 of the empty state, p_1 of level E_1, and p_2 of level E_2. The steady state flux can be calculated as $I = \nu_1 p_1^{(st)} - \nu_2 p_2^{(st)}$, where $p_{1,2}^{(st)}$ are steady state populations. Straightforward (but somewhat lengthy) calculations yield Equation 36.

From the structure of this equation it is immediately clear that the flux can be positive for positive $\Delta\mu$ (real pumping) by considering, e.g., the limit: $k_1^{(1)} \gg k_{-2}^{(1)}$, $k_{-1}^{(2)} \ll k_2^{(2)}$, $k_1^{(2)} \ll k_{-2}^{(2)}$, $k_2^{(1)} \ll k_{-1}^{(1)}$, and $\nu_1 \gg \nu_2$. Physically, it is obvious when $E_1 < \mu_1$, and $E_2 > \mu_2$, together with $k_1^{(1)} \gg k_{-2}^{(1)}$ (i.e., the level E_1 is easily filled from μ_1, but not from μ_2 because of a large barrier on the right side – the entrance of pump is practi-

cally closed from the right), and $k_2^{(2)} \gg k_{-1}^{(2)}$ (i.e., the particle easily goes from E_2 to μ_2 and cannot go back to μ_1 because the left entrance is now almost closed). Under these conditions, also $k_1^{(2)} \ll k_{-2}^{(2)}$ and $k_2^{(1)} \ll k_{-1}^{(1)}$ are well justified. Hence, we obtain for the pumping rate

$$I \approx \frac{\nu_1 k_1^{(1)} k_2^{(2)}}{k_1^{(1)} k_2^{(2)} + \nu_1\left(k_1^{(1)} + k_2^{(2)}\right)}. \tag{37}$$

This expression looks like a standard Michaelis–Menthen rate of enzyme operation, which is customly used in biophysics [3] for modeling molecular motors and pumps. The elevation of the $E(t)$ level from E_1 to E_2 can be effected, e.g., by ATP binding in the case of ionic pumps, with $\nu_1 \propto c_{ATP}$, where c_{ATP} is the ATP concentration. This is a simple, basic model for pumps. From Equation 37 it follows that $I \approx \nu_1$ at $\nu_1 \tau \ll 1$, where $\tau = 1/k_1^{(1)} + 1/k_2^{(2)}$ is the sum of filling and emptying times, and it reaches the maximal pumping rate $I_{max} \approx 1/\tau$, for $\nu_1\tau \gg 1$. The thermodynamic efficiency of such a pump is $R = \Delta\mu/\Delta E$, where $\Delta E = E_2 - E_1$ is the energy invested in pumping. The derivation of the approximation in Equation 37 requires that $\exp(\varepsilon_{1,2}/k_BT) \gg 1$, where $\varepsilon_1 = \mu_1 - E_1$, and $\varepsilon_1 = E_2 - \mu_2$, which is already well-satisfied for $\varepsilon_{1,2} > 2k_BT$. Hence, $R = \Delta\mu/(\Delta\mu + \varepsilon_1 + \varepsilon_2)$ can be close to one for a large $\Delta\mu \gg \varepsilon_1 + \varepsilon_2$. Take for example $\Delta E = 20k_BT_r \approx 0.5$ eV, which corresponds to the typical energy released by ATP hydrolysis. Then, for $\Delta\mu = 0.4$ eV and $\varepsilon_1 = \varepsilon_2 = 2k_BT_r \approx 0.05$ eV, $R = 0.8$. Notice that a typical thermodynamic efficiency of a Na-K pump is about $R \approx 0.75$. Such a nonadiabatic pumping can be indeed highly thermodynamically efficient with small heat losses. One should note, however, that the question of whether or not the efficiency at the maximum of power, $P_W = I\Delta\mu$, can be larger than one-half or even approach one within this generic model is not that simple. To answer this question, one cannot neglect the backward transport, especially when $\Delta\mu$ becomes close to ΔE ($P_W(\Delta\mu = \Delta E) = 0$), and a concrete model for the rates must be specified in the exact result (Equation 36). In the case of an electronic pump, like the one used in nature in nitrogenase enzymes, this can be quantum tunneling rates [60], similar to the Marcus–Levich–Dogonadze rate above. Moreover, imposing a very high barrier (intermittent in time) either on the left or right can physically correspond to the interruption of the electron tunneling pathway due to ATP-induced conformational changes, that is, to the modulation of tunnel coupling $V_{tun}(t)$

$$I = \frac{\nu_1\left(k_1^{(1)} + k_{-2}^{(1)}\right)\left(k_{-1}^{(2)} + k_2^{(2)}\right) - \nu_2\left(k_1^{(2)} + k_{-2}^{(2)}\right)\left(k_{-1}^{(1)} + k_2^{(1)}\right)}{\sum_i k_i^{(1)} \sum_j k_j^{(2)} + \nu_1\left(\sum_j k_j^{(2)} + k_1^{(1)} + k_{-2}^{(1)}\right) + \nu_2\left(\sum_j k_j^{(1)} + k_1^{(2)} + k_{-2}^{(2)}\right)}. \tag{36}$$

synchronized with the modulation of $E(t)$, as occurs in nitrogenase. This question of efficiency at maximum power will be analyzed elsewhere in detail, both for the classical and quantum rate models.

To summarize this section, the concept of the adiabatic operation of molecular machines is sound and should be pursued further. However, the simplest known adiabatic pump operates in fact at nearly zero thermodynamical efficiency, while a power stroke mechanism can be highly efficient within the same model. It seems obvious that in order to realize a thermodynamically efficient adiabatic pumping, the gentle operation of a molecular machine without erratic jumps, a continuum of states is required (or possibly many states depending continuously on an external modulation parameter). Further research is thus highly desirable and necessary.

How can biological molecular motors operate highly efficiently in highly dissipative, viscoelastic environments?

As it has been clarified above, Brownian motors can work highly efficiently in dissipative environments, causing arbitrarily strong viscous friction acting on a motor. This corresponds to the case of normal diffusion,

$$\left\langle \left[\delta x(t) \right]^2 \right\rangle = 2Dt,$$

in a force-free case. In a crowded environment of biological cells, diffusion can be, however, anomalously slow,

$$\left\langle \left[\delta x(t) \right]^2 \right\rangle = 2D_\alpha t^\alpha \Big/ \Gamma(1+\alpha),$$

where $0 < \alpha < 1$ is the power law exponent of subdiffusion and D_α is the subdiffusion coefficient [61,62]. There is a huge body of growing experimental evidence for subdiffusion of particles of various sizes, from 2–3 nm (typical for globular proteins) [63,64] to 100–500 nm [65-69] (typical for various endosomes), both in living cells and in crowded polymer and colloidal solutions (complex fluids) physically resembling cytoplasm. There are many theories developed to explain such a behavior [61,62]. One is based on the natural viscoelasticity of such complex liquids (see [70,71] for a review and details), which has a deep dynamical foundation (see above). Viscoelasticity that leads to the above subdiffusion corresponds to a power law memory kernel $\eta(t) = \eta_\alpha t^{-\alpha}/\Gamma(1-\alpha)$ in Equation 3 and Equation 6. In this relation, η_α is a fractional friction coefficient related to D_α by the generalized Einstein relation, $D_\alpha = k_B T/\eta_\alpha$. Using the notion of the fractional Caputo derivative, the dissipative term in Equation 3 can be abbreviated as $\eta_\alpha d^\alpha x/dt^\alpha$, where the fractional de-

rivative operator $d^\alpha f(t)/dt^\alpha$ acting on an arbitrary function $f(t)$ is just defined by this abbreviation. The corresponding GLE is named the fractional Langevin equation (FLE). Its solution yields the above subdiffusion scaling exactly in the inertialess limit, $M \to 0$, corresponding precisely to the fractional Brownian motion [70,72], or asymptotically otherwise. The transport in the case of a constant force applied, f_0, is also subdiffusive,

$$\left\langle \delta x(t) \right\rangle = (f_0/\eta_\alpha) t^\alpha \Big/ \Gamma(1+\alpha) = \frac{f_0}{2k_B T} \left\langle \left[\delta x(t) \right]^2 \right\rangle.$$

These results correspond exactly to a sub-ohmic model of the spectral density of a thermal bath [16], $J(\omega) = \eta_\alpha \omega^\alpha$, within the dynamical approach to the generalized Brownian motion. They can be easily understood with an ad hoc Markovian approximation to the memory kernel, which yields a time-dependent viscous friction, $\eta_M(t)\dot{x}(t)$ with $\eta_M(t) \propto t^{1-\alpha}$. It diverges, $\eta_M(t) \to \infty$, when $t \to \infty$, which leads to subdiffusion and subtransport within this Markovian approximation. Such an approximation can, however, be very misleading in other aspects [73]. Nevertheless, it provokes the question: How can molecular motors, such as kinesin, work very efficiently in such media characterized by virtually infinite friction, interpolating in fact between simple liquids and solids? It is important to mention that in any fluid-like environment the effective macroscopic friction, $\eta_{eff} = \int_0^\infty \eta(t) dt$, must be finite. Hence, a memory cutoff time, τ_{max}, must exist so that $\eta_{eff} \propto \eta_\alpha \tau_{max}^{1-\alpha}$. In real life, τ_{max} can be as large as minutes, or even longer than hours. Hence, on a shorter time scale and on a corresponding spatial mesoscale, it is subdiffusion (characterized by η_α) that can be physically relevant indeed and not the macroscopic limit of normal diffusion characterized by η_{eff}. This observation opens the way for multidimensional Markovian embedding of subdiffusive processes with long range memory upon introduction of a finite number, N, of auxiliary stochastic variables. It is based on a Prony series expansion of the power-law memory kernel into a sum of exponentials, $\eta(t) = \sum_{i=1}^N k_i \exp(-\nu_i t)$, with $\nu_i = \nu_0/b^{i-1}$ and $k_i \propto \nu_i^\alpha$. This can be made numerically accurate (which is controlled by the scaling parameter, b). Apart from $\tau_{max} = \tau_{min} b^{N-1}$, it possesses also a short cutoff $\tau_{min} = 1/\nu_0$. The latter naturally emerges in any condensed medium beyond a continuous medium approximation because of its real, atomistic nature. In numerics, it can be made of the order of a time integration step. Hence, it does not even matter within the continuous medium approximation. Even with a moderate $N \approx 10$–100 (number of auxiliary degrees of freedom), Markovian embedding can be done for any realistic time scale of anomalous diffusion with sufficient accuracy [70,74]. A very efficient numerical approach based on the corresponding Markovian embedding has been developed for subdiffusion in [70,74], and for superdiffusion ($\alpha > 1$) in [75-77]. The idea of

Markovian embedding is also very natural from the perspective that any non-Markovian GLE dynamics presents a low-dimensional projection of a hyper-dimensional, singular Markovian process described by dynamical equations of motion with random initial conditions. This fact is immediately clear from a well-known dynamical derivation of GLE, reproduced above. Somewhat surprising is, however, that so few $N \approx 10\text{--}20$ are normally sufficient in practical applications.

The action of a motor on subdiffusing cargo can be simplistically modeled (with the simplest possible theory) by a random force $f(t)$ alternating its direction when the motor steps on a random network of cytoskeleton [78]. The driven cargo follows a diffusional process $\langle [\delta x(t)]^2 \rangle_{t'} \propto t^{\beta}$, with some exponent β, which is defined by a trajectory averaging of squared displacements $\delta x(t|t') = x(t + t') - x(t')$ over sliding t'. Within such a model, β clearly cannot exceed 2α [79], which corresponds to subtransport with alternating direction in time. Hence, for $\alpha < 0.5$, cargo superdiffusion ($\beta > 1$) could not be caused by motors within such a simple approach. However, experiments show [80,81] that freely subdiffusing cargos (e.g., $\alpha = 0.4$ [80,82]) can superdiffuse when they are driven by motors also for $\alpha < 0.5$ (e.g., $\beta = 1.3$ for $\alpha = 0.4$ [80])). Therefore, a more appropriate modeling of the transport by molecular motors in viscoelastic environments is required. This was quite recently developed in [83-85], by generalizing the pioneering works on subdiffusive rocking [70,86-89] and flashing [90] ratchets.

Viscoelastic effects should be considered on the top of viscous Stokes friction caused by the water component of cytosol. Then, a basic 1D model for a large cargo (20–500 nm) pulled by a much smaller motor (2–10 nm) on an elastic linker (cf., Figure 6) can be formulated as follows [85]

$$\eta_c \dot{y} = -\int_0^t \eta(t - t') \dot{y}(t') dt' - \frac{k_L(y - x)}{1 - (y - x)^2 / r_{\max}^2} \quad (38)$$
$$+ \xi_c(t) + \xi(t),$$

$$\eta_m \dot{x} = \frac{k_L(y - x)}{1 - (y - x)^2 / r_{\max}^2} - \frac{\partial}{\partial x} U(x, \varsigma(t)) - f_L + \xi_m(t). \quad (39)$$

This presents a generalization of a well-known model of molecular motors [91-93] by coupling the motor to a subdiffusing cargo on an elastic linker. Here, both the motor (coordinate x) and the cargo (coordinate y) are subjected to independent, thermal white noise of the environment, $\xi_m(t)$, and $\xi_c(t)$, respectively, which obey the corresponding FDRs. Both of the particles are overdamped and characterized by Stokes frictional forces with frictional constants η_m, and η_c. In addition, viscoelastic frictional force acts on the cargo and is characterized by the memory kernel discussed above (fractional friction model) and the corresponding stochastic thermal force, $\xi(t)$, with algebraically decaying correlations. It obeys a corresponding FDR. The motor can pull cargo on an elastic linker with spring constant k_L (small extensions) and maximal extension length $r_{\max}$ (the so-called finite extension nonlinear elastic (FENE) model [94] is used here). The motor (kinesin) is bound to a microtubule and can move along it in a periodic potential, $U(x + L, \zeta(t)) = U(x, \zeta(t))$, reflecting the microtubule spatial period L, and it can do useful work against a loading force, f_L, directed against its motion caused by cyclic conformational fluctuations $\zeta(t)$. The microtubule is a polar periodic structure with a periodic but asymmetric distribution of positive and negative charges (overall charge is negative) [95]. The kinesin is also charged and its charge fluctuates upon binding nega-
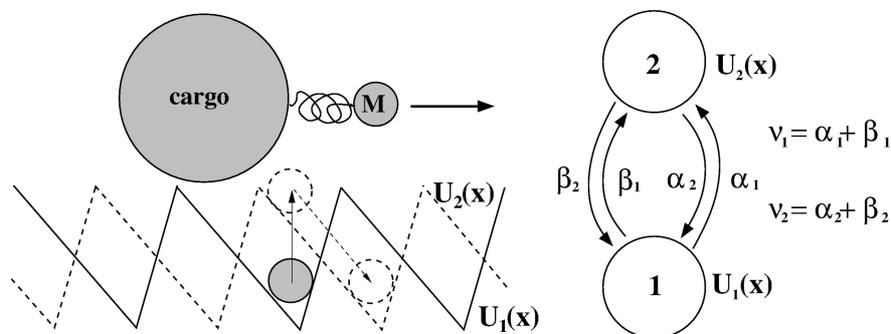
Figure 6: Motor pulling cargo on an elastic linker. The motor can be trapped in a flashing periodic potential (here, two realizations shifted by a half of a spatial period are shown). These fluctuations are caused and driven by conformational fluctuations of the motor protein. The pertinent, minimalist, two-state cyclic model of the corresponding biochemical enzymatic cycle is shown on the right. Mechanical motion, induced by cycling, exerts a back influence on cycling via spatially dependent transition rates. This can cause anomalously slow enzyme kinetics that cannot be characterized by a turnover rate in viscoelastic environments [85].

tively charged ATP molecules and dissociation of the products of ATP hydrolysis. This leads to dependence of the binding potential on the conformational variable $\zeta(t)$. Given two identical heads of kinesin, the minimalist model is to assume that there are only two conformational states of the motor (this is a gross oversimplification, of course) with $U_{1,2}(x) := U(x,\zeta_{1,2})$, and $U_1(x + L/2) = U_2(x)$ as an additional symmetry condition, so that a half-step, $L/2$, is associated with conformational fluctuations $1 \rightarrow 2$, or $2 \rightarrow 1$. During one cycle $1 \rightarrow 2 \rightarrow 1$ in the forward direction with the rates $\alpha_1(x)$ and $\beta_2(x)$, one ATP molecule is hydrolyzed. However, if this cycle is reversed in the backward direction with the rates $\beta_1(x)$ and $\alpha_2(x)$ (Figure 6), one ATP molecule is synthesized. The dependence of chemical transition rates on the position x through the potential $U_{1,2}(x)$ reflects a two-way mechano-chemical coupling. It is able to incorporate allosteric effects, which indeed can be very important for optimal operation of molecular machines [6]. Such effects can possibly emerge, for example, because the probability of binding an ATP molecule (substrate) to a kinesin motor or the release of products can be influenced by the electrostatic potential of the microtubule. In the language of [6], this corresponds to an information ratchet mechanism to distinguish it from the energy ratchet, where the rates of potential switches do not depend on the motor states (no feedback) and are fixed. Such an allostery can be used to create highly efficient molecular machines [6]. In accordance with the general principles of nonequilibrium thermodynamics applied to cyclic kinetics [2],

$$\frac{\alpha_1(x)\beta_2(x)}{\alpha_2(x)\beta_1(x)} = \exp\left[|\Delta\mu_{ATP}|/(k_B T)\right], \qquad (40)$$

for any x, where $|\Delta\mu_{ATP}|$ is the free energy released in ATP hydrolysis and used to drive one complete cycle in the forward direction. It can be satisfied, e.g., by choosing

$$\frac{\alpha_1(x)}{\alpha_2(x)} = \exp\left[\left(U_1(x) - U_2(x) + |\Delta\mu_{ATP}|/2\right)/(k_B T)\right],$$
$$\frac{\beta_1(x)}{\beta_2(x)} = \exp\left[\left(U_1(x) - U_2(x) - |\Delta\mu_{ATP}|/2\right)/(k_B T)\right]. \qquad (41)$$

The total rates

$$\nu_1(x) = \alpha_1(x) + \beta_1(x), \qquad (42)$$

$$\nu_2(x) = \alpha_2(x) + \beta_2(x) \qquad (43)$$

of the transitions between two energy profiles must satisfy

$$\frac{\nu_1(x)}{\nu_2(x)} = \exp\left[\left(U_1(x) - U_2(x)\right)/(k_B T)\right] \qquad (44)$$

at thermal equilibrium. This is a condition of the thermal detailed balance, where the dissipative fluxes simultaneously vanish both in the transport direction and within the conformational space of a motor [91,92]. It is obviously satisfied for $|\Delta\mu_{ATP}| \rightarrow 0$. Furthermore, on symmetry grounds, not only $\alpha_{1,2}(x + L) = \alpha_{1,2}(x)$, $\beta_{1,2}(x + L) = \beta_{1,2}(x)$, but also, $\alpha_1(x + L/2) = \beta_2(x)$ and $\alpha_2(x + L/2) = \beta_1(x)$. It should be emphasized that linear motors such as kinesin I or II work only one way: they utilize the chemical energy of ATP hydrolysis for doing mechanical work. They cannot operate in reverse on average, i.e., they cannot use mechanical work in order to produce ATP in a long run, even if a two-way mechano-chemical coupling can provide such an opportunity in principle. This is very different from rotary motors such as F0F1-ATPase, which is completely reversible and can operate in two opposite directions. Allosteric effects can also play a role to provide such a directional asymmetry in the case of kinesin motors. Allostery should be considered as generally important for the proper design of various motors best suited for different tasks.

For kinesins, neither cargo nor external force f_L should explicitly influence the chemical rate dependencies on the mechanical coordinate x. This leaves still some freedom in the use of different rate models. One possible choice is shown in Equation 45 [85].

In Equation 45, $\alpha_1(x) = \alpha_1$ within the $\pm\delta/2$ neighborhood of the minimum of potential $U_1(x)$ and is zero otherwise. Correspondingly, the rate $\beta_2(x) = \alpha_1$ relates to the $\pm\delta/2$ neighborhood of the minimum of potential $U_2(x)$. The rationale behind this choice is that these rates correspond to lump reactions of ATP binding and hydrolysis, and if the amplitude of the binding potential is chosen to be about $|\Delta\mu_{ATP}|$, with a sufficiently large δ, the rates $\nu_{1,2}(x)$ can be made almost independent of the position of the motor along the microtubule [85], when allosteric effects are considered to be almost negligible. This allows for the comparison of this model, featured by bidirectional mechano-chemical coupling, with a corresponding flashing energy ratchet model,

$$\nu_1(x) = \alpha_1(x) + \alpha_1(x + L/2)\exp\left[-\left(U_2(x) - U_1(x) + |\Delta\mu_{ATP}|/2\right)/(k_B T)\right],$$
$$\nu_2(x) = \alpha_1(x)\exp\left[-\left(U_1(x) - U_2(x) + |\Delta\mu_{ATP}|/2\right)/(k_B T)\right] + \alpha_1(x + L/2), \qquad (45)$$

where the switching rates between two potential realizations are spatially independent constants, $\nu_1 = \nu_2 = \alpha_1$. The latter model has been developed in [84]. Notice that even for reversible F1-ATPase motors, such an energy ratchet model can provide very reasonable and experimentally relevant results [96]. Moreover, if the linker is very rigid, $k_L \rightarrow \infty$, one can exclude the dynamics of the cargo and consider a one compound particle with a renormalized Stokes friction and the same algebraically decaying memory kernel that moves subdiffusively in a flashing potential. Such an anomalous diffusion molecular motor model has been proposed and investigated in [83]. The main results of [83], which were confirmed and further generalized in [84,85], create the following emerging coherent picture of molecular motors pulling subdiffusing (when free) cargos in viscoelastic environments of living cells. First, if a normally diffusing (when free) motor is coupled to subdiffusing cargo, it will be eventually enslaved by the cargo and also subdiffuse [84]. However, when the motor is bound to a microtubule, it can be guided by the binding potential fluctuations, which are eventually induced by its own cyclic conformation dynamics driven by the free energy released in ATP hydrolysis. It either tends towards a new potential minimum after each potential change, as demonstrated in Figure 6, or can escape by fluctuation to another minimum. A large binding potential amplitude $U_0 \gg k_{\mathrm{B}}T$ exceeding 10–$12 k_{\mathrm{B}}T$ (see Figure 6 and the corresponding discussion in [84] to understand why) makes the motor strong. For a large U_0, the probability to escape is small, and the motor will typically slide down to a new minimum and its mechanical motion along the microtubule will be completely synchronized with the potential flashes and conformational cycles. It then steps (stochastically, but unidirectionally) to the right in Figure 6 with mean velocity $v = L\alpha_1/2$. In such a way, using a power-stroke-like mechanism, a strong motor such as kinesin II (with stalling force $F \approx 6$–8 pN) can completely overcome subdiffusion and transport even subdiffusing (when free) cargos very efficiently. This requires, however, that the flashing occurs slower than the relaxation. The larger the cargo, the larger also the fractional friction coefficient η_α, and the slower the relaxation. The relaxation is algebraically slow. However, it can be sufficiently fast in absolute terms on the time scale $1/\alpha_1$, thus this mechanism is realized for sufficiently small cargos. The results of [83-85] indicate that smaller cargos, 20–100 nm, will typically be transported by strong kinesin motors quite normally, $\langle y(t) \rangle \sim \langle x(t) \rangle \propto t^{\alpha_{\mathrm{eff}}}$, with $\alpha_{\mathrm{eff}} = 1$, at typical motor turnover frequencies $\nu = \alpha_1/2 \approx 1$–$200$ Hz, provided that $f_L = 0$. This already explains why the diffusional exponent $\beta \approx 2\alpha_{\mathrm{eff}}$ can be larger than 2α. However, for larger cargos of 100–300 nm, larger turnover frequencies, and when the motor works against a constant loading force f_L, an anomalous transport regime emerges with $\alpha \leq \alpha_{\mathrm{eff}} \leq 1$. Clearly, when f_L approaches the stalling force F, the transport becomes anom-

alous. The effective transport exponent α_{eff} is thus essentially determined by the binding potential strength, motor operating frequency, cargo size, and loading force, apart from α.

It is very surprising that the thermodynamic efficiency of such a transport can be very high even within the anomalous transport regime. This result is not trivial at all. Indeed, the useful work done by a motor in the anomalous regime against loading force f_L scales sublinearly in time, $W(t) = f_L \langle x(t) \rangle \propto t^{\alpha_{\mathrm{eff}}}$ [83,88,89]. However, the free energy transformed into directional motion scales generally as $E_{\mathrm{in}}(t) \propto t^\gamma$, where $0 < \gamma \leq 1$. $\gamma = 1$ for rocking, or flashing ratchets driven by either by periodic or random two-state force, or by random fluctuations of potential characterized by a well-defined mean turnover rate $\nu = \nu_1\nu_2/(\nu_1 + \nu_2)$. Then, $E_{\mathrm{in}}(t) \propto \nu t$. In the energy balance, the rest, $E_{\mathrm{in}}(t) - W(t)$, is dissipated as a net heat $Q(t)$ transferred to the environment. The thermodynamic efficiency is thus [85]

$$R(t) = W(t) \big/ E_{\mathrm{in}}(t) \propto 1 \big/ t^\lambda \qquad (46)$$

where $\lambda = \gamma - \alpha_{\mathrm{eff}}$. Hence, $R(t) \propto 1 \big/ t^{1-\alpha_{\mathrm{eff}}}$ for $\gamma = 1$. It declines algebraically in time, like the mean power $P_W(t) = W(t)/t \propto 1 \big/ t^{1-\alpha_{\mathrm{eff}}}$. However, temporally, for the typical time required to relocate a cargo within a cell, it can be very high, especially when α_{eff} is close to one. An even more interesting result occurs in the case of bidirectional, mechanochemical coupling, because the biochemical cycling rates $\nu_{1,2}(x)$ in this case can strongly depend on the mechanical motion for a sufficiently large U_0, when allosteric effects start to play a very profound role. Indeed, if the available $|\Delta\mu_{\mathrm{ATP}}|$ becomes smaller than the sum of energies required to enhance the potential energy of the motor by two potential flashes (see vertical arrow in Figure 6) during two halves of one cycle, then the enzyme cycling in its conformational space will not generally stop. It can, however, start to occur anomalously slow with a power exponent $\gamma < 1$. The average number of forward enzyme turnovers occurring with consumption of ATP molecules scales then as $\langle N(t) \rangle \propto t^\gamma$ in time, and $E_{\mathrm{in}}(t) = |\Delta\mu_{\mathrm{ATP}}| \langle N(t) \rangle \propto t^\gamma$. This indeed happens within the model we consider here, see [85] for a particular example with $U_0 = 30 k_{\mathrm{B}}T_r \approx 0.75$ eV, $|\Delta\mu_{\mathrm{ATP}}| = 20 k_{\mathrm{B}}T_r \approx 0.5$ eV, where $\gamma \approx 0.62$ and $\alpha_{\mathrm{eff}} \approx 0.556$ at the optimal load $f_L \approx 8.5$ pN, when the motor pulls a large cargo at the same time. The thermodynamic efficiency declines in this case very slowly, with $\lambda \approx 0.067$, so that $R(t)$ is still about 70%(!) at the end point of simulations corresponding to a physical time of 3 s. Such a high efficiency is very surprising and provides one more lesson that challenges our intuition and allows us to learn and recognize the power of FDT on the nano-

scale. For microscopic and nanoscopic motion occurring at thermal equilibrium, the energy lost in frictional processes is regained from random thermal forces. Therefore, heat losses can, in principle, be small even for an anomalously strong dissipation. This is the reason why the attempts to reduce friction on the nanoscale are misguided. This can, quite counter-intuitively, even hamper efficiency, down to zero as the so-called dissipationless Hamiltonian (pseudo)-motors reveal. One should think differently.

The efficiency at maximum power can also be high in the normal transport operating regime within the discussed model. Indeed, for $U_0 = 30k_{\rm B}T_r$ and smaller cargo in [85], the transport remains almost normal until the maximum of efficiency is reached at about 80% for an optimal $f_L^{(\max)} \approx 9$ pN (see Figure 8 in [85], where f_0 corresponds to f_L here). The nearly linear dependence of the efficiency on load until it reaches about 70% indicates that the motor steps with almost the same maximal velocity as at zero loading force f_L. The following simple heuristic considerations can be used to rationalize the numerical results. The motor develops a maximal driving force F, which depends on U_0, the motor turnover rate, and temperature (via an entropic contribution), see Figure 6 in [84], where $F = f_0^{stall}$. This is the stalling force. The larger U_0, the stronger the motor and larger F. Let us assume that the motor stepping velocity declines from v_0 to zero with increasing loading force, f_L, as $v(f_L) = v_0[1 - (f_L/F)^a]$, where $a \geq 1$ is a power-law exponent. Within the linear minimalist model of the motor considered above (and also in an inefficient transport regime within the considered model), $a = 1$, i.e., the motor velocity declines linearly with load. However, in a highly efficient nonlinear regime, this dependence is strongly nonlinear, $a >> 1$. The maximum of the motor power $P_W(f_L) = f_L v(f_L)$ is reached at $f_L^{(\max)} = F/(1 + a)^{1/a}$, with $v\left(f_L^{(\max)}\right) = av_0/(1 + a)$. For $a = 1$, $f_L^{(\max)} = F/2$ and the dependence $P_W(f_L)$ is parabolic. With the increase of U_0, a is also strongly increased and the dependence $P_W(f_L)$ becomes strongly skewed, in agreement with numerics. Since the input motor power, $P_{\rm in}$, does not depend on load within our model in the energy ratchet regimes, the motor efficiency $R = P_W/P_{\rm in}$ just reflects that of P_W. Hence, the maximum of R versus f_L does correspond to the maximum efficiency at maximum power and can exceed 1/2. The same heuristic considerations can be applied to the results presented in [93] for very efficient normal motors. Of course, these results are not necessarily experimentally relevant for, e.g., known kinesin I motors whose maximal efficiency is about 50% [3]. However, our theory can be very relevant for devising artificial motors having other tasks because it provides a biophysically very reasonable model where efficiency at maximum power can be larger than the Jacobi bound of linear stochastic dynamics. It must be stressed, however, that in the anomalous transport regime, one cannot define power and one should introduce the notion of sub-power [88,89].

One should also note the following. Even at $f_L = 0$, when the thermodynamic efficiency is formally zero, $R(t) = 0$, something useful is done: the cargo is transferred over a certain distance by overcoming the dissipative resistance of the environment. However, neither the potential energy of the motor, nor that of the cargo is increased. This is actually normal modus operandi of linear molecular motors like kinesins I or II, very different from ionic pumps whose the primary goal is to increase the (electro)chemical potential of transferred ions (i.e., to charge a battery). Such a $R = 0$ regime, should, however, be contrasted with the zero efficiency of frictionless rocking pseudo-ratchets. In our case, the useful work is done against the environment. Pseudo-ratchets are not capable of doing any useful work in principle.

Conclusion

In this contribution, some of the main operating principles of minuscule Brownian machines operating on the nano- and microscale are reviewed. Unlike in macroscopic machines, thermal fluctuations and noise play a profound and moreover very constructive role in the microworld. In fact, thermal noise plays the role of a stochastic lubricant, which supplies energy to the Brownian machines to compensate for their frictional losses. This is the very essence of the fluctuation–dissipation theorem: both processes (i.e., frictional losses and energy gain from the thermal noise) are completely compensated on average at thermal equilibrium. Classically, thermal noise vanishes at a temperature of absolute zero (which physically cannot be achieved anyway, in accordance with the third law of thermodynamics), and only then would friction win (classically). However, quantum noise (vacuum zero-point fluctuations) is present even at absolute zero. Therefore, friction cannot win even at absolute zero and quantum Brownian motion never stops. These fundamental facts allow, in principle, for a complete transfer of the driver energy into useful work by isothermal Brownian engines. Their thermodynamic efficiency approaches unity when the net heat losses vanish. This happens when the motor operates close to thermal equilibrium and can be done at any, arbitrarily strong dissipation at ambient temperature. It is not necessary to perform work in the deep quantum cold or to strive for high-quality quantum coherence. A striking example of this is provided by the high transport and thermodynamic efficiency of molecular motors in the subdiffusive transport regime. Operating anomalously slow (in mathematical terms, i.e., exhibiting sublinear dependence of both the transport distance and the number of motor turnovers on time), such motors can be quite fast in absolute terms and can work under a heavy load [85]. In this, and also in other aspects, the intuitive understanding of

subdiffusion and subtransport as being extremally slow can be very misleading [97-99]. On the other hand, the frictionless rocking pseudo-ratchets cannot do any useful work, as we clarified in this review.

A scientifically sound possibility to approach the theoretical maximum of thermodynamic efficiency of isothermal motors at arbitrarily strong dissipation and ambient temperatures is intrinsically related to the possibility of reversible dissipative classical computing without heat production. However, such an adiabatic operation would be infinitesimally slow. Clearly, such a motor or computer is not of practical use. Moreover, the adiabatic operation of dissipative pumps involving discrete energy levels is possible only for a vanishing load. Here, a natural question emerges: What is the thermodynamic efficiency at maximum power? The linear dynamics result that $R_{max} = 1/2$ is the theoretical upper bound is, however, completely wrong within nonlinear stochastic dynamics, as shown in this review with three examples. This opens the door for the design of highly efficient Brownian and molecular motors. Moreover, the recent model results in [85] for a normal transport of sufficiently small subdiffusing (when free) cargos by a kinesin motor with a very high thermodynamical efficiency at optimal external load do imply that thermodynamic efficiency at maximum power within that model can also be well above 50%. The earlier results for normal diffusion molecular motors within a very similar model [91,92] obtained in [93] also corroborate such conclusions. Such models are able to mimic allosteric interactions within minimalist model setups. Chemical allosteric interactions, which are intrinsically highly nonlinear, can optimize the performance of various molecular motors. This line of reasoning is especially important for the design of artificial molecular motors [6] and should be pursued further.

Quantum effects are also important to consider to design highly efficient molecular machines, even when quantum coherence does not play any role (that is, on the level of rate dynamics with quantum rates, like in the Pauli master equation). In particular, it has been shown in this review within the simplest model possible that quantum effects (related to the inverted regime of quantum particle transfer) can lead to thermodynamic efficiencies at maximal power larger than one-half for the machine operating both in forward and reverse directions. Quantum coherence could also play a role here, which should be clarified in further research. Undoubtedly, quantum coherence is central for quantum computing, which is obviously reversible [55]. However, this is a different story.

I hope that the readers of this review will find it especially useful in liberating themselves (and possibly others) from some common fallacies, both spoken and unspoken, which unfortu-

nately have pervaded the literature and hinder progress. With this work, a valid, coherent picture emerges.

Acknowledgements

References

1. Pollard, T. D.; Earnshaw, W. C.; Lippincott-Schwarz, J. *Cell Biology,* 2nd ed.; Saunders Elsevier: Philadelphia, PA, U.S.A., 2008.
2. Hill, T. L. *Free Energy Transduction and Biochemical Cycle Kinetics;* Springer: Berlin, Germany, 1980.
3. Nelson, P. *Biological Physics: Energy, Information, Life;* W. H. Freeman: New York, NY, U.S.A., 2003.
4. Kay, E. R.; Leigh, D. A.; Zerbetto, F. *Angew. Chem., Int. Ed.* **2006,** *46,* 72–191. doi:10.1002/anie.200504313
5. Erbas-Cakmak, S.; Leigh, D. A.; McTernan, C. T.; Nussbaumer, A. L. *Chem. Rev.* **2015,** *115,* 10081–10206. doi:10.1021/acs.chemrev.5b00146
6. Cheng, C.; McGonigal, P. R.; Stoddart, J. F.; Astumian, R. D. *ACS Nano* **2015,** *9,* 8672–8688. doi:10.1021/acsnano.5b03809
7. Callen, H. B. *Thermodynamics and an Introduction to Thermostatistics,* 2nd ed.; John Wiley & Sons: New York, NY, U.S.A., 1985.
8. Curzon, F. L.; Ahlborn, B. *Am. J. Phys.* **1975,** *43,* 22–24. doi:10.1119/1.10023
9. Yoshida, M.; Muneyuki, E.; Hisabori, T. *Nat. Rev. Mol. Cell Biol.* **2001,** *2,* 669–677. doi:10.1038/35089509
10. Kubo, R. *Rep. Prog. Theor. Phys.* **1966,** *29,* 255. doi:10.1088/0034-4885/29/1/306
11. Bogolyubov, N. N. On some Statistical Methods in Mathematical Physics. Ukranian Academy of Sciences: Kiev, Ukraine, 1945; pp 115–137. In Russian.
12. Ford, G. W.; Kac, M.; Mazur, P. *J. Math. Phys.* **1965,** *6,* 504. doi:10.1063/1.1704304
13. Ford, G. W.; Lewis, J. T.; O'Connell, R. F. *Phys. Rev. A* **1988,** *37,* 4419–4428. doi:10.1103/PhysRevA.37.4419
14. Caldeira, A. O.; Leggett, A. J. *Ann. Phys.* **1983,** *149,* 374–456. doi:10.1016/0003-4916(83)90202-6
15. Toyabe, S.; Okamoto, T.; Watanabe-Nakayama, T.; Taketani, H.; Kudo, S.; Muneyuki, E. *Phys. Rev. Lett.* **2010,** *104,* 198103. doi:10.1103/PhysRevLett.104.198103
16. Weiss, U. *Quantum Dissipative Systems,* 2nd ed.; World Scientific Publishing Co Pte Ltd: Singapore, 1999.
17. Gardiner, C. W.; Zoller, P. *Quantum Noise: a Handbook of Markovian and Non-Markovian Quantum Stochastic Methods with Applications to Quantum Optics;* Springer: Berlin, Germany, 2000.
18. Lindblad, G. *Commun. Math. Phys.* **1976,** *48,* 119. doi:10.1007/BF01608499
19. Nakajima, S. *Prog. Theor. Phys.* **1958,** *20,* 948–959. doi:10.1143/PTP.20.948
20. Zwanzig, R. *J. Chem. Phys.* **1960,** *33,* 1338–1341. doi:10.1063/1.1731409
21. Argyres, P. N.; Kelley, P. L. *Phys. Rev. A* **1966,** *134,* A98. doi:10.1103/PhysRev.134.A98
22. Goychuk, I.; Hänggi, P. *Adv. Phys.* **2005,** *54,* 525–584. doi:10.1080/00018730500429701

23. Sekimoto, K. *J. Phys. Soc. Jpn.* **1997,** *66,* 1234–1237. doi:10.1143/JPSJ.66.1234

24. Wyman, J. *Proc. Natl. Acad. Sci. U. S. A.* **1975,** *72,* 3983–3987.

25. Rozenbaum, V. M.; Yang, D.-Y.; Lin, S. H.; Tsong, T. Y. *J. Phys. Chem. B* **2004,** *108,* 15880–15889. doi:10.1021/jp048200a

26. Qian, H. *J. Phys.: Condens. Matter* **2005,** *17,* S3783–S3794. doi:10.1088/0953-8984/17/47/010

27. Goychuk, I.; Grifoni, M.; Hänggi, P. *Phys. Rev. Lett.* **1998,** *81,* 649–652. doi:10.1103/PhysRevLett.81.649

28. Lamoreaux, S. K. *Rep. Prog. Phys.* **2005,** *68,* 201–236. doi:10.1088/0034-4885/68/1/R04

29. Schmiedl, T.; Seifert, U. *EPL* **2008,** *83,* 30005. doi:10.1209/0295-5075/83/30005

30. Seifert, U. *Phys. Rev. Lett.* **2011,** *106,* 020601. doi:10.1103/PhysRevLett.106.020601

31. Van den Broeck, C.; Kumar, N.; Lindenberg, K. *Phys. Rev. Lett.* **2012,** *108,* 210602. doi:10.1103/PhysRevLett.108.210602

32. Golubeva, N.; Imparato, A.; Peliti, L. *EPL* **2012,** *97,* 60005. doi:10.1209/0295-5075/97/60005

33. Stratonovich, R. L. *Radiotekh. Elektron. (Moscow, Russ. Fed.)* **1958,** *3,* 497.

34. Stratonovich, R. L. *Topics in the Theory of Random Noise;* Gordon and Breah: New York, NY, U.S.A., 1967; Vol. II.

35. Risken, H. *The Fokker-Planck Equation: Methods of Solution and Applications,* 2nd ed.; Springer: Berlin, Germany, 1989.

36. Reimann, P. *Phys. Rep.* **2002,** *361,* 57–265. doi:10.1016/S0370-1573(01)00081-3

37. Wikström, M. *Biochim. Biophys. Acta* **2004,** *1655,* 241–247. doi:10.1016/j.bbabio.2003.07.013

38. Atkins, P.; de Paula, J. *Physical Chemistry;* Oxford University Press: Oxford, United Kingdom, 2006; pp 896–904.

39. Nitzan, A. *Chemical Dynamics in Condensed Phases: Relaxation, Transfer and Reactions in Condensed Molecular Systems;* Oxford University Press: Oxford, United Kingdom, 2007.

40. Goychuk, I. A.; Petrov, E. G.; May, V. *Chem. Phys. Lett.* **1996,** *253,* 428–437. doi:10.1016/0009-2614(96)00323-5

41. Goychuk, I. A.; Petrov, E. G.; May, V. *Phys. Rev. E* **1997,** *56,* 1421–1428. doi:10.1103/PhysRevE.56.1421

42. Goychuk, I. A.; Petrov, E. G.; May, V. *J. Chem. Phys.* **1997,** *106,* 4522–4530. doi:10.1063/1.473495

43. Flach, S.; Yevtuschenko, O.; Zolotaryuk, Y. *Phys. Rev. Lett.* **2000,** *84,* 2358–2361. doi:10.1103/PhysRevLett.84.2358

44. Goychuk, I.; Hänggi, P. Directed current without dissipation: reincarnation of a Maxwell-Loschmidt demon. In *Lecture Notes in Physics: Stochastic Processes in Physics, Chemistry, and Biology;* Freund, J.; Pöschel, T., Eds.; Springer: Berlin, Germany, 2000; Vol. 557, pp 7–20.

45. Wonneberger, W.; Breymayer, H.-J. *Z. Phys. B* **1984,** *56,* 241–246. doi:10.1007/BF01304177

46. Goychuk, I.; Hänggi, P. *Europhys. Lett.* **1998,** *43,* 503–509. doi:10.1209/epl/i1998-00389-2

47. Goychuk, I.; Hänggi, P. *J. Phys. Chem. B* **2001,** *105,* 6642–6647. doi:10.1021/jp010102r

48. Dykman, M. I.; Rabitz, H.; Smelyanskiy, V. N.; Vugmeister, B. E. *Phys. Rev. Lett.* **1997,** *79,* 1178. doi:10.1103/PhysRevLett.79.1178

49. Gaspard, P. *Physica A* **2006,** *369,* 201–246. doi:10.1016/j.physa.2006.04.010

50. Paschotta, R. *Opt. Photonik* **2009,** *4,* 48–50. doi:10.1002/opph.201190028

51. Astumian, R. D. *Proc. Natl. Acad. Sci. U. S. A.* **2007,** *104,* 19715–19718. doi:10.1073/pnas.0708040104

52. Landauer, R. *Physica A* **1999,** *263,* 63–67. doi:10.1016/S0378-4371(98)00513-5

53. Bennet, C. H. *Int. J. Theor. Phys.* **1982,** *21,* 905–940. doi:10.1007/BF02084158

54. Fredkin, E.; Toffoli, T. *Int. J. Theor. Phys.* **1982,** *21,* 219–253. doi:10.1007/BF01857727

55. Feynman, R. *Feynman Lectures on Computation;* Addison-Wesley: Reading, MA, U.S.A., 1996.

56. Kish, L. B. *Phys. Lett. A* **2002,** *305,* 144–149. doi:10.1016/S0375-9601(02)01365-8

57. Jardetzky, O. *Nature (London)* **1966,** *211,* 969. doi:10.1038/211969a0

58. Anandan, J.; Christian, J.; Wanelik, K. *Am. J. Phys.* **1997,** *65,* 180–185. doi:10.1119/1.18570

59. Sinitsyn, N. A.; Nemenman, I. *EPL* **2007,** *77,* 58001. doi:10.1209/0295-5075/77/58001

60. Goychuk, I. *Mol. Simul.* **2006,** *32,* 717–725. doi:10.1080/08927020600857297

61. Barkai, E.; Garini, Y.; Metzler, R. *Phys. Today* **2012,** *65,* 29–37. doi:10.1063/PT.3.1677

62. Höfling, F.; Franosch, T. *Rep. Prog. Phys.* **2013,** *76,* 046602. doi:10.1088/0034-4885/76/4/046602

63. Guigas, G.; Kalla, C.; Weiss, M. *Biophys. J.* **2007,** *93,* 316–323. doi:10.1529/biophysj.106.099267

64. Saxton, M. J.; Jacobson, K. *Annu. Rev. Biophys. Biomol. Struct.* **1997,** *26,* 373–399. doi:10.1146/annurev.biophys.26.1.373

65. Seisenberger, G.; Ried, M. U.; Endress, T.; Büning, H.; Hallek, M.; Bräuchle, C. *Science* **2001,** *294,* 1929–1932. doi:10.1126/science.1064103

66. Golding, I.; Cox, E. C. *Phys. Rev. Lett.* **2006,** *96,* 098102. doi:10.1103/PhysRevLett.96.098102

67. Tolić-Nørrelykke, I. M.; Munteanu, E.-L.; Thon, G.; Oddershede, L.; Berg-Sørensen, K. *Phys. Rev. Lett.* **2004,** *93,* 078102. doi:10.1103/PhysRevLett.93.078102

68. Jeon, J.-H.; Tejedor, V.; Burov, S.; Barkai, E.; Selhuber-Unkel, C.; Berg-Sørensen, K.; Oddershede, L.; Metzler, R. *Phys. Rev. Lett.* **2011,** *106,* 048103. doi:10.1103/PhysRevLett.106.048103

69. Parry, B. R.; Surovtsev, I. V.; Cabeen, M. T.; O'Hern, C. S.; Dufresne, E. R.; Jacobs-Wagner, C. *Cell* **2014,** *156,* 183–194. doi:10.1016/j.cell.2013.11.028

70. Goychuk, I. Viscoelastic Subdiffusion: Generalized Langevin Equation Approach. In *Advances in Chemical Physics;* Rice, S. A.; Dinner, A. R., Eds.; Wiley: Hoboken, NJ, U.S.A., 2012; Vol. 150, pp 187–253. doi:10.1002/9781118197714.ch5

71. Waigh, T. A. *Rep. Prog. Phys.* **2005,** *68,* 685. doi:10.1088/0034-4885/68/3/R04

72. Goychuk, I.; Hänggi, P. *Phys. Rev. Lett.* **2007,** *99,* 200601. doi:10.1103/PhysRevLett.99.200601

73. Goychuk, I. *Phys. Rev. E* **2015,** *92,* 042711. doi:10.1103/PhysRevE.92.042711

74. Goychuk, I. *Phys. Rev. E* **2009,** *80,* 046125. doi:10.1103/PhysRevE.80.046125

75. Siegle, P.; Goychuk, I.; Talkner, P.; Hänggi, P. *Phys. Rev. E* **2010,** *81,* 011136. doi:10.1103/PhysRevE.81.011136

76. Siegle, P.; Goychuk, I.; Hänggi, P. *Phys. Rev. Lett.* **2010,** *105,* 100602. doi:10.1103/PhysRevLett.105.100602

77. Siegle, P.; Goychuk, I.; Hänggi, P. *EPL* **2011,** *93,* 20002. doi:10.1209/0295-5075/93/20002

78. Caspi, A.; Granek, R.; Elbaum, M. *Phys. Rev. E* **2002,** *66,* 011916. doi:10.1103/PhysRevE.66.011916

79. Bruno, L.; Levi, V.; Brunstein, M.; Despósito, M. A. *Phys. Rev. E* **2009,** *80,* 011912. doi:10.1103/PhysRevE.80.011912

80. Robert, D.; Nguyen, T.-H.; Gallet, F.; Wilhelm, C. *PLoS One* **2010,** *4,* e10046. doi:10.1371/journal.pone.0010046

81. Harrison, A. W.; Kenwright, D. A.; Waigh, T. A.; Woodman, P. G.; Allan, V. J. *Phys. Biol.* **2013,** *10,* 036002. doi:10.1088/1478-3975/10/3/036002

82. Bruno, L.; Salierno, M.; Wetzler, D. E.; Despósito, M. A.; Levi, V. *PLoS One* **2011,** *6,* e18332. doi:10.1371/journal.pone.0018332

83. Goychuk, I.; Kharchenko, V. O.; Metzler, R. *PLoS One* **2014,** *9,* e91700. doi:10.1371/journal.pone.0091700

84. Goychuk, I.; Kharchenko, V. O.; Metzler, R. *Phys. Chem. Chem. Phys.* **2014,** *16,* 16524–16535. doi:10.1039/C4CP01234H

85. Goychuk, I. *Phys. Biol.* **2015,** *12,* 016013. doi:10.1088/1478-3975/12/1/016013

86. Goychuk, I. *Chem. Phys.* **2010,** *375,* 450–457. doi:10.1016/j.chemphys.2010.04.009

87. Goychuk, I.; Kharchenko, V. *Phys. Rev. E* **2012,** *85,* 051131. doi:10.1103/PhysRevE.85.051131

88. Kharchenko, V. O.; Goychuk, I. *Phys. Rev. E* **2013,** *87,* 052119. doi:10.1103/PhysRevE.87.052119

89. Goychuk, I.; Kharchenko, V. O. *Math. Modell. Nat. Phenom.* **2013,** *8,* 144–158. doi:10.1051/mmnp/20138210

90. Kharchenko, V.; Goychuk, I. *New J. Phys.* **2012,** *14,* 043042. doi:10.1088/1367-2630/14/4/043042

91. Jülicher, F.; Ajdari, A.; Prost, J. *Rev. Mod. Phys.* **1997,** *69,* 1269. doi:10.1103/RevModPhys.69.1269

92. Astumian, R. D.; Bier, M. *Biophys. J.* **1996,** *70,* 637–653. doi:10.1016/S0006-3495(96)79605-4

93. Parmeggiani, A.; Jülicher, F.; Ajdari, A.; Prost, J. *Phys. Rev. E* **1999,** *60,* 2127. doi:10.1103/PhysRevE.60.2127

94. Herrchen, M.; Öttinger, H. C. *J. Non-Newtonian Fluid Mech.* **1997,** *68,* 17. doi:10.1016/S0377-0257(96)01498-X

95. Baker, N. A.; Sept, D.; Joseph, S.; Holst, M. J.; McCammon, J. A. *Proc. Natl. Acad. Sci. U. S. A.* **2001,** *98,* 10037–10041. doi:10.1073/pnas.181342398

96. Perez-Carrasco, R.; Sancho, J. M. *Biophys. J.* **2010,** *98,* 2591–2600. doi:10.1016/j.bpj.2010.02.027

97. Goychuk, I. *Phys. Rev. E* **2012,** *86,* 021113. doi:10.1103/PhysRevE.86.021113

98. Goychuk, I. *Fluct. Noise Lett.* **2012,** *11,* 1240009. doi:10.1142/S0219477512400093

99. Goychuk, I.; Kharchenko, V. O. *Phys. Rev. Lett.* **2014,** *113,* 100601. doi:10.1103/PhysRevLett.113.100601

Invariance of molecular charge transport upon changes of extended molecule size and several related issues

Ioan Bâldea[1,2]

Full Research Paper

Address:
[1]Theoretische Chemie, Universität Heidelberg, INF 229, 69120 Heidelberg, Germany and [2]Institute of Space Sciences, National Institute for Lasers, Plasma, and Radiation Physics, National Institute for Lasers, Plasma, and Radiation Physics, 077125, Bucharest-Măgurele, Romania

Email:
Ioan Bâldea - ioan.baldea@pci.uni-heidelberg.de

Abstract

As a sanity test for the theoretical method employed, studies on (steady-state) charge transport through molecular devices usually confine themselves to check whether the method in question satisfies the charge conservation. Another important test of the theory's correctness is to check that the computed current does not depend on the choice of the central region (also referred to as the "extended molecule"). This work addresses this issue and demonstrates that the relevant transport and transport-related properties are indeed invariant upon changing the size of the extended molecule, when the embedded molecule can be described within a general single-particle picture (namely, a second-quantized Hamiltonian bilinear in the creation and annihilation operators). It is also demonstrates that the invariance of nonequilibrium properties is exhibited by the exact results but not by those computed approximately within ubiquitous wide- and flat-band limits (WBL and FBL, respectively). To exemplify the limitations of the latter, the phenomenon of negative differential resistance (NDR) is considered. It is shown that the exactly computed current may exhibit a substantial NDR, while the NDR effect is absent or drastically suppressed within the WBL and FBL approximations. The analysis done in conjunction with the WBLs and FBLs reveals why general studies on nonequilibrium properties require a more elaborate theoretical than studies on linear response properties (e.g., ohmic conductance and thermopower) at zero temperature. Furthermore, examples are presented that demonstrate that treating parts of electrodes adjacent to the embedded molecule and the remaining semi-infinite electrodes at different levels of theory (which is exactly what most NEGF-DFT approaches do) is a procedure that yields spurious structures in nonlinear ranges of current–voltage curves.

Introduction

Even restricted to the steady-state regime, studying charge transport through molecular devices is a difficult nonequilibrium problem, and the variety of methods to approach this problem utilized in the literature [1-4] may be taken as a manifestation of this difficulty. As a self-consistency test for the various approaches utilized [5-7], a check of whether the charge conser-

vation condition is obeyed by the method in question is an aspect that has occasionally received consideration [2,4]. With a few exceptions [8-13], wherein the independence of the current of the position of the area traversed by current was also investigated, most studies of this kind only checked the fact that the current at the "left" and "right" ends of the molecule are equal [1,14,15]. Except (if at all) for simpler interface effects (e.g., those accounted for through ohmic contact resistances), conduction through macroscopic solids contacted to electrodes is determined by the properties of the solid itself, which are practically unaffected by the electrodes [16].

Things drastically change in molecular junctions. There, upon contacting to infinite electrodes, the properties of the embedded molecule can be substantially modified with respect to the isolated molecule. This is particularly true in (chemisorption) cases where the anchoring groups form covalent bonds to the electrodes. Within current approaches to molecular charge transport, mostly based on nonequilibrium Keldysh Green's functions (NEGF) combined with density functional theory (DFT), the molecular device is partitioned into a central region (also referred to as the "extended molecule", "transport region", "scattering region", or "cluster") linked to two semi-infinite "left" (L) and "right" (R) electrodes. This partitioning is inherently arbitrary. This arbitrariness is related to the arbitrariness in choosing the size of the extended molecule, which, in addition to the physical molecule, contains adjacent atomic layers (usually up to four) of (metallic) electrodes (for more specific details, see the subsection "Impact of screening and external biases"). An important problem related to this procedure is that metal atoms belonging to the extended molecule and metal atoms belonging to the electrodes are treated at different levels of theory. An unpleasant consequence is that this procedure may be a source of unphysical scattering for the electrons traveling from one electrode to another. The behavior, discussed later, is an illustration of such spurious effects. This may affect the theoretical current, yielding spurious structures (e.g., oscillations, shoulders or inflection points like those presented below) in computed *I–V* characteristics. A minimal mandatory requirement ("sanity test") for any theory is whether the transport properties are independent of how this partitioning is made as shown in Figure 1. We are not aware of previous attempts in the literature to demonstrate or even check this invariance. Addressing this issue is one of the main aims of the present work.

Results and Discussion
General considerations

The considerations that follow refer to many-electron systems wherein correlation effects are negligible (i.e., the single-Slater determinant description applies). In such situa-
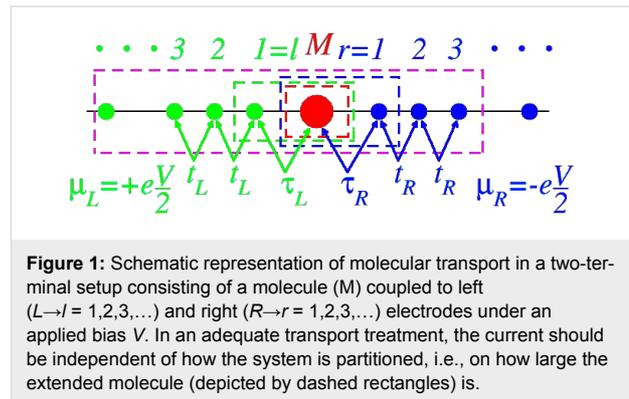
Figure 1: Schematic representation of molecular transport in a two-terminal setup consisting of a molecule (M) coupled to left ($L \rightarrow l$ = 1,2,3,…) and right ($R \rightarrow r$ = 1,2,3,…) electrodes under an applied bias *V*. In an adequate transport treatment, the current should be independent of how the system is partitioned, i.e., on how large the extended molecule (depicted by dashed rectangles) is.

tions, the retarded Green's function of the central region, $\mathbf{G}_C$, linked to biased ($V \neq 0$) electrodes is related to the retarded Green's function of the isolated system, $\mathbf{G}_{0,C} = (\varepsilon - \mathbf{H}_C)^{-1}$ (i.e., uncoupled to electrodes) via the Dyson equation [1,4,16]:

$$
\begin{aligned}
\mathbf{G}_C^{-1}(\varepsilon) &= \mathbf{G}_{0,C}^{-1}(\varepsilon) - \mathbf{\Sigma}_L^C(\varepsilon) - \mathbf{\Sigma}_R^C(\varepsilon) \\
&= \underbrace{\varepsilon \mathbf{1}_C - \mathbf{H}_C}_{\mathbf{K}_C} - \underbrace{\mathbf{\Sigma}_L^C(\varepsilon) - \mathbf{\Sigma}_R^C(\varepsilon)}_{\mathbf{\Sigma}_C} \equiv \mathbf{Q}_C.
\end{aligned} \tag{1}
$$

Here, $\mathbf{1}_C$ is the identity matrix, $\mathbf{H}_C$ is the Hamiltonian of the central region, and $\mathbf{\Sigma}_{L,R}^C$ are embedding retarded self-energies, which characterize the coupling of the molecule to the left and right electrodes, respectively. Throughout this text, boldface symbols denote matrices in the electronic space of the central region (*C*). To simplify notation in the analysis that follows, orthonormal basis sets will be assumed throughout and matrices are referred to rather than operators. For nonorthonormal basis sets, the nondiagonal overlap matrix $\mathbf{S}_C$ would replace the identity matrix $\mathbf{1}_C$ of Equation 1. Switching between orthonormal and nonorthonormal basis sets leaves the diagonal matrix elements (on-site energies) unchanged while renormalizing the nondiagonal matrix elements (hopping integrals). See Chapter 4.1.2 of [4], which provides further details. Whenever possible, for convenience, the energy (ε measured from the equilibrium Fermi energy of the electrodes, $E_F = 0$) is omitted as well as other arguments of various functions entering the formulas given below. In the absence of correlations, the retarded Green's function, $\mathbf{G}_C$, remains, like in the equilibrium case, the key quantity allowing for the expression of all the relevant nonequilibrium properties. To illustrate this, the expressions of the transmission function, $\mathcal{T}$, local spectral density of states, and charge densities are given below. The local densities of states (location indicated by μ) are given by the diagonal elements, $D_{\mu,\mu}^C$, of the matrix $\mathbf{D}_C$

$$
\mathbf{D}_C(\varepsilon) = -\frac{2}{\pi} \mathrm{Im}\,\mathbf{G}_C(\varepsilon). \tag{2}
$$

The charge densities n_μ are expressed by the diagonal elements $n_\mu \equiv \rho_{\mu,\mu}^C$ of the matrix $\boldsymbol{\rho}_C = \left(\rho_{\mu,\nu}^C\right)$ [16]:

$$\rho_{\mu,\nu}^C = \left\langle c_\mu^\dagger c_\nu \right\rangle = -i\left(\mathbf{G}_C^<\right)_{\mu,\nu}(t=0) = \frac{1}{2\pi}\int d\varepsilon \left(\mathbf{G}_C^<\right)_{\mu,\nu}(\varepsilon), \quad (3)$$

$$\mathbf{G}_C^<(\varepsilon) = if_L(\varepsilon)\mathbf{G}_C(\varepsilon)\boldsymbol{\Gamma}_L^C(\varepsilon)\mathbf{G}_C^\dagger(\varepsilon) \\ + if_R(\varepsilon)\mathbf{G}_C(\varepsilon)\boldsymbol{\Gamma}_R^C(\varepsilon)\mathbf{G}_C^\dagger(\varepsilon), \quad (4)$$

where c_μ and $c_\nu^\dagger$ are electron annihilation and creation operators (entering the expression of the second quantized Hamiltonians, see below), and $\mathbf{G}^<$ is the so-called lesser Green's function [16]. The transmission function is given by the trace formula [2,8,17]

$$\mathcal{T}(\varepsilon) = \mathrm{Tr}\left[\boldsymbol{\Gamma}_L^C(\varepsilon)\mathbf{G}^C(\varepsilon)\boldsymbol{\Gamma}_R^C(\varepsilon)\mathbf{G}^{C\dagger}(\varepsilon)\right], \quad (5)$$

where the width functions

$$\boldsymbol{\Gamma}_x^C = -2\mathrm{Im}\boldsymbol{\Sigma}_x^C \quad (6)$$

are determined by the imaginary parts of the retarded embedding self-energies $\boldsymbol{\Sigma}_x^C$, characterizing the molecule–electrode couplings ($x = L,R$). Within the Landauer approach, which provides a general framework to describe the molecular transport within the elastic, uncorrelated transport approximation, the (steady-state) current I through a molecular junction is obtained by integrating the transmission function $\mathcal{T}(\varepsilon)$ [2,8]

$$I = \frac{2e}{h}\int d\varepsilon \left[f_L(\varepsilon) - f_R(\varepsilon)\right]\mathcal{T}(\varepsilon). \quad (7)$$

The difference between the Fermi distributions $f_{L,R}(\varepsilon) \equiv f(\varepsilon - \mu_{L,R})$ of the biased ($V \neq 0$) electrodes characterized by unbalanced Fermi energies $\mu_{L,R} = \pm eV/2$ has an important role (albeit not the only one, see Figure 3 below) in determining the energy window of allowed (elastic) electron transfer processes contributing to the current. For simplicity, it is assumed that $V > 0$. Taking the limit $V \to 0$ in Equation 7, one gets the well-known formula for conductance, $\mathcal{G}$, i.e., "conductance is transmission":

$$\mathcal{G}/\mathcal{G}_0 = \mathcal{T}(\varepsilon)\Big|_{\varepsilon=0}, \quad (8)$$

where $\mathcal{G}_0 = 2e^2/h$ is the conductance quantum. The second-quantized Hamiltonian of the molecular junction considered below, which is schematically depicted in Figure 1, reads

$$\mathcal{H} = -\sum_{1\leq l<\infty}\left(t_L a_l^\dagger a_{l+1} + \mathrm{h.c.}\right) + \mu_L \sum_{1\leq l<\infty} a_l^\dagger a_l \\ - \sum_{1\leq r<\infty}\left(t_R b_r^\dagger b_{r+1} + \mathrm{h.c.}\right) + \mu_R \sum_{1\leq r<\infty} b_r^\dagger b_r \\ + \mathbf{H} - \underbrace{\left(\tau_L a_1^\dagger c_1 + \mathrm{h.c.}\right)}_{\mathbf{h}_{LM}} - \underbrace{\left(\tau_R c_N^\dagger b_1 + \mathrm{h.c.}\right)}_{\mathbf{h}_{MR}} \quad (9)$$

$$\mathbf{H} = \sum_{\mu,\mu'=1}^N H_{\mu\mu'} c_\mu^\dagger c_{\mu'}. \quad (10)$$

In the equations above, a_l ($a_l^\dagger$), b_r ($b_r^\dagger$), and c_μ ($c_\mu^\dagger$) stand for annihilation (creation) operators for electrons in the left and right electrodes and in the "small" molecule, respectively. Restricting to spin-independent interactions for convenience, the spin label can be omitted and its contribution included by a factor of 2, like in Equation 7. For simplicity, the left and right electrodes will be modeled as semi-infinite chains described as a collection of sites (l and r, respectively), each site being characterized by a single level of site-independent energy $\mu_{L,R} = \pm eV/2$ (remember that the equilibrium Fermi energy is chosen as origin $E_F = 0$) and nearest-neighbor hopping integral t_x ($x = L,R$). The coupling between molecule and the left and right electrodes will be described in terms of the transfer integrals, τ_L and τ_R, which quantify the hopping between the left and right molecular ends ("anchoring groups", denoted by labels 1 and N, respectively) and the adjacent electrode ends (labels $l = 1$ and $r = 1$ for left and right electrodes in Equation 9). In Equation 9, the small molecule, which needs not to be one dimensional, is described by a Hermitean Hamiltonian matrix, $\mathbf{H} \equiv \left(H_{\mu,\mu'}\right)_{1\leq\mu,\mu'\leq N} = \mathbf{H}^\dagger$, whose elements (possibly complex numbers) are arbitrary.

Real systems described within the framework provided by Equation 9 and Equation 10 include atomic chains, quantum wires, carbon nanotubes, and (possibly DNA-based) bio- and larger organic molecules. For concrete cases, the model parameters ($H_{\mu,\mu'}$, $\tau_{L,R}$, $t_{L,R}$) can be obtained within density-functional-based, tight binding (DFTB) frameworks [18-20], which represent the state-of-the-art for such larger systems.

In a biased junction, they may also nontrivially depend on V and, if applicable, on gate potentials. In the description underlying Equation 9, the central region corresponds to the "small" molecule whose Hamiltonian is $\mathbf{H}$. Equation 9 can be repartitioned by considering an extended molecule (Hamiltonian $\mathbf{H}_{ext}$) that includes parts of adjacent electrodes (l_0 "layers" from the left electrode and r_0 "layers" from the right electrode)

$$\mathcal{H} = -\sum_{l_0+1\leq l<\infty}\left(t_L a_l^\dagger a_{l+1}+\text{h.c.}\right)+\mu_L\sum_{l_0+1\leq l<\infty}a_l^\dagger a_l$$

$$-\sum_{r_0+1\leq r<\infty}\left(t_R b_r^\dagger b_{r+1}+\text{h.c.}\right)+\mu_R\sum_{r_0+1\leq r<\infty}b_r^\dagger b_r \qquad (11)$$

$$+\mathbf{H}_{\text{ext}}\left(l_0,r_0\right)\underbrace{-\left(t_L a_{l_0+1}^\dagger a_{l_0}+\text{h.c.}\right)}_{\mathbf{H}_{LM}}\underbrace{-\left(t_R b_{r_0+1}^\dagger b_{r_0}+\text{h.c.}\right)}_{\mathbf{H}_{MR}}$$

$$\mathbf{H}_{\text{ext}}\left(l_0,r_0\right)=-\sum_{l=1}^{l_0}\left(t_L a_l^\dagger a_{l+1}+\text{h.c.}\right)+\mu_L\sum_{l=1}^{l_0}a_l^\dagger a_l$$

$$+\mathbf{H}+\mathbf{h}_{LM}+\mathbf{h}_{MR} \qquad (12)$$

$$-\sum_{r=1}^{r_0}\left(t_R b_r^\dagger b_{r+1}+\text{h.c.}\right)+\mu_R\sum_{r=1}^{r_0}b_r^\dagger b_r\,.$$

Whether using the small-molecule or the extended-molecule representation (i.e., Hamiltonians $\mathbf{H}$ or $\mathbf{H}_{\text{ext}}(l_0, r_0)$, respectively), the electrodes are semi-infinite, homogeneous chains characterized by site-independent nearest-neighbor hopping integrals, t_x, and on-site energies, μ_x, (Equation 9 and Equation 11). In both aforementioned descriptions of the central region, the contact to each electrode consists of a single point, and the matrices $\boldsymbol{\Sigma}_{L,R}^C$ and $\boldsymbol{\Gamma}_{L,R}$ have a single, nonvanishing element. By choosing the small molecule as the central region, the embedding self-energy has the form

$$\left[\boldsymbol{\Sigma}_C\left(\varepsilon\right)\right]_{\mu,\nu}=\Sigma_L\left(\varepsilon\right)\delta_{\mu,1}\delta_{\nu,1}+\Sigma_R\left(\varepsilon\right)\delta_{\mu,N}\delta_{\nu,N}. \qquad (13)$$

In the energy range of interest, the "surface" Green's function, $g_x(\varepsilon)$, has the form [2,8,21]:

$$g_x\left(\varepsilon\right)=g\left(z_x\right)=\frac{1}{2\left|t_x\right|^2}\left(z_x-i\sqrt{4\left|t_x\right|^2-z_x^2}\right),$$

$$z_x\equiv\varepsilon-\mu_x;\left|z_x\right|<2\left|t_x\right|. \qquad (14)$$

The embedding self-energy, $\tilde{\Sigma}_x(\varepsilon)$, (a tilde is used for a generic, unspecified central region) can be obtained as

$$\tilde{\Sigma}_x\left(\varepsilon\right)=\left|\tilde{\tau}_x\right|^2 g_x\left(\varepsilon\right), \qquad (15)$$

which via Equation 6 yields

$$\tilde{\Gamma}_x\left(\varepsilon\right)=-2\text{Im}\tilde{\Sigma}_x\left(\varepsilon\right)=\theta\left(2\left|t_x\right|-\varepsilon\right)\frac{\left|\tilde{\tau}_x\right|^2}{\left|t_x\right|^2}\sqrt{4\left|t_x\right|^2-z_x^2}, \qquad (16)$$

where θ is the Heaviside step function. Notice that the relevant energy range is $|z_x| = |\varepsilon - \mu_x| < 2|t_x|$ since otherwise $\Gamma_x \equiv 0$ and the contributions to Equation 2, Equation 4, and Equation 5 vanish. The quantity $\tilde{\tau}_x$ entering Equation 15 and Equation 16 is the hopping integral at the "interface" (in fact, the contact point) between the central region and electrode x. In the small molecule representation, $\tilde{\tau}_{L,R} \equiv \tau_{L,R}$. In the extended molecule representation, $\tilde{\tau}_x \equiv t_x$ at the contact x where a certain number of electrode "layers" are included in the central region. The central region corresponding to the Hamiltonian operators expressed by Equation 9 and Equation 11 is different, namely, the "small" molecule (with Hamiltonian $\mathbf{H}$) and the extended ("larger") molecule (with Hamiltonian $\mathbf{H}_{\text{ext}}$), respectively. However, these two total Hamiltonians describe the same total physical systems and are mathematically identical. Therefore, whether computed within the description based on the small molecule or on an extended molecule, all the physical properties (e.g., transmission, current, local density of states, charge densities) should be identical. The proof that these properties indeed coincide, which represents an important sanity test for theory, will be given below.

For demonstration, a "minimally" extended molecule is considered, obtained by adding one extra electrode "layer" to the small molecule, namely the leftmost electrode site ($r = 1$) of the right electrode. This extended molecule having the Hamiltonian

$$\overline{\mathbf{H}}\equiv\mathbf{H}_{\text{ext}}\left(l_0=0,\ r_0=1\right) \qquad (17)$$

is schematically represented by the blue dashed rectangle in Figure 1. The demonstration goes as follows. We first show that the properties computed within the small molecule representation coincide with those based on the minimally extended molecule described above. Then, the demonstration for larger extended molecules follows immediately by induction. In the next step, the minimally extended molecule is taken as a new "small" molecule and choose the new extended molecule augmented with the next site of the right electrode. That is, $\mathbf{H}_{\text{ext}}(l_0=0, r_0=1)\rightarrow\mathbf{H}$ and $\mathbf{H}_{\text{ext}}(l_0=0, r_0=2)\rightarrow\overline{\mathbf{H}}$. Notice that this is possible because, like $\mathbf{H}$ of Equation 10, the Hamiltonian $\mathbf{H}_{\text{ext}}(l_0=0, r_0=1)$ is bilinear in the operators $c_1,...,c_N,b_{r_0}$ and $c_1^\dagger,...,c_N^\dagger,b_{r_0}^\dagger$ pertaining to the corresponding "small" molecule. Obviously, this procedure can be reiterated by indefinitely pushing the right end of the extended molecule toward the right. Likewise, by interchanging the "left" and "right" labels one can gradually include (in addition to sites from the left electrode also) sites belonging to the right electrode ($l_0 = 1, 2,...$ in Equation 12).

Demonstration that the representations based on the small molecule and minimally extended molecule yield identical physical properties

In the following, the quantities needed to compute the relevant properties are discussed for the cases where the small molecule and the minimally extended molecule are chosen as the central regions. All mathematical details and expressions needed for this explanation are given in Supporting Information File 1. Some key results are summarized in Table 1.

As developed in Supporting Information File 1 from Equations S4, S8, S12 and S14 (for $\eta = 1$)

$$\frac{\overline{G}_{1,N+1}}{G_{1,N}} = -\frac{\tau_R^*}{|t_R|}\frac{1}{w} \Rightarrow \frac{\overline{\Gamma}_R}{\Gamma_R}\frac{\left|\overline{G}_{1,N+1}\right|^2}{\left|G_{1,N}\right|^2} = \frac{1}{|w|^2} = 1 \quad (18)$$

and therefore the ratio of the two transmission functions equals unity:

$$\frac{\overline{\mathcal{T}}}{\mathcal{T}} = \frac{\Gamma_L\left|\overline{G}_{1,N+1}\right|^2\overline{\Gamma}_R}{\Gamma_L\left|G_{1,N}\right|^2\Gamma_R} = 1. \quad (19)$$

This fact is a direct consequence of Equation S11 in Supporting Information File 1. The equality of the local density of states computed in the small molecule and minimally extended molecule representation,

$$\frac{\overline{G}_{\eta,\eta}}{G_{\eta,\eta}} = 1 \Rightarrow \overline{D}_{\eta,\eta} = D_{\eta,\eta}, \quad (20)$$

is the consequence of Equation S13a (for $\xi = 1$), Equation S13b (for $\mu = \nu$), Equation S4, Equation S8, and Equation S12

$(1 \leq \eta \leq N)$ as defined in Supporting Information File 1. Equation S13a (for $\eta = 1$), S14, S4, S8, and S12 yield

$$\frac{\overline{G}_{\mu,1}}{G_{\mu,1}} = 1;$$

$$\frac{\overline{G}_{\mu,N+1}}{G_{\mu,N}} = -\frac{\tau_R^*}{|t_R|}\frac{1}{w} \Rightarrow \frac{\overline{\Gamma}_R}{\Gamma_R}\frac{\left|\overline{G}_{\mu,N+1}\right|^2}{\left|G_{\mu,N}\right|^2} = \frac{1}{|w|^2} = 1. \quad (21)$$

For the presently considered case, Equation 4 reads

$$G_{\mu,\nu}^< = i f_L G_{\mu,1}\Gamma_L G_{\nu,1}^* + i f_R G_{\mu,N}\Gamma_R G_{\nu,N}^*, \quad (22)$$

$$\overline{G}_{\mu,\nu}^< = i f_L \overline{G}_{\mu,1}\Gamma_L \overline{G}_{\nu,1}^* + i f_R \overline{G}_{\mu,N+1}\overline{\Gamma}_R \overline{G}_{\nu,N+1}^*, \quad (23)$$

and then Equation 3 yields

$$\overline{n}_\mu = n_\mu. \quad (24)$$

To sum up, Equation 19, Equation 20, and Equation 24 demonstrate that relevant nonequilibrium properties obtained within the small molecule and the minimally extended molecule representations coincide.

Approximations of wide- and flat-electrode bands and related issues

At first sight, the concept of the invariance of the transport properties upon the choice of the extended molecule size may seem of merely academic interest (possibly a part of a Ph.D. tutorial) or useful for checking the correctness of numerical code to compute transport properties (which should not change whatever the size of the central region chosen). To see that the results presented above are also relevant for more pragmatic purposes, the effect of negative differential resistance (NDR) is discussed next in conjunction with common approximations used in transport approaches. In the preceding subsection, it is

Table 1: Hopping integrals at the left and right contacts ($\tilde{\tau}_{L,R}$), transmission function $\mathcal{T}$, diagonal elements of the lesser Green's function $G_{\mu,\mu}^<$, and the local density of states $D_{\mu,\mu}$ for the cases where either the small molecule or the minimally extended molecule (as defined in the main text) are chosen to be the central region. The quantities in the same typeface (magenta, blue, and red) color are equal (cf. Equation 19, Equation 24, and Equation 20).

central region	$\tilde{\tau}_L$	$\tilde{\tau}_R$	$\mathcal{T}$	$-iG_{\mu,\mu}^<$ $(1\leq\mu\leq N)$	$-\dfrac{\pi}{2}D_{\mu,\mu}$ $(1\leq\mu\leq N)$
small molec.	τ_L	τ_R	$\Gamma_L\Gamma_R\left|G_{1,N}\right|^2$	$f_L\Gamma_L\left|G_{\mu,1}\right|^2 + f_R\Gamma_R\left|G_{\mu,N}\right|^2$	$\mathrm{Im}\,G_{\mu,\mu}$
min. ext. molec.	τ_L	t_R	$\Gamma_L\overline{\Gamma}_R\left|\overline{G}_{1,N+1}\right|^2$	$f_L\Gamma_L\left|\overline{G}_{\mu,1}\right|^2 + f_R\overline{\Gamma}_R\left|\overline{G}_{\mu,N+1}\right|^2$	$\mathrm{Im}\,\overline{G}_{\mu,\mu}$

shown that the invariance of the transport is the direct consequence of Equations S10 and S11 from Supporting Information File 1, which follow from the exact expressions in Equation 15 and Equation 14. Whether they are also satisfied when approximate expressions are used instead of the exact ones will be discussed below. Here, the commonly employed limits of wide- and flat-electrode bands (labeled WBL and FBL, respectively) will be considered. Assuming embedding self-energies of the form ($x = L,R$),

$$\Sigma_x^{WBL}(\varepsilon) \rightarrow \Sigma_x^0 \equiv -\frac{i}{2}\Gamma_x(\varepsilon)\Big|_{\varepsilon=0}$$
$$= -\frac{i}{2}\Gamma_x^0, \Gamma_x^0 = 2\frac{|\tau_x|^2}{|t_x|} \qquad (25)$$

for all ε (wide-band limit, WBL), all energies in the Fermi window,

$$-eV/2 = \mu_R < \varepsilon < \mu_L = +eV/2 \qquad (26)$$

contribute to the integration entering Equation 7. This is an ubiquitous approximation not only in transport studies based on model Hamiltonians [1,4]; it is also an attractive approximation for realistic calculations (particularly for more reliably but computationally much more expensive approaches beyond NEGF-DFT treatments), as computation times can be radically reduced; see section "WBL-based schemes and realistic calculations" for more details. The restriction expressed by Equation 26 is imposed by the difference of the Fermi distributions, which are step functions at zero temperature, the case which is referred to below. The method based on Equation 25 and Equation 26, to which, as usual, is referred to as the wide-band limit (WBL), comprises in fact two approximations. It assumes (i) featureless (flat) electrode bands, characterized by energy-independent densities of states, and therefore $\Sigma_x(\varepsilon)$ is taken at the zero-bias Fermi energy $\varepsilon = \mu_x = E_F = 0$ and (ii) electrode bandwidths of $\approx 4|t_{L,R}|$ much larger than any other characteristic energies (e.g., orbital energy offsets relative to the Fermi level and widths functions $\Gamma_{L,R}$). This is the rationale to extend the integration over energy in Equation 7 up to infinity. Another possible approximation, which will be referred to as the flat-band limit (FBL) below, is to consider the energy-independent embedding self-energy, Σ_x, given by Equation 25 but only in the finite energy range $|z_x| = |\varepsilon - \mu_x| < 2|t_x|$. The flat-band limit (FBL) is defined by Equation 27.

By taking $\varepsilon = 0$ and $V = 0$, Equations S10 and Equation S11 from Supporting Information File 1 are satisfied when the approximate expressions of Equation 25 and Equation 27 are employed. In this case, the approximate self-energies from Equation 25 and Equation 27 coincide with the exact one (Equation 15). Via Equation 8 and Equation 2 (see also Table 1), this implies that conductance and local density of states at equilibrium ($V = 0$) and zero temperature computed within the wide- or flat-band approximations are exact. Therefore, these quantities (as well as other properties corresponding to $\varepsilon = V = 0$) do not depend on the size of the central region. However, a straightforward inspection reveals that, in general (i.e., at arbitrary values of ε and V), Equations S10 and S11 from Supporting Information File 1 are no longer satisfied when the approximate expressions of Equation 25 and Equation 27 are employed. So, in general, the wide- and flat-band approximations do yield properties that depend on the size of the central region.

The following presents a further elaboration on this aspect, which is unphysical. In the illustrative examples presented below, the (small) molecule will be described as a single site (or level) of energy ε_M whose Hamiltonian is given by

$$\mathbf{H} = \varepsilon_M c^\dagger c, \qquad (28)$$

where $N \equiv 1$, $c \equiv c_1 \equiv c_N$, $c^\dagger \equiv c_1^\dagger \equiv c_N^\dagger$ in Equation 10. Notice that Equation 28 does not necessarily refer to a system consisting of a single site. It can describe a molecule wherein, as is often the case [22-24], the transport is dominated by a single molecular orbital.

Impact on the *I–V* curves

Figure 2 depicts various *I–V* curves computed for this case and various sizes of the extended molecule $N_{ext} \geq N = 1$. While agreeing with the exact *I–V* curves at lower biases ($eV < 2\varepsilon_M$), the approximate *I–V* curves significantly differ from the exact ones at higher biases. The wide-band approximation fails to describe the NDR regime exhibited by the exact *I–V* curves (Figure 2a). This is due to the fact that the width of the allowed energy window within the WBL (which is the Fermi energy window of Equation 26) contributing to the current (Equation 7) continuously increases with increasing $V > 0$. In fact, as depicted in Figure 3, this is true only for biases $eV < 2t$, as shown in Figure 3a. (To simplify the analysis, $|t_L| = |t_R| = t$ is assumed.)

$$\Sigma_x^{FBL}(\varepsilon) = \begin{cases} \Sigma_x^0 \equiv -\frac{i}{2}\Gamma_x(\varepsilon)\Big|_{\varepsilon=0} = -\frac{i}{2}\Gamma_x^0, \text{ for } |\varepsilon - \mu_x| \leq 2|t_x|; \\ 0, \text{ for } |\varepsilon - \mu_x| > 2|t_x|. \end{cases} \qquad (27)$$
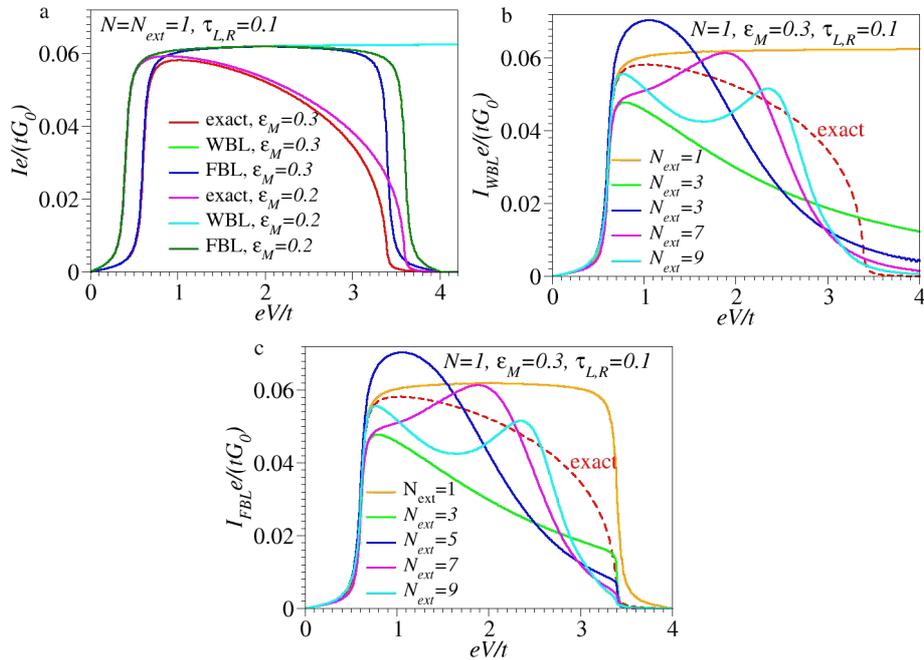
Figure 2: Dimensionless *I–V* curves computed for a small molecule consisting of a single site/level (*N* = 1) of energy ε$_M$. (a) Exact results along with those obtained within the WBL and FBL, considering an extended molecule identical to the small molecule (*N* = *N*$_{ext}$ = 1). (b,c) Exact results along with those obtained within the WBL (panel b) and FBL (panel c) using an extended molecule containing a number of sites *N*$_{ext}$ = 1, 3, 5, 7, and 9. This mimics realistic calculations wherein up to four adjacent layers from electrodes are added to the small molecule. The energy unit is *t* = *t*$_{L,R}$ = 1, and the other model parameters are given in the inset.
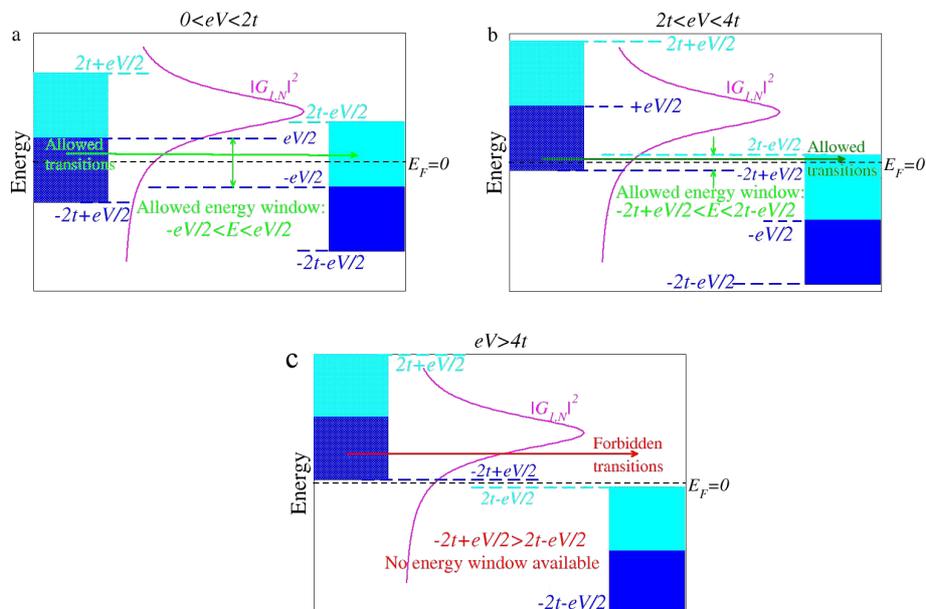
Figure 3: Schematic representation of the energy window available for elastic electron transitions at zero temperature (*t* = |*t*$_L$| = |*t*$_R$|, *V* > 0). (a) At biases 0 < *eV* < 2*t*, the (Fermi) energy window for allowed electron transitions becomes broader as the bias increases. (b) At biases 2*t* < *eV* < 4*t*, the energy window of allowed electron transitions (−2*t* + *eV*/2 < ε < 2*t* − *eV*/2) is narrower than the Fermi energy window (−*eV*/2 < ε < *eV*/2); it becomes narrower as the bias increases. This is reflected in a current decrease, i.e., a negative resistance behavior. (c) The current vanishes for *eV* > 4*t*, a bias range wherein there are no allowed electron transitions.

For biases $2t < eV < 4t$, the width of the energy window of the allowed (elastic) transitions,
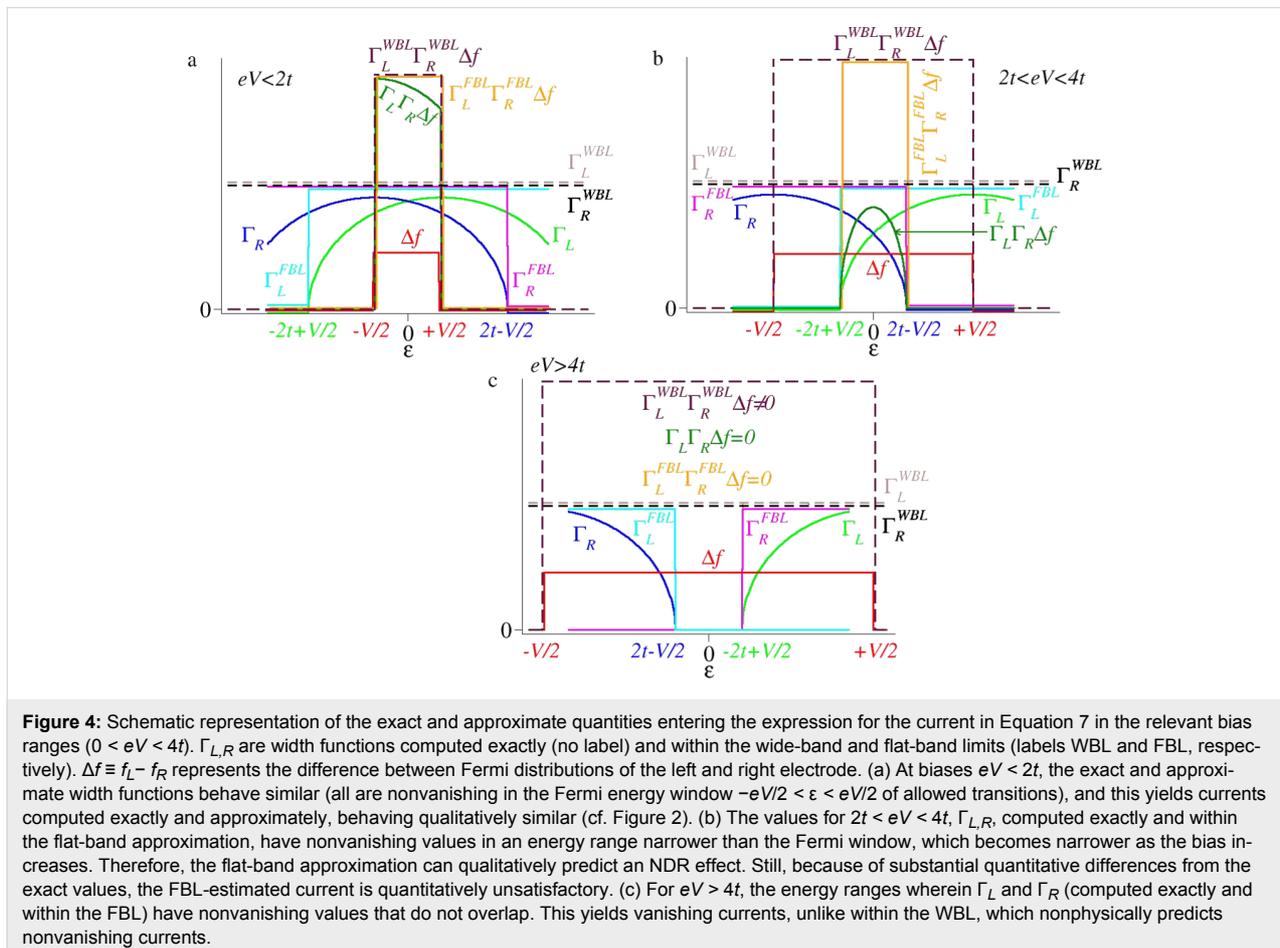
$$-2t + eV/2 < \varepsilon < 2t - eV/2, \qquad (29)$$

is narrower than that of the Fermi energy window (eV) determined by the difference of the Fermi distributions entering Equation 7. This is the straightforward consequence of the finite electrode bandwidths, as shown in Figure 3b. The fact that this energy width $\Delta\varepsilon = 2t - V/2 - (-2t + V/2) = 4t - V$ decreases with increasing V is reflected in a negative differential resistance (NDR) effect, which characterizes this regime. The physics underlying Equation 29 is correctly accounted for within the flat-band approximation (see the last line of Equation 27). This is why the description of the NDR effect is qualitatively correct within this approximation (cf. Figure 3b). Quantitatively, as visible in Figure 2, the FBL description of NDR is rather poor. This occurs because the energy window of the allowed transition (when correctly accounted for) is
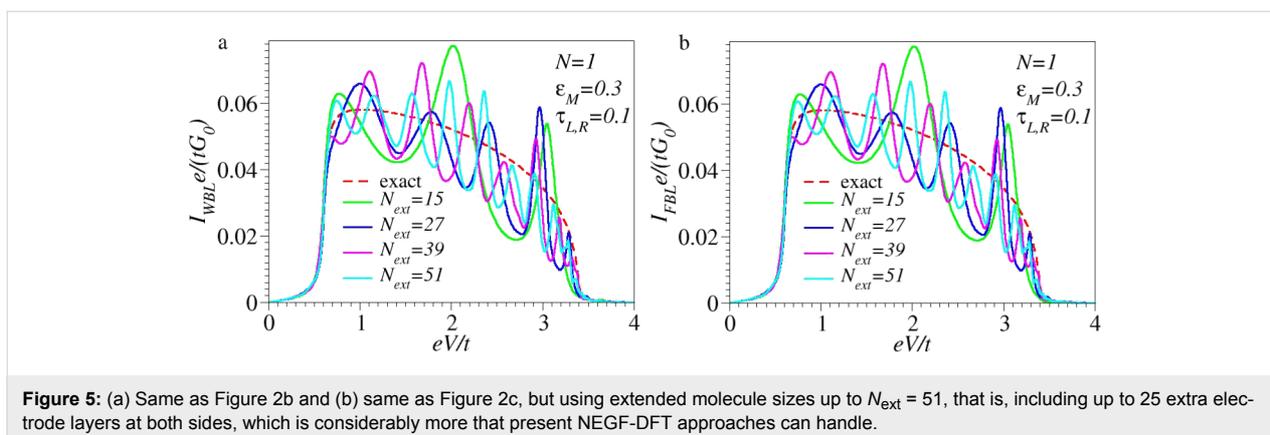
$$\max\left(-eV/2, -2t + eV/2\right) < \varepsilon < \min\left(+eV/2, 2t - eV/2\right) \quad (30)$$

and not the Fermi energy window of Equation 26, and thus the energy dependence of the width functions $\Gamma_{L,R}$ is neglected within the FBL. As schematically shown in Figure 4, the ε-dependence of the width functions, which is weak at lower biases (cf. Figure 4a), becomes strong in the range defined by Equation 29, as shown in Figure 4b.

The fact that the NDR effect is overall underestimated within the FBL is due to the fact that the energy-dependence of $\Gamma_{L,R}$ is substantial (Equation 16). This yields a significant NDR even at biases $eV < 2t$, as revealed by the inspection of the exact *I–V* curves in the ranges $2|\varepsilon_M| < eV < 2t$ (cf. Figure 2 and Figure 5). As illustrated by Figure 2a, there is no NDR within FBL for biases $eV < 2t$; in this bias range, the FBL and WBL results coincide (cf. Figure 3a, Equation 27 and Equation 25).

To complete this analysis, it is noted that the current vanishes for $eV > 4t$ because there are no states available for elastic charge transfer processes (cf. Figure 3c and Figure 4c). While qualitatively this feature is correctly retained within the flat-band approximation, it is ignored within the wide-band approximation, which nonphysically predicts nonvanishing currents at

Figure 4: Schematic representation of the exact and approximate quantities entering the expression for the current in Equation 7 in the relevant bias ranges ($0 < eV < 4t$). $\Gamma_{L,R}$ are width functions computed exactly (no label) and within the wide-band and flat-band limits (labels WBL and FBL, respectively). $\Delta f \equiv f_L - f_R$ represents the difference between Fermi distributions of the left and right electrode. (a) At biases $eV < 2t$, the exact and approximate width functions behave similar (all are nonvanishing in the Fermi energy window $-eV/2 < \varepsilon < eV/2$ of allowed transitions), and this yields currents computed exactly and approximately, behaving qualitatively similar (cf. Figure 2). (b) The values for $2t < eV < 4t$, $\Gamma_{L,R}$, computed exactly and within the flat-band approximation, have nonvanishing values in an energy range narrower than the Fermi window, which becomes narrower as the bias increases. Therefore, the flat-band approximation can qualitatively predict an NDR effect. Still, because of substantial quantitative differences from the exact values, the FBL-estimated current is quantitatively unsatisfactory. (c) For $eV > 4t$, the energy ranges wherein Γ_L and Γ_R (computed exactly and within the FBL) have nonvanishing values that do not overlap. This yields vanishing currents, unlike within the WBL, which nonphysically predicts nonvanishing currents.

Figure 5: (a) Same as Figure 2b and (b) same as Figure 2c, but using extended molecule sizes up to $N_{ext} = 51$, that is, including up to 25 extra electrode layers at both sides, which is considerably more that present NEGF-DFT approaches can handle.

these biases. Although the NDR effect per se is not the main focus of this paper, it is still noted that the NDR effect discussed above for a single site/level model is the consequence of the combined effect of the finite bandwidth and the energy dependence of the width functions (or, alternatively, the density of states at the contacts [21]). Electron correlations, which escape the conventional Landauer framework utilized here, can further enhance the NDR [25-27]. Besides finite bandwidth and energy-dependent densities of states, for systems with more than one site, the potential drop across the molecular bridge can be an additional source of NDR [28,29]. In accord with the general arguments presented above, Figure 2b,c illustrates that currents computed within the WBL and FBL, respectively, do depend (and significantly so) on the choice of the central region. The sizes utilized in these figures (up to $N_{ext} = 9$) mimic current NEGF-DFT transport calculations based on extended molecules including up to four adjacent layers from each electrode. Because the extended molecule considered in the present study is treated exactly, one may expect that by sufficiently increasing the size of the extended molecule, currents computed within the WBL and FBL would approach the values computed exactly. From this perspective, the results presented in Figure 5 are interesting. They show that even for extended molecules that are much larger than NEGF-DFT calculations can handle (given presently available computing resources), quantitative and qualitative deviations from the exact results for current beyond the ohmic regime are substantial.

The handful of examples presented above neither aimed at an exhaustive comparison of the exact results with those deduced within the wide- and flat-band approximations nor at a detailed discussion of NDR effects. They mainly aimed at demonstrating that in addition to the unphysical fact of breaking the invariance of the properties upon varying the size of the extended molecule, these approximations overlook significant physical effects. Even worse, as will be discuss next and anticipated in the Introduction, the WBL and FBL can predict spurious

structures in the *I–V* curves at higher voltages. The examples depicted in Figure 5 fully support this idea: As visible there, the features exhibited by the WBL and FBL curves at high biases (oscillations, shoulders, inflection points), which have no counterpart on the exact curves, simply represent artifacts of inadequate approaches.

Impact on the charge distribution

The unphysical dependence on the size of the extended molecule predicted by the aforementioned approximations does not only affect *I–V* curves and other nonequilibrium properties (which imply $V \neq 0$), but also charge densities (or occupancies of molecular orbitals) at equilibrium ($V = 0$), to which energies other than the Fermi energy ($\varepsilon = 0$) contribute (cf. Equation 3) are affected. As a first example in this context one can mention the Friedel sum rule. The Friedel sum rule establishes an "exact" (see below why this word is put in quotation marks) relationship between two conceptually different quantities – ohmic conductance and level occupancy – for a nontrivial, single-level Hubbard–Anderson model. This model cannot be solved exactly in the general case because of the on-site Hubbard–Anderson interaction ($U \neq 0$) between electrons of opposite spins occupying the same site/level, which is a source of (strong) electron correlations [30-33]. The approximation made to deduce this "exact" result (which also applies in the case $U = 0$, when the Hubbard–Anderson model reduces to the uncorrelated model described by Equation 28) is nothing but the wide-band approximation considered above. To see to what extent the "exact" Friedel sum rule is affected by the WBL one can compare the exact level occupancy with the occupancy obtained within the WBL. For the parameter values of Figure 2, the level occupancy estimated within the WBL deviates by 19% from the exact occupancy value. Although not dramatic, the error introduced by the WBL is still significant. As a second example, Figure 6 shows the occupancies n_l^{WBL} of several electrode sites at distance l from the embedded (small) molecule modeled as a single level/site computed within WBL using ex-
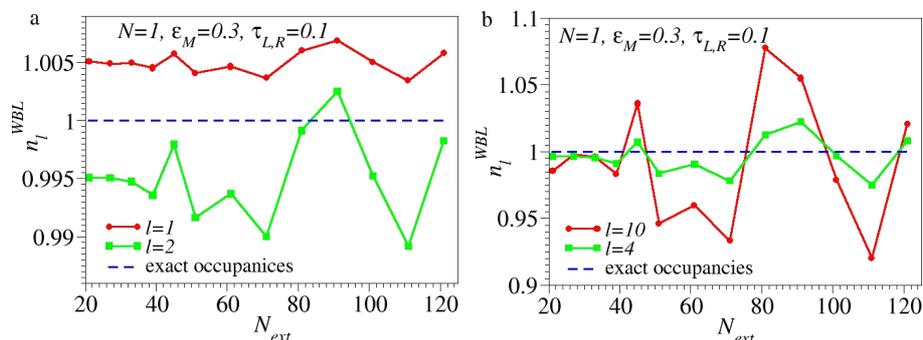
Figure 6: Even when increasing the size, N_{ext}, of the extended molecule well beyond that which current computational facilities that employ NEGF-DFT implementations can handle ($N_{\text{ext}} = 121$ amounts to 60 electrode "layers" on either side), the occupancies n_l^{WBL} computed within the WBL do not approach the exactly computed values (the exact values represented by the blue horizontal lines differ from 1 by approx. 10^{-5}). (a) Results for the first ($l = 1$) and second ($l = 2$) neighboring sites, and (b) fourth ($l = 4$) and tenth ($l = 10$) neighboring sites within electrodes relative to the "small" molecule, modeled as a single site and parameter values as given in Figure 2.

tended molecules up to very large sizes ($N_{\text{ext}} \leq 121$, i.e., up to 60 "layers" in each electrode). While the small deviations from the exact values of occupancies of the electrode sites close to the (small) molecule ($l = 1,2$, Figure 6a) computed within WBL are acceptable, those for more distant sites (e.g., $l = 4$ and $l = 10$, Figure 6b) are unacceptably large. They amount to effective doping levels varying within up to approx. 10%, that is, they are comparable to the largest doping levels achieved experimentally in electronic devices of nanoscopic sizes [34,35]. These deviations of n_l^{WBL} from the exact values, n_l^{exact}, act as spurious charged scattering centers and are responsible for the artifacts in the *I–V* curves calculated within the WBL.

Additional remarks
Impact of screening and external biases
As noted in the Introduction, the three-piece partitioning in an extended molecule linked to the left and right side of semi-infinite electrodes is a mental construct that is inherently arbitrary and should by no means affect the current and other physical properties. This is a minimal mandatory requirement for any valid theoretical approach. However, although conceptually arbitrary, for practical purposes, it is convenient that the partitioning fulfills certain conditions [36]. Unnecessary, more demanding computational effort can be avoided if the junction is partitioned such that: (i) the properties of the electrodes are homogeneous and do not differ from those of the bulk materials (metals), (ii) there is no direct interaction between the left and right electrodes, and (iii) interactions between the extended molecule and the two electrodes are merely confined to the extended molecule–electrode interfaces. "Screening" is the term under which conditions (i)–(iii) are usually listed in the context of realistic (DFT) calculations. The "extended" molecule should be taken large enough so that effects of the cluster to the (Kohn–Sham) potential outside the scattering region is

screened. Outside the sufficiently large, extended molecule, screening effects should be altogether negligible, the potential should smoothly evolve into that of perfectly homogeneous bulk electrodes, and the charge distribution should match across the boundary of the scattering region and leads [37]. The inclusion of a sufficient number of additional electrode layers to satisfy these screening-related conditions may be an issue even for metallic electrodes and is a serious challenge for nonmetallic electrodes. One should note that the results presented in Figure 6, illustrating that even at sizes computationally prohibitive for microscopic studies, the charge density at the ends of the extended molecule computed within the WBL does not properly evolve into that of the bulk electrodes. The rather general model Hamiltonian of Equation 9 does satisfy these conditions. Condition (i) is satisfied because the electrodes' parameters (on-site energies $\mu_{L,R}$ and hopping integrals $t_{L,R}$) are independent of the position (l,r). Condition (ii) is satisfied because $\mathcal{H}$ does not contain products (e.g., $a_l^\dagger b_r$) mixing operators from different electrodes. Condition (iii) is also satisfied because $\mathcal{H}$ merely contains products involving nearest neighboring sites at the contacts, such as $a_1^\dagger c_1$ and $b_1^\dagger c_N$ by choosing the small molecule described by the Hamiltonian **H** as central region, or $a_{l_0+1}^\dagger a_{l_0}$ and $b_{r_0+1}^\dagger b_{r_0}$ by choosing an extended molecule described by the Hamiltonian $\mathbf{H_{ext}}(l_0, r_0)$ of Equation 12, which includes l_0 "layers" of the left electrode and r_0 "layers" of the right electrode. As discussed in subsection "Impact of screening and external biases", in the model employed in this paper, all conditions for perfect screening are satisfied by using the "small" molecule as central region. Normally, to meet these conditions, several electrode layers are added to the "physical" molecule. For example, using the present nomenclature, the "small" molecule consists of a benzene dithiol (BDT = "physical") molecule and several gold layers in the benchmark Au–BDT–Au junctions. For this reason, the term "small" mole-

cule used in this paper refers to the smallest molecule ("smallest extended molecule") satisfying the perfect screening conditions (i) to (iii) formulated in the text. The detailed demonstration exposed above clearly reveals that the invariance discussed in this paper also holds for situations wherein both the properties of the molecule and those of the interactions at molecule–electrode interfaces are affected by the applied bias V, gate potentials V_G, defects (implying nonvanishing imaginary parts of the matrix elements):

$$H^{*}_{\mu,\mu'} \neq H_{\mu,\mu'} \equiv H_{\mu,\mu'}\left(V,V_G,\ldots\right), \qquad (31)$$

$$\tau^{*}_{L,R} \neq \tau_{L,R} \equiv \tau_{L,R}\left(V,V_G,\ldots\right). \qquad (32)$$

Although the electron spin has not been considered in order to simplify the presentation, the invariance discussed in this paper also holds in the presence of magnetic fields. One can see, for instance, that the quantities entering the relevant equations do not contain $t_{L,R}$ and $t^{*}_{L,R}$ or $\tau_{L,R}$ and $\tau^{*}_{L,R}$ separately, but only $|t_{L,R}|$ and $|\tau_{L,R}|$. However complicated the dependencies in the right hand side of Equation 31 and Equation 32 might be, they do not break the invariance demonstrated above. So, this invariance holds regardless of the potential profile across the junction and how the (possibly very nontrivial) potential drop depends on the electrode–molecule contact interactions. This holds regardless of how involved the self-consistent procedures needed to determine the potential landscape are. Needless to say, these are all highly nontrivial tasks for realistic/DFT approaches, for which even the correct description of the both (positive and negative) bias polarities in simpler molecular junctions is an issue (see, e.g., the discussion related to Figure 5 in [22]).

WBL-based schemes and realistic calculations

Within all treatments of uncorrelated transport based on Equation 1 and Equation 5 (which is the case of all NEGF-DFT flavors), the WBL represents a computationally attractive approximation. The fact that the WBL embedding self-energies $\Sigma^{C}_{L,R}$ (hence also the width functions $\Gamma^{C}_{L,R}$ in Equation 6) become ε-independent has a two-fold advantage. This scheme enables one to perform conventional DFT calculations for a finite, isolated, extended molecule (i.e., uncoupled to semi-infinite electrodes). In principle, this can be done with any common DFT package. The implementation is easy, because the post-processing step of adding ε-independent self energies (Equation 1) does not require any DFT-code modification. A further advantage is that the diagonalization can be done before performing transport calculations. This fact drastically reduces the computational effort, as emphasized recently [38]. By defin-

ition, the WBL (as well as the FBL) amounts to replacing the exact ε-dependent embedding self-energy with its value at the Fermi energy of the unbiased system, $\Sigma^{C,WBL}_{x} \equiv \Sigma^{C,exact}_{x}\left(\varepsilon\right)\big|_{\varepsilon=0}$. As can be seen from the inspection of Equation 1, Equation 5, and Equation 6, the transmission at the Fermi energy (zero-bias conductance) computed within the WBL coincides with the exact transmission. Therefore,

$$\mathcal{T}^{WBL}\left(\varepsilon\right)\big|_{\varepsilon=0} \equiv \mathcal{T}^{exact}\left(\varepsilon\right)\big|_{\varepsilon=0}, \qquad (33)$$

provided that $\mathbf{G}_{C,0}$ is computed exactly, otherwise

$$\mathcal{T}^{WBL}\left(\varepsilon\right) \neq \mathcal{T}^{exact}\left(\varepsilon\right). \qquad (34)$$

This is a general result that applies to any exact treatment of uncorrelated transport based on the trace formula of Equation 5. Two WBL schemes have been recently utilized within an NEGF-DFT framework [38], termed WBL-Molecule and WBL-Metal; the latter corresponds to a central region including 3 to 6 electrode layers (Figure 4b of [38]). In the present paper, the counterpart of WBL-Molecule is a junction wherein the central region has the Hamiltonian $\mathbf{H}$ (Equation 9), and the counterpart of WBL-Metal is a central region having the Hamiltonian $\mathbf{H}_{\mathbf{ext}}(l_0, r_0)$ (Equation 11, $3 \leq l_0 = r_0 \leq 6$). In both cases, the corresponding Hamiltonians are supplemented with WBL ε-independent embedding self-energies via Equation 1.

It is instructive to inspect the transmissions $\mathcal{T}\left(\varepsilon\right)$ computed at arbitrary energies and $V = 0$ within the full NEGF-DFT (full-SCF in the nomenclature of [38]), the WBL-Molecule, and the WBL-Metal methods shown in Figure 4b of [38].

In the light of Equation 34, the fact that those methods predict transmission values at arbitrary energies $\mathcal{T}\left(\varepsilon\right)$ that substantially differ from each other is not at all surprising. An initially surprising point in the present analysis is that (as seen in Figure 4b of [38]) even the transmissions $\mathcal{T}\left(\varepsilon = 0\right)$ computed at the Fermi energy via the three aforementioned methods do also significantly differ from each other, i.e.,

$$\mathcal{T}^{\text{Full-SCF}}(\varepsilon = 0) \neq \mathcal{T}^{\text{WBL-Metal}}(\varepsilon = 0) \neq \mathcal{T}^{\text{WBL-Molecule}}(\varepsilon = 0)$$
$$\neq \mathcal{T}^{\text{Full-SCF}}(\varepsilon = 0).$$

In fact, as expressed by Equation 33, these transmissions should have been equal, i.e.,

$$\mathcal{T}^{\text{Full-SCF}}(\varepsilon = 0) = \mathcal{T}^{\text{WBL-Metal}}(\varepsilon = 0) = \mathcal{T}^{\text{WBL-Molecule}}(\varepsilon = 0),$$

only if all values of $\mathbf{G}_{C,0}$ were exact. The differences between these values,

$$\mathcal{T}^{\text{Full-SCF}}(\varepsilon = 0) \neq \mathcal{T}^{\text{WBL-Metal}}(\varepsilon = 0) \neq \mathcal{T}^{\text{WBL-Molecule}}(\varepsilon = 0)$$
$$\neq \mathcal{T}^{\text{Full-SCF}}(\varepsilon = 0),$$

are due to the fact that, unlike the exact model calculation presented in this paper, neither the DFT-method employed to treat the full embedding (full NEGF-DFT), nor that for the isolated molecule (WBL-Molecule), or that for the molecule merely including several electrode layers (WBL-Metal) are exact. Even for a small isolated molecule (here named the WBL-Molecule case), the DFT results represent nothing but more or less (in)accurate approximations. The aforementioned differences also clearly reveal that, even within treatments at the same level of theory (e.g., using the same exchange-correlation functional and basis sets), the results for different molecular sizes are affected by (absolute and relative) errors in a different way. The above analysis also emphasizes that and why, based on "realistic" DFT state-of-the-art transport calculations, it is impossible to demonstrate the invariance envisaged in the present paper. These DFT-based approaches are too inaccurate for this purpose. To eliminate differences resulting from unreliable approaches one should go beyond the DFT level and resort to elaborate many-body schemes [16,39]. These many-body schemes are numerically prohibitive even at the lowest (*GW* [40]) level. For this reason, to be feasible, calculations cannot avoid treating electrodes within WBL(-type) approximations, justifiable only at low energies/biases. From this perspective, the results reported in this paper unfortunately do not convey a very optimistic message. While substantial theoretical improvements within the linear response limit are possible, reliable results for molecular transport beyond the ohmic range cannot be expected from elaborate ab initio many-body approaches (combined with WBL methods) even at (nowadays) numerically completely prohibitive molecular sizes (Figure 5 and Figure 6).

Conclusion

The results reported in the present paper can be summarized as follows: (i) The independence on the size of the extended molecule used to calculate both the equilibrium and nonequilibrium properties of a nanojunction is a minimal mandatory requirement of any sound theory of molecular transport. It was demonstrated that this invariance property is strictly obeyed for all molecules that can be described within single-particle pictures linked to chain-like electrodes. To the best of our knowledge, the present paper is the first rigorous study and demonstration of this invariance, which is a nontrivial result even for the simplest case of a molecule modeled as a single energy level. Real systems described within this framework include, e.g., atomic chains, quantum wires, carbon nanotubes, and (possibly DNA-based) bio and large organic molecules. To determine the

model parameter values, density functional based tight binding (DFTB) frameworks [18-20] represent the state-of-the-art. It is worth emphasizing the generality of the demonstration given in this study. The description of the molecules considered in this paper goes beyond conventional tight-binding nearest-neighbor (extended Hückel) approximations, wherein, for an *N*-site molecular chain, the only nonvanishing matrix elements are the on-site energies $H_{\mu,\mu} = \alpha$ ($1 \leq \mu \leq N$) and the nearest-neighbor hopping integrals $H_{\mu,\mu+1} = H_{\mu+1,\mu} = -\beta$ ($1 \leq \mu \leq N - 1$). Moreover, the Hermitean Hamiltonian matrix **H** of the "physical" molecule does not need to be real ($H_{\mu,\nu} = H_{\nu,\mu}^*$), and the molecule does not need to be one dimensional. Provided that electron correlations are neglected (they are ruled out by the bilinear form of **H** of Equation 10), **H** can include interactions with impurities, applied electric fields (e.g., source–drain bias, gate potentials), static (e.g., Peierls) distortions or proximity to other molecules from the environment. The fact that the matrix elements $H_{\mu,\nu}$ may depend on the bias *V* (e.g., Stark shift of orbital energies) [22,41-43] is particularly noteworthy. (ii) Considering a specific molecule or even a specific class of homologous molecular series, the demonstration of the envisaged invariance property would have been restricted to certain fixed values of the parameters $H_{\mu,\nu}$, possibly exhibiting specific and highly nontrivial bias dependence. From this perspective, it is important to re-emphasize that the invariance demonstrated in this paper holds for arbitrary values of the matrix elements $H_{\mu,\nu}$ and for arbitrary dependencies (e.g., on biases) of these matrix elements. Therefore, in particular, it is not limited to some nanojunctions based on certain molecular species. (iii) Further, it was shown that unlike the exact approach, the approximate approaches based on the limits of wide- and flat-electrode bands nonphysically predict nonequilibrium properties that depend on the size of the central region utilized in calculations. In conjunction with these approximations, the effect of negative differential resistance (NDR) was discussed. It was found that, although qualitatively correct, the quantitative treatment of NDR is unsatisfactory within the FBL. Because the quantitative difference between the exact treatment and FBL is the energy dependence of the width functions $\Gamma_{L,R}$ (or, equivalently, the density of states at the contacts), this finding can be reframed as an indication that achieving NDR effects stronger than obtained so far [44] may primarily be a problem of contact engineering. (iv) The analysis done in conjunction with the WBL and FBL has made it clear that studies on nonequilibrium transport properties at finite temperatures require more elaborated theoretical levels than studies on linear response ($V \rightarrow 0$) properties at zero temperature. Low-temperature properties like the low bias conductance (and therefore also the related β factor of exponential attenuation with increasing molecular size) as well as other properties (e.g., thermopower $S \propto [\partial \log \mathcal{T}(\varepsilon) / \partial \varepsilon]_{\varepsilon=0}$ [45]), to which only energies very close

to the equilibrium Fermi level contribute, can be obtained within the WBL/FBL. However, studies on the properties away from equilibrium (besides *I–V* curves one can also mention current noise power [46-48], for which the knowledge of transmission at the Fermi energy does not suffice [49]) should go beyond the WBL or FBL. (v) Last but not least, it was demonstrated (Figure 2b,c, and Figure 5a,b) that transport calculations with an exact treatment of electrodes adjacent to the active molecule and semi-infinite electrodes within the currently employed WBL or FBL may yield spurious "predictions" of unphysical features in theoretically calculated *I–V* curves at higher biases. This procedure, which is equivalent to treating electrode layers included in the extended molecule and semi-infinite electrodes at different levels of theory, resembles current procedures used in "realistic" NEGF-DFT approaches. Therefore, these findings deserve consideration in molecular transport studies beyond the ohmic regime.

Supporting Information

Supporting Information File 1

Mathematical details for the demonstration that the small molecule and minimally extended molecule yield identical physical properties.
[http://www.beilstein-journals.org/bjnano/content/supplementary/2190-4286-7-37-S1.pdf]

Acknowledgements

References

1. Haug, H. J. W.; Jauho, A.-P. *Quantum Kinetics in Transport and Optics of Semiconductors,* 2nd ed.; Springer Series in Solid-State Sciences, Vol. 123; Springer: Berlin, Germany, 2008.
2. Datta, S. *Electronic Transport in Mesoscopic Systems;* Cambridge University Press: Cambridge, United Kingdom, 1997.
3. Datta, S. *Quantum Transport: Atom to Transistor;* Cambridge University Press: Cambridge, United Kingdom, 2005.
4. Cuevas, J. C.; Scheer, E. *Molecular Electronics: An Introduction to Theory and Experiment;* World Scientific Publishing: Singapore, 2010.
5. Baym, G.; Kadanoff, L. P. *Phys. Rev.* **1961,** *124,* 287–299. doi:10.1103/PhysRev.124.287
6. Baym, G. *Phys. Rev.* **1962,** *127,* 1391–1401. doi:10.1103/PhysRev.127.1391
7. Kadanoff, L.; Baym, G. *Quantum Statistical Mechanics;* Benjamin: Reading, MA, U.S.A., 1962.
8. Caroli, C.; Combescot, R.; Nozieres, P.; Saint-James, D. *J. Phys. C: Solid State Phys.* **1971,** *4,* 916. doi:10.1088/0022-3719/4/8/018
9. Caroli, C.; Combescot, R.; Lederer, D.; Nozieres, P.; Saint-James, D. *J. Phys. C: Solid State Phys.* **1971,** *4,* 2598. doi:10.1088/0022-3719/4/16/025
10. Bâldea, I.; Köppel, H. *Phys. Rev. B* **2008,** *78,* 115315. doi:10.1103/PhysRevB.78.115315
11. Bâldea, I.; Köppel, H. *Phys. Rev. B* **2009,** *80,* 165301. doi:10.1103/PhysRevB.80.165301
12. Bâldea, I.; Köppel, H. *Phys. Rev. B* **2010,** *82,* 087302. doi:10.1103/PhysRevB.82.087302
13. Bâldea, I.; Köppel, H. *Phys. Rev. B* **2011,** *84,* 037305. doi:10.1103/PhysRevB.84.037305
14. Meir, Y.; Wingreen, N. S. *Phys. Rev. Lett.* **1992,** *68,* 2512–2515. doi:10.1103/PhysRevLett.68.2512
15. Jauho, A.-P.; Wingreen, N. S.; Meir, Y. *Phys. Rev. B* **1994,** *50,* 5528–5544. doi:10.1103/PhysRevB.50.5528
16. Mahan, G. D. *Many-Particle Physics;* Plenum Press: New York, NY, U.S.A., 1990.
17. Fisher, D. S.; Lee, P. A. *Phys. Rev. B* **1981,** *23,* 6851–6854. doi:10.1103/PhysRevB.23.6851
18. Elstner, M.; Porezag, D.; Jungnickel, G.; Elsner, J.; Haugk, M.; Frauenheim, T.; Suhai, S.; Seifert, G. *Phys. Rev. B* **1998,** *58,* 7260–7268. doi:10.1103/PhysRevB.58.7260
19. Pecchia, A.; Di Carlo, A. *Rep. Prog. Phys.* **2004,** *67,* 1497. doi:10.1088/0034-4885/67/8/R04
20. DFTB codes. http://www.dftb.org/codes/ (accessed Feb 11, 2016).
21. Bâldea, I.; Köppel, H. *Phys. Rev. B* **2010,** *81,* 193401. doi:10.1103/PhysRevB.81.193401
22. Bâldea, I. *Phys. Rev. B* **2012,** *85,* 035442. doi:10.1103/PhysRevB.85.035442
23. Bâldea, I.; Xie, Z.; Frisbie, C. D. *Nanoscale* **2015,** *7,* 10465–10471. doi:10.1039/C5NR02225H
24. Xie, Z.; Bâldea, I.; Smith, C.; Wu, Y.; Frisbie, C. D. *ACS Nano* **2015,** *9,* 8022–8036. doi:10.1021/acsnano.5b01629
25. Parida, P.; Pati, S. K.; Painelli, A. *Phys. Rev. B* **2011,** *83,* 165404. doi:10.1103/PhysRevB.83.165404
26. Einhellinger, M.; Cojuhovschi, A.; Jeckelmann, E. *Phys. Rev. B* **2012,** *85,* 235141. doi:10.1103/PhysRevB.85.235141
27. Pertsova, A.; Stamenova, M.; Sanvito, S. *J. Phys.: Condens. Matter* **2013,** *25,* 105501. doi:10.1088/0953-8984/25/10/105501
28. Tanaka, Y.; Yonemitsu, K. *J. Phys. Soc. Jpn.* **2014,** *83,* 124704. doi:10.7566/JPSJ.83.124704
29. Bâldea, I. *Phys. Chem. Chem. Phys.* **2015,** *17,* 20217–20230. doi:10.1039/C5CP02595H
30. Langreth, D. C. *Phys. Rev.* **1966,** *150,* 516–518. doi:10.1103/PhysRev.150.516
31. Shiba, H. *Prog. Theor. Phys.* **1975,** *54,* 967–981. doi:10.1143/PTP.54.967
32. Ng, T. K.; Lee, P. A. *Phys. Rev. Lett.* **1988,** *61,* 1768–1771. doi:10.1103/PhysRevLett.61.1768
33. Glazman, L. I.; Raikh, M. E. *JETP Lett.* **1988,** *47,* 452–455.
34. Wang, S.; Ha, M.; Manno, M.; Frisbie, C. D.; Leighton, C. *Nat. Commun.* **2012,** *3,* No. 1210. doi:10.1038/ncomms2213
35. Xie, W.; Wang, S.; Zhang, X.; Leighton, C.; Frisbie, C. D. *Phys. Rev. Lett.* **2014,** *113,* 246602. doi:10.1103/PhysRevLett.113.246602
36. Reuter, M. G.; Harrison, R. J. *J. Chem. Phys.* **2013,** *139,* 114104. doi:10.1063/1.4821176

37. Roland, C.; Meunier, V.; Larade, B.; Guo, H. *Phys. Rev. B* **2002,** *66,* 035332. doi:10.1103/PhysRevB.66.035332

38. Verzijl, C. J. O.; Seldenthuis, J. S.; Thijssen, J. M. *J. Chem. Phys.* **2013,** *138,* 094102. doi:10.1063/1.4793259

39. von Niessen, W.; Schirmer, J.; Cederbaum, L. S. *Comput. Phys. Rep.* **1984,** *1,* 57–125. doi:10.1016/0167-7977(84)90002-9

40. Aryasetiawan, F.; Gunnarsson, O. *Rep. Prog. Phys.* **1998,** *61,* 237–312. doi:10.1088/0034-4885/61/3/002

41. Zahid, F.; Paulsson, M.; Datta, S. Electrical Conduction through Molecules. In *Advanced Semiconductors and Organic Nano-Techniques;* Morkoç, H., Ed.; Academic Press: Cambridge, MA, U.S.A., 2003.

42. Medvedev, I. G. *Phys. Rev. B* **2007,** *76,* 125312. doi:10.1103/PhysRevB.76.125312

43. Bâldea, I. *Phys. Chem. Chem. Phys.* **2014,** *16,* 25942–25949. doi:10.1039/C4CP04316B

44. Xu, B.; Dubi, Y. *J. Phys.: Condens. Matter* **2015,** *27,* 263202. doi:10.1088/0953-8984/27/26/263202

45. Paulsson, M.; Datta, S. *Phys. Rev. B* **2003,** *67,* 241403. doi:10.1103/PhysRevB.67.241403

46. Blanter, Ya. M.; Büttiker, M. *Phys. Rep.* **2000,** *336,* 1–166. doi:10.1016/S0370-1573(99)00123-4

47. Djukic, D.; van Ruitenbeek, J. M. *Nano Lett.* **2006,** *6,* 789–793. doi:10.1021/nl060116e

48. Kiguchi, M.; Tal, O.; Wohlthat, S.; Pauly, F.; Krieger, M.; Djukic, D.; Cuevas, J. C.; van Ruitenbeek, J. M. *Phys. Rev. Lett.* **2008,** *101,* 046801. doi:10.1103/PhysRevLett.101.046801

49. Bâldea, I. *J. Phys. Chem. C* **2014,** *118,* 8676–8684. doi:10.1021/jp412675k

50. bwHPC-C5 -Startseite. http://www.bwhpc-c5.de/en/index.php (accessed Feb 11, 2016).